The synthesis of novel tungsten precursors for the CVD of tungsten oxide

Williams, Paul Andrew

Award date:
2000

Awarding institution:
University of Bath

THE SYNTHESIS OF NOVEL TUNGSTEN PRECURSORS FOR THE CVD OF TUNGSTEN OXIDE

submitted by Paul Andrew Williams

for the degree of PhD
of the University of Bath
2000

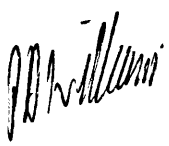

ProQuest LLC
789 East Eisenhower Parkway
P.O. Box 1346
Ann Arbor, MI 48106-1346

CONTENTS

Chapter Three : Fluorinated Oxotetraalkoxide

Chapter Four : Donor-functionalized Alkoxides

Appendices

ABSTRACT

The research described in this thesis has been concerned with the synthesis and characterisation of a range of tungsten(VI) compounds for the CVD of tungsten oxide thin films. Three classes of compounds have been investigated; phenoxide compounds, donor-functionalised alkoxides and a fluorinated oxotetraalkoxide.

Chapter One - Introduction - provides information on the applications of tungsten oxide thin films and a brief overview of the various deposition techniques available. Chemical vapour deposition (CVD) is then discussed with particular emphasis on atmospheric-pressure CVD (APCVD) and aerosol-assisted CVD (AACVD), followed by a review of precursors previously used for the deposition of tungsten oxide thin films. The chemistry of tungsten(VI) is then briefly discussed.

Chapter Two - Tungsten(VI) Hexaphenoxides - details the synthesis, characterisation and subsequent AACVD of three tungsten(VI) hexaphenoxide compounds. The compounds have been characterised by NMR spectroscopy and single crystal X-ray diffraction before being used as AACVD precursors. Deposition conditions are described, followed by analysis of the films composition and optical properties.

Chapter Three - Fluorinated Oxotetraalkoxide - describes the synthesis and characterisation of a monomeric fluorinated oxotetraalkoxide compound. The compound was characterised as monomeric by NMR and mass spectroscopy, and subsequently tested as an APCVD precursor. APCVD conditions are provided, followed by compositional and optical analysis of the thin films deposited.

Chapter Four - Donor-functionalized Alkoxides - details the synthesis and characterisation of two tungsten(VI) donor-functionalized alkoxides and their subsequent use as AACVD precursors. Compounds have been characterised by variable temperature NMR spectroscopy before testing as AACVD precursors. Details of the AACVD conditions used, and the film analysis are included.

There follows a brief conclusions section highlighting precursor properties and films deposited, in addition to suggestions for further work in this area. The appendices give crystallographic data, ICDD pattern number data and details of the instrumentation. Details of the CVD reactor and precursor delivery techniques used during this research are also included.

ACKNOWLEDGEMENTS

Firstly, I would like to thank my supervisor, Dr. Kieran Molloy for all his guidance and support during this work, and especially during the writing of the this thesis and the VTNMR analysis included. I am also extremely grateful to Dr. Mike Whittlesey for countless hours spent running VTNMR experiments, and to Dr. Andrew Weller and the whole group, for their assistance while analysing all the VTNMR spectra. I would also like to thank Dr. Mary Mahon and Dr. Jon Steed (King's College London) for the crystallographic data included. Financial support from the E.P.S.R.C. and Pilkington plc is gratefully acknowledged.

I would like to thank the technical staff, Robert, Ahmed and Sheila for their help and co-operation during practical work, and Alan Carver, Dave and Harry for the microanalysis and NMR spectroscopy. I would especially like to thank Dave for his patience while running tungsten NMR spectra.

I must also thank all at Lathom for their assistance, and for making me feel welcome during several visits, particularly Simon Hurst, for getting samples analysed, Dr. Kevin Sanderson, for assistance in analysing XRD patterns, and John Ridealgh for his excellent bed and breakfast facilities.

I would also like to thank all who have come and gone in the lab during my time at Bath, particularly Tony Swain, Tom Hibbert, Virginie Ogrodnik, Marie Barret, Graeme Horley, Jo Stanley, Kim Wong and Aliki Kana, thanks for making the last three years such good fun.

Finally, I would like to thank my Father for his continued support, and my brother for owning a faster car then me, and letting me drive it occasionally.

ABBREVIATIONS

AACVD	:	Aerosol-Assisted CVD	L	:	Ligand
Ac	:	Acetate	LPCVD	:	Low-Pressure CVD
acac	:	2,4-Pentanedione	m	:	multiplet
APCVD	:	Atmospheric Pressure CVD	m.p.	:	melting point
Ar	:	Aryl	Me	:	Methyl
b.p.	:	boiling point	MOCVD	:	Metal-Organic CVD
Bu	:	Butyl	NMR	:	Nuclear Magnetic Resonance
^{t}Bu	:	Tertiary Butyl	PAA	:	Polyacrylic Acid
Cp*	:	Pentamethylcyclopentadienyl	Ph	:	Phenyl
CVD	:	Chemical Vapour Deposition	ppm	:	parts per million
d	:	Doublet	^{i}Pr	:	Isopropyl
dd	:	Doublet of doublets	q	:	quartet
diars	:	1,2-bis(dimethylarsino) benzene	r.t.	:	room temperature
dien	:	Diethylenetriamine	R_f	:	Fluorinated Alkyl Group
dmae	:	Dimethylaminoethoxide	s	:	singlet
dmap	:	Diethylaminopropoxide	SEM	:	Scanning Electron Microscopy
dme	:	Dimethylether	t	:	triplet
EI	:	Electron Impact	tach	:	1,3,5-Triaminocyclohexane
esd	:	Estimated Standard Deviation	tfac	:	1,1,1-Trifluoro-2,4-pentanedione
Et	:	Ethyl	THF	:	Tetrahydrofuran
FTIR	:	Fourier Transform Infra-Red	UV	:	Ultraviolet
H_2eg	:	1,2-Ethanediol	VTNMR	:	Variable Temperature NMR
IR	:	Infra-Red	XPS	:	X-Ray Photoelectron Spectroscopy
hfac	:	1,1,1,5,5,5-Hexafluoro-2,4-pentanedione	XRD	:	X-Ray Diffraction
ICDD	:	International Centre for Diffraction Data			

Chapter One

Introduction

1.1 INTRODUCTION

The work during the preparation of this thesis has involved the synthesis of several novel tungsten(VI) compounds for use as precursors for the growth of tungsten oxide thin films by chemical vapour deposition. The aim of this first chapter is to provide some background information on the applications of tungsten oxide thin films, to summarise the CVD process and different precursor delivery techniques available, and to briefly discuss tungsten(VI) chemistry relevant to precursor design.

1.1.1 Tungsten(VI) Oxide Thin Films

Tungsten oxide was the first electrochromic material to be discovered.[1] It was first discussed by Deb[2] in 1969, although it is thought the electrochromic nature had been observed long before that time. There are several tungsten oxides known, the two stoichiometric phases of tungsten oxide are tungsten trioxide (WO_3) and tungsten dioxide (WO_2). However, tungsten oxide also has a tendency to form sub-stoichiometric phases.

Stoichiometric WO_3 is yellow in colour, the tungsten atoms are in the +VI oxidation state with the tungsten 5*d* shell empty.[3] The crystal structure of stoichiometric WO_3 is of the perovskite-type. The perovskite structure, of configuration CMO_3, is illustrated in Figure 1.1. The metal ions (M) occupy the corners of a primitive unit cell and the oxygen ions bisect the unit cell edges. The central atom (C) is absent in most oxides. This gives rise to the defect perovskite configuration (MO_3) which is often referred to as the rhenium oxide structure.[1]

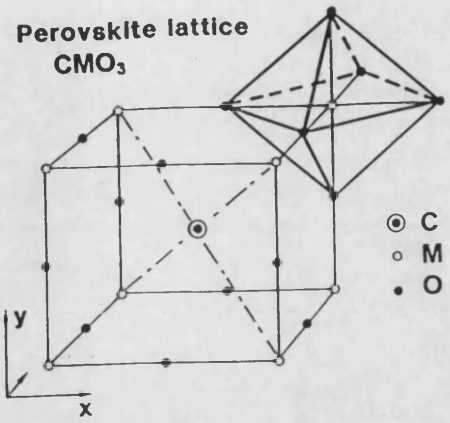

Figure 1.1 Unit cell for perovskite lattice.[1]

The structure of stoichiometric WO_3 consists of a three-dimensional array of corner linked WO_6 octahedra building up to give a slightly distorted ReO_3 type structure. The ReO_3 type structure in WO_3 is slightly distorted due to interactions between the molecular orbitals on the tungsten and oxygen atoms.[4] Additionally, some atomic displacements and rotations of the WO_6 octahedra normally occur so that tetragonal, orthorhombic, monoclinic or triclinic symmetries are found.

The second known stoichimetric form of tungsten oxide is tungsten dioxide (WO_2). Tungsten dioxide has a distorted rutile structure as displayed in Figure 1.2. The tungsten dioxide structure is again built up from WO_6 octahedra. However, unlike the distorted pervoskite configuration in tungsten trioxide, where the octahedra are corner sharing, the distorted rutile type structure is generally built up from edge sharing octahedra.[1,4,5]

In addition to the two stoichiometric phases of tungsten oxide, sub-stoichiometric, (or Magnéli) phases of tungsten oxide are also known. As oxygen is progressively eliminated from the distorted ReO_3 type structure a whole series of W_nO_{3n-1} stoichiometries are possible. Studies were carried out by Magnéli on both tungsten and molybdenum oxide systems. For tungsten oxide systems Magnéli found, and structurally determined, essentially four phases: WO_3, $W_{20}O_{58}$ ($WO_{2.9}$), $W_{18}O_{49}$

oxide is usually coloured blue. The blue colour is generally attributed to an excess of electron charge localised at the octahedra base units $[W^{5+}O_6]$.[3,4,7]

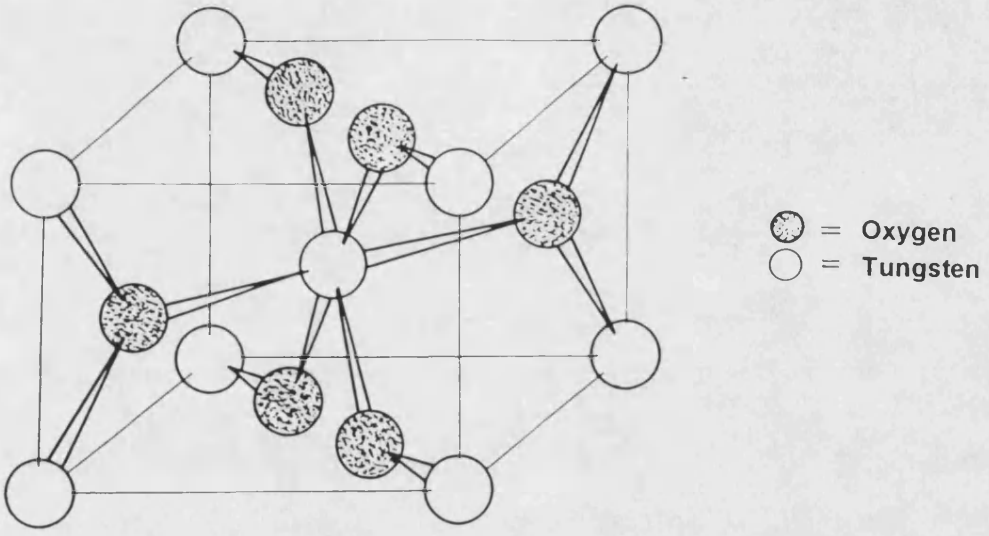

Figure 1.2 Rutile structure.

1.2 APPLICATIONS OF TUNGSTEN OXIDE THIN FILMS

1.2.1 Electrochromic devices

Electrochromism is the ability of a material, or system, to change its optical properties in a reversible and persistent manner in response to an applied external voltage. There are many inorganic and organic materials with electrochromic properties, examples of which are MoO_3, Nb_2O_5, TiO_2 and 4,4-bipyridinium salts. The main advantage of organic electrochromic materials is their rapid switching capability. However, an undesired and irreversible side reaction of the weakly bound hydrogen or

nitrogen ions is a general disadvantage of organic electrochromic materials and is one of the reasons for their short lifetimes and poor UV stability.[8] Transition metal oxides are generally more stable and have been studied in great detail, the most widely investigated and applied electrochromic substance is tungsten trioxide (WO_3).[9-19]

The basic design for a five layer electrochromic device is shown in Figure 1.3. The device consists of an active *electrochromic layer* (WO_3) that is coloured or bleached by the injection or ejection of charged species. A counter electrode or *ion storage electrode*, storing the charged species that are not in the electrochromic layer. An *electrolyte*, which is ion conducting but electron insulating, placed between the electrochromic layer and the counter electrode. Two *conductive metal oxide* layers which are sandwiched between a *substrate*, usually glass.

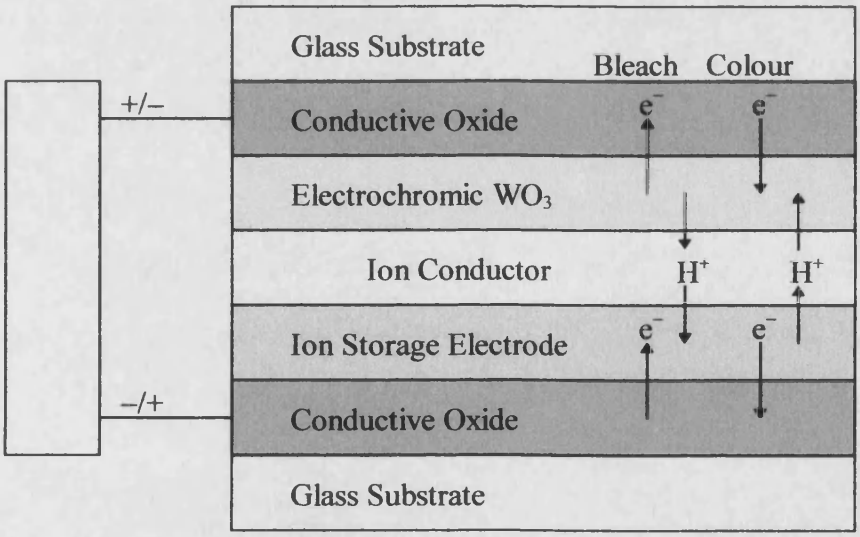

Figure 1.3 Basic design of an electrochromic device.[12]

The charge injection in tungsten trioxide can be represented highly schematically by the following equation :

$$\underset{\textit{colourless}}{WO_3} + xI^+ + xe^- \leftrightarrow \underset{\textit{blue}}{I_xWO_3} \qquad [1.1]$$

$$\textit{bleached} \qquad\qquad \textit{coloured}$$

where I^+ is a singly charged small ion such as hydrogen or lithium and $0 < x < 1$. Electrochromic devices can be used in the construction of displays, active optical filters, automotive rear-view mirrors with adjustable reflectance and smart windows with adjustable absorption and reflectance in the visible and near infrared wavelengths.[1,8,12]

1.2.2 Gas sensors

Gas sensors operate by reversible chemisorption of a reactive gas at the surface of a metal oxide film. The adsorption of a gaseous species changes the conductivity of the metal oxide film and the gaseous species is thus detected. The conductance changes in semiconductor materials are caused primarily by changes in the carrier concentration due to charge exchange with the adsorbed gaseous species.[20]

Tungsten oxide thin films have only recently been studied for use in gas sensing applications. Gas species which have been studied using tungsten oxide films include ammonia,[21,22] in which the films were loaded with gold or polyacrylic acid, hydrogen sulfide[23,24,25] and NO_x gaseous species.[26-30] Tungsten oxide films which have been used for sensing hydrogen sulfide gas have been both amorphous and crystalline. It was discovered that the crystalline films were more sensitive and displayed faster response characteristics. The films were initially deposited as amorphous films then annealed to yield a distorted rhenium oxide type crystal structure.[23]

Tungsten oxide thin films which were deposited by r.f. sputtering techniques were analysed for their ability to detect NO_x gaseous species. The d.c. electrical response of WO_3 films was measured for a selection of gaseous species over a temperature range of 100-400°C. The films displayed an increase in electrical resistance

with a good sensitivity toward NO_x gaseous species at 250°C. The tungsten oxide films were also shown to detect NH_3, H_2, H_2S and SO_2 gases by a decrease in their electrical resistance. The deposited films were shown to be practically insensitive to interfering gases like CO and CH_4 in the same temperature range.[28,29]

1.2.3 Solar control

Tungsten oxide thin films have displayed optical properties that could make them suitable for use as solar control coatings.[11,31,32,33] Solar control coatings allow the transmittance of visible light, 350-780nm, but reflect the near infrared wavelengths. Figure 1.4 displays solar spectrum as seen on earth.

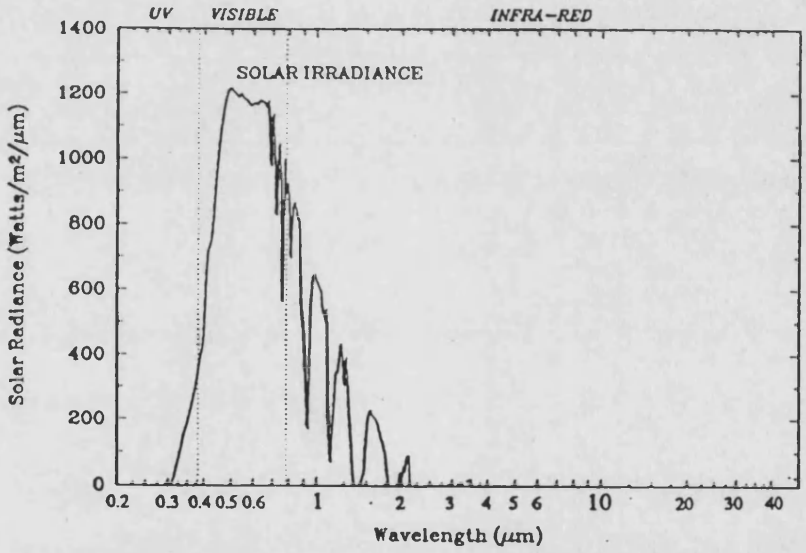

Figure 1.4 Solar spectrum from the surface of the earth.[34]

The solar spectrum can be split into three regions; UV, visible and infrared radiation. The infrared region of the solar spectrum is between approximately 780-2000nm. Glass is appreciated for its transparency to visible radiation and is used extensively in the building industry. However, in a hot climate the transmittance of the whole of the solar spectrum, including the infrared portion, is often undesirable as it can lead to the over heating of the building.[35] Therefore, it is desirable to apply a coating to the glass surface that allows the transmission of visible radiation from the sun but reflects the infrared portion of the solar spectrum. The deposition of tungsten oxide films and, in part, their suitability as solar control coatings forms the substance of this thesis.

1.3 THIN FILM DEPOSITION TECHNIQUES

Tungsten oxide thin films have been deposited by a variety of different techniques, which include conventional atmospheric pressure chemical vapour deposition (APCVD),[36,37] APCVD of a tungsten metal film followed by an annealing step to give the desired metal oxide film,[10,31,38,39] spray pyrolysis,[40,41] low pressure CVD,[42] Sol-gel[43,44] and sputtering.[14,30,45]

In this thesis both APCVD and aerosol-assisted CVD (AACVD) have been used. Therefore, CVD as a general technique will be discussed in greater detail than the other possible techniques for the deposition of tungsten oxide thin films.

1.3.1 Chemical Vapour Deposition

CVD consists of a reaction involving one or more gaseous species forming a thin film on a solid surface.[46,47] Metallic oxides are usually deposited by the vaporisation of an organometallic precursor followed by its in-situ oxidation to give the thin film. The CVD technique has found widespread use for the deposition of thin metallic oxide films

CVD technique has found widespread use for the deposition of thin metallic oxide films in both the electronic and building industries.[35,48] During the CVD process, chemical reactions may occur in the gas phase, at the surface of the substrate or both. The conditions within a CVD reactor and the chemistry involved often make it difficult to determine the exact mechanism of film growth, however, a number of important key steps in the CVD process have been identified (Figure 1.5).[48-50]

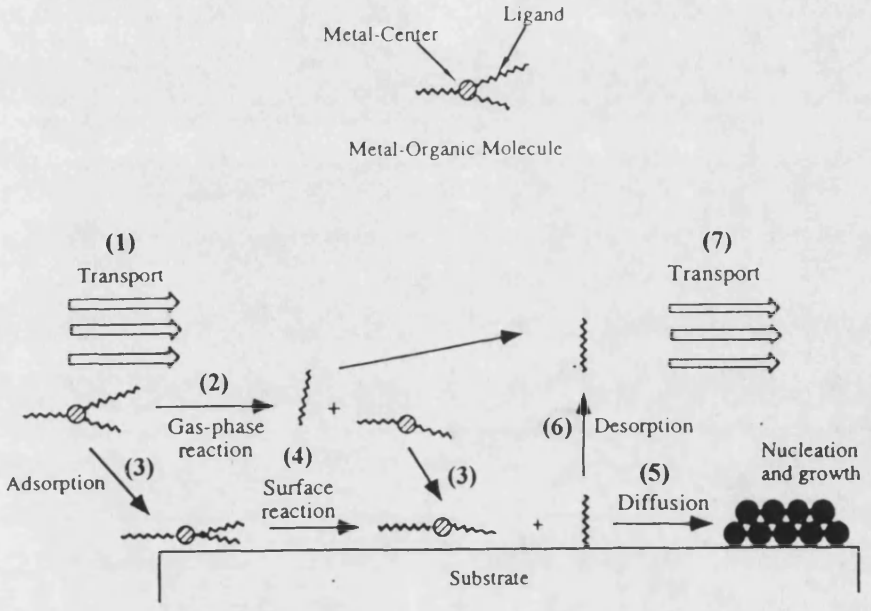

Figure 1.5 Key steps in the CVD process.[50]

(1) *Mass transport of the precursor in a gas flow from the reactor inlet to the substrate.*

(2) *Gas phase reactions leading to the formation of film precursors and by-products.*

(3) *Adsorption of film precursors on the substrate.*

(4) *Surface diffusion of film precursors to nucleation site.*

(5) *Surface reactions and incorporation of film constituents in to the growing film.*

(6) *Desorption of the by-products of the surface reaction.*

(7) *Transport of the by-products in the bulk gas flow away from the growing film towards reactor exit.*

The key steps in the CVD process generally apply to the deposition of thin films from all CVD deposition techniques. For the CVD process to be of any value it must produce thin films with reproducible and controllable properties. The purity, composition, thickness, adhesion, microstructure and surface morphology of the deposited films must be reproducible for the same reactor conditions. The rate of film deposition should be reasonable, and the growth process of the film should have no significant effect on the substrate.

1.3.1.1 CVD Growth Process

Gas phase transport and adsorption of the precursor to the substrate are the most common rate limiting steps during the CVD growth process. Once adsorbed to the substrate surface the precursor may diffuse to a nucleation site. The growth of the film then typically occurs by one of three primary mechanisms, Figure 1.6.[52]

(a) *Layer or Franck-van der Merwe growth.*

(b) *Layer plus Island or Stranski-Krastanov growth.*

(c) *Island or Volmer-Weber growth.*

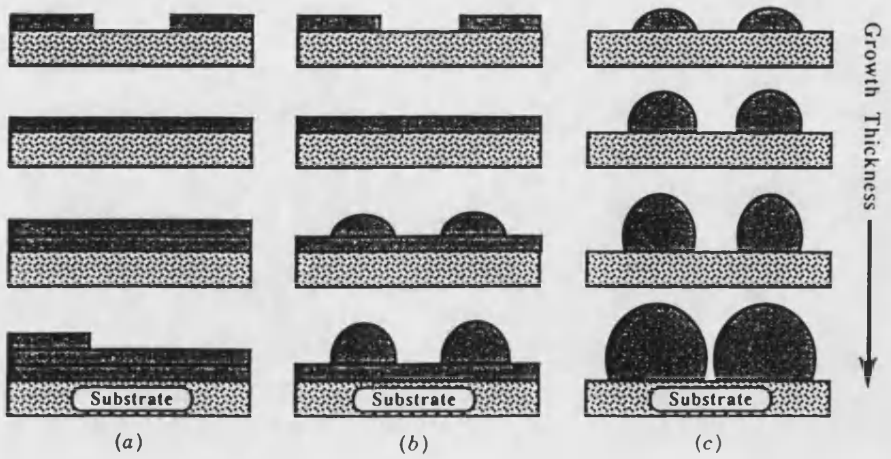

Figure 1.6 CVD growth modes.

These simplified growth modes are assumed to occur on a substrate with no surface defects. The formation of films by a particular growth mechanism is dictated by the nature of the interaction between the growing film and the substrate, the thermodynamics of adsorption and the kinetics of crystal growth.

In layer, or Franck-van der Merwe, growth the atoms deposited are equally or less strongly bound to each other than the substrate. The first layer formed is typically a monolayer covering the whole surface. This is then covered by a more weakly bound second layer, then a third layer and thus the film is deposited. It is also possible for a second layer to begin growing on the first prior to the complete coverage of the substrate. This growth process is referred to as simultaneous multilayer growth and its occurrence depends on the relative rates of nucleation and growth of the film.

In layer plus island, or Stranski-Krastanov, growth a layer is initially deposited on the substrate. However, after several layers have been deposited layer growth becomes unfavourable and islands form on the previously deposited layers. This growth is thought to occur when the molecular orientation of the precursor that leads to layer growth is no longer possible in successive layers. Highly strained intermediate monolayers can be formed and deposition on these strained layers leads to the formation and growth of islands. This type of growth process is highly dependent on the nature of the substrate and the deposition temperature.

The final type of typical deposition is island, or Volmer-Weber, growth. Small droplets or clusters nucleate directly on the substrate and grow into islands of the film material. These islands eventually coalesce to form a continuous film. This type of film growth occurs when the atoms are more strongly bound to each other than to the substrate surface.

1.3.1.2 Reactor Design

The CVD of metal oxides has been carried out in many types of reactor and the choice of reactor can have a profound affect on the deposition process. However, the two most common reactors used for CVD are hot-walled and cold-walled reactors. The difference between these two types of reactor is fairly self explanatory.

Hot-wall reactors have been used extensively on the laboratory scale, however, they do have significant disadvantages.

(1) *Decomposition of the precursor can not only occur on the substrate but on the reactor walls. These deposits will eventually fall off and contaminate the substrate surface.*

(2) *Precursor consumption is high due to the relatively large area coated (both the walls and the substrate).*

(3) *Since reactions occur on the walls of the reactor, the fraction of the surface area of the reactor on which deposition has occurred can change with time during an experiment and from one experiment to another. This can lead to problems reproducing deposition conditions.*

These disadvantages generally limit hot-wall reactors to quantitative measurements of reaction kinetics and in circumstances where precursors of high vapour pressure are readily available.

Cold-wall reactors are generally more widely used in the laboratory and in industry. Cold-wall reactors are relatively simple in construction with control of pressure and temperature possible within the reactor. Since the walls of the reactor are not being coated the quantity of precursor required is generally smaller, therefore, higher deposition rates can be attained than for hot-wall reactors. Cold-wall reactors are particularly suitable for selective deposition studies as deposition on the reactor walls does not occur. However, cold-wall reactors are more prone to turbulence and secondary flow effects brought about by temperature gradients within the reactor.

1.3.1.3 Typical Precursor Properties

There are a number of key steps in the CVD process (section 1.3.1). Therefore, when designing a precursor to deposit a particular metal oxide thin film its properties should facilitate these steps. The general criteria for precursor properties are:[53]

(1) *The precursor should have good volatility to enable easy transport to the reactor.*
(2) *Precursors which are liquids at the bubbler temperature are preferred so the transport rate of the precursor to the reactor is constant.*
(3) *The precursor should be thermally stable during its vaporisation and transport to the substrate.*
(4) *Decomposition of the precursor should be clean, thereby eliminating any impurities from the metal oxide film.*
(5) *The precursor should be of high purity.*
(6) *It is advantageous for the precursor and its decomposition products to be non-toxic and non-pyrophoric.*
(7) *A precursor which is both air and moisture stable is advantageous for handling and storage.*
(8) *The precursor should be readily available at low cost.*

While this list displays the properties that are ideally required from a precursor, some of these criteria are more important than others. For example, it is possible to use precursors which are both air and moisture sensitive so long as care is taken in their use.

Volatility of the precursor is considered one of the most important criteria for its use in CVD. It is important to achieve a high vapour pressure to ensure transport of a constant quantity of precursor to the substrate. Typical methods of engineering a compound with a good vapour pressure are to ensure the polarizability, dipoles and interaction between molecules (e.g. suppression of H-bonds or dimerisation) are minimised. Liquid precursors at the bubbler temperature are preferred, as when a solid

reagent is used the carrier over of the precursor can vary during the deposition process due to the changing surface area of the solid as it is consumed.

Organometallic and metal-organic precursors have been extensively used for CVD and are generally preferred to inorganic precursors for the following reasons:

(1) *They often decompose at lower temperatures.*

(2) *They usually have higher vapour pressures.*

(3) *They are often liquids which can simplify the delivery of the precursor.*

However, organometallic and metal-organic precursors do have one crucial disadvantage when compared to inorganic precursors, that of impurity incorporation in the films deposited. The incorporation of impurities from the ligand can be overcome by a suitable decomposition pathway which removes the organic groups from the reactor before contaminating the growing film. One example of this is found in the deposition of aluminium metal films from triisobutylaluminum, where a β-hydride elimination reaction cleaves the metal-carbon bond producing an aluminium film (Figure 1.7).[54]

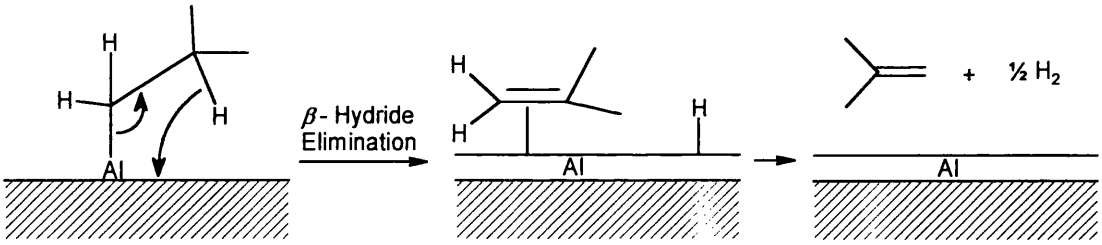

Figure 1.7 β-hydride elimination reaction proposed for the growth of aluminium films from triisobutylaluminum.

Figure 1.7 shows the proposed decomposition pathway for the reaction of triisobutylaluminum at the substrate surface. The β-hydride elimination reaction gives pure aluminium films with no carbon incorporation at temperatures between 450-600°C and evolves hydrogen and isobutylene as the by-products. This example illustrates the

advantage of organometallic or metal-organic precursors when compared with inorganic precursors.

1.3.1.4 Advantages of CVD

CVD is widely used as a deposition technique and has a number of advantages over other techniques used for the deposition of thin metal or metal oxide films.

(1) *Low deposition temperatures compared to other techniques.*
(2) *Lower temperatures frequently lead to a clean and controllable stoichiometric deposition process.*
(3) *Significant reduction in migration at the film-substrate interface (non-CVD techniques carried out at higher temperatures often display interlayer diffusion and result in ill-defined interlayer junctions).*
(4) *Conformal coverage (the ability to deposit a thin film of a uniform thickness on a complex topographical surface).*
(5) *Selective area and pattern deposition capabilities.*
(6) *The deposited films are of high quality.*
(7) *High film deposition rates.*
(8) *Experimental ease of depositing from the starting precursor.*
(9) *Ability for larger scale production process.*
(10) *Low cost.*

Metal oxide thin films have been deposited by the vaporisation of a metal containing compound followed by the subsequent *in-situ* oxidation of the compound to give a metal oxide film on the substrate. The vaporised precursor is carried in the gas phase by an inert gas (usually nitrogen, but argon and helium have also been used) to the reactor where the film is deposited. At some stage during this transport process an oxidising agent, usually oxygen, may be added to the reactive gas flow. Despite the simplicity of the process there are a number of variables; e.g. precursor temperature,

substrate temperature, gas flow rates and deposition time. Therefore, the initial deposition conditions must be estimated until the process can be optimised.

For the deposition of tungsten oxide thin films reported in the literature the addition of an oxidising agent has been problematic and the premixing of oxygen with the reactive gas flow has met with little success.[9,10] Typically, tungsten metal is deposited by CVD then annealed in an oxygen environment.[9,10,31,42] High quality tungsten oxide films have been deposited in a single step by r.f. sputtering techniques, which are briefly discussed later. CVD encompasses a range of slightly varying techniques such as LPCVD, APCVD and AACVD, and since AACVD has been utilised during this work this technique is discussed in greater depth.

1.3.2 Aerosol-Assisted CVD

One of the key steps in the CVD process is the transport of the precursor to the reactor. In conventional APCVD the precursor is transported in the vapour phase. This transport technique relies on the precursor possessing a reasonable vapour pressure at moderate temperatures. The vapour pressure of the precursor can be increased by raising the temperature, however, the precursor may decompose before a suitable vapour pressure can be attained. This limitation of the CVD process can be avoided by the use of an alternative delivery method such as creating an aerosol containing the precursor as opposed to vaporising it.

The precursor is dissolved in an organic solvent and is transported to the substrate in the form of an aerosol. Once transported to the reactor the precursor can decompose on the heated substrate to deposit a thin metal or metal oxide film. The process of thin film growth by CVD and other possibilities such as the formation of particles in the gas phase are displayed in Figure 1.8.

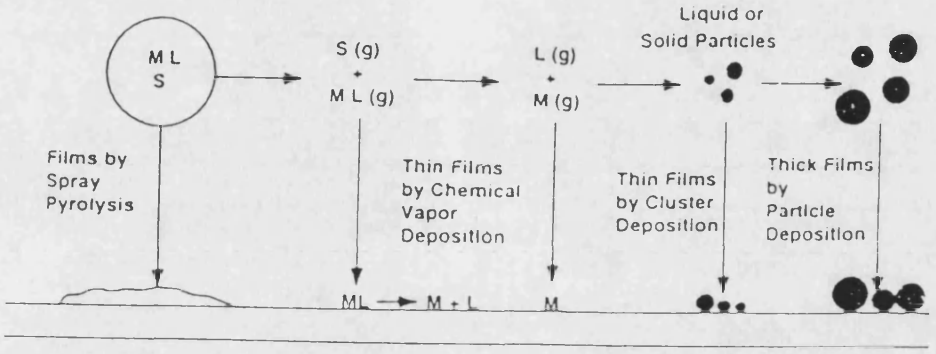

M = Metal Centre.

L = Ligand.

S = Solvent.

Figure 1.8 Film formation via aerosol routes.[55]

The aerosol deposition technique has several advantages in addition to those for traditional CVD highlighted in Section ***1.3.1.4***.

(1) *Premature thermal degradation of precursors does not occur (the precursor is held out side the reactor at room temperature).*

(2) *The precursor delivery rate is constant with time (the ratio and concentration of precursor in solution and the droplet size do not vary with time).*

(3) *The need for the precursor to have a good vapour pressure is eliminated.*

Despite these additional advantages there is one disadvantage in using an aerosol delivery technique. An impurity has been added to the deposition process in the form of the solvent used to dissolve the precursor and create the aerosol. The solvent present in the reactive gas flow may take part in the chemistry of the deposition process or be incorporated in the film deposited.[50,55]

1.3.2.1 Aerosol Generation

The atomisation of the precursor solution into droplets to allow its transportation to the reactor is an important step in the deposition process. The aerosol generator characteristics determine the production rate and droplet size distribution, and thus the growth rate for the film deposited. Many different types of aerosol generators exist which include collision nebulisers, air-assist generators, rotating disk and rotating cup sprayers. These are discussed in a number of reviews.[54-56]

Perhaps the simplest and most commonly used route to the production of an aerosol is via an ultrasonic technique. Ultrasonic droplet generators consist of a piezoelectric transducer which vibrates underneath the solution containing the precursor when a high frequency electric field is applied. This rapid vibration causes the formation of an aerosol containing the dissolved precursor. The aerosol can then be transported to the reactor in an inert gas such as nitrogen or helium. The main disadvantage of aerosol production via this method is the general low aerosol production rates when compared to other systems.

1.4 OTHER THIN FILM DEPOSITION TECHNIQUES

1.4.1 Sputtering of Tungsten Oxide Thin Films

Sputtering is a common deposition method for thin films and has been used for the deposition of tungsten oxide. Sputtering generally produces films of higher quality than CVD. However, the equipment is more complex and expensive than that used for CVD.

The sputtering technique accelerates ions from a plasma in a partial vacuum towards a target having a negative potential (cathode). The target is made from the

material which is to be deposited. The positive ions bombard the target whose atoms are then vapourised in all directions and in particular towards the substrate where they condense to form a thin film. Sputtered oxide films tend to be oxygen deficient so oxygen gas can be added during the sputtering process to control the stoichiometry of the film produced.[12,20,59]

This technique has been used for the deposition of high quality tungsten oxide (WO_3) films for possible gas sensor applications. Films have been deposited from tungsten metal targets in a partial argon-oxygen atmosphere[13,14] and from a tungsten oxide target again using an argon-oxygen atmosphere.[30]

1.4.2 Sol-Gel Production of Tungsten Oxide Thin Films

Film deposition by the sol-gel technique involves the substrate being dipped in a pre-prepared solution of the intended coating material or its precursor. Once dipped, the substrate is removed and allowed to dry (and, if necessary, thermally decomposed) producing a thin film of the desired material on the substrate surface. Sol-gel production of films has several advantages over other deposition techniques :

(1) *Low temperature processing.*
(2) *Simple inexpensive and uncomplicated equipment.*
(3) *Easy control of the film thickness.*
(4) *Good film uniformity.*
(5) *Ability to coat large complex shapes.*

As far as can be determined this technique has not been widely used for the deposition of tungsten oxide thin films.[22,43,44] A composite film of PAA-WO_3 (PAA = polyacrylic acid) has been prepared by the sol-gel technique. The PAA-WO_3 film was deposited by dipping the glass substrate into an aqueous solution of PAA and WO_3-NH_4OH. The film was then heated at low temperature (100°C) and treated with HCl to replace the ammonium ion with a proton. The films deposited were characterised by

Raman spectroscopy and XRD which showed the films to be amorphous, probably due to limited thickness of the films.[22]

1.5 THE CVD OF TUNGSTEN OXIDE THIN FILMS

Tungsten oxide films are probably the most used and hence most thoroughly studied electrochromic layer used in electrochromic devices. However, the methods and precursors used for depositing these films are few when compared to other semi-conducting metal oxide films. The next section aims to highlight the precursors used to date for depositing tungsten oxide films.

1.5.1 Inorganic Precursors

Tungsten oxide thin films have been prepared by the CVD of tungsten hexacarbonyl [$W(CO)_6$]. Initially, a tungsten metal film is deposited and then subsequently annealed in an oxygen atmosphere to give the desired WO_3 film. The first step in this deposition process was carried out in an argon atmosphere at approximately 400°C. The tungsten metal film was then held between 500-750°C for approximately four hours in an oxygen environment to yield the WO_3 film.[9,10,31] Attempts to deposit tungsten trioxide thin films in single step process using $W(CO)_6$ by premixing oxygen yielded films of tungsten oxide containing additional phases to the desired WO_3.[9,10]

Tungsten hexafluoride has been used for the CVD of fluorine-doped tungsten oxide films ($WO_{3-x}F_x$) and the process is subject to a patent by Ford Motor Company.[37] Tungsten hexafluoride is reacted with an oxygen containing compound such as isopropyl alcohol and a fluorine containing compound such as 1,1-difluoroethane at 350-450°C to yield the thin film. The major disadvantage with this system is that highly corrosive HF is produced as a decomposition product.

1.5.2 Metal Organic Precursors

Until recently there has been little interest in the synthesis of volatile metal organic precursors for the CVD of tungsten oxide films. However, in the past six years several such compounds have been synthesised.

Both tungsten(V) and tungsten(VI) ethoxide have been used for the deposition of non-stoichiometric tungsten oxide thin films. The films were deposited in a single step at atmospheric pressure. The precursors are air and moisture sensitive so two concentric tubes were used to ensure the alkoxide did not react with the oxygen source prior to entering the reactor. The deposition temperatures used were between 100-350°C while at temperatures in excess of 350°C powdery blue deposits were produced which were presumed to be sub-stoichiometric tungsten oxide. The films deposited were all amorphous with O/W ratios between 2.7-3.2 which were determined by Rutherford backscattering experiments.[36]

A range of volatile tungsten(VI) oxo alkoxide/β-diketonate complexes have been synthesised and used for the deposition of tungsten oxide thin films via LPCVD. The precursors used during these experiments were of the type $WO(OR)_4$ (R = Bu^t, Pr^i, Et, OCH_2Bu^t) and $WO(OR)_3L$ (R = Bu^t, Pr^i; L = acac, hfac). The deposition temperatures ranged between 120-390°C depending on the precursor used. All the films deposited were initially amorphous until annealed at 400°C for several hours. Once annealed the films were analysed by XRD and gave diffraction patterns consistent with WO_3. Films annealed at 1000°C displayed XRD patterns which indicated the presence of both WO_3 and WO_2.[42]

Amorphous tungsten oxide films doped with phosphorus have been deposited by LPCVD using single-source volatile precursors. The precursors synthesised for these deposition experiments were $W_2(CO)_8(\mu\text{-}PR_2)_2$ (R = Me, Et) and $W(CO)_4L_2$ [L = PEt_3 (*cis* and *trans* isomers), $P(OEt)_3$ (*trans* isomer)]. All of the deposition experiments were

carried out at 400°C and the films deposited were all amorphous and were characterised by XPS.[15]

Tetra(allyl)tungsten [$W(\eta^3\text{-}C_3H_5)_4$] has also been used to deposit a tungsten oxide film by LPCVD. A tungsten metal film was initially deposited and this was then annealed under oxygen at 400°C to produce a transparent colourless WO_3 film by XRD. However, the film did contain significant amounts of carbon (17 atom%).[60]

1.6 TUNGSTEN CHEMISTRY

1.6.1 Background

Tungsten, the element, was first discovered in 1781 in a mineral, scheelite, whose main constituent is $CaWO_4$; other known tungsten ores are, wolframite, $(Fe,Mn)WO_4$, and stolzite, $PbWO_4$. Tungsten steel was invented in 1855 and the first alloys containing tungsten were manufactured in 1868. The primary application for tungsten has been the filament in electric light bulbs, due to its high melting point (3410°C). More recently there has been interest in tungsten alloys for high temperature applications and tungsten carbide for applications where great wear resistance and hardness are required. One example of this is as a composite used in the construction of Formula 1 cars.[61]

Tungsten is located in the *d*-block with an electronic configuration of $5d^4\ 6s^2$. The availability of *d*-orbitals enables the formation of both σ and π bonds with ligands which gives tungsten a wide range of accessible oxidation states. Tungsten complexes are known for oxidation states -IV to +VI with. The oxidation states and geometries of a selection of tungsten complexes are summarised in Table 1.1.

Oxidation State	Co-ordination Number	Geometry	Example
-IV (d^{10})	4	Tetrahedral	$[W(CO)_4]^{4-}$
-II (d^8)	5		$[W(CO)_5]^{2-}$
O (d^6)	6	Octahedral	$W(CO)_6$
II (d^4)	5		$W_2Cl_4(dppe)_2$
	6	Octahedral	$Me_2W(PMe_3)_4$
	9	Cluster Compound	W_6Cl_{12}
III (d^3)	4	Tetrahedral	$W_2(NR_2)_6$
	6	Octahedral	$[W_2Cl_9]^{3-}$
IV (d^2)	6	Octahedral	$[WCl_6]^{2-}$
	8	Dodecahedral	$[W(CN_8)]^{4-}$
V (d^1)	6	Octahedral	WF_6^-
	9		$W(\eta^5\text{-}C_5H_5)_2H_3$
VI (d^0)	4	Tetrahedral	$[WO_4]^{2-}$
	6	Octahedral	$WOCl_4(s)$
	7	Pentagonal bipyramidal	$WOCl_4(diars)$

Table 1.1 Oxidation states and stereochemistry of selected tungsten compounds.

Tungsten has similar chemistry to molybdenum, however, there are some important differences. Tungsten(VI) oxide is soluble in neutral and alkaline solutions but an insoluble hydrated oxide, $WO_3.nH_2O$, is precipitated from acid solutions. In contrast, molybdenum(VI) oxide dissolves in acid solutions due to the formation of chloro-complexes. The oxidation state free energy diagram for tungsten, molybdenum and chromium illustrates the greater relative stability of the lower oxidation states of molybdenum compared to those tungsten (Figure 1.9).[62]

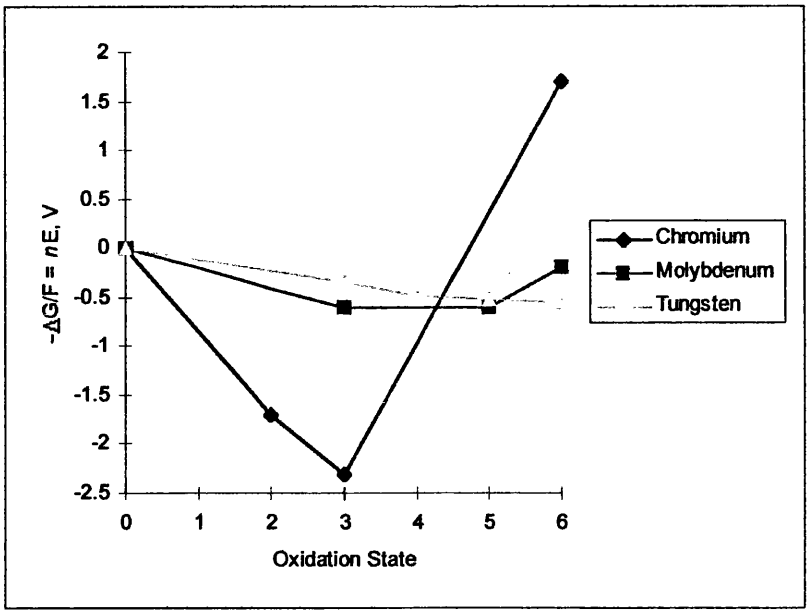

Figure 1.9 Oxidation state free energy diagram for chromium, tungsten and molybdenum.

Tungsten and molybdenum share little in common with the lightest member of this transition metal group, chromium. The main differences between the heavier elements within the group, tungsten and molybdenum, and the lighter element, chromium, are those of size, co-ordination number and stability. These differences, which are generally seen across the *d*-block, are brought about by the effects of the lanthanide contraction. This effect dies out towards the right of the *d*-block. Higher oxidation states and greater co-ordination numbers are generally more stable for the heavier elements. Therefore, chromium(VI) is strongly oxidizing while molybdenum and tungsten are relatively stable in the +VI oxidation state.

There are several reviews fully covering tungsten chemistry.[60-62] Due to the desire to synthesise precursors for the deposition of tungsten(VI) oxide thin films the aim of the work reported in this thesis has been to synthesise tungsten(VI) compounds containing tungsten oxygen bonds. Therefore, only tungsten(VI) chemistry is elaborated on here, with particular emphasis on known tungsten(VI) species which incorporate WO, WO_2 or WO_3 fragments.

1.6.2 Tungsten(VI) Chemistry

As already noted, tungsten(VI) is the most stable oxidation state which leads to a varied chemistry in this oxidation state. This is mainly due to the stability of the tungsten hexahalides which give rise to substitution products of the type $[WX_{6-n}L_n]$ (n = 1-6) in addition to complexes containing the WO, WO_2 and WO_3 structural units. Co-ordination numbers higher than six are also possible for tungsten(VI) complexes and are reasonably common due to the stability and size of the tungsten(VI) atom.

1.6.2.1 Tungsten(VI) Halides and Derivatives

Tungsten hexahalides of the type WX_6 (X = F, Cl, Br) are known. Tungsten hexachloride and tungsten hexabromide are blue black moisture sensitive solids while tungsten hexafluoride is a colourless gas. Mixed tungsten halides of fluorine and chlorine are also known and have been characterised by ^1H and ^{19}F NMR spectroscopy. Spectroscopic data has been used to establish the chemical configurations for *cis*- and *trans*-WCl_2F_4, *cis*- and *trans*-WCl_4F_2 and *mer*- and *fac*-WCl_3F_3.[66]

Halide substitution by ligands containing good π-donor atoms such as oxygen, nitrogen and sulphur are known. Hexakis(dimethylamido)tungsten(VI) has been synthesised from the reaction between WCl_6 and $LiNMe_2$.[67] It was reported the reaction yielded two products, $W(NMe_2)_6$ and $W_2(NMe_2)_6$. However, red crystals of the desired product, $W(NMe_2)_6$, could be recrystallised from a *t*-BuOH/benzene solution and its octahedral nature established by crystallography (Figure 1.10).[68] The crystals were remarkably moisture stable and only decomposed over a period of hours in the atmosphere. The planarity of the *trans* C_2N-W-NC_2 units suggest nitrogen to tungsten (p_π-d_π) π bonding.

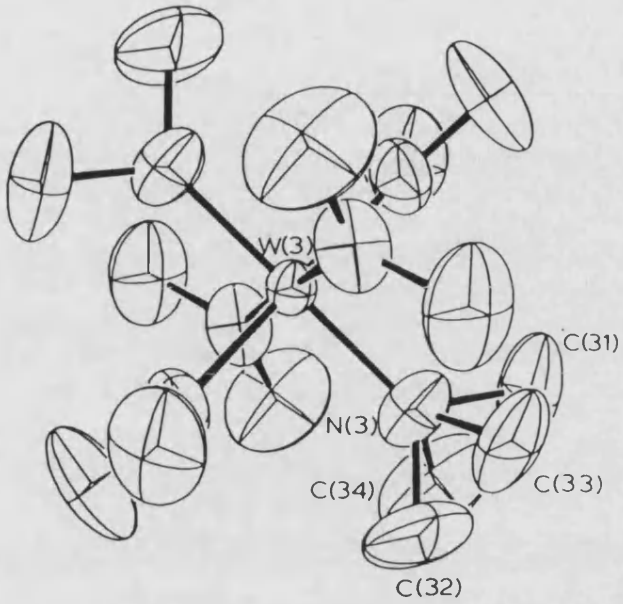

Figure1.10 Crystal structure of $W(NMe_2)_6$.

$W(NMe_2)_6$ reacts with alcohols, ROH, at room temperature to give a series of tungsten alkoxides $W(OR)_6$ (R = Me, Et, *n*-Pr, *i*-Pr and allyl).[69] The observed order of reactivity of ROH with $W(NMe_2)_6$ (R = Me> Et> Pr>> *t*-Bu) can be understood in terms of acidity and steric demands of the alcohol [pK_a (MeOH) = 15.5; pK_a (t-BuOH) ≥ 19]. The tungsten(VI) alkoxides synthesised, $W(OR)_6$, are low melting solids or liquids at room temperature and are thermally stable at temperatures <100° allowing their purification by vacuum sublimation or distillation.[69] $W(NMe_2)_6$ also undergoes insertion reactions with both carbon dioxide, CO_2, and carbon disulphide, CS_2. The insertion reaction utilising CO_2 yields *fac*-$W(NMe_2)_3(O_2CNMe_2)_3$ whose structure is shown in Figure 1.11.

Probably the most significant feature of this structure is the short tungsten nitrogen bond distance, 1.922 Å. This is approximately 0.1 Å shorter than in $W(NMe_2)_6$ and indicates significant N→W π donation, which has been suggested an important factor in limiting the insertion reaction to only three CO_2 molecules. Additionally, the planarity of the WNC_2 units and the *fac*-WN_3O_3 octahedral geometry are all suggestive of significant nitrogen to tungsten π bonding. In contrast to the CO_2 insertion reaction the equivalent reaction involving CS_2 reduces tungsten(VI) to tungsten(IV) to give

where $Cr(S_2CNEt_2)_3$ and $Nb(S_2CNMe_2)_4$ are produced from $Cr(NEt_2)_4$ and $Nb(NMe_2)_5$, respectively, by the insertion of carbon disulphide.

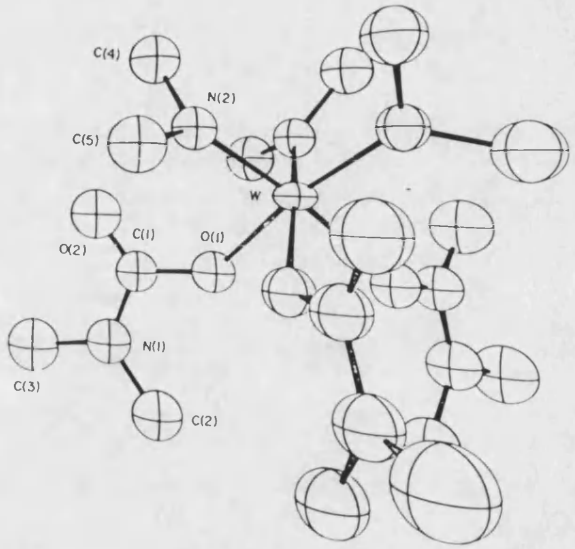

Figure 1.11 Molecular structure of $W(NMe_2)_3(O_2CNMe_2)_3$.

As mentioned earlier, the reaction between WCl_6 and $LiNMe_2$ yields two products, $W(NMe_2)_6$ and $W_2(NMe_2)_6$. The second of these compounds, $W_2(NMe_2)_6$, was found to contain a triple bond between the tungsten atoms. This compound became the first fully characterised molecule containing a W≡W triple bond (Figure 1.12).[72]

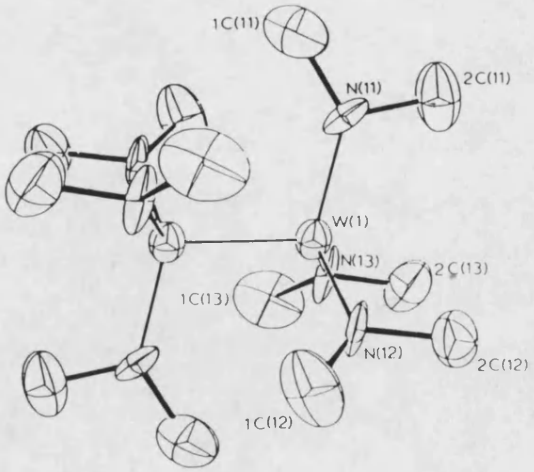

Figure 1.12 Crystal structure of $W_2(NMe_2)_6$.

The W≡W bond distance in $W_2(NMe_2)_6$ is 2.294(1) Å. The corresponding isomorphous molybdenum compound has a metal metal bond length which was approximately 0.08 Å shorter than the tungsten example. This difference can be explained by the increase in metal radii of 0.04 Å for the tungsten atom.

Analogous dinuclear alkoxides, $W_2(OR)_6$, can be synthesised from $W_2(NMe_2)_6$ by an alcoholysis reaction.[73] However, compounds of this type are restricted to bulky R groups (R = Bu^t, Pr^i, CH_2Bu^t, cyclohexyl, $SiMe_2Bu^t$, $CMe_2(CF_3)$, $CMe(CF_3)_2$ and 2,6-$Me_2C_6H_3$).[74]

The W≡W bond can best be described for $W_2(OR)_6$ by the following model. Considering the *z* axis to be coincident with the triple bond axis, the metal d_{z^2} orbitals may interact to form σ and σ* W-W molecular orbitals. The d_{xz} and d_{yz} can form π and π* orbitals. The over all charge on the tungsten triple bond unit is +VI. Therefore, each individual tungsten atom has on oxidation state of +III. In this oxidation state each metal has the d^3 configuration and thus a W≡W triple bond of configuration $\sigma^2\pi^4$ can be formed. The tungsten atoms may use *s*, p_x and p_y atomic orbitals to form three σ bonds with the OR ligands, and the tungsten d_{xy}, $d_{x^2-y^2}$ and p_z atomic orbitals have appropriate symmetry to form π bonds with the oxygen filled *p* atomic orbitals.[75]

Numerous organometallic derivatives are known, typified by WMe_6, which has been prepared from the reaction between WCl_6 and Me_6Al_2.[76] This compound undergoes reactions with a variety different reagents[77] to yield previously known compounds which include $W(OMe)_6$[78] and $W(OPh)_6$.[79] Hexamethyltungsten reacts with NO to form an eight co-ordinate tungsten complex, $WMe_4(O_2N_2CH_3)_2$[80] (Figure 1.13).

Other tungsten(VI) complexes with a co-ordination number greater than six are known. Seven co-ordinate tungsten complexes are formed by the reaction between WMe_6 and tertiary phosphines to yield WMe_6L (L = $PMePh_2$, PMe_2Ph, $PEtPh_2$, PMe_3).[77,81]

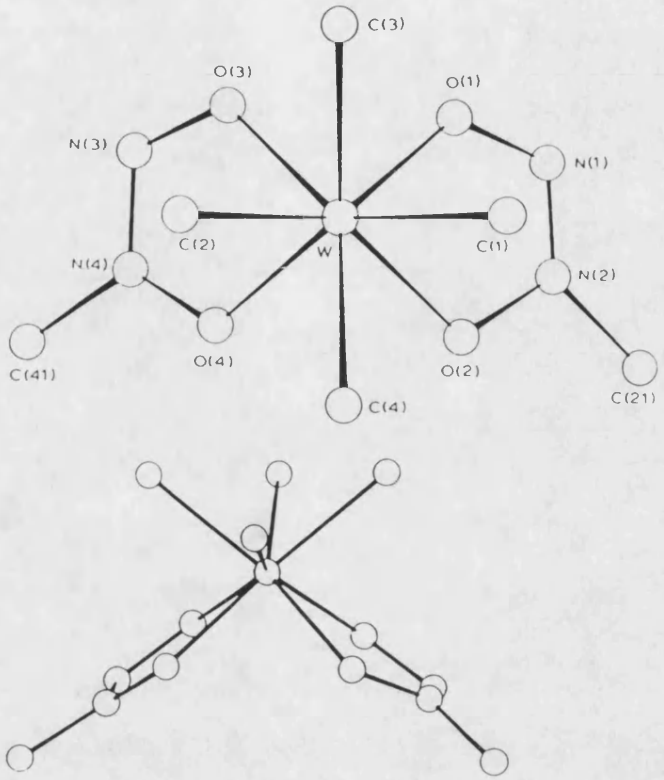

Figure 1.13 Two views of the molecular structure of $WMe_4(O_2N_2CH_3)_2$.[82]

1.6.2.2 Complexes Containing the WO Structural Unit

The oxo ligand forms a strong multiple bond with tungsten(VI) by utilising both σ and π donation. The σ and π donation results in a short tungsten-oxygen bond length and a strong infrared absorption band at around 950 cm^{-1}.

Tungsten oxo halo complexes containing one terminal oxygen of the general type $W(O)X_4$ (X = F, Cl, Br) are known. The structures of $W(O)Cl_4$ and $W(O)Br_4$ are isostructural and consist of chains of slightly distorted octahedra formed by two oxygen atoms and four chlorine or bromine atoms. The octahedra are connected by oxygen bridges with tungsten oxygen distances of 1.8 and 2.1 Å (Figure 1.14).[83]

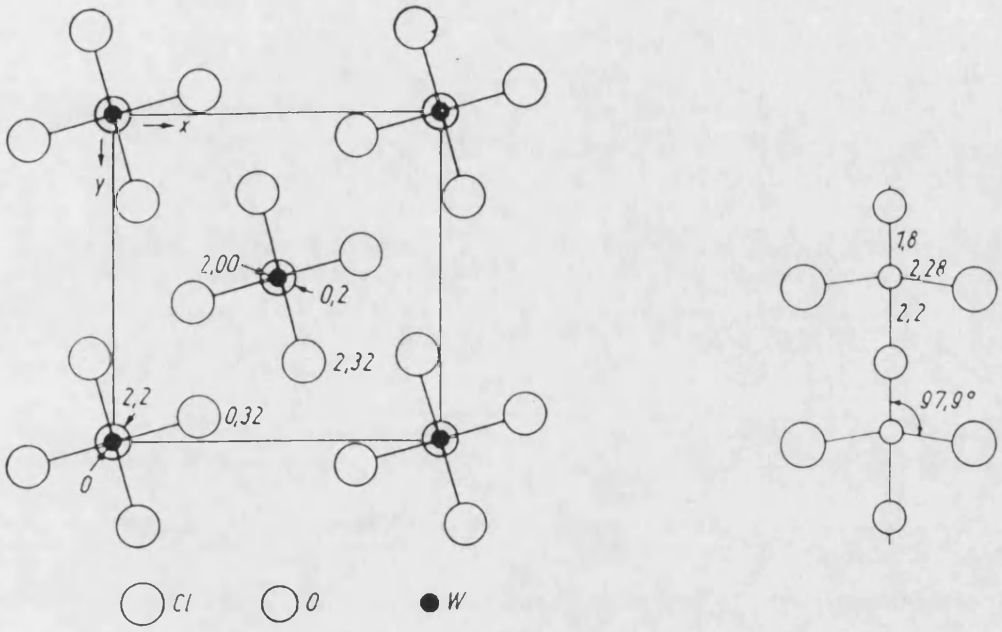

Figure 1.14 Crystal structure of $W(O)Cl_4$.[83]

In contrast, the structure for $W(O)F_4$ is tetrameric in the solid state. It was initially suggested that the compound structure contained oxygen bridges,[84] in contrast to the analogous molybdenum structure which is fluorine bridged. However, on the basis of infrared and Raman spectroscopy,[85] and a molecular orbital analysis comparing bond lengths,[86] a structure utilising fluorine bridges is now the accepted configuration for $W(O)F_4$ (Figure 1.15)

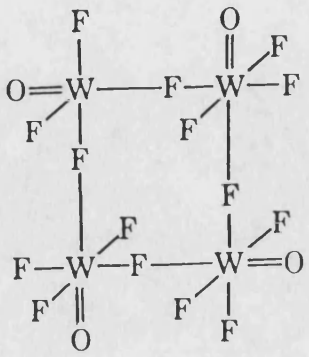

Figure 1.15 Accepted configuration for $W(O)F_4$.[86]

Tungsten (oxo) halo complexes of the type $W(O)X_4$ are co-ordinatively unsaturated. Therefore, the (oxo) halo complexes can form six co-ordinate adducts of the type $W(O)X_4L$ (L = alkyl cyanides, THF, pyridine).[87,88] The reaction of diars with $W(O)Cl_4$ yields a seven co-ordinate (pentagonal bipyramidal) product, $W(O)Cl_4$diars.[89] Axial positions around the tungsten are filled by oxygen atoms and one chlorine atom. The remaining three chlorine atoms and the two arsenic atoms from the diars ligand take up the five equatorial positions. However, the structure of this compound is unusual as the W-Cl bond *trans* to the terminal oxygen is shorter than the *cis* W-Cl bond.

Six co-ordinate, monomeric tungsten(VI) compounds have also been synthesised using the bidentate catechol ligand. The use of one or two equivalents of the catechol ligands leads to the formation of two different products. One equivalent of catechol yields $W(O)Cl_3(O,HO\text{-}C_6H_4)\cdot O(C_2H_5)_2$ which has been characterised by spectroscopic methods. Two equivalents of catechol lead to the formation of $W(O)Cl(O_2\text{-}C_6H_4)(O,OH\text{-}C_6H_4)\cdot O(C_2H_5)_2$, which has been structurally characterised (Figure 1.16).[90]

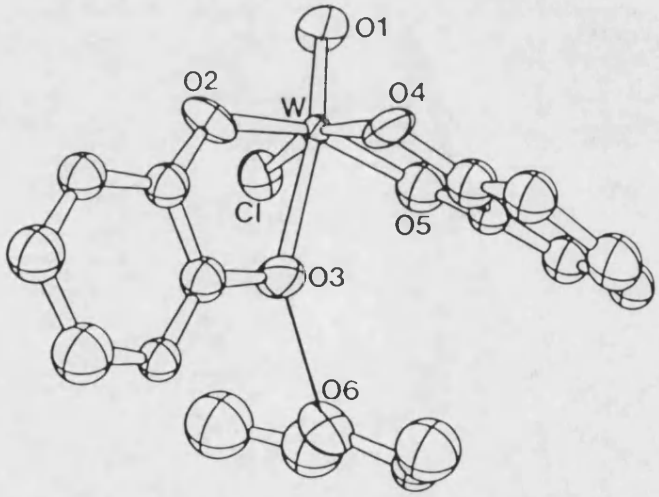

Figure 1.16 Perspective view of $W(O)Cl(O_2\text{-}C_6H_4)(O,OH\text{-}C_6H_4)\cdot O(C_2H_5)_2$

The tungsten atom is coordinated to four catechol oxygen atoms, one oxo and one chloro ligand in a distorted octahedral geometry. A diethyl ether molecule is strongly hydrogen bonded to the hydroxy group of one of the catechol ligands. The W=O bond length of 1.65 Å indicates significant oxygen to tungsten π donation. The infrared band for the W=O stretch is observed at $981cm^{-1}$, as expected for a terminal

oxygen. Infrared bands arising for W-O-W bridges are typically observed between 700-900cm^{-1}.[91] A series of tungsten(VI) oxotetraalkoxides of the type $WO(OR)_4$ (R = Me, Et, Pr^i or cyclo-C_6H_{11}), which contain the WO unit, have been synthesised and are discussed in greater detail later.[92]

1.6.2.3 Complexes Containing the WO_2 Structural Unit

The (oxo) halo complexes containing the WO_2 structural unit of the type WO_2X_2 (X = F, Cl, Br, I) are all known. The structure of WO_2Cl_2 has been shown to be polymeric in the solid state and monomeric in the gas phase.[93] The absence of any characteristic W=O adsorptions in the infrared spectrum suggests only bridging oxygen atoms are present in the solid state (Figure 1.17).[94]

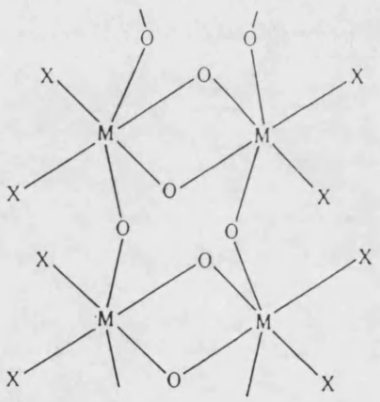

Figure 1.17 Proposed solid state structure for WO_2Cl_2.[94]

X-ray powder diffraction data suggests that all four of the tungsten (oxo) halo compounds are isomorphous, exhibiting the same structure.[94,95]

Despite the polymeric nature of tungsten dioxochloride and its insolubility in common organic solvents, complexes of the type $WO_2Cl_2L_2$ (L = dimethylformamide, triphenylphosphine oxide, dimethyl sulfoxide, acetonitrile, hexamethylphosphoramide, tetramethyl sulfoxide) have been prepared.[96] One further example of a more soluble adduct of WO_2Cl_2 is dimethoxyethane-dichlorodioxo-tungsten(VI), WO_2Cl_2(dme),[97] whose structure has been determined by crystallography and is displayed in Figure 1.18.

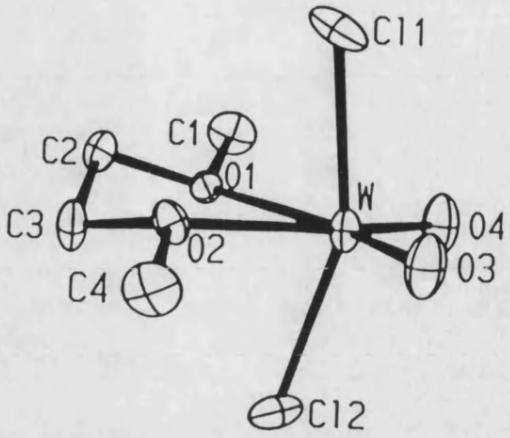

Figure 1.18 Perspective view of WO_2Cl_2(dme) molecule.[97]

The tungsten is six co-ordinate and has an octahedral geometry. The two terminal oxygen atoms are in a *cis* configuration with the two characteristic infrared adsorption bands at 976 and 933cm^{-1}. The bond lengths for both W=O bonds were determined as 1.69(1) Å.

Bidentate ligands have been utilised to give a series of complexes, WO_2Cl_2L, (L = bipryidyl, phenanthroline) which again have the oxygen atoms in a *cis* configuration.[96] Compounds of the type WO_2L_2 where L is a bidentate ligand are also known. One example of this is found using the 2,4-pentanedione ligand.[98] Infrared studies of this compound showed the two characteristic WO_2 absorption bands at 954 and 908cm^{-1}.[99]

The crystal structure of a (selenolate)oxotungsten complex, *cis*-{$HB(Me_2C_3N_2H)_3$}WO_2(SePh), has been determined and is displayed in Figure 1.19.[100] The molecule incorporates a six co-ordinate tungsten atom in a distorted octahedral geometry. The tungsten atom is co-ordinated by a selenophenolate ligand, a tridentate tris-pyrazolyl borate ligand and two *cis* terminal oxo ligands. The infrared spectrum of this species showed two strong absorption bands between 900-915 and 935-960cm^{-1} which is typical of the WO_2 unit in *cis* configuration.

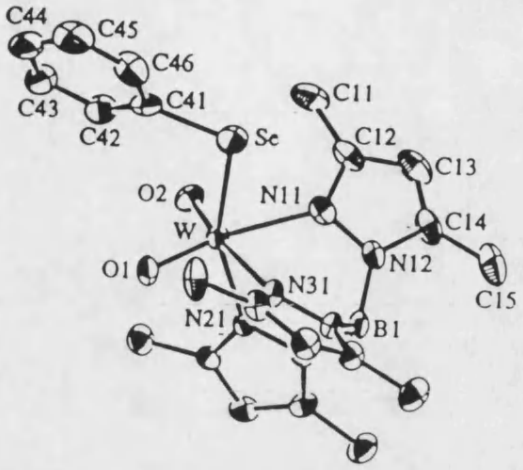

Figure 1.19 Molecular structure of tungsten selenophenolate complex.[100]

All of the complexes synthesised containing the WO_2 structural unit display two strong infrared absorption bands around the 910-920 and 950-970 cm^{-1} regions. These two strong absorption bands have been assigned to a discrete O=W=O group with *cis* rather than *trans* oxygen atoms. The tendency for the WO_2 unit to assume cis configuration can be explained in terms of multiple π-bonding between the oxygen and the tungsten atoms. It has been suggested that the maximum overlap of dative π-bonding between the oxygen and the tungsten is attained for the *cis* configuration. The strongly π-donating oxo-ligands have exclusive use of one of the tungsten *d*-orbitals (d_{xz} for O_x and d_{yz} for O_y) and share a third (d_{xy}). For the unfavoured *trans* configuration the oxo-ligands would share two tungsten metal *d*-orbitals (d_{xy} and d_{xz}) and leave one non-bonding metal orbital (d_{yz}). The same argument can also be applied for the molybdenum analogues.[101]

1.6.2.4 Complexes Containing the WO_3 Structural Unit

Complexes containing the WO_3 structural unit have been the least well studied and only a very limited number of complexes have been synthesised and well characterised. Trioxo(diethylenetriamine)tungsten(VI), WO_3(dien), has been isolated although only appears to have been characterised by microanalysis, infrared and Raman spectroscopy.[102] However, the data is consistent with that for the molybdenum analogue MoO_3(dien).[102]

Several salts containing the $[WO_3Cp^*]^-$ ($Cp^* = \eta^5\text{-}C_5Me_5$) anion have been synthesised and characterised by single crystal X-ray diffraction.[103,104] The crystal structure for $[Bu^tNH_3][Cp^*WO_3]\cdot\frac{1}{2}[Bu^tNH_3]Cl$ is shown in Figure 1.20.

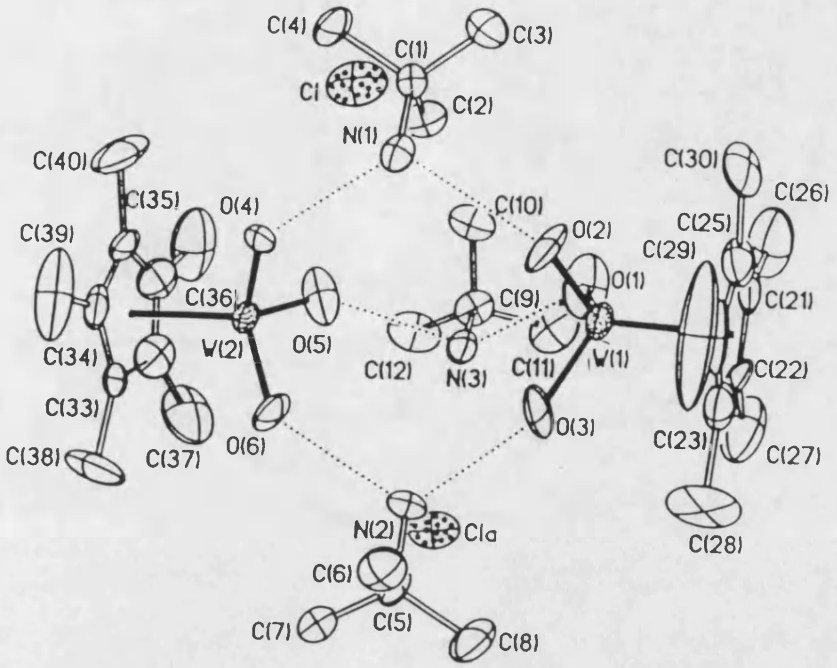

Figure 1.20 ORTEP drawing for $[Bu^tNH_3][Cp^*WO_3]\cdot\frac{1}{2}[Bu^tNH_3]Cl$.

The average W=O bond length in this complex was determined as 1.751 Å. The average length for a W=O bond found in the Cambridge Crystallographic Database is 1.692 Å. The increase in length can be accounted for by the need for the oxo ligands to donate only two electrons each to the tungsten metal to achieve a satisfactory $18e^-$ count. This is in contrast to most tungsten oxo complexes where the oxo ligands are considered to be formally $4e^-$ donors. Therefore, the oxo ligands present in the above anionic complex should be more weakly bound and hence have a longer than typical bond length.[104]

A chloride-free salt $[Bu^t(EtC\{O\}CH_2CH_2)NH_2][Cp^*WO_3]$ also containing the $[Cp^*WO_3]^-$ core has been synthesised and characterised by single crystal X-ray diffraction (Figure 1.21).

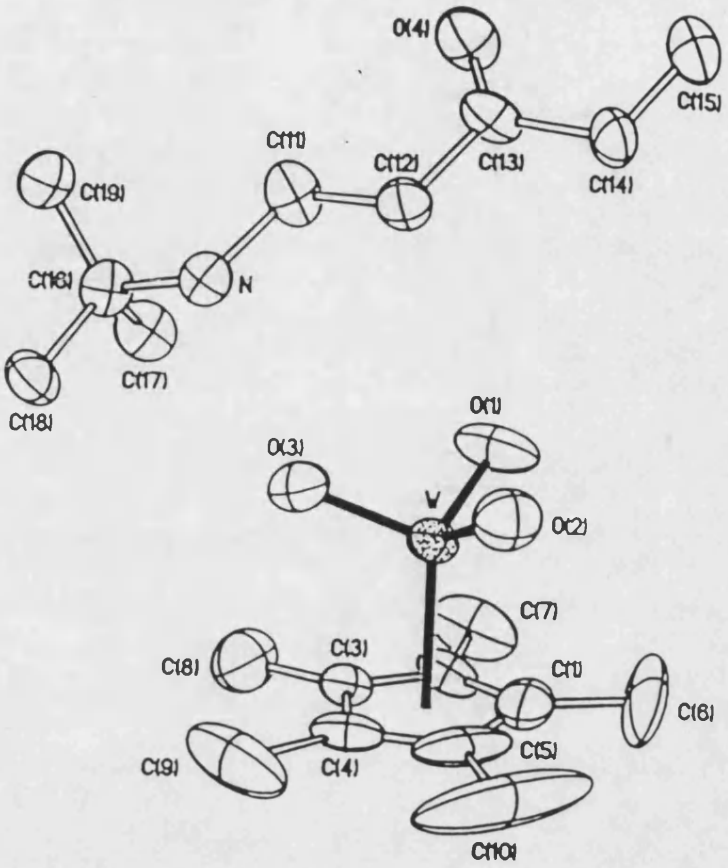

Figure 1.21 ORTEP drawing for $[Bu^t(EtC\{O\}CH_2CH_2)NH_2][Cp^*WO_3]$.

The average tungsten oxygen bond length in this compound was found to be 1.746 Å, again slightly longer than typical for a tungsten oxygen double bond.[104] Related σ-alkyl tungsten trioxide anions $[(Me_3CCH_2)WO_3]^-$ and $[(Me_3SiCH_2)WO_3]^-$ are also known.[105]

1.7 AIMS AND SYNTHETIC STRATEGIES

It has been the aim of the work described in this thesis to prepare tungsten containing compounds that will allow the production of a tungsten oxide thin film on a

glass substrate via APCVD in a single step. To this end, a series of tungsten(VI) compounds have been synthesised and fully characterised.

When synthesising the compounds described within this thesis, the aim was to :

(1) *synthesise tungsten compounds which were volatile at atmospheric pressure and at a reasonable temperature, 75 ℃-190 ℃.*

(2) *synthesise compounds where the oxidation state of the tungsten centre is +VI.*

(3) *synthesise tungsten compounds containing oxygen, to aid the deposition of an oxide film.*

Once synthesised the precursors were tested by either APCVD or AACVD depending on their volatility and the quality of the deposited film evaluated.

Chapter Two

Tungsten(VI) Hexaphenoxides

2.1 INTRODUCTION

Metal alkoxides and phenoxides have been widely studied due to their many applications in organometallic and catalytic chemistry.[106] Tungsten phenoxides, of the type $WCl_{6-x}(OAr)_x$ and $WOCl_{4-y}(OAr)_y$, are used as air stable precursors for two-component catalyst systems, typically in the presence of tin or lead organometallic reagents. The general advantage of phenoxide ligands, when compared with alkoxide ligands, is the ability to easily change the substituents present on the ring which can vary their electron-withdrawing properties. Additionally, bulky substituents can be used to effect the steric properties of the compounds.[107,108]

Tungsten(VI) hexaphenoxide, along with several other substituted tungsten(VI) hexaphenoxides, are known and have been partially characterised. The relatively low melting point of $W(OPh)_6$ (95-96°C)[79] indicated that these compounds may be suitable precursors for the deposition of tungsten oxide thin films.

2.1.1 Advantages and Disadvantages

There are several advantages to the possible use of tungsten(VI) hexaphenoxide compounds as precursors for tungsten oxide films.

1. *The compounds are air and moisture stable making handling and storage of the synthesised compounds uncomplicated.*
2. *They are monomeric compounds which should aid their volatility.*
3. *The tungsten atom is in the +VI oxidation state.*
4. *The synthetic methodology is undemanding.*
5. *The compounds are readily soluble in most organic solvents.*

However, the major difficulty associated with these types of compound are their high carbon content. This is a problem as once the deposition process is underway the carbon atoms present in the ligand could become incorporated in the growing film. The incorporation of carbon in the film would alter its stoichiometry and thus change the

optical properties of the film being deposited. Additionally, the decomposition of the ligand could leave a fine layer of carbon on the surface of the film. This is not a big problem on the laboratory scale as it can be easily removed, however, on the industrial scale this becomes more problematic.

The following chapter will describe the known synthetic routes to tungsten hexaphenoxide and its substituted derivatives, and a brief look at its structural chemistry. This will be followed by details of the synthesis, characterisation and deposition studies of the three tungsten(VI) hexaphenoxide compounds synthesised during the course of this work. As already mentioned, $W(OPh)_6$ was known prior to this work and its stability and low melting point made it an attractive precursor for the deposition of tungsten oxide films. The additional two tungsten(VI) hexaphenoxide compounds synthesised during the course of this work contained fluorinated phenol ligands. The addition of fluorinated ligands can lead to enhanced volatility due to the low polarisability of the fluorine atom. Generally the more volatile the molecule the easier it becomes to deliver to the reactor, hence, two fluorinated tungsten(VI) hexaphenoxide compounds have also been synthesised in addition to $W(OPh)_6$.

2.2 SYNTHETIC ROUTES

$W(OPh)_6$ was first synthesised in 1937 by a relatively simple phenolysis reaction involving tungsten hexachloride and phenol in the absence of solvent. The reaction was carried out under a nitrogen atmosphere and the final product was extracted using an alcohol.[109]

$$WCl_6 + 6PhOH \xrightarrow{heat} W(OPh)_6 + 6HCl_{(g)} \qquad [2.1]$$

The compound isolated was described as a brick red powder and found to be air and moisture stable. The compound was characterised as $W(OPh)_6$ by microanalysis and a sharp melting point was observed at 98°C indicating a pure compound. A partially

substituted derivative $[WCl_2(OPh)_4]$ was also obtained by carrying out the reaction in the presence of carbon tetrachloride.

$W(O)Cl_4$ has also been used as a starting material in the synthesis of $W(OPh)_6$. $W(O)Cl_4$ is far more air and moisture sensitive than the previously used WCl_6. The increase in sensitivity of the starting material makes the initial stages of the reaction more difficult as greater care is needed when handling $W(O)Cl_4$. $W(O)Cl_4$ is also significantly more expensive than WCl_6. However, a similar reaction can be carried out.[110]

$$W(O)Cl_4 + 6PhOH \xrightarrow{heat} W(OPh)_6 + 4HCl_{(g)} + H_2O \qquad [2.2]$$

The reaction was considered complete once the evolution of HCl gas had ceased. The final product $[W(OPh)_6]$ was abstracted from the reaction as red crystals using a methanol solution and the crystals were characterised by micro analysis. This reaction has also been carried out in the presence of chlorobenzene. The work up of the reaction mixture used was far more complicated and involved several extraction steps, washing with a sodium hydroxide solution and the use of an alumina column. However, the yield from the reaction was increased over the previous synthetic routes mentioned. The final product from this method was characterised by microanalysis and its melting point was recorded as between 95-96°C, which is consistent with previous reports.[79] This methodology was also used to prepare a series of substituted tungsten(VI) hexaphenoxide compounds, $W(OC_6H_4X)_6$, where the substituents, X, were *o*-CH_3, *p*-CH_3, *p*-Bu^t, *o*-Cl, *p*-Cl, *p*-Br and *p*-Ph. The hexaaryloxide, $W(OC_6H_4Me\text{-}4)_6$, has also been prepared by the reaction of $NaOC_6H_4Me$-4 with tungsten(VI) oxychloride.[92]

Mono-phenoxy (oxo) tungsten(VI) complexes have also been prepared by the phenolysis methodology. One example is the preparation of $[W(O)Cl_3(O\text{-}C_6H_3Me_2\text{-}2,6)]_2$.[111]

$$2W(O)Cl_4 + 2HOC_6H_3Me_2\text{-}2,6 \xrightarrow{diethyl\ ether} [W(O)Cl_3(OC_6H_3Me_2\text{-}2,6)]_2 + 2HCl \qquad [2.3]$$

The work up of this reaction involved extraction into hexane followed by recrystallisation from hexane to yield purple crystals which were moisture sensitive and were suitable for X-ray studies. These X-ray studies revealed that the compound formed dimers by chlorine bridging. A considerable excess of $W(O)Cl_4$ was used to prevent the formation of the bis-phenoxide complex which was always found to be present with $[W(O)Cl_4]$:phenol ratios less than 1.5:1.

Recently, $W(OPh)_6$ has been synthesised by a transesterification reaction, the final products melting point was found to be 97°C which is consistent with previous literature examples.[112]

$$W(eg)_3 + 6PhOAc \xrightarrow{\text{chlorobenzene}} W(OPh)_6 + 3Ac_2eg \qquad [2.4]$$

The main advantage to this method is that the starting material, tris(1,2-ethanediolato)tungsten(VI), is not air and moisture sensitive. This is in contrast to the previous starting materials used, WCl_6 and $W(O)Cl_4$, which are both air and moisture sensitive.

2.3 STRUCTURAL CHEMISTRY

The following section briefly summarises the structures determined for a selection of tungsten(VI) hexaphenoxide compounds found in the literature. Table 2.7 (Section 2.5) provides the relevant bond lengths for the following three examples cited here. The *para*-methylphenyl derivative $[W(OC_6H_4Me\text{-}4)_6]$ (Figure 2.1) was synthesised by a sodium salt reaction and crystals were grown from an acetonitrile solution. The tungsten centre has a slightly distorted octahedral co-ordination geometry with a mean tungsten oxygen bond length of 1.895(9) Å. The acute O-W-O angles in the molecule vary from 86.1(2) to 94.7(1)°.[92]

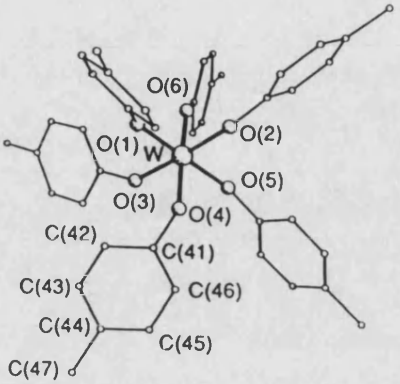

Figure 2.1 Molecular structure of $W(OC_6H_4Me\text{-}4)_6$.

The hexaphenoxotungstate(V) anion contains two crystallographically independent anions, each located on centres of symmetry. The counter ion (tetramethylammonium) was on a general position with no imposed symmetry. One of the $[W(OPh)_6]^-$ ions present showed some disorder among the phenoxide ligands but both anions displayed the same structure, Figure 2.2.

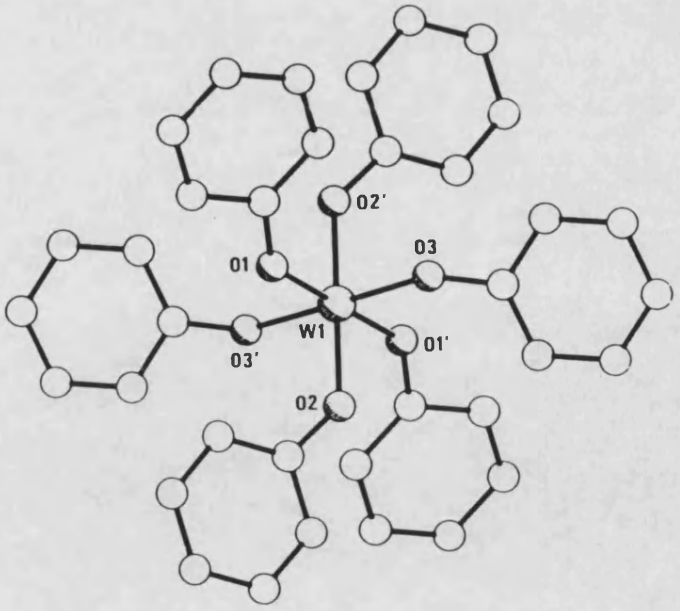

Figure 2.2 Structure of the hexaphenoxotungstate(V) ion.[113]

As expected, the ion has a closely octahedral geometry with a mean tungsten oxygen bond length of 1.934 Å. The tungsten oxygen bond length is significantly longer than seen in the previous example, which is probably due to the lower charge on the tungsten ion and the negative charge of the unit.[113]

During the course of the work described in this thesis, the structure of $W(OPh)_6$ has been reported (Figure 2.3).

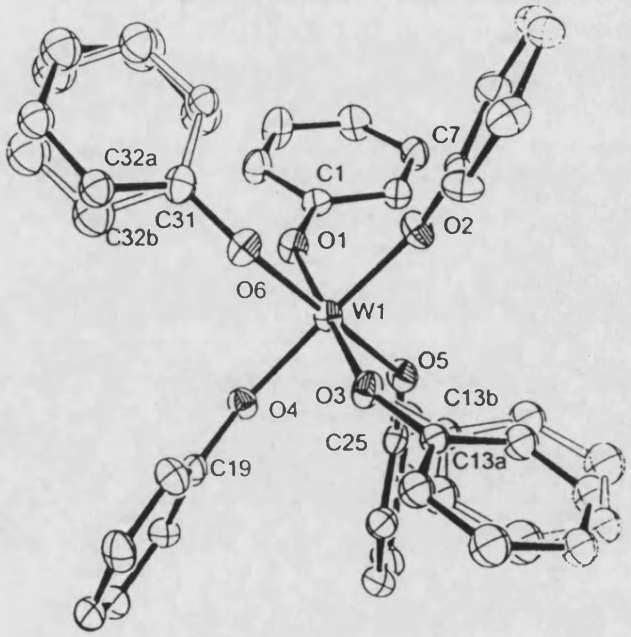

Figure2.3 ORTEP drawing of $W(OPh)_6$.

The compound is seen to form monomers with the tungsten centre in a slightly distorted octahedral geometry. Two of the phenyl groups showed different solid state orientations, one with two rotamers in a 1:1 ratio with a rotation angle of 23(1)° the second in two positions with a 60-40 ratio. The geometry of the structure is very similar to that shown in Figure 2.1 for $W(OC_6H_4Me\text{-}4)_6$. The tungsten oxygen bond lengths in $W(OPh)_6$ vary from 1.883(4) to 1.917(4) Å with the acute angles varying from 87.5(2) to 92.6(2)°. Therefore, the tungsten atom is found in a more regular octahedral site than seen in $W(OC_6H_4Me\text{-}4)_6$ (Figure 2.1).

2.4 RESULTS AND DISCUSSION

2.4.1 Synthesis

Three tungsten(VI) hexaphenoxide compounds have been synthesised in order to carry out the CVD experiments. The compounds synthesised for this study were $W(OPh)_6$ **(1)**, $W(OC_6H_4F\text{-}4)_6$ **(2)**, and $W(OC_6H_3F_2\text{-}3,4)_6$ **(3)**. $W(OPh)_6$ was previously known and its low melting point (95°C) and its stability made it a possible candidate for APCVD. In addition, representative derivatives of related fluorinated ligands have been synthesised since such ligands have, in other systems, led to enhanced volatility. Therefore, two fluorinated tungsten(VI) hexaphenoxide compounds were also synthesised **(2, 3)**.

The three tungsten(VI) hexaphenoxide compounds synthesised during this work were prepared by a literature method, using $W(O)Cl_4$ as the starting material with an excess of the phoxide ligand.[110] The initial stages of this reaction were carried out under a nitrogen atmosphere due to the moisture sensitivity of $W(O)Cl_4$. However, once the reaction was complete (no HCl evolved) no special handling techniques were required.

$$W(O)Cl_4 + 6ROH \xrightarrow{heat} W(OR)_6 + 4HCl_{(g)} + H_2O \qquad [2.5]$$

R = 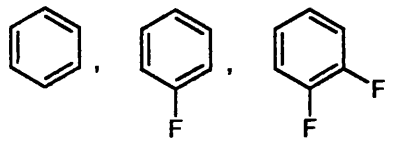

(1) **(2)** **(3)**

During the initial synthesis of $W(OPh)_6$ the literature work up was followed and after a second extraction with methanol a small quantity of dark red crystals were recovered. The melting point recorded for these crystals was 95°C which was consistent with the literature values for $W(OPh)_6$. This strongly indicated that the red crystals

obtained were $W(OPh)_6$. However, the yield from the reaction was poor at only about 8%. During the work up stages of the reaction no steps had been taken to remove the excess phenol that was used. Therefore, in subsequent preparations, the excess phenol used during the reaction was sublimed off. The remaining solid was then extracted into ether which was then washed with a sodium hydroxide solution. This ensured the removal of any remaining phenol. The ether was then removed *in vacuo* to give a red solid which was dissolved in hot methanol. Dark red crystals of tungsten(VI) hexaphenoxide **(1)** were obtained from the methanol solution in a 26% yield. The modified work up method had increased the yield from the reaction by approximately 18%. This method was subsequently used for the preparation of **(2)** and **(3)** and give yields of 28 and 22% respectively.

2.4.2 NMR Spectroscopy

^{1}H, ^{13}C and ^{183}W NMR spectra were recorded for all three compounds synthesised in this chapter. In addition, ^{19}F NMR spectra were recorded for compounds **(2)** and **(3)**.

2.4.2.1 ^{183}W NMR Spectroscopy

There has been little interest in direct observation of the four NMR active Group 6 nuclei (^{53}Cr, ^{95}Mo, ^{97}Mo and ^{183}W) mainly because of their low sensitivity.[114] Therefore, to enable ^{183}W NMR spectra to be recorded in a reasonable time frame samples of high concentration are required. ^{183}W NMR spectra were recorded for all three compounds synthesised and the results are displayed in Table 2.1.

Table 2.1 Tungsten Chemical Shift Values for Synthesised Compounds.

Compound		Chemical Shift (ppm)[a]
$W(OPh)_6$	**(1)**	-474.8
$W(OC_6H_4F\text{-}4)_6$	**(2)**	-416.3
$W(OC_6H_3F_2\text{-}3,4)_6$	**(3)**	-446.3[b]

[a] referenced to 1 mol dm^{-3} Na_2WO_4/D_2O.[115]
[b] 80°C.

The synthesised compounds were all reasonably soluble in toluene. However, compound **(3)** was less soluble in toluene so the spectrum was recorded at a higher temperature, 80°C. All three compounds showed a single peak in the ^{183}W MNR spectra which can be taken to indicate a single tungsten environment present in each compound. The chemical shift values of all three compounds (-410 and -475ppm) were consistent with each other. The similarity in tungsten shift values for the three synthesised tungsten(VI) phenoxide species was as expected as the three compounds are broadly similar. The tungsten atoms are six co-ordinate, being surrounded by six oxygen atoms from the phenol ligands. Tungsten is also in the +VI oxidation state in all three of the compounds synthesised.

Due to the low sensitivity of the tungsten nucleus, other examples of ^{183}W NMR shifts are not common so firm conclusions on the implications of this data are difficult to reach. However, there are a couple of other examples to be found in the literature.

^{183}W NMR chemical shifts span approximately 5000ppm with the resonance position being strongly affected by the nature of the co-ordinated ligand.[114] The most highly shielded compound is WF_6 which has a chemical shift of -1117ppm. Substitution of the fluorine atoms by ligands containing oxygen donors causes deshielding of the tungsten nucleus. The ^{183}W NMR chemical shift of $WF_5(OMe)$ is -1065ppm and the shift of $WF_5(OPh)$ is -916ppm.[116] Similarly, substitution of all the fluorine atoms by chlorine atoms leads to significant deshielding: the ^{183}W NMR shift for WCl_6 is +2181ppm. ^{183}W NMR signals have also been detected for two compounds containing

the *cis*-WO_2 unit, $WO_2(Et_2NO)_2$ and $WO_2(C_5H_{10}NO)_2$.[117] The chemical shift values were -330ppm and -337ppm respectively.

^{183}W NMR studies have also been carried out on a series of tungsten oxotetraalkoxide compounds of the type $WO(OR)_4$ where R = Me, Et, *cyclo*-C_6H_{11}, Bu^t, $C_6H_3Pr^i_2$-2,6).[92] All these compounds, apart from the $C_6H_3Pr^i$-2,6 and Bu^t derivative, are dimers with alkoxide bridges. The ^{183}W NMR chemical shift values recorded for these compounds are shown in Table 2.2.

Table 2.2 Tungsten Chemical Shift Values for Alkoxide Compounds Found in the Literature.[92]

R	Chemical shift (ppm)[a]	Temperature (K)
Me	-62.9	295
Et	-126.3	293
cyclo-C_6H_{11}	-140.3	298
Bu^t	-386.9	300
$C_6H_3Pr^i_2$-2,6	-493.6	295

[a] referenced to 2 mol dm^{-3} aqueous Na_2WO_4.

These results show that as the steric bulk of the alkyl substituent is increased the chemical shift value decreases. Additionally, single crystal X-Ray diffraction studies have shown that the Me derivative is binuclear, and hence six co-ordinate, and that the $C_6H_3Pr^i_2$-2,6 derivative is mononuclear and hence five co-ordinate. Therefore, the two extremes in the ^{183}W NMR chemical shift data could reflect the differing co-ordination number at the tungsten centre.[92]

The ^{183}W NMR chemical shift values obtained from the compounds synthesised in this chapter were -474.8, -416.3 and -446.3ppm. These compounds are six co-ordinate but are more similar to the datum for the $C_6H_3Pr^i_2$-2,6 derivative which is five co-ordinate rather than the Me derivative which is six co-ordinate. However, it is

unlikely the ^{183}W NMR shifts from **(1)**, **(2)** and **(3)** are comparable with any of the oxotetraalkoxide compounds due to the presence of the W=O unit. This would greatly affect the distribution of electrons in the tungsten atoms orbitals and hence the ^{183}W NMR chemical shift as indicated by the extended MO Hückel calculations.[118]

Analysis of ^{183}W NMR chemical shifts in polyoxometalates has been carried out using extended Hückel MO calculations. The calculations were carried out for single WO_6 octahedra of different symmetries using five d→d* energy differences. The sum $\Sigma 1/(E_d \rightarrow E_d^*)$, where E_d and E_d^* are the calculated weight average energies for bonding and anti-bonding orbitals, has been calculated and plotted against the chemical shift for corresponding tungsten atoms and a practically linear relationship has been found. These calculations have indicated the electronic influence on the ^{183}W NMR chemical shift value.[118]

2.4.2.2 ^{1}H, ^{13}C and ^{19}F NMR Spectroscopy

The ^{1}H NMR spectra recorded for compound **(1)** showed two complex unresolved multiplets in the aromatic region due to the protons on the phenol rings. The sets of peaks were centred at 6.86 and 7.21ppm. Integrals showed the peaks to be representative of 18 and 12 protons respectively. The chemical shift and the integral of these peaks were consistent with the published data for this compound.[112]

The ^{1}H NMR for **(2)** displayed two unresolved multiplets at 6.79 and 6.91ppm in the ratio of 1:1. This was as expected as the fluorine is located in the para position on the phenol ring thereby creating two equivalent proton environments.

The proton spectrum recorded for compound **(3)** showed three unresolved multiplets in the aromatic region with chemical shift values of 6.58, 6.71 and 7.06ppm. The multiplets were in a ratio of 1:1:1. The fluorine atoms are in the meta and para positions on the phenol rings which give three unique proton positions, hence three signals with a 1:1:1 ratio. Since the individual couplings of the protons could not be

determined for any of the three compounds synthesised it suggests that the six phenol rings present on each molecule are not freely rotating in solution and thus giving equivalent positions for the protons on the six rings.

The ^{13}C NMR for compound **(1)** showed four peaks corresponding to the four carbon environments present in the phenol ring. The peaks seen at 120.4, 123.4 and 128.8ppm can be assigned to CH carbons. The remaining peak seen in the spectrum at 161.8ppm can be attributed to the CO group present in the phenol ring.

The ^{13}C spectrum recorded for compound **(2)** indicated the presence of four carbon environments. However, due to the fluorine atom present in the para position on the phenol ring all the carbon signals were split into doublets as a result of carbon fluorine coupling. The carbon-fluorine coupling constants for **(2)** are displayed in Table 2.3.

Table 2.3 Chemical Shifts and Carbon-Fluorine Coupling Constants for $W(OC_6H_4F\text{-}4)_6$.

	Chemical Shift (ppm)	Coupling Constant (Hz)	Assigned Group
$^1J_{CF}$	159.1	243	para CF
$^2J_{CF}$	115.5	24	meta CH
$^3J_{CF}$	121.2	8	ortho CH
$^4J_{CF}$	157.6	2	CO

The coupling constant values obtained for **(2)** are typical carbon-fluorine coupling values. Carbon-fluorine coupling constants recorded for mono-fluorobenzene are displayed in Table 2.4.[119] It was possible to assign individual carbon atoms in **(2)** as the position of the fluorine atom was known, therefore, the carbon atoms could be deduced from the coupling constant magnitudes.

Table 2.4 Carbon Fluorine Coupling Constants for Mono-Fluorobenzene.[119]

	Coupling Constant (Hz)
$^1J_{CF}$	245
$^2J_{CF}$	21
$^3J_{CF}$	8
$^4J_{CF}$	3

The ^{13}C NMR spectra for **(3)** was more complex as two fluorine atoms are present on the phenol ring. However, there are now six carbon signals as the symmetry in the phenol ring is broken by having fluorine atoms in the 3 and 4 positions. Due to fluorine carbon coupling these signals are split into doublets and doublets of doublets. The chemical shifts and coupling constants are shown in Table 2.5.

Table 2.5 Chemical Shifts and Carbon Fluorine Constants for $W(OC_6H_3F_2\text{-}3,4)_6$.

	Chemical Shift (ppm)	Coupling Constant (Hz)	Carbon Atom*
$^1J_{CF}$	147.6 (dd)	247	d or c
	149.8 (dd)	251	d or c
$^2J_{CF}$	147.6 (dd)	14	d or c
	149.8 (dd)	14	d or c
	109.5 (d)	19	b or e
	117.1 (d)	19	b or e
$^3J_{CF}$	115.9 (dd)	6	f
	156.6 (d)	9	a
$^4J_{CF}$	115.9 (dd)	3	f

* Carbon Atom Labelling for **(3)**.

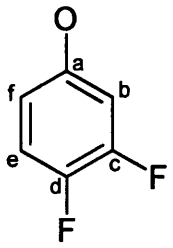

The carbon fluorine coupling constant values for compound **(3)** are consistent with those in the literature and those recorded for compound **(2)**. The expected carbon spectrum for **(3)** should show doublets of doublets for the carbon atoms at e and b from $^{2}J_{CF}$ and $^{3}J_{CF}$ couplings. However, only doublets are observed, presumably from $^{2}J_{CF}$ couplings from the nearest fluorine atom.

^{19}F NMR was carried out on compounds **(2)** and **(3)** since they contained fluorine atoms. The ^{19}F NMR spectra obtained for **(2)** showed a single unresolved multiplet at -118.8ppm. The ^{19}F NMR of the free ligand has a peak at approximately -123ppm which is consistent with the synthesised compound.[120] The ^{19}F NMR spectra recorded for **(3)** showed two unresolved multiplets with chemical shift values of -134.3 and -141.6ppm.

2.5 CRYSTAL STRUCTURES

Crystals of acceptable quality from all three tungsten(VI) hexaphenoxide compounds synthesised were grown from methanol solutions which had been placed in a freezer overnight. The crystals from **(1)**, **(2)** and **(3)** were dark red needles and were stable in the atmosphere. Table 2.7 summarises the relevant bond lengths of the three compounds in addition to three literature examples of similar molecules.

The crystal structure obtained for **(1)** is illustrated in Figure 2.4 with relevant bond angles and distances for this compound summarised in Tables 2.6 and 2.7 respectively.

Table 2.6 Selected Bond Angles for $W(OPh)_6$.

	Angle (°)		Angle (°)
O(4)-W(1)-O(3)	178.9(3)	O(2)-W(1)-O(6)	90.4(3)
O(4)-W(1)-O(2)	88.5(3)	O(5)-W(1)-O(6)	175.5(3)
O(3)-W(1)-O(2)	90.5(3)	O(4)-W(1)-O(1)	88.1(3)
O(4)-W(1)-O(5)	92.3(3)	O(3)-W(1)-O(1)	92.9(3)
O(3)-W(1)-O(5)	88.2(3)	O(2)-W(1)-O(1)	176.6(3)
O(2)-W(1)-O(5)	91.5(3)	O(5)-W(1)-O(1)	88.6(3)
O(4)-W(1)-O(6)	91.9(3)	O(6)-W(1)-O(1)	89.8(3)
O(3)-W(1)-O(6)	87.6(3)		

Crystal structure determination showed the tungsten atom to be surrounded by six oxygen atoms, from the phenol rings, in a slightly distorted octahedral geometry. The crystal structure data is consistent with an other structural analysis obtained for **(1)** which appeared during the course of this work.

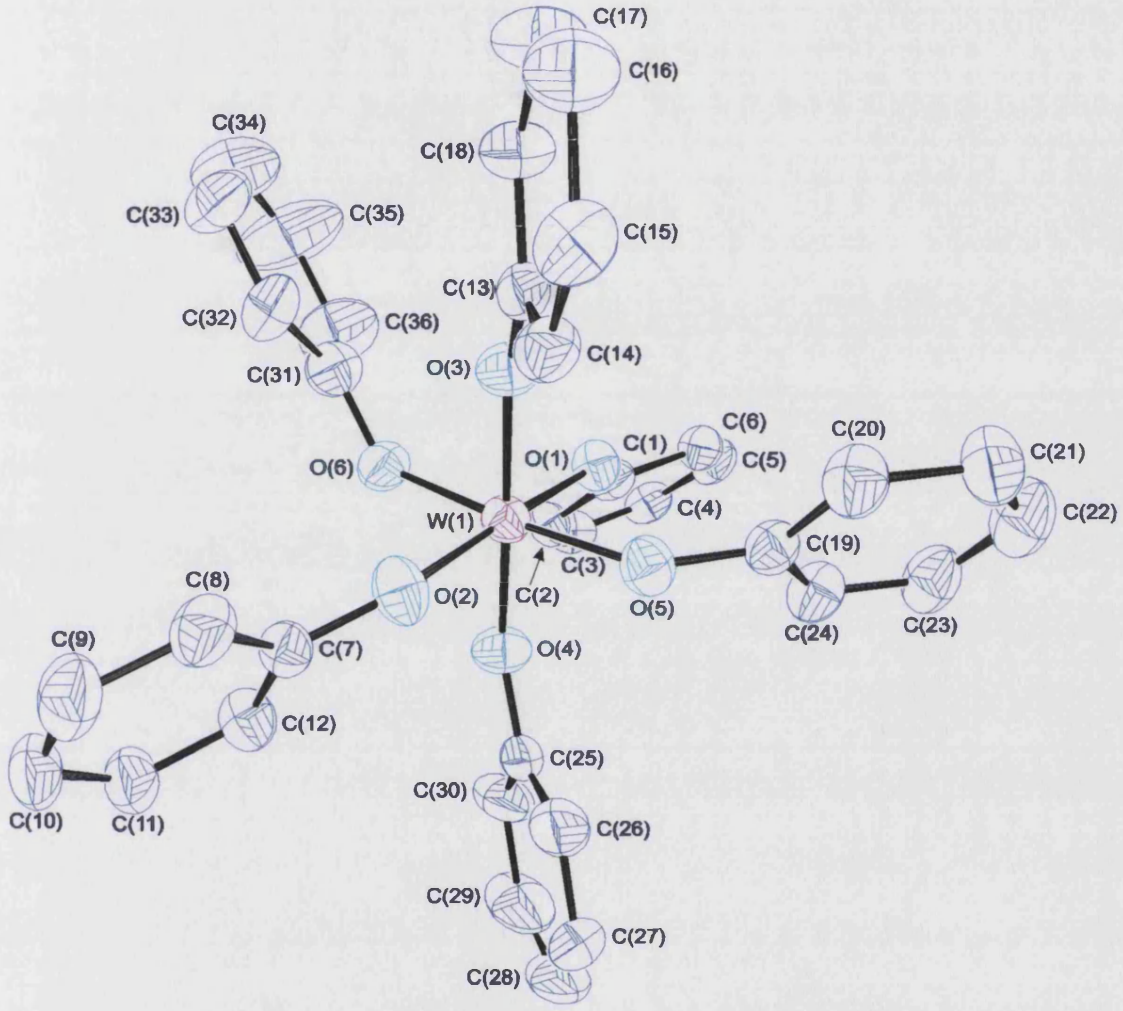

Figure 2.4 Crystal Structure determined for $W(OPh)_6$ **(1)**.

Table 2.7 Summary of Tungsten Oxygen Bond Lengths (Å) and *cis* O-W-O (°)[a] Angles in **(1)**, **(2)**, **(3)** and Related compounds.

	(1)	**(2)**	**(3)**	$W(OPh)_6$	$W(OC_6H_4Me\text{-}4)_6$	$[W(OPh)_6]^{-}$ [b]
W(1)-O(1)	1.896(6)	1.910(8)	1.879(12)	1.883(4)	1.894(4)	n/a
W(1)-O(2)	1.878(7)	1.887(8)	1.896(12)	1.884(4)	1.887(3)	n/a
W(1)-O(3)	1.878(6)	1.871(8)	1.932(11)	1.897(4)	1.896(3)	n/a
W(1)-O(4)	1.874(7)	1.899(8)	1.899(12)	1.908(4)	1.889(3)	1.932(5)
W(1)-O(5)	1.884(6)	1.912(8)	1.882(13)	1.905(4)	1.913(3)	1.956(4)
W(1)-O(6)	1.892(6)	1.916(8)	1.883(13)	1.917(4)	1.891(3)	1.940(5)
Mean	1.884(6)	1.899(8)	1.895(12)	1.899(4)	1.895(9)	1.943
O-W-O	88.1(3)	85.7(4)	88.6(6)	87.5(2)	86.1(2)	88.1
	92.9(3)	94.6(4)	92.1(6)	92.6(2)	94.7(1)	91.9

[a] Max, min values. [b] $[Et_4N]^{+}$.

The tungsten oxygen bond lengths in compound **(1)** varied between 1.874(7) and 1.896(6) Å with acute bond angles between 88.1(3) and 92.9(3)°. The mean tungsten oxygen bond length was 1.884(6) Å. The only other analytical data for $W(OPh)_6$ available in the literature when this work commenced were unit cell parameters but the structure had not been fully solved.[121] However, recently, $W(OPh)_6$ was synthesised by a transesterification reaction and its crystal structure determined.[112] The tungsten oxygen bond lengths for this molecule are also summarised in Table 2.7. The tungsten oxygen bond lengths in $W(OPh)_6$ vary from 1.883(4) to 1.917(4) Å with a mean tungsten oxygen bond length of 1.899(4) Å. Once the estimated standard deviation (esd) is taken into account the mean bond length for this molecules can be considered identical to those seen in **(1)**. The acute tungsten oxygen bond angles reported in the earlier study vary from 87.5(2) to 92.6(2)°, this is again identical to the acute angle variation seen in **(1)**. The structure of $W(OPh)_6$ in the literature and compound **(1)** are consistent with each other apart from the disorder seen in the literature example which could well be caused by the use of a different recrystallisation solvent.

The mean tungsten oxygen bond length in **(1)** [1.884(6) Å] is significantly shorter than that seen in $[W(OPh)_6]^-$ (1.943 Å). The longer mean tungsten oxygen bond distance observed for the W(V) ion is probably due to the lower charge on the tungsten atom.

The crystal structure was determined for **(2)** and is displayed in Figure 2.5. The relevant bond lengths and angles are located in Tables 2.7 and 2.8. The crystal structure was found to contain a tungsten atom in a six co-ordinate geometry. The tungsten atom was located in a slightly distorted octahedral position surrounded by six parafluorophenol ligands. The tungsten oxygen bond lengths in **(2)** vary between 1.916(8) and 1.871(8) Å with a mean bond length of 1.899(8) Å. The mean tungsten oxygen bond length is consistent with the other synthesised compounds, **(1)** and **(3)**, and similar compound in the literature. However, as seen in **(1)** the mean tungsten oxygen bond length for **(2)** is considerably shorter than that observed for $[W(OPh)_6]^-$ (Table 2.7). The acute bond angles between the tungsten and oxygen atoms in **(2)** vary between 85.7(4) and 94.6(4)°. This is a significantly greater variation in bond angle than seen in

(1) which displayed acute bond angles between 88.1(3) and 92.9(3)°. The variation in acute O-W-O bond angles in **(2)** is similar to that seen in $W(OC_6H_4Me\text{-}4)_6$ where the bond angles vary between 86.1(2) and 94.7(1)°.[92] This similarity in bond angle variation is perhaps no surprise as both $W(OC_6H_4Me\text{-}4)_6$ and **(2)** have substituted groups in the para position on the phenol ring.

Table 2.8 Selected Bond Angles for $W(OC_6H_4F\text{-}4)_6$.

	Angle (°)		Angle (°)
O(3)-W(1)-O(2)	175.3(3)	O(4)-W(1)-O(5)	174.3(4)
O(3)-W(1)-O(4)	87.0(4)	O(1)-W(1)-O(5)	85.7(4)
O(2)-W(1)-O(4)	90.2(4)	O(3)-W(1)-O(6)	90.5(4)
O(3)-W(1)-O(1)	94.6(4)	O(2)-W(1)-O(6)	86.0(4)
O(2)-W(1)-O(1)	89.0(3)	O(4)-W(1)-O(6)	94.5(4)
O(4)-W(1)-O(1)	89.1(4)	O(1)-W(1)-O(6)	173.9(3)
O(3)-W(1)-O(5)	91.2(4)	O(5)-W(1)-O(6)	90.9(4)
O(2)-W(1)-O(5)	91.9(4)		

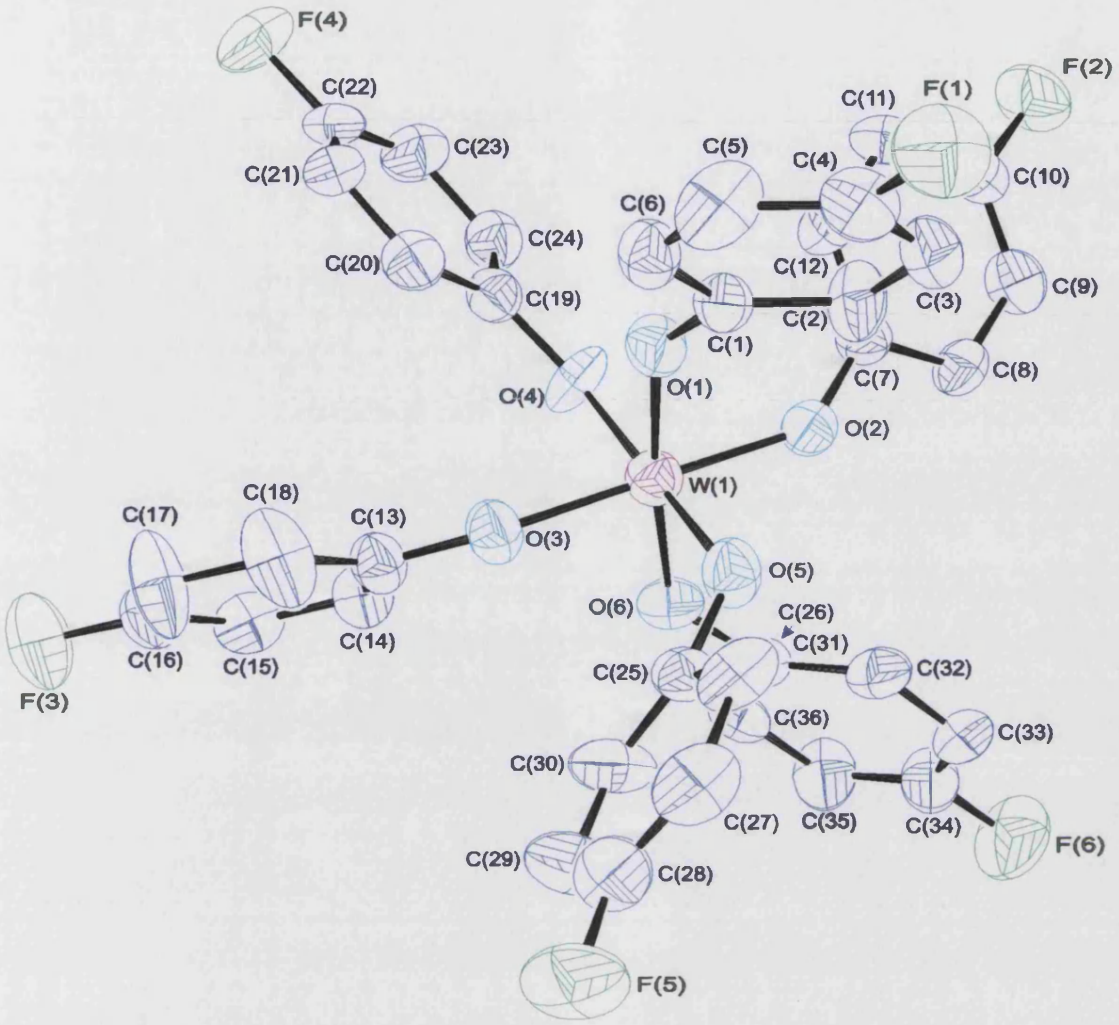

Figure 2.5 Crystal Structure of $W(OC_6H_4F\text{-}4)_6$ **(2)**.

The structure of **(3)** was determined by single crystal X-ray diffraction and is shown in Figure 2.6. Relevant bond angles and lengths are summarised in Tables 2.9 and 2.7 respectively. Structural determination showed compound **(3)** to be monomeric with the tungsten atom surrounded by six oxygen atoms in a slightly distorted octahedral centre. This structure is in keeping with the previous two compounds synthesised. The tungsten oxygen bond lengths vary from 1.882(13) to 1.932(11) Å, with a mean tungsten oxygen bond length of 1.895(12) Å. This is in agreement with compounds **(1)** and **(2)** and the tungsten(VI) hexaphenoxide derivatives found in the literature. However, this is again significantly shorter than the mean tungsten oxygen bond length seen in

$[W(OPh)_6]^-$. The acute tungsten oxygen bond angles in **(3)** vary between 88.6(6) and 92.1(6)°. The acute bond angle variations in **(1)** and **(2)** were between 88.1(3) and 92.9(3)°, and between 85.7(4) and 94.6(4)° respectively. The greatest acute bond angle variation is seen in **(2)** $[W(OC_6H_4F\text{-}4)_6]$ which is mirrored by the bond angle variation seen in $W(OC_6H_4Me\text{-}4)_6$ [86.1(2) to 94.7(1)°], both of these compounds have substituted groups in the para position on the phenol rings. However, **(3)** has substituted groups in the meta and para positions on the phenol ring and does not exhibit such a large tungsten oxygen acute bond angle variation which is somewhat surprising.

Table 2.9 Selected Bond Angles for $W(OC_6H_3F_2\text{-}3,4)_6$.

	Angle (°)		Angle (°)
O(1)-W(1)-O(5)	92.1(6)	O(6)-W(1)-O(4)	91.6(6)
O(1)-W(1)-O(6)	89.5(5)	O(2)-W(1)-O(4)	179.0(6)
O(5)-W(1)-O(6)	177.8(6)	O(1)-W(1)-O(3)	178.2(5)
O(1)-W(1)-O(2)	89.6(6)	O(5)-W(1)-O(3)	89.8(6)
O(5)-W(1)-O(2)	89.1(6)	O(6)-W(1)-O(3)	88.6(6)
O(6)-W(1)-O(2)	89.4(6)	O(2)-W(1)-O(3)	90.5(5)
O(1)-W(1)-O(4)	90.7(5)	O(4)-W(1)-O(3)	89.2(5)
O(5)-W(1)-O(4)	89.8(6)		

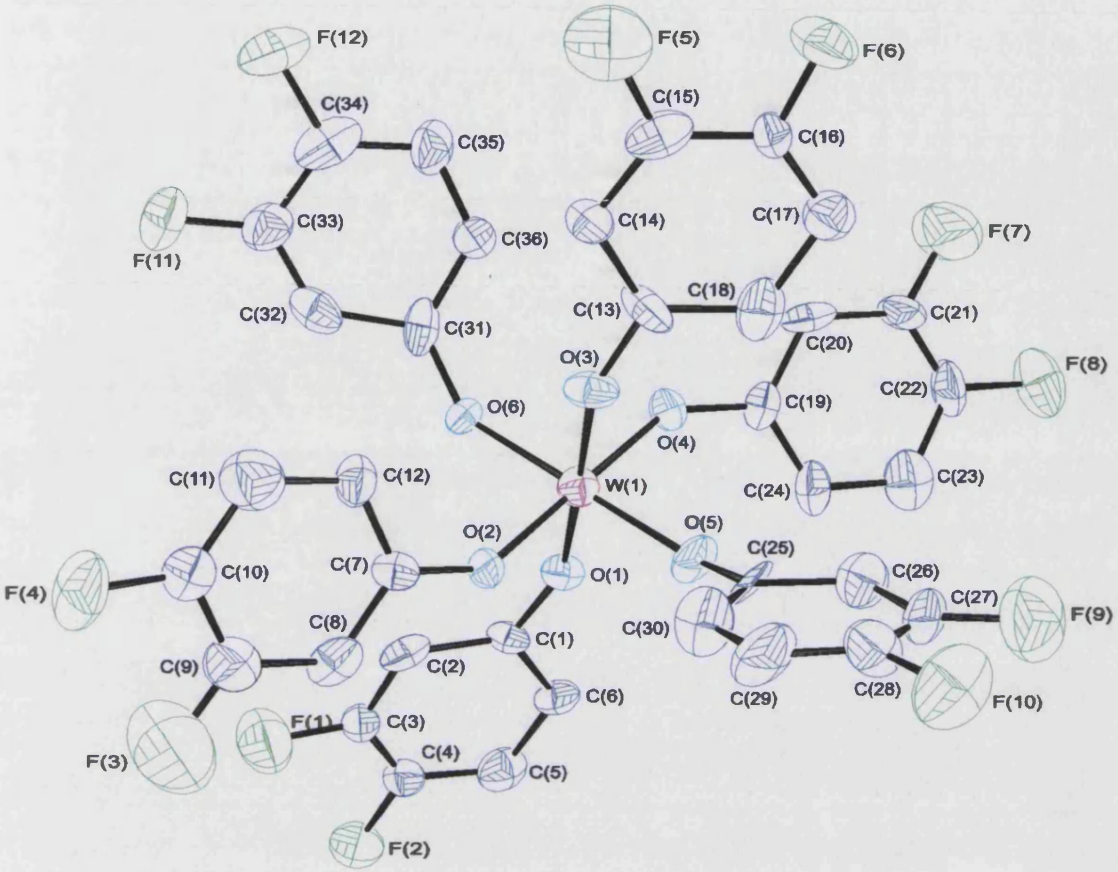

Figure 2.6 Crystal Structure Determined for $W(OC_6H_3F_2\text{-}3,4)_6$ **(3)**.

2.6 CVD TESTING OF PRECURSORS

The primary reason for studying **(1)**-**(3)** was their low melting points. However, once $W(OPh)_6$ had been synthesised it was discovered that it was insufficiently volatile at atmospheric pressure to allow APCVD. A limited APCVD study using the apparatus described in Appendix 7 was undertaken with **(1)**. A range of bubbler temperatures from 90 to 180°C was tried in an attempt to deposit a suitable film using this precursor. The final deposition experiment in this series had a bubbler temperature of 180°C with a run time of one hour. This run deposited what may have been a very thin film on the glass substrate. However, it was far to thin to warrant any analysis and no further APCVD experiments using this precursor were attempted.

Since **(1)** was found to be insufficiently volatile at atmospheric pressure to allow APCVD it was hoped the two fluorinated derivatives synthesised using the same methodology would have enhanced volatility. The melting points of compounds **(2)** and **(3)** were 101°C and 105-107°C respectively. This represented a slight increase in melting point from that seen in **(1)** (m.p. 95°C). However, the volatility at atmospheric pressure for **(2)** and **(3)** was still not sufficient for APCVD. Brief experiments conducted on a low pressure CVD reactor indicated that $W(OPh)_6$ may be volatile under reduced pressure so could be suitable for LPCVD. Under reduced pressure and at ca. 220°C the precursor was seen to sublime from the heated vessel in which it was contained and condense on the unheated gas lines. At the time of the study heating the gas lines was proving difficult so this experiment was never repeated. Therefore, all three compounds synthesised in this section were delivered to the reactor by an aerosol delivery technique. This section gives details of the deposition conditions used for film growth as well as analysis for a representative selection of the films deposited.

Films were deposited on a 4mm glass substrate which had been coated with a thin film of SiCO which acts as a blocking layer to prevent sodium diffusion into the film deposited. The precursor was dissolved in a solvent (toluene in all cases) and

substrate as an aerosol using a nitrogen carrier gas. Details of the horizontal cold wall reactor used during these experiments can be found in Appendix 7.

Toluene was chosen as the solvent primarily because all three precursors were reasonably soluble in it. The other advantage of toluene is its high boiling point. This enables the precursors to be transported into the reactor with out evaporation of the solvent in the reactor baffle and hence precursor deposition in advance of the glass substrate. Despite the precursors stability, toluene freshly distilled over sodium-benzophenone was used during the CVD experiments. In all the deposition experiments carried out in this chapter no oxygen was added to the reactive gas flow. Therefore, any oxygen present in the films deposited has come from the precursor being tested.

Once deposited the films were analysed by glancing angle X-ray diffraction to determined their composition, and by SEM to give an indication of the surface morphology of the film. The transmission-reflectance spectra of the films were also recorded to determine if any selectivity to solar radiation was evident.

2.6.1 Deposition Conditions

AACVD experiments were conducted on all three of the compounds synthesised in this chapter. The compounds were stable in the atmosphere so no special handling techniques were required. Several runs were carried out with each precursor in an attempt to deposit a suitable film for analysis. Deposition conditions for the films which have been analysed are displayed in Table 2.10. Both low temperature (300°C) and high temperature (> 400°C) runs were carried out for **(2)** and **(3)** to ascertain any differences in the films deposited.

Table 2.10 Summary of Conditions used for AACVD Experiments using **(1)** **(2)** and **(3)**.

Compound	(1)	(2)	(2)	(3)	(3)
Film ID	r1	r2	r3	r4	r5
Solution concentration gcm^{-3}	0.01	0.01	0.01	0.01	0.01
Reactor temp. °C	475	300	450	300	400
Carrier gas (N_2) flow rate $lmin^{-1}$	1.2	1.0	1.2	1.0	1.0
Run time min	26	30	40	30	30

2.6.2 Film Analysis

Films r1, r3 and r5 covered the full length of the glass substrate (22cm) and had a powdery surface layer which could be easily removed with a soft tissue. This left a well adhered deep blue film with coloured interference fringes visible. Once removed the surface powder was seen to be dark blue or black in colour and was most likely carbon from the precursor, or from the solvent which was used to create the aerosol. However, it is also possible this soft surface layer could have been powdered tungsten oxide.

Films r2 and r4, which were deposited at a lower temperature (300°C), were well adhered to the glass surface and were deep blue in colour with coloured interference fringes visible. The films covered the full length of the glass substrate, however, there was no powdery surface layer present as seen with the higher temperature deposition experiments (r1, r3 and r5).

All five of the films were very similar in appearance with the lower temperature films being a more visually appealing shade of blue. None of the five films showed any discolouration on storage before analysis was completed.

2.6.2.1 Glancing Angle X-Ray Diffraction

Glancing angle X-ray diffraction studies were performed to determine if the films were crystalline or amorphous and whether a tungsten oxide film had been deposited. This technique also gives information about which phase or phases of tungsten oxide could be present in the film.

The X-ray diffraction patterns were obtained using low angle X-ray diffraction with the incident angle, θ, fixed at 1.5°. The X-ray diffraction patterns were acquired over the 2 theta range 0° to 75° with a collection time of 45 minutes. All the analysis in this section was performed in collaboration with Plikington Glass Ltd.

The glancing angle X-ray diffraction patterns of the films deposited at low temperature (r2 and r4) showed no crystalline peaks, however, between 15 and 30° an amorphous hump was seen (Figure2.7). This indicates that either the film contains a non-crystalline component or is relatively thin and the amorphous hump represents sampling of the glass substrate. Since both these films appeared thick, as indicated by optical interference fringes on the coated surface, the hump strongly indicates that these films are amorphous. Therefore, the composition of the films cannot be determined by this technique. However, the blue colour of the films does point to them being tungsten oxide as this is a characteristic colour for non-stoichiometric WO_{3-x}.

Glancing angle X-ray diffraction of the films deposited at high temperature (r1, r3 and r5) gave diffraction patterns. These patterns indicated that the films were crystalline and composed of tungsten oxide. The diffraction pattern obtained from r1 is displayed in Figure 2.8.

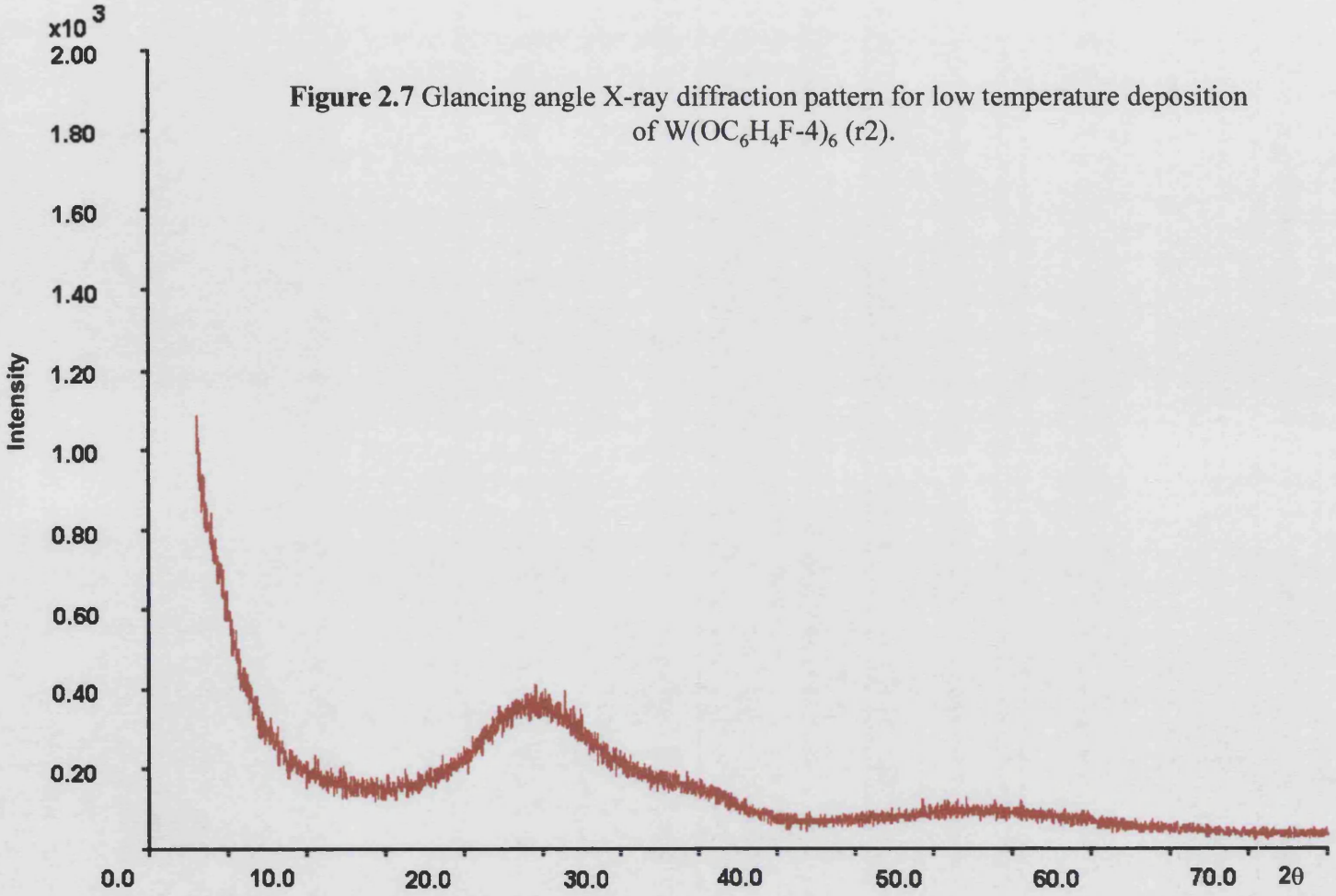

Figure 2.7 Glancing angle X-ray diffraction pattern for low temperature deposition of $W(OC_6H_4F\text{-}4)_6$ (r2).

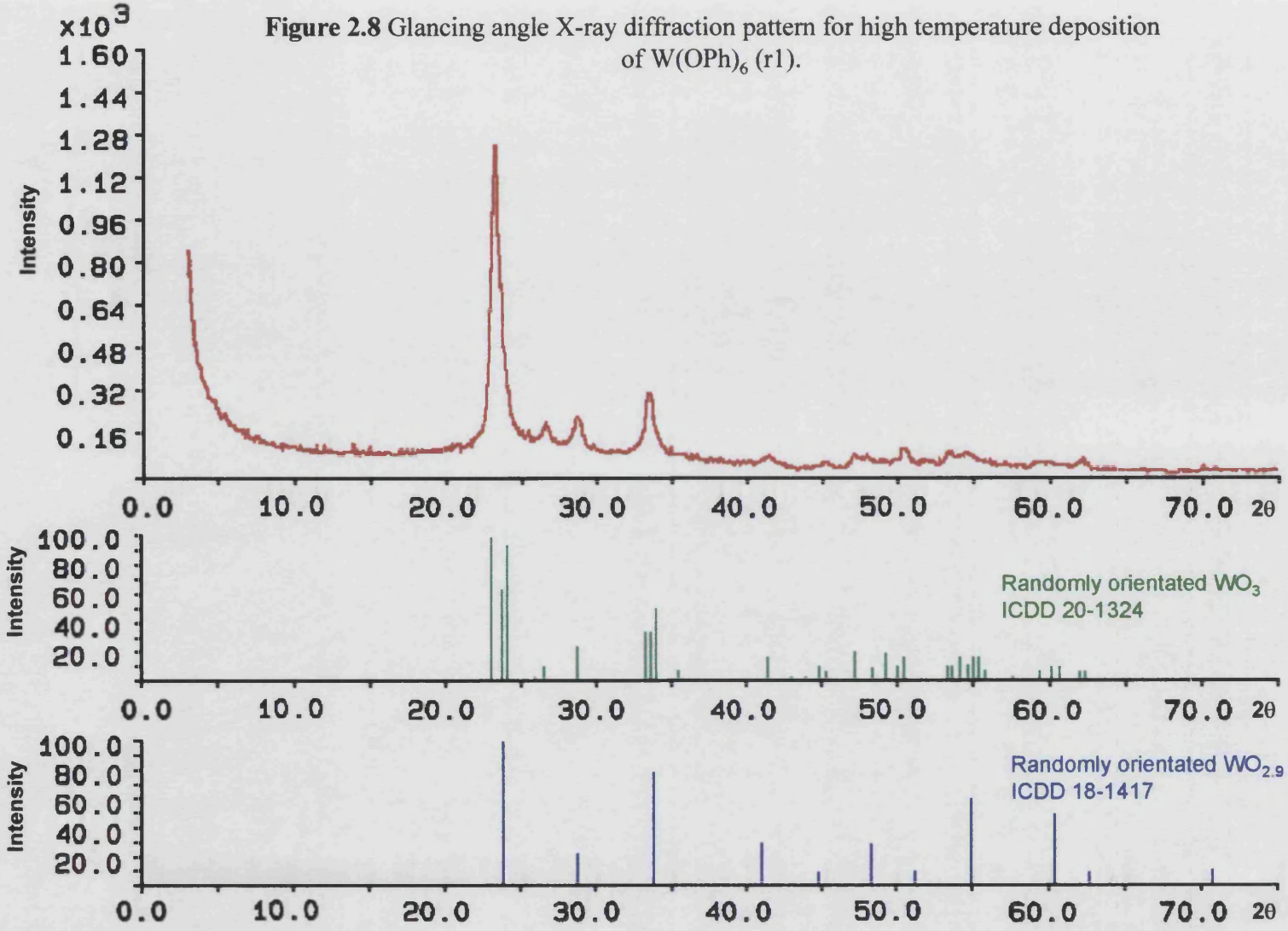

Figure 2.8 Glancing angle X-ray diffraction pattern for high temperature deposition of $W(OPh)_6$ (r1).

Peak match software suggested two possible phases of tungsten oxide present in film r1. A stoichiometric tungsten oxide phase (WO_3) and a non-stoichiometric $WO_{2.9}$ phase. Examination of the peaks from the spectra collected indicates that the film is mainly stoichiometric WO_3. The large peak observed at about 23° in the collected data is clearly several peaks as seen in the randomly orientated WO_3 spectra (ICDD 20-1324, Appendix 5) as opposed to the single peak present in the $WO_{2.9}$ spectra (ICDD 18-1417, Appendix 5). Additionally, the peak observed in the collected spectra at ca. 26° is unique to the WO_3 phase and is not seen in the $WO_{2.9}$ phase. However, the presence of a small amount of $WO_{2.9}$ cannot be ruled out as several of the peaks from each phase are coincidental with each other. Additionally, the film was blue in colour which indicates the presence non-stoichiometric tungsten oxide. Therefore, it seems reasonable to conclude that the film is mainly composed of WO_3 along with some $WO_{2.9}$ as indicated by the blue colour of the film.

The diffraction pattern obtained from film r3 is illustrated in Figure 2.9. As with the film r1, deposited at high temperature from $W(OPh)_6$, the two suggested tungsten oxide phases present are WO_3 and $WO_{2.9}$. The most intense peak in the spectra (ca. 23°) is clearly from the WO_3 phase, as is the small peak seen at about 26°. However, the intensities of the various peaks have changed when compared to the spectrum recorded for r1. The relative intensities of the peaks, when compared to the standard spectra, can give an indication as to any preferred orientation within the crystalline film. The standard spectra for WO_3 (ICDD 20-1324) is obtained from a randomly orientated crystalline sample. Therefore, if the intensities of the peaks in the collected spectra do not match the randomly orientated sample there could be a degree of preferred orientation within the film. In Figure 2.9 the peak seen at about 23° is relatively intense when compared with other peaks which indicates a possible preferred orientation along the 001 plane in the crystalline film. The glancing angle X-ray diffraction experiments do not rule out the presence of some non-stoichiometric $WO_{2.9}$ in the film. This is supported by the blue colour of the film which is characteristic of non-stoichiometric tungsten oxide. In conclusion, r3 is probably composed of mainly WO_3 with possible preferred orientation in the 001 plane, however, a small amount of $WO_{2.9}$ is also present as indicated by the blue colour of the film.

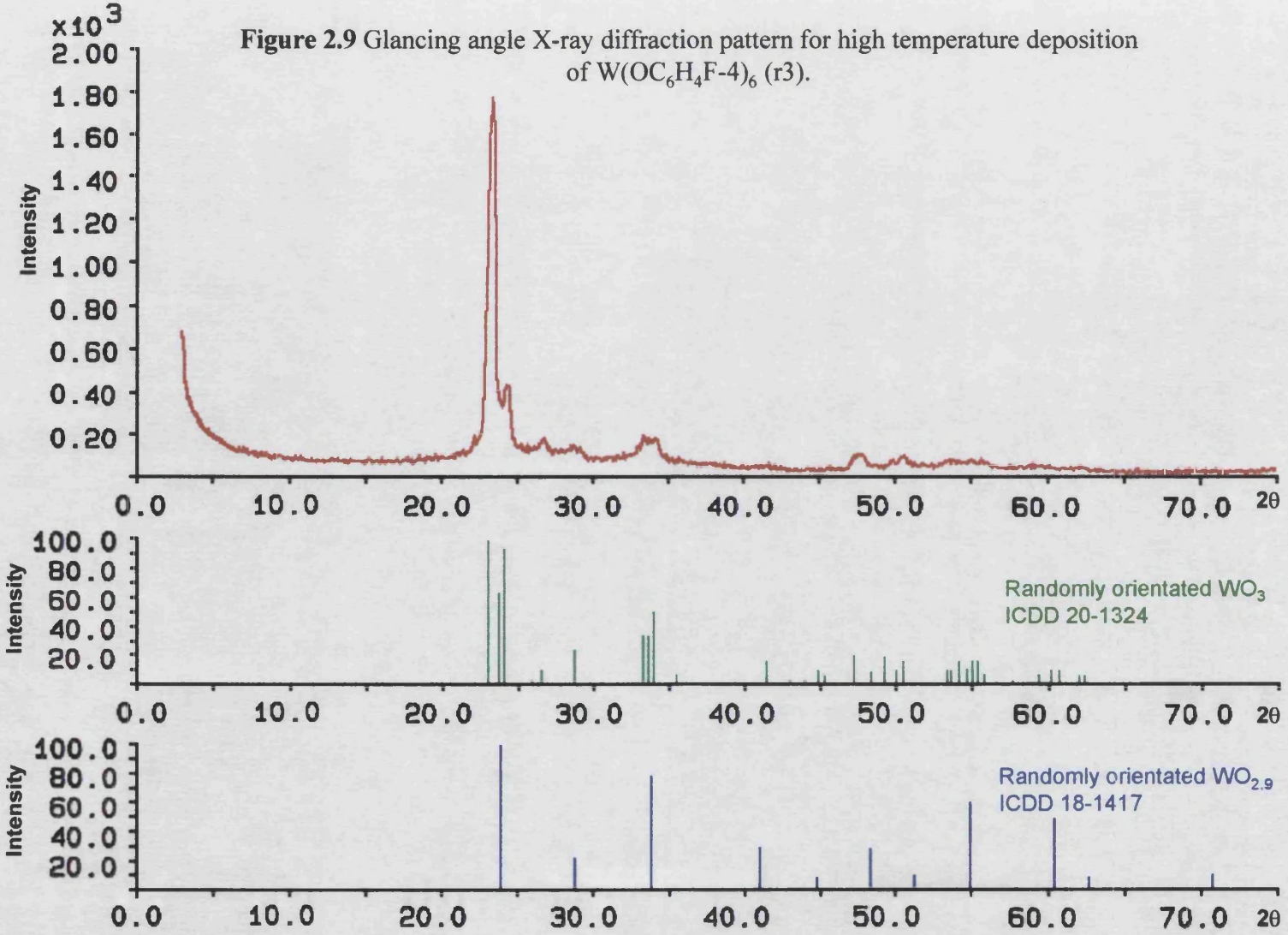

Figure 2.9 Glancing angle X-ray diffraction pattern for high temperature deposition of $W(OC_6H_4F\text{-}4)_6$ (r3).

The glancing angle X-ray diffraction pattern recorded for r5 is displayed in Figure 2.10. As with the previous two films (r1, r3) there are two possible phases of tungsten oxide present in the crystalline film, WO_3 and $WO_{2.9}$. The most intense peak seen in the diffraction pattern is characteristic of the WO_3 phase and has been seen in all of the films reported in this chapter. However, the clear shoulder on this peak at ca. 23° does correspond to the peak seen at ca. 23° in the $WO_{2.9}$ phase. The presence of this peak, and the blue colour of the film, is good evidence for the presence of some non-stoichiometric $WO_{2.9}$ within this crystalline film.

In summary, the glancing angle X-ray diffraction experiments have provided good evidence that crystalline WO_3 films have been deposited in a single step from the high temperature deposition runs. There is also evidence to suggest that some slightly non-stoichiometric tungsten oxide ($WO_{2.9}$) is present in these films. However, amorphous films were deposited from the low temperature deposition experiments although their blue colour indicates these could also be tungsten oxide films.

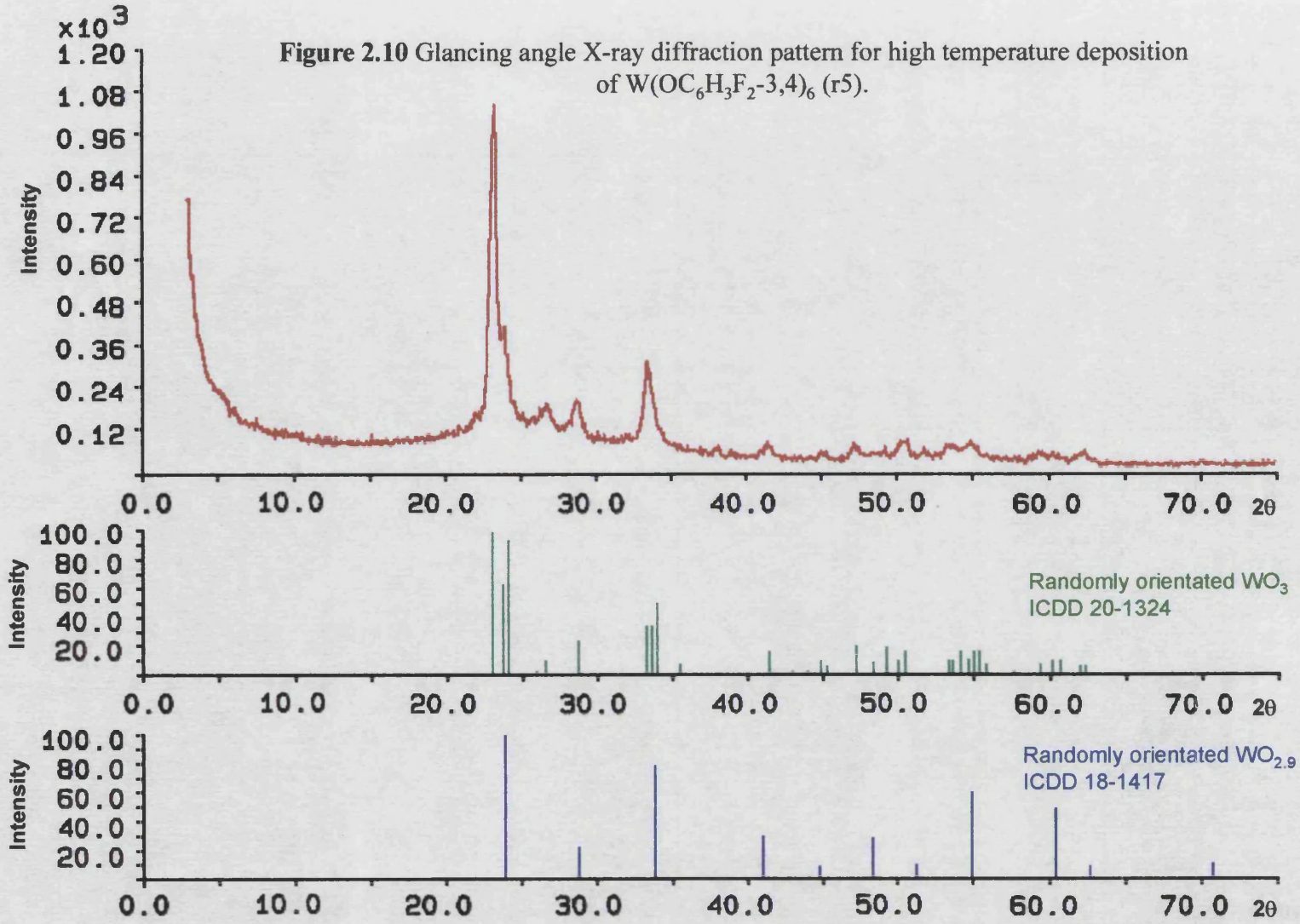

Figure 2.10 Glancing angle X-ray diffraction pattern for high temperature deposition of $W(OC_6H_3F_2\text{-}3,4)_6$ (r5).

2.6.2.2 SEM

Scanning Electron Microscopy (SEM) was performed in collaboration with Pilkington Glass Ltd on the three films which were deposited at high temperature (r1, r3 and r5), the results of which are illustrated in Figures 2.11-2.19. Figures 2.12, 2.15 and 2.18 show r1, r3 and r5 respectively from an 80° tilt angle. Figure 2.15 clearly shows the glass surface, the SiCO undercoat on the glass surface and then the crystalline tungsten oxide film which has been deposited.

Figures 2.11, 2.14 and 2.17 show films r1, r3 and r5 respectively from a reduced magnification. The straight lines seen on the surface of r1 are most likely to be scratch marks probably from storage of the film or cleaning of the film before optical measurements were performed, lines of this type were also seen on r3 (Figure 2.14). However, no lines are seen on r5 (Figure 2.17) which could indicate a harder film. The islands seen on the film could indicate the film was deposited via island growth. The difference between r5 and the other two films deposited (r1 and r3) is also clearly seen on the 90° tilt SEM's illustrated in Figures 2.13, 2.16 and 2.19. The images show the glass substrate at the bottom of the picture, then the undercoat and finally the film which has been deposited. In the images from r1 and r3 (Figures 2.13 and 2.16 respectively) the crystallinity of the films can clearly be seen. However, in r5 (Figure 2.19) the film surface appears smoother and the film almost looks amorphous in nature. The glancing angle X-ray diffraction data for this film showed it to be crystalline but also clearly indicated the presence of some non-stoichiometric $WO_{2.9}$ in the film which was not so clearly evident in r1 and r3. One possible explanation for these differences could be the deposition temperatures for the three high temperature films. Films r1 and r3 were deposited at 475 and 450°C respectively, however, r5 was deposited at 400°C. Other films deposited during these experiments at 300°C were all found to be amorphous, therefore, a deposition temperature of 400°C could be close to the point where a crystalline film rather than an amorphous film is deposited. Further studies would be necessary to confirm this observation.

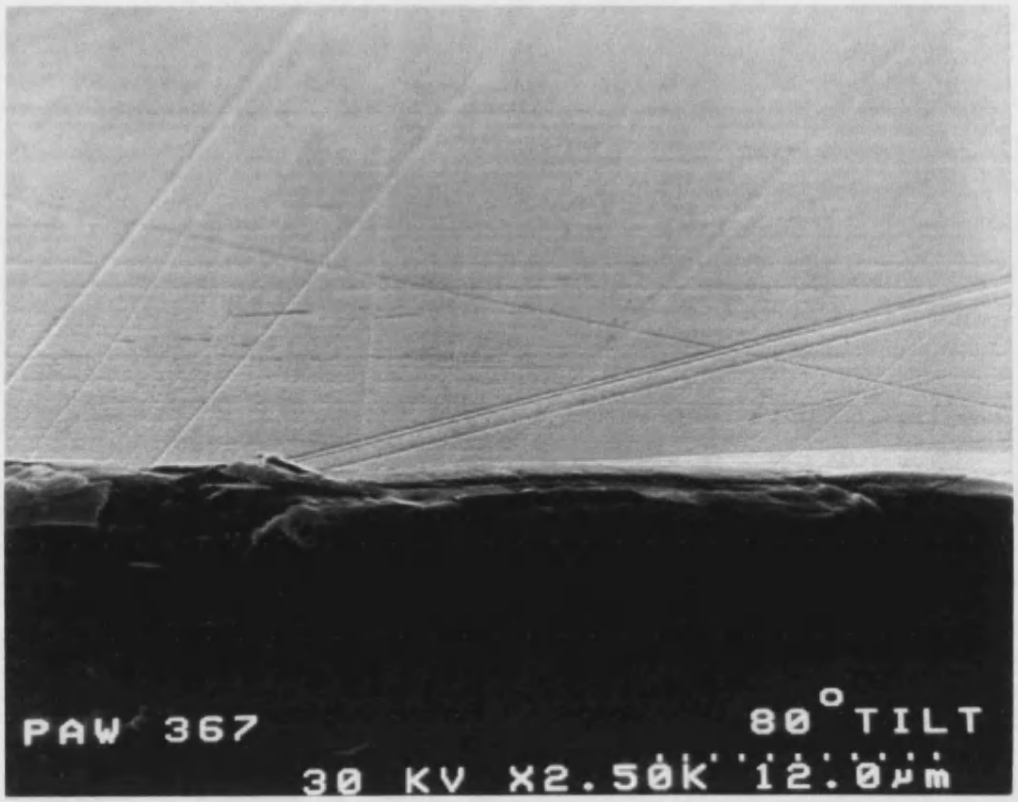

Figure 2.11 80° tilt SEM image from film r1.

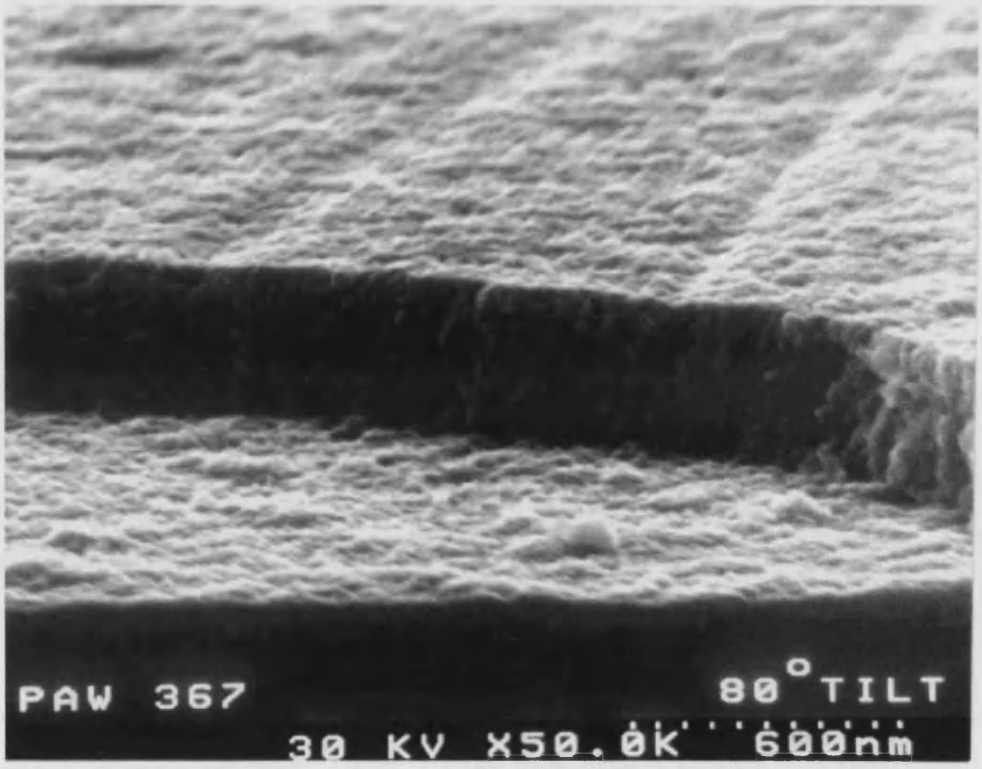

Figure 2.12 80° tilt SEM image from film r1 at higher magnification.

Figure 2.13 90° tilt SEM image from r1.

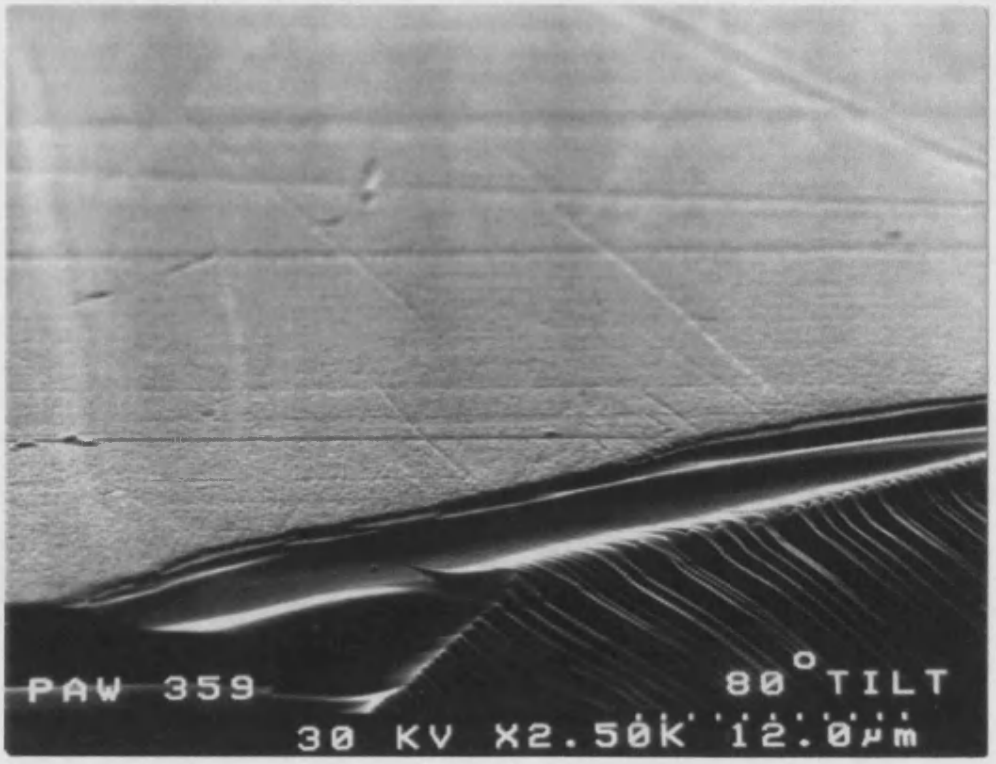

Figure 2.14 80° tilt SEM image from film r3.

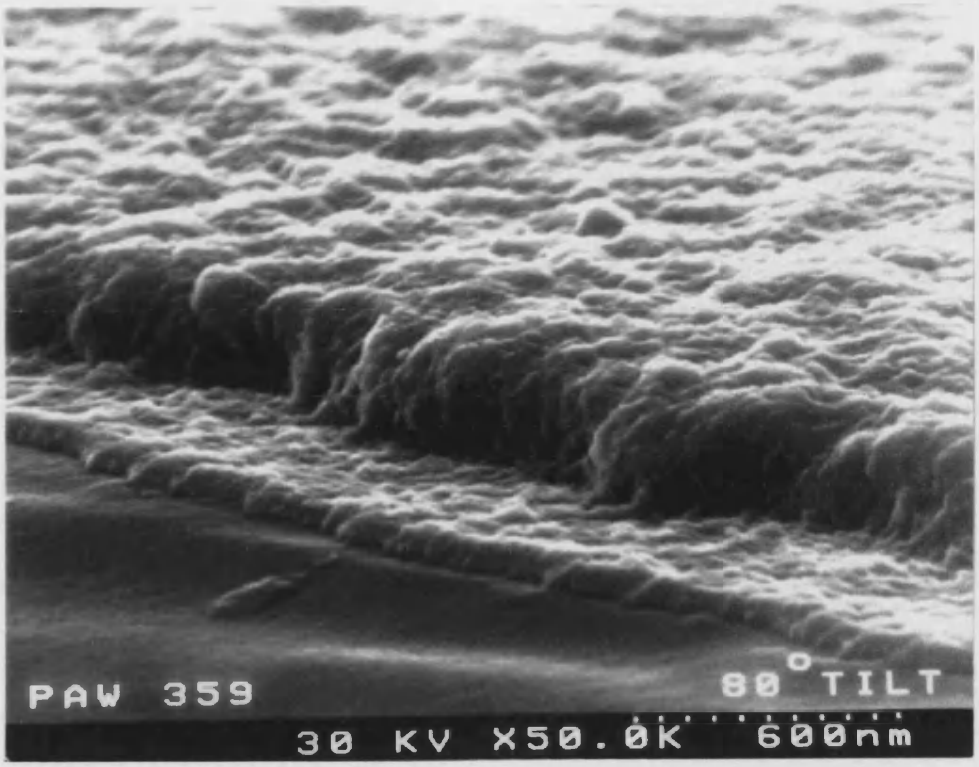

Figure 2.15 80° tilt SEM image from film r3 at higher magnification.

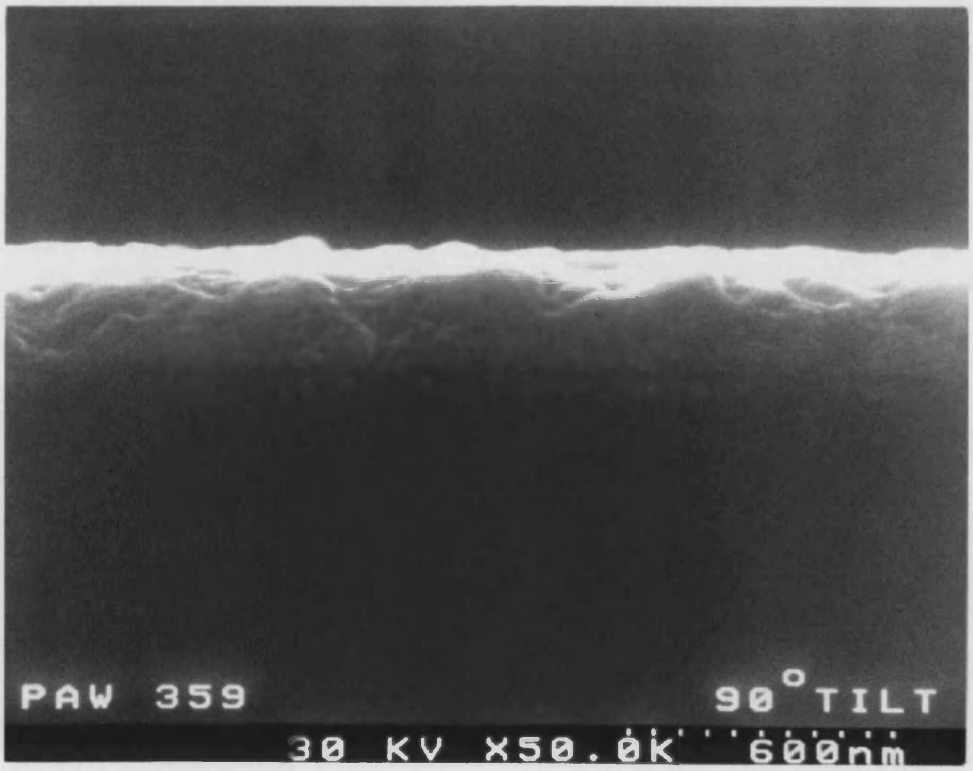

Figure 2.16 90° tilt SEM image from r3.

Figure 2.17 80° tilt SEM image from film r5.

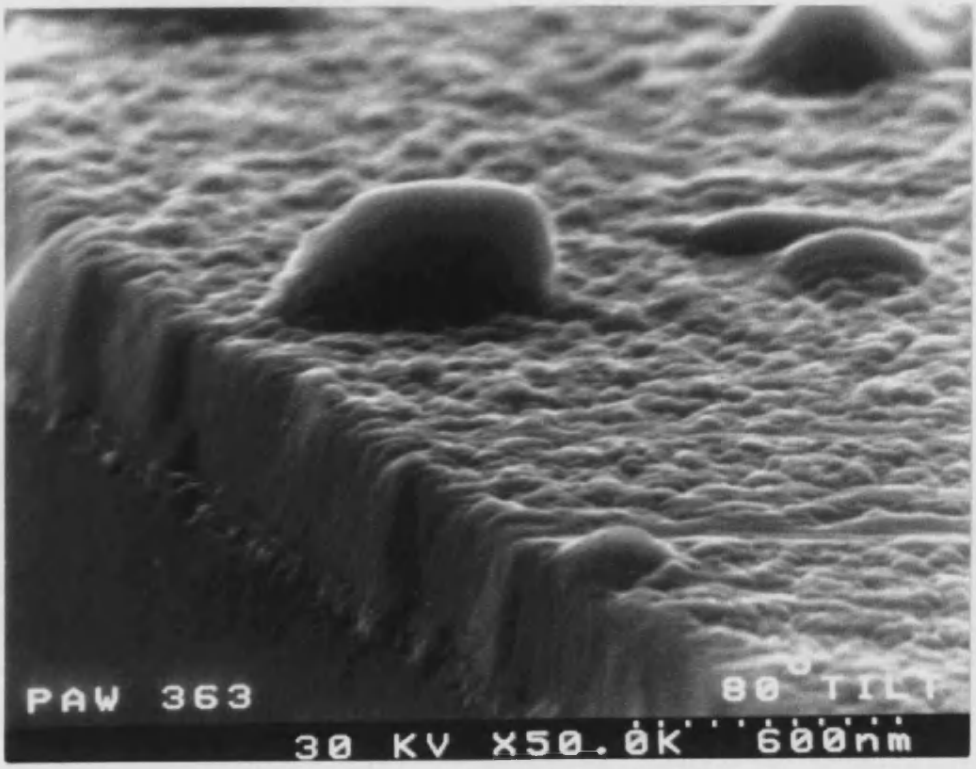

Figure 2.18 80° tilt SEM image from film r5 at higher magnification.

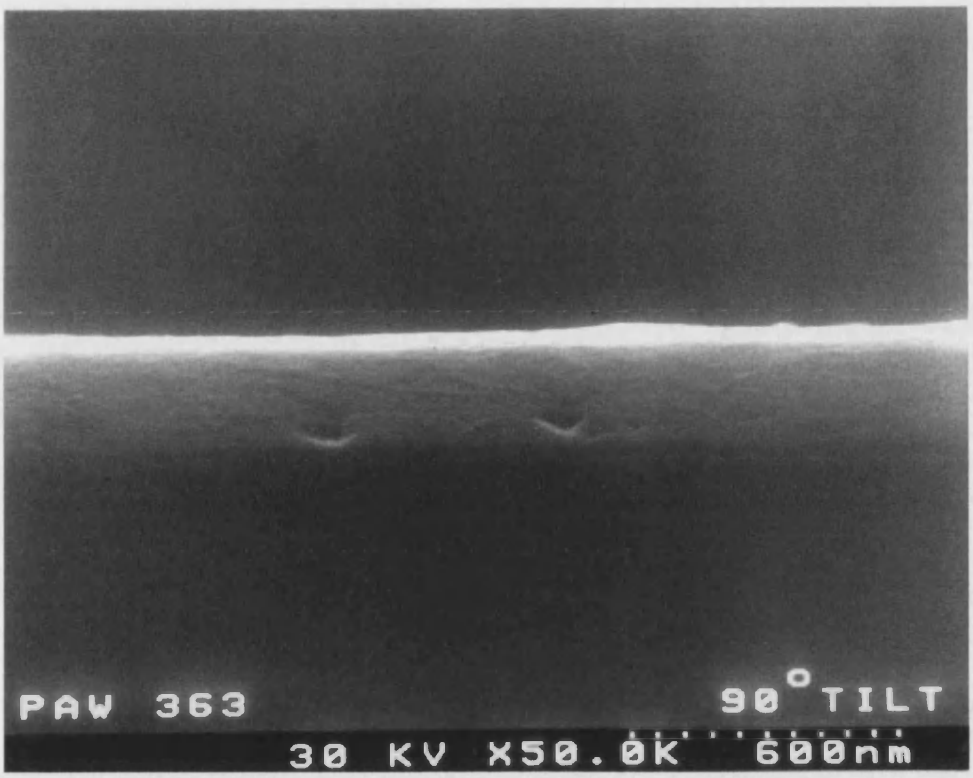

Figure 2.19 90° tilt SEM image from r5.

The 90° SEM images also give an indication as to the thickness of the films deposited. However, it should be remembered that this thickness measurement is at a single point on the film and the films deposited during these experiments were all non-uniform (Table 2.11).

Table 2.11 Approximate film thickness from SEM images.

Film ID	Thickness (Å)
r1	3500
r3	2300
r5	2300

2.6.2.3 Transmission-reflectance spectra

The transmission-reflectance spectra for all the films deposited were measured and are discussed in the following section. The transmission and reflectance of radiation from a film can be greatly affected by the thickness of the film. Since all the films deposited were non-uniform, as indicated by the presence of optical interference fringes, the spectra recorded inevitably came from an area on the film of varying thickness. This must be considered when drawing any conclusions from the following data.

Transmission-reflectance spectra recorded for the amorphous films deposited from the low temperature experiments (r2 and r4) are illustrated in Figures 2.20 and 2.21.

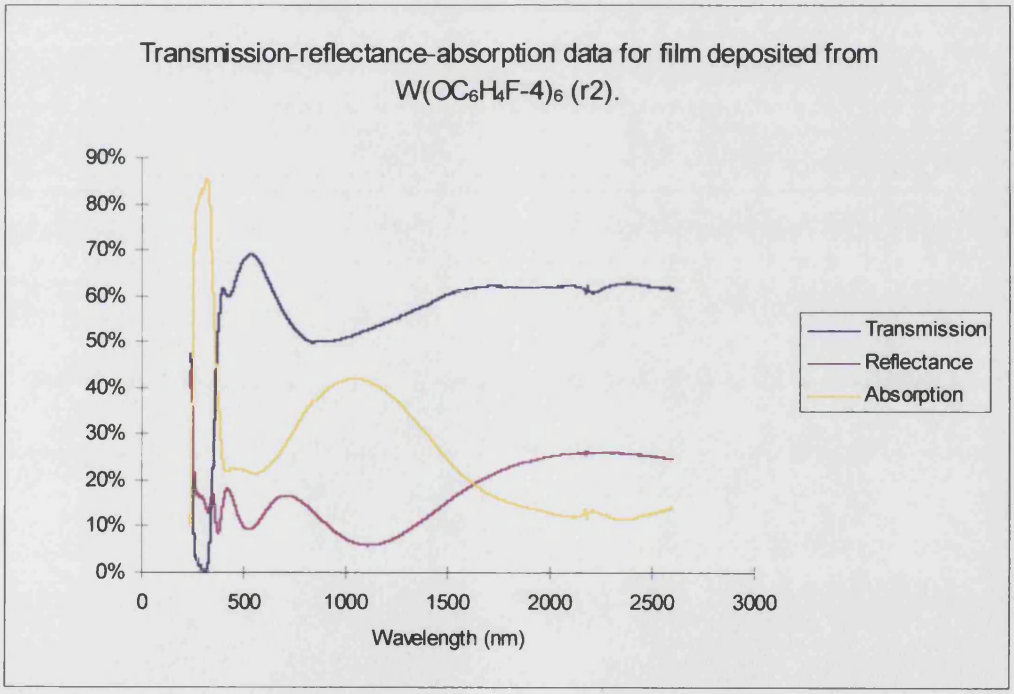

Figure 2.20 Transmission-reflectance-absorption spectra recorded for r2.

The absorption curve plotted in Figure 2.20, and in all the subsequent spectral data presented, was calculated from equation 2.6.

$$\text{Absorption} = 100\% - (\text{Transmission} + \text{Reflectance}) \qquad [2.6]$$

The visible region of the solar spectrum is from approximately 350 to 780nm, therefore, good transmission from the film is required in this region. The infrared portion of the solar spectrum is from approximately 780 to 2000nm. Therefore, for the film to have the potential application of a solar control coating it should block the infrared region of the solar spectrum while allowing transmission of the visible region. The spectra recorded for r2 (Figure 2.20) does show some selectivity in the infrared region of the solar spectrum. The transmission of radiation is less than 50% at around 825nm and almost 70% at around 550nm, this illustrates that the coating is selectively blocking the infrared radiation in this region of the spectrum. The calculated absorption curve shows that the film has a region of high absorbance from about 600 to 1500nm. This area of high absorption is in the right region to block the infrared portion of the solar spectrum. However, in does extend into the visible region of the spectrum hence the blue colour of the film.

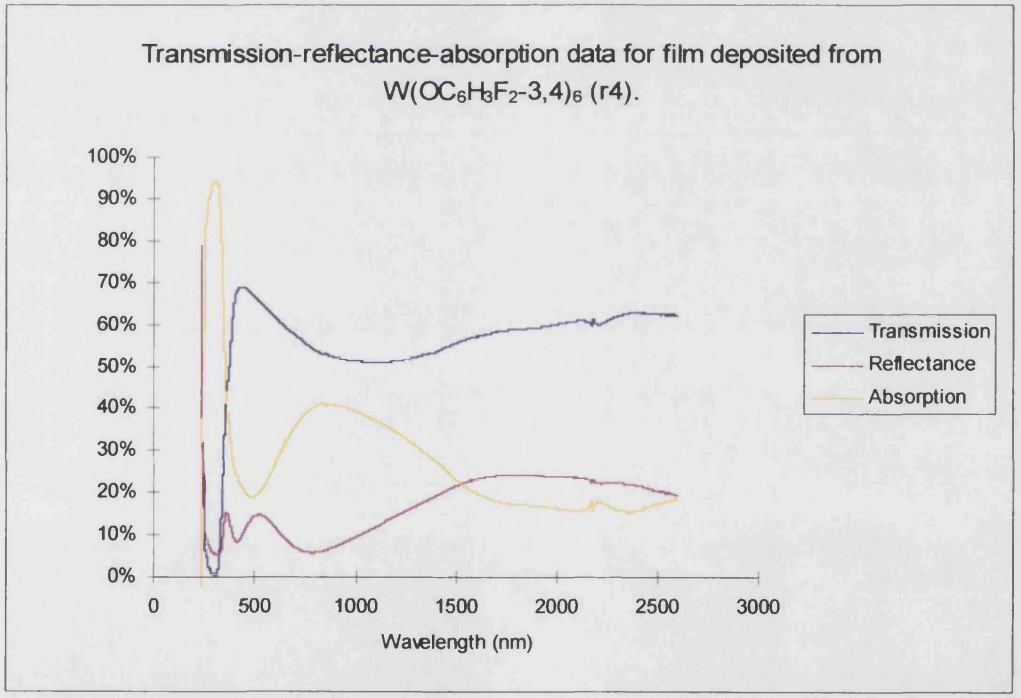

Figure 2.21 Transmission-reflectance-absorption spectra recorded for r4.

The spectra recorded for r4 (Figure 2.21) has broadly the same characteristics as for the previous example of WO_3 deposited at low temperature. The transmission of radiation in the visible region of the spectrum is reasonably high, approximately 70% at

500nm. The transmission through the film then reduces reaching its lowest point at about 1100nm with a transmission near 50%. As before the calculated absorption curve shows than the majority of the non-transmitted radiation in the near infrared region is being absorbed. There is a gradual rise in reflectance from the film as the wavelength increases, peaking at about 25% at around 1500nm.

The transmission-reflectance spectra for the three high temperature runs (r1, r3 and r5) which deposited crystalline tungsten oxide films were also recorded. These spectra are displayed in Figures 2.22, 2.23 and 2.24.

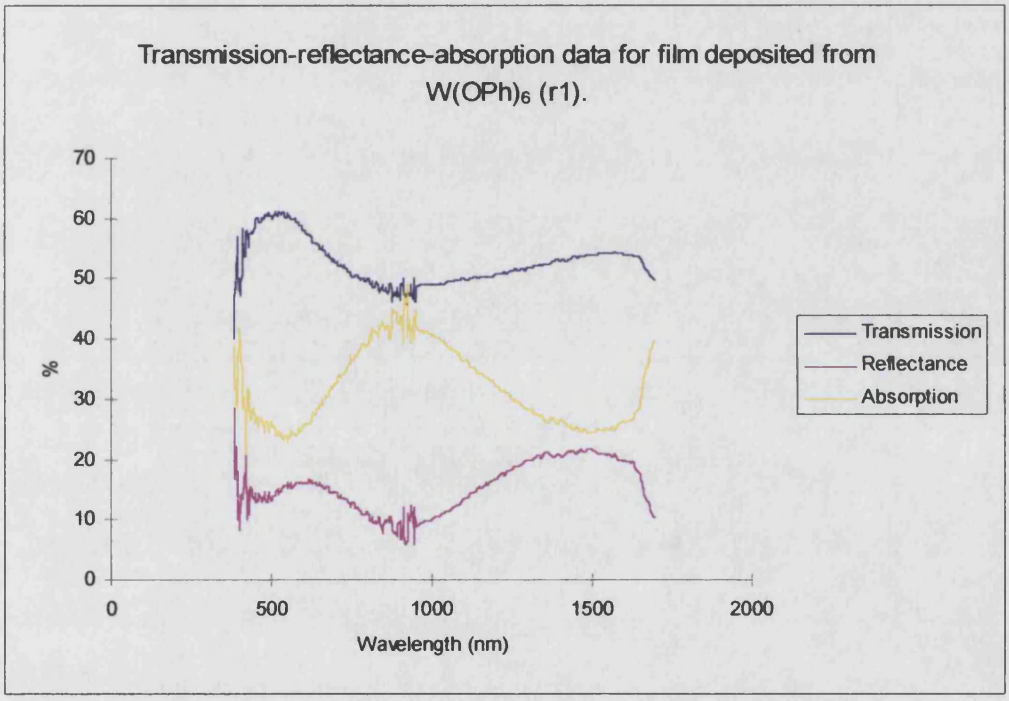

Figure 2.22 Transmission-reflectance-absorption spectra recorded for r1.

The transmission curve recorded for r1 is similar to those recorded for the amorphous films. The transmission in the visible region of the spectrum (520nm) is approximately 60%. In the infrared region of the solar spectrum the transmission falls away, however, there is no corresponding increase in reflectance from the film for the same wavelengths. The calculated absorption curve illustrated there is a region of high absorption from about 600 to 1500nm which extends slightly into the visible region of the spectrum, this is consistent with the blue colour of the film. However, this region of

high absorption is in the right area to block the infrared portion of the solar spectrum demonstrating this film does have some selectively to the solar spectrum.

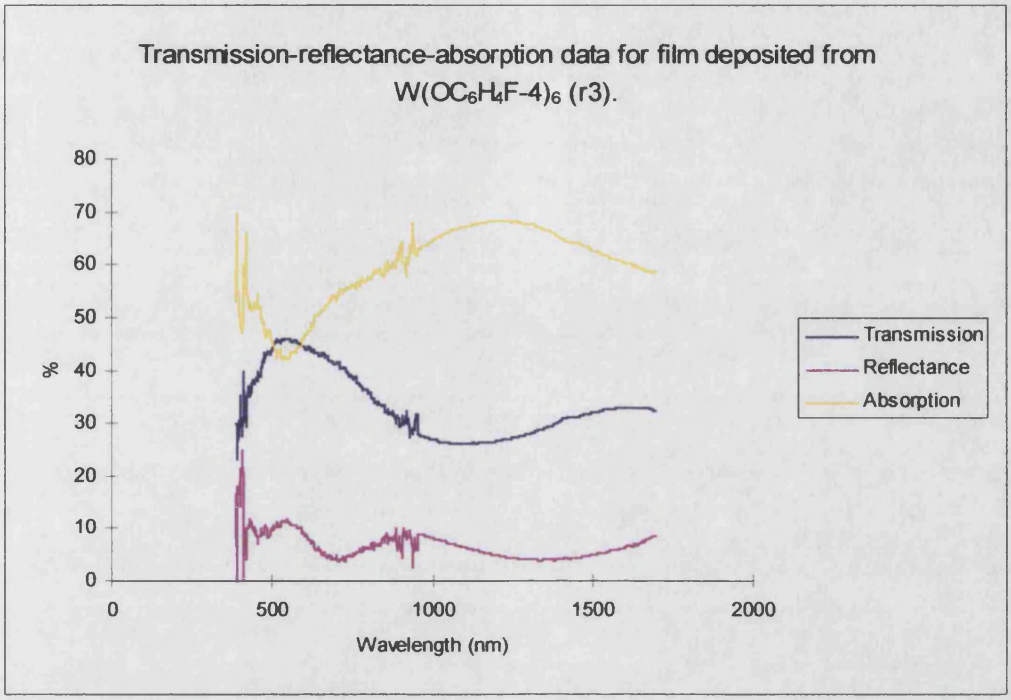

Figure 2.23 Transmission-reflectance-absorption spectra recorded for r3.

The transmission curve for r3 has a similar appearance to the previous spectra recorded, however, the maximum transmission of visible radiation is only 45% at 540nm. This is the lowest visible transmission recorded for the five films analysed in this chapter and could be due to the thickness of the film although this is not supported by the thickness measurement obtained from the SEM image of the film which indicated that the thickness of the film (2300Å) is similar to r5 (2300Å) and not as thick as r1 (3500Å). There is some selectivity in the infrared region as the transmission drops to approximately 26% at 1100nm. The absorption curve for r3 shows the majority of the radiation is absorbed, however, there is still some selectivity in the absorption curve in the infrared region. The curve increases from around 40%, in the visible region, to over 65% absorption at approximately 1200nm. This film is obviously highly absorbing but still displays some selectivity to the infrared region of the solar spectrum.

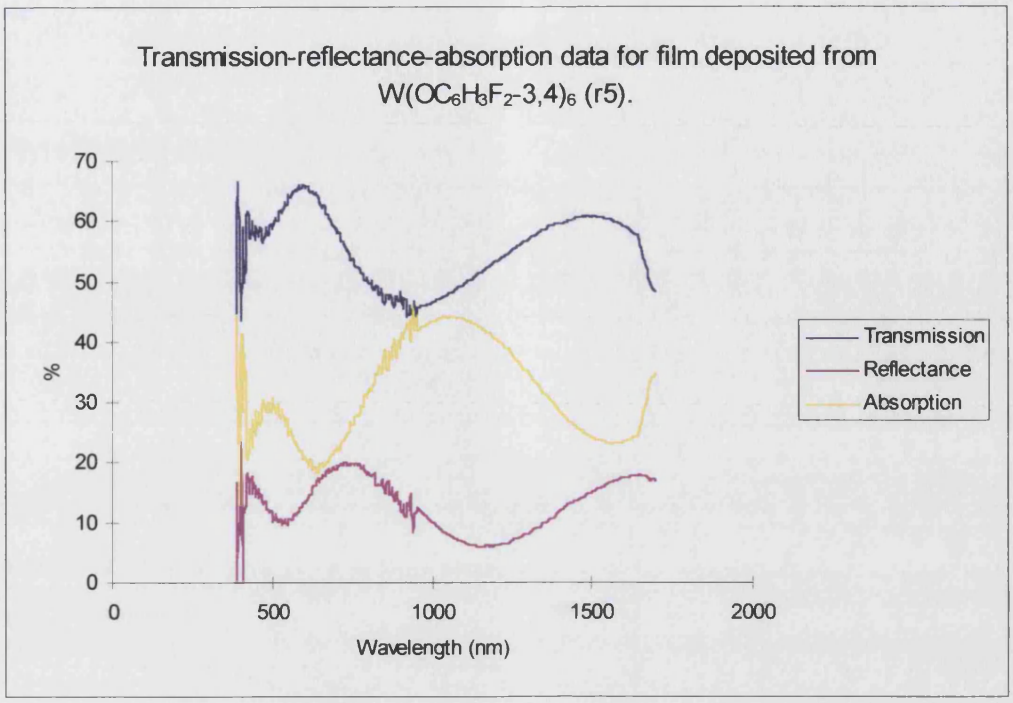

Figure 2.24 Transmission-reflectance-absorption spectra recorded for r5.

The transmission curve for r5 shows good transmission in the visible region of the spectrum, approximately 65% at 600nm. The transmission of radiation through the coated glass falls away in the infrared region of the solar spectrum (45% at 950nm). It can be seen from the calculated absorption curve that the radiation in this region is being absorbed rather that reflected by the crystalline tungsten oxide coating. There is also a slight increase in the reflectance between about 550 to 800nm which has not been seen in the previous two crystalline films analysed. The transmission-reflectance-absorption properties displayed by this film are perhaps the most encouraging from the solar control coating point of view as there is good visible transmission and high absorption in the near infrared region. It is also worth point out that glancing angle X-Ray diffraction of this film provided clear evidence for the presence of the non-stoichiometric $WO_{2.9}$ phase, as also indicated by the blue colour of the film. Additionally the SEM images of this film seemed to show a smoother surface with evidence of island growth and perhaps a less crystalline structure to the film.

In summary, all the film deposited in this chapter have shown some selectivity to the solar spectrum in the infrared region. They have maintained reasonable transmission

of visible radiation while blocking the infrared energy. The calculated absorption curves suggest most of this infrared energy is absorbed by the film and then subsequently re-radiated rather than reflected.

2.7 EXPERIMENTAL

All manipulations of tungsten oxychloride were carried out under a nitrogen or argon atmosphere using standard Schlenk techniques or in a dry-box fitted with a recirculation system. Once the reactions were complete no special handling of the synthesised compounds are required.

2.7.1 Synthesis of $W(OC_6H_5)_6$ (1)

Phenol (38.0g, 0.410mol) was added to tungsten oxychloride (13.8g, 41.0mmol) in the absence of any solvent. The reaction mixture was then refluxed for six hours with occasional stirring. The excess phenol was then sublimed from the reaction mix to yield a dark red solid. Extraction with approximately 500ml of ether gave a dark red solution which was washed with ~5% NaOH solution (3 × 100ml). The ether was then removed *in vacuo* to give a red solid. Which was recrystallised from methanol to yield dark red needle crystals of tungsten hexa(phenoxide) that were suitable for single crystal X-ray diffraction. Yield 7.99g (26%). Melting point 95°C.

Analysis : Found (calculated for $C_{36}H_{30}O_6W$) : C, 57.9 (58.2); H, 4.06 (4.05)%.

^{183}W nmr [δ(ppm), d^8 Toluene soln.] : -474.8, s.

^{1}H nmr [δ(ppm), $CDCl_3$ soln.] : 6.86 [18H, m, 18C*H*]; 7.21 [12H, m, 12C*H*].

^{13}C nmr [δ(ppm), $CDCl_3$ soln.] : 120.4 [*C*H]; 123.4 [*C*H]; 128.8 [*C*H]; 161.8 [*C*O].

IR data (NaCl plates, nujol mull, cm^{-1}) : 1583, 1228, 1161, 1068, 877, 860, 752, 686, 646.

2.7.2 Synthesis of $W(OC_6H_4F\text{-}4)_6$ (2)

Tungsten hexa(parafluorophenoxide) was prepared by a similar method to that used for compound **1**. Tungsten oxychloride (2.12g, 5.85mmol) and parafluorophenol (6.58g, 58.5mmol) were used in the absence of any solvent to give red crystals of the expected product. Yield 1.41g (28%). Melting point 101°C.

Analysis : Found (calculated for $C_{36}H_{24}F_6O_6W$) : C, 50.8 (50.8); H, 2.84 (2.84)%.

^{183}W nmr [δ(ppm), d^8 Toluene soln.] : -416.3, s.

^1H nmr [δ(ppm), $CDCl_3$ soln.] : 6.79 [12H, m, 12C*H*]; 6.91 [12H, m, 12C*H*].

^{13}C nmr [δ(ppm), $CDCl_3$ soln.] : 115.5 [d, *C*H], $^2J_{CF}$ = 24Hz; 121.2 [d, *C*H], $^3J_{CF}$ = 8Hz; 157.6 [d, *C*O], $^4J_{CF}$ = 2Hz; 159.1 [d, *C*F], $^1J_{CF}$ = 243Hz.

^{19}F nmr [δ(ppm), $CDCl_3$ soln.] : -118.8 [m, C*F*].

IR data (NaCl plates, nujol mull, cm^{-1}) : 1493, 1246, 1196, 1145, 1087, 879, 831, 796.

2.7.3 Synthesis of $W(OC_6H_3F_2\text{-}3,4)_6$ (3)

Crystals of tungsten hexa(3,4-difluorophenoxide) were synthesized by the same methodology as for compound **1** using 3,4-difluorophenol (8.21g, 60.9mmol) and tungsten oxychloride (2.08g, 6.09mmol) in the absence of any solvent. Yield 1.23g (22%). Melting point 105-107°C.

Analysis : Found (calculated for $C_{36}H_{18}F_{12}O_6W$) : C, 45.4 (45.1); H, 2.00 (1.89)%.

^{183}W nmr [δ(ppm), d^8 Toluene soln., 80°C] : -446.3, s.

^{1}H nmr [δ(ppm), $CDCl_3$ soln.] : 6.58 [6H, m, 6C*H*]; 6.71 [6H, m, 6C*H*]; 7.06 [6H, m, 6C*H*].

^{13}C nmr [δ(ppm), $CDCl_3$ soln.] : 109.5 [d, *C*H], $^{2}J_{CF}$ = 19Hz; 115.9 [dd, *C*H], $^{3}J_{CF}$ = 6Hz, $^{4}J_{CF}$ = 3Hz; 117.1 [d, *C*H], $^{2}J_{CF}$ = 19Hz; 147.6 [dd, *C*F], $^{1}J_{CF}$ = 247 Hz, $^{2}J_{CF}$ = 14Hz; 149.8 [dd, *C*F], $^{1}J_{CF}$ = 251Hz, $^{2}J_{CF}$ = 14Hz; 156.6 [d, *C*O], $^{3}J_{CF}$ = 9Hz.

^{19}F nmr [δ(ppm), $CDCl_3$ soln.] : -141.6 [m, C*F*]; -134.3 [m, C*F*].

IR data (NaCl plates, nujol mull, cm^{-1}) : 1506, 1309, 1248, 1199, 1151, 1103, 966, 810, 721, 667.

Chapter Three

Fluorinated Oxotetraalkoxide

3.1 INTRODUCTION

Metal alkoxides are an important class of compound whose applications depend on their reactivity, volatility and solubility in organic solvents. Metal alkoxides are very attractive precursors for the MOCVD of metal oxides as their volatility is usually high and an MO_x core is established in the precursor.[122,123,106] A series of tungsten(VI) hexaalkoxides [$W(OR)_6$ R = Me, Et, *n*-Pr, *i*-Pr and allyl] and tungsten(VI) oxotetraalkoxides [$W(O)(OR)_4$ R = Me, Et, Pr^i, Bu^t and *cyclo*-C_6H_{11}] have been synthesised by a variety of methods.[69,92]

The synthetic routes currently available for tungsten(VI) hexaalkoxides are relatively complicated and low yielding. Additionally, tungsten(V) and tungsten(VI) ethoxides are commercially available and have been used as precursors for the APCVD of tungsten oxide. The precursors are volatile enough to allow deposition using a stainless steel bubbler, however, a concentric tube arrangement was used to ensure the precursors did not react with oxygen until within the reactor. The films deposited were all grown at temperatures under 350°C and were all amorphous. The films grown during these experiments remain the only atmospheric pressure, single step tungsten oxide films deposited by CVD reported in the literature.[36] The CVD of tungsten(VI) oxotetraalkoxides are now reported for comparison.

The volatility of a given compound is an important consideration when considering it for use as a precursor for MOCVD. Previous studies have shown that the steric bulk of the ligand present can greatly affect the volatility of the precursor.[122,124] This can arise from increased shielding of the positively charged metal centre by bulky R groups which reduces intermolecular interactions and hence increases the volatility of the precursor. It was discovered that metal alkoxides containing less bulky ligands (e.g. Me, Et) could be oligomers with the alkoxide ligand being either terminal or bridging (Figure 3.1).

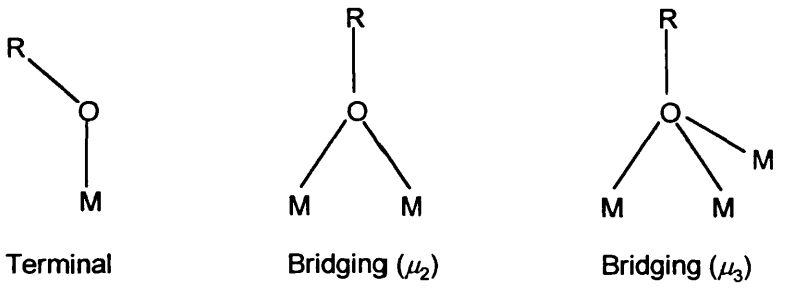

Figure 3.1 Bonding possibilities for metal alkoxides.

The tungsten(VI) oxotetraalkoxides $W(O)(OR)_4$ (R = Me, Et, Pr^i and *cyclo*-C_6H_{11}) have all been found to be dimers with alkoxide bridges in the solid state. The driving force for the dimerisation seen is for the metal centre to increase its co-ordination number from five to six so greater stability from an octahedral complex can be achieved (Figure 3.2).

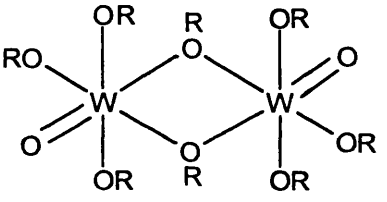

Figure 3.2 alkoxo bridged dimer.

However, $W(O)(OBu^t)_4$ has been characterised by ^1H NMR as a monomeric species although it was not found to be volatile enough for APCVD.[69]

There are two possible approaches to increasing the volatility of tungsten(VI) oxotetraalkoxides.

(1) *The use of fluorinated alcohol ligands.*

(2) *The use of bidentate ligands to break up the dimers and still give compounds containing six co-ordinate tungsten.*

The bidentate ligand approach has been used during the course of this work (as detailed in Chapter Four) and also by others to synthesise compounds of the type $W(O)(OR)_3L$ (R = Pr^i; L = acac and hfac) which have subsequently been used for LPCVD of amorphous tungsten oxide thin films.[42]

The work highlighted during this Chapter has used a fluorinated alcohol in an attempt to increase the volatility of the oxotetraalkoxides. The volatility of metal β-diketonates has been seen to increase by the addition of fluorine to the ligands, for example, the volatility decreases in the order $Zr(hfac)_4 > Zr(tfac)_4 > Zr(acac)_4$.[125] From a structural point of view, fluoro-alkoxides present contrasting properties. The electronegative nature of the OR_f makes the metal more Lewis acidic than corresponding OR compounds, thereby promoting dimerisation. On the other hand, the same electron withdrawing property renders the lone pair on the oxygen less basic which favours the formation of monomers. It is impossible to predict which factor will dominate, however, a series of organotin fluoroalkoxides, R_3SnOR_f, have all been found to be monomers incorporating four co-ordinate tin, in contrast to R_3SnOR' compounds which have all been characterised as dimers except in the case where R is very bulky.[34] This would suggest that R_f has a greater effect on reducing the basicity of oxygen, it's nearest neighbour, rather than increasing the Lewis acidity of the more remote metal.

This Chapter describes the synthesis, characterisation and subsequent APCVD of a fluorinated tungsten(VI) oxotetraalkoxide compound synthesised using 2,2,2-trifluoroethanol as the fluorinated ligand. 2,2,2-trifluoroethanol was chosen as the ligand as it is widely available and relatively cheap.

3.2 SYNTHETIC ROUTES

Tungsten(VI) oxotetraalkoxides of the type $W(O)(OR)_4$ (R = Me, Et, Pr^i, *cyclo*-C_6H_{11}) have been prepared by an alcoholysis reaction using $W(O)Cl_4$, the appropriate alcohol and a base (NH_3) to remove the liberated HCl.[92]

$$W(O)Cl_4 + 4ROH + 4NH_3 \xrightarrow{THF} W(O)(OR)_4 + 4NH_4Cl \qquad [3.1]$$

Once the precipitated NH_4Cl has been filtered off and the solvent removed under reduced pressure, the remaining solid was extracted into hot toluene, filtered, and the solvent removed to yield the desired product.

$W(O)(OBu^t)_4$ has been prepared by the metathesis reaction between $W(O)Cl_4$ and $NaOBu^t$ in tetrahydrofuran[126] and has also been prepared using a similar reaction involving $W(O)Cl_4$ and $LiOBu^t$ in diethyl ether.[92] A series of fluorinated tungsten(VI) alkoxide compounds have been prepared of the type $W(Cl)_{(6-x)}(OCH_2CF_3)_x$ (x = 1-5). Surprisingly, these compounds have been synthesised by the direct reaction of trifluoroethanol with WCl_6 in the absence of base.[127]

$$WCl_6 + xCF_3CH_2OH \longrightarrow W(Cl)_{6-x}(OCH_2CF_3)_x + xHCl \qquad [3.2]$$

The success of this latter synthetic route has been explained by two possible arguments. First, the trifluoroethanol ligand is less susceptible to chlorination than the equivalent ethanol ligand. Second, trifluoroethanol has a higher acidity than ethanol [pK_a (CH_3CH_2OH) = 15.9; pK_a (CF_3CH_2OH) = 11.4].[127] The fully substituted fluorinated tungsten(VI) alkoxide could not be synthesised by the direct method and was prepared by the reaction of $WCl_2(OCH_2CF_3)_4$ with $NaOCH_2CF_3$. All the compounds were found to be moisture sensitive, low-melting yellow solids or oils, and were generally purified by vacuum distillation.

3.3 STRUCTURAL AND SOLUTION CHEMISTRY

The tungsten(VI) hexaalkoxides of the type $W(OR)_6$ (R = Me, Et, Pr^i, *cyclo*-C_6H_{11}, OCH_2CF_3) are all liquids or low-melting solids so no structural studies have been carried out. However, the tungsten(VI) oxotetraalkoxides are solids and the crystal structures of several have been determined. The structures of $[W(O)(OMe)_4]_2$ and $[W(O)(OC_6H_{11})_4]_2$ are illustrated in Figures 3.3 and 3.4 respectively.

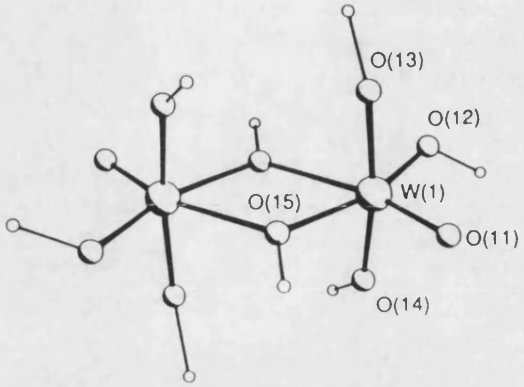

Figure 3.3 Crystal structure of $[W(O)(OMe)_4]_2$.[92]

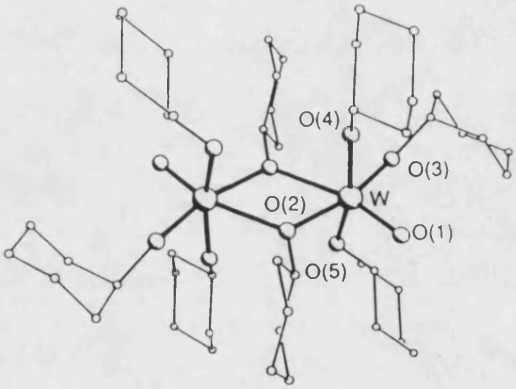

Figure 3.4 Crystal structure of $[W(O)(OC_6H_{11})_4]_2$.[92]

As can been seen from the crystal structures both the compounds incorporate alkoxide bridges forming dimers in the solid state. This increases the co-ordination number at the tungsten atom from five to six. Both the dimers display bioctahedral geometries with terminal W=O bond lengths of 1.702Å and 1.691Å for $[W(O)(OMe)_4]_2$ and $[W(O)(OC_6H_{11})_4]_2$, respectively. However, once in solution, variable temperature ^{1}H NMR experiments have shown that the compounds are fluxional on the NMR time scale indicating that the dimer structure is not static in solution. For $[W(O)(OMe)_4]_2$ no ^{1}H NMR signal corresponding to the monomer were observed indicating that the terminal and bridging OMe groups present undergo facile intramolecular alkoxide

^{1}H NMR signals corresponding to the monomer were observed indicating that the terminal and bridging OMe groups present undergo facile intramolecular alkoxide exchange by W-O bond rotation rather than complete dissociation. However, for $[W(O)(OC_6H_{11})_4]_2$, the alkoxide ligands are too bulky to allow the exchange of terminal/bridging alkoxide ligands by W-O bond rotation. Therefore, five co-ordinate monomers are intermediates in the exchange of terminal/bridging alkoxide ligands rather than the sterically unfavoured bond rotation.[92]

The crystal structure for $WCl_4[OC(CH_3)(CF_3)_2]_2$ has also been determined and is shown in Figure 3.5.

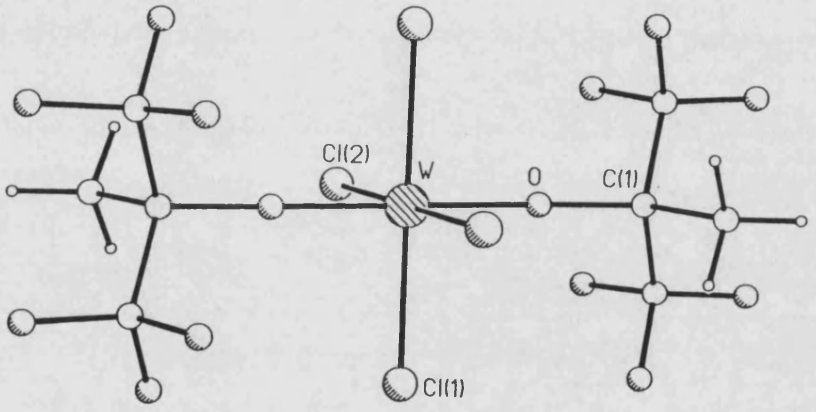

Figure 3.5 Crystal structure of $WCl_4[OC(CH_3)(CF_3)_2]_2$.[127]

The tungsten atom sits in an octahedral position with the six ligand atoms arranged at 90° with respect to each other. The tungsten-oxygen bond lengths in this molecule are 1.819(6) Å which are shorter than seen for the tungsten(VI) phenoxide compounds reported in Chapter 2 (cf. **(1)** 1.884(6); **(2)** 1.899(8); **(3)** 1.895(12) Å) and other known W-O single bond species.[128] The relatively short tungsten-oxygen bond lengths in this compound indicate a significant amount of π donation from the oxygen atoms to the tungsten.

3.4 RESULTS AND DISCUSSION

3.4.1 Synthesis

As previously noted, a series of tungsten(VI) oxotetraalkoxides have been synthesised by others and a selection of these used for LPCVD experiments. It was hoped the synthesis of an analogous fluorinated compound would enhance the volatility sufficiently to allow APCVD experiments to be carried out. Since a reliable and high yielding synthetic pathway was known for the synthesis of oxotetraalkoxides this methodology was used for the synthesis of the 2,2,2-trifluoroethanol **(4)** derivative during this work **[3.3]**.

$$W(O)Cl_4 + 4CF_3CH_2OH + 4NH_3 \xrightarrow{THF} \underset{\textbf{(4)}}{W(O)(OCH_2CF_3)_4} + 4NH_4Cl \qquad \textbf{[3.3]}$$

Once the reaction was complete the initial work-up gave an off white powder. Initially this was assumed to be a pure product, however, during melting point analysis it was seen to sublime up the melting point tube to give a pure white compound leaving and a dark brown/black residue at the base of the melting point tube. ^{1}H NMR, infrared and microanalysis were performed on the off white powder and these techniques indicated it was an impure compound. Therefore, the off white powder was sublimed to give a white compound which can be best described as cotton wool like in appearance **(4)**. Only relatively small quantities of **(4)** were recovered indicating that it may only be a minor product from the reaction or that the reaction its self was just low yielding (yield 16%). Compound **(4)** was sensitive in the atmosphere as was demonstrated by a colour change from white to pale blue on standing for several minutes in air. The dark brown/black material remaining after each sublimation was found to contain no peaks in the infrared spectrum between 4000-400cm^{-1} and could not be dissolved in any common organic solvents.

Based on reported synthesis described here previously, it is possible there could be several products from reaction **[3.3]** (Figure 3.6). There is the desired monomeric oxotetraalkoxide species (*a*), which should have greater volatility than a dimeric species; a dimer (*b*), containing alkoxide bridges as seen in the non-fluorinated compounds; and a six co-ordinate tungsten(VI) species (*c*).

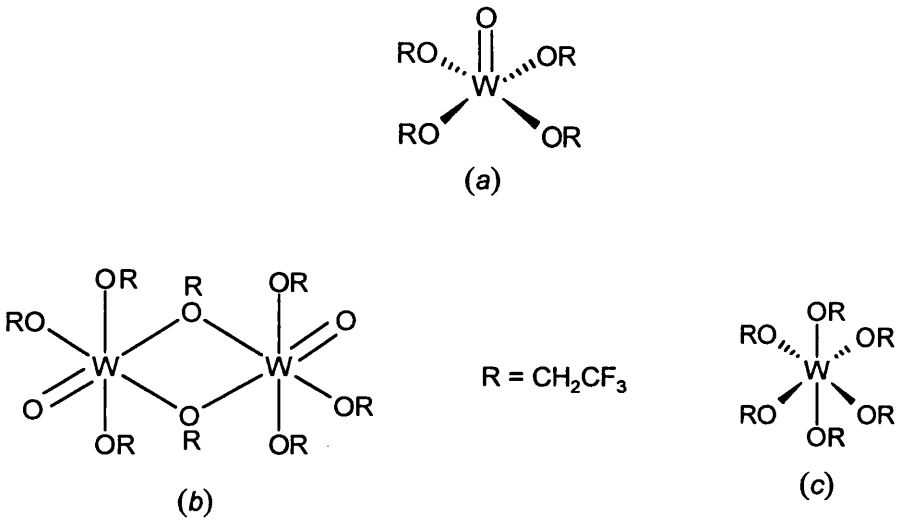

Figure 3.6 Possible alkoxide products from **[3.4]**.

The six co-ordinate species, as seen for the analogous reactions involving phenol, could be a possibility as 2,2,2-trifluoroethanol is a stronger acid than its ethanol analogue [pK_a (CH_3CH_2OH) = 15.9; pK_a (CF_3CH_2OH) = 11.4].[129] Phenol is a considerably stronger acid than 2,2,2-trifluoroethanol [pK_a (PhOH) = 9.95],[130] however, 2,2,2-trifluoroethanol has been shown strong enough to react with WCl_6 in the absence of base to yield a substituted tungsten(VI) species whereas ethanol does not. Therefore, in the presence of base a six co-ordinated product could be a possibility from this reaction.

3.4.2 NMR Spectroscopy

^{1}H, ^{13}C, ^{19}F and ^{183}W NMR experiments were performed on **(4)**.

3.4.2.1 ^{1}H, ^{13}C and ^{19}F NMR Spectroscopy

The ^{1}H NMR spectrum recorded for **(4)** showed a quartet centred at 4.85ppm which can be accounted for by the CH_2 group present on the ligand. The quartet has a $^{3}J_{HF}$ coupling constant of 8.9Hz which is consistent with literature data (cf. $^{3}J_{HF}$ 8Hz).[127] There is an accompanying unresolved multiplet at about 3.8ppm, however, this was approximately 20 times smaller than the quartet seen at 4.85ppm. The ^{1}H NMR spectra recorded of the free ligand (CF_3CH_2OH) showed the CH_2 quartet to be at approximately 3.9ppm. Therefore, the unresolved multiplet seen in the ^{1}H NMR spectrum of **(4)** could be a small amount of free ligand present in the NMR sample, possibly due to the compound decomposing.

The presence of a simple quartet in the ^{1}H NMR spectrum would seem to discount the possibility of **(4)** being a dimer as no bridging alkoxides groups were seen in the spectrum. The ^{1}H NMR spectrum does not appear to be fluxional, based on the sharp peaks present, although no variable temperature experiments have been carried out on **(4)**. However, the ^{1}H NMR spectrum does not discount the possibility of the six co-ordinated product as the spectrum for both monomeric $WO(OCH_2CF_3)_4$ and $W(OCH_2CF_3)_6$ would probably be very similar.

Despite weak signal strength, the ^{13}C NMR spectra recorded for **(4)** showed two quartets centred at 125.7 and 71.8ppm which are due to the CF_3 and CH_2 groups present on the ligand respectively. The carbon-fluorine coupling constants obtained from **(4)**, which are consistent with literature values, are displayed in Table 3.1.

Table 3.1 Chemical Shifts and Carbon Fluorine Coupling Constants for **(4)**.

	Chemical Shift (ppm)	Coupling Constant (Hz)	Assigned Group
$^1J_{CF}$	125.7	277	CF_3
$^2J_{CF}$	71.8	35	CH_2

As before, the ^{13}C NMR spectrum for both the six co-ordinate hexaalkoxide and the five co-ordinate oxotetraalkoxide derivatives would be expected to be very similar.

The ^{19}F NMR spectra recorded for **(4)** showed a triplet centred at -76.9ppm due to coupling with the protons present on the CH_2 group. The coupling constant was 8.7Hz which is consistent with that seen in the proton spectrum. As with the other NMR spectra recorded, this would be the expected spectrum for both the six co-ordinate alkoxide and the five co-ordinate oxotetraalkoxide, i.e. the presence of one type of fluorinated ligand.

3.4.2.2 ^{183}W NMR Spectroscopy

Despite the sample not being very concentrated it was possible to record a ^{183}W NMR spectrum, although the accumulation of the data required sixteen hours. The spectrum showed a single peak at -249.7ppm (referenced to 1 mol dm^{-3} Na_2WO_4/D_2O) with a linewidth of 6 Hz.

As previously noted, a series of tungsten(VI) oxotetraalkoxide compounds of the type $W(O)(OR)_4$ have been synthesised and the ^{183}W NMR data for those compounds are displayed in Table 2.2.

The methyl, ethyl and cyclo derivatives have been characterised by single crystal X-ray diffraction and/or ^1H NMR studies as six co-ordinate dimers with alkoxide bridges of the type $[W(O)(OR)_4]_2$. The *tert*-butyl and $C_6H_3Pr^i_2$-2,6 derivatives have been characterised as monomeric five co-ordinate compounds of the type $W(O)(OR)_4$. It has

therefore been suggested that the difference seen in the ^{183}W NMR chemical shift values may reflect the five *vs.* six co-ordinate metal environments. For compound **(4)** the ^{183}W NMR chemical shift recorded was -249.7ppm which could place it in either category. However, ^{1}H NMR spectra recorded for **(4)** have shown no evidence of alkoxide bridges so the ^{183}W NMR chemical shift value recorded is likely to be that for a five co-ordinate monomeric compound, $W(O)(OCH_2CF_3)_4$. Based on the six co-ordinate tungsten(VI) phenoxide compounds described in Chapter 2 (cf. $W(OPh)_6$ ^{183}W NMR chemical shift = -474.8ppm) a ^{183}W NMR chemical shift value of -249.7ppm would seem to indicate that **(4)** is not the six co-ordinate alkoxide.

3.4.3 Mass Spectrometry

The electron ionisation (EI) mass spectrum of **(4)** was recorded and the results are summarised in Table 3.2. EI mass spectrometry was used as it was hoped this would fragment the molecule in a similar fashion to the decomposition process which occurs during CVD. Any fragments containing tungsten atoms are easily identifiable as the tungsten atom has several isotopes giving a characteristic pattern in the mass spectra recorded.

No parent molecular ions of the type $[W(O)(OCH_2CF_3)_4]^+$ or $[W(OCH_2CF_3)_6]^+$ were seen in the mass spectrum and there was no evidence to suggest any dimerised species were present. The most intense tungsten containing fragment was centred at m/z 497 and corresponds to $[W(O)(OCH_2CF_3)_3]^+$ which would seem to indicate that **(4)** is the five co-ordinate monomeric oxotetraalkoxide derivative. The tungsten containing fragments then decrease in units of 80 m/z which are consistent with the loss of a molecule of empirical formula $C_2H_2F_2O$. The loss of 80 m/z units continues until the last recorded tungsten fragment at 257 m/z which corresponds to $[W(O)F_3]^+$.

Table 3.2 Summary of EI Mass Spectrometry Data Obtained for **(4)**.

m/z (^{184}W)	Ion	Abundance %
679	$W(OCH_2CF_3)_5^+$	<0.5
599	$WF(OCH_2CF_3)_4^+$	3
519	$WF_2(OCH_2CF_3)_3^+$	6
497	$W(O)(OCH_2CF_3)_3^+$	89
439	$WF_3(OCH_2CF_3)_2^+$	4
417	$W(O)F(OCH_2CF_3)_2^+$	53
359	$WF_4(OCH_2CF_3)^+$	13
337	$W(O)F_2(OCH_2CF_3)^+$	30
257	$W(O)F_3^+$	34

A similar decomposition has been seen to occur in $Zr(OR_f)_4$ species. The mass spectra recorded for $Zr[OCMe_2(CF_3)]_4$ showed loss of units of 108 m/z which correspondes to the empirical formula $C_4H_6F_2O$. This would seem to suggest the production of a ketone, in this example 3,3-difluorobutan-2-one, which would result from the transfer of a fluorine atom to the metal centre in addition to the breaking of the Zr-O bond and a 1,2-methyl migration.[131] This type of decomposition pathway can be applied to **(4)** (Figure 3.7).

Several signals seen in the mass spectra recorded were identified as corresponding to $[W(OCH_2CF_3)_5]^+$, $[WF(OCH_2CF_3)_4]^+$, $[WF_2(OCH_2CF_3)_3]^+$, $[WF_3(OCH_2CF_3)_2]^+$ and $[WF_4(OCH_2CF_3)]^+$ which would most naturally arise from the fragmentation of a six co-ordinate hexaalkoxide. However, these peaks were typically one order of magnitude small when compared with other tungsten fragments seen in the spectrum suggesting that the six co-ordinate alkoxide compound is only present as an impurity in the sample analysed, or may indeed arise from the rearrangement of $W(O)(OR)_4$.

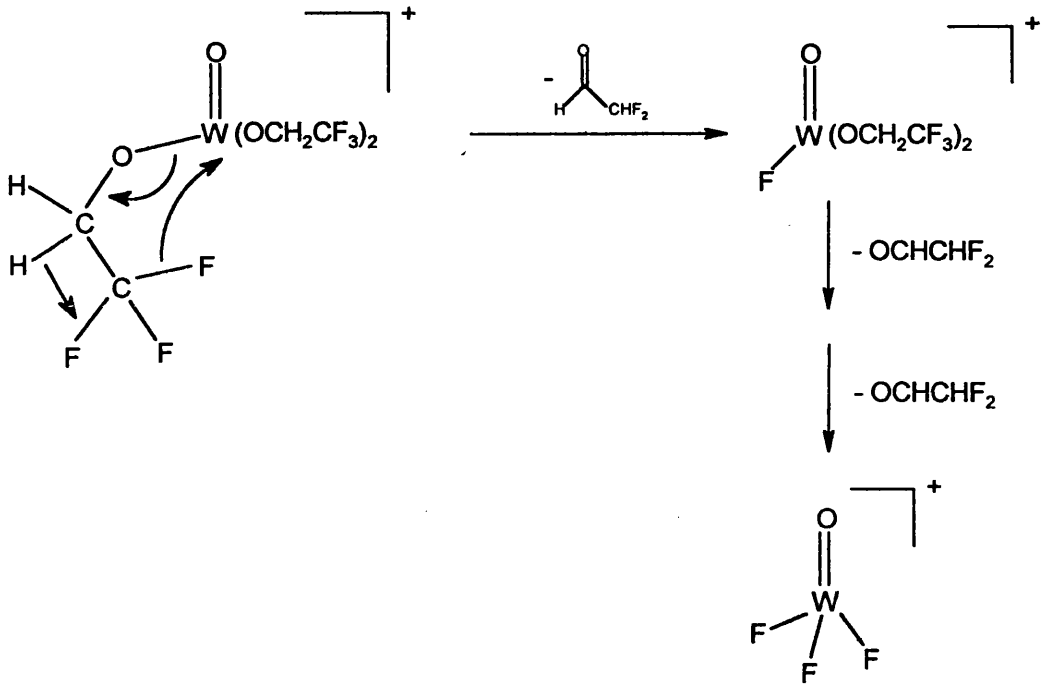

Figure 3.7 Possible decomposition pathway for $WO(OCH_2CF_3)_4$.

Considering all the data now accumulated on **(4)** the most likely product would seem to be the desired monomeric $W(O)(OCH_2CF_3)_4$ and not the dimer or the six co-ordinate alkoxide derivatives which have been postulated. Since the fluorinated-alkoxide ligand used was not bulky, the driving force for the formation of the monomer must be on electronic grounds rather than steric grounds. This would seem to suggest that, in this case at least, the electron withdrawing effect of the fluorine atoms on the oxygen, lowering its basicity, has out weighed the fluorine atoms effect on the metal centre. The monomer synthesised during this work has also displayed increased volatility when compared to the previously known non-fluorinated oxotetraalkoxides.

3.5 CVD TESTING OF PRECURSOR

The aim of this section of work was to synthesise a tungsten(VI) oxotetraalkoxide compound with greater volatility than those previously described in the literature. 2,2,2-trifluoroethanol was used as the ligand in the hope that the fluorine

atoms present would enhance the volatility of the dimeric species currently known. From the analysis conducted on **(4)** this would appear to have been successful up to the point where conventional APCVD experiments were possible using this compound. As briefly mentioned elsewhere in this Chapter, tungsten oxide thin films have been deposited in a single step at atmospheric pressure before. However, the only example to date has been using tungsten(V) and tungsten(VI) ethoxides as the precursors. The problem of pre-mixing oxygen was overcome by using a concentric pipe for the delivery of the reactive gases separately to the reactor. This ensured no pre-reaction could take place by preventing the tungsten precursor from reacting with the oxygen until within the reactor. The films were all deposited at low temperatures (<350°C) and were all amorphous. Since the films deposited were not crystalline they were analysed by Rutherford backscattering spectrometry, which showed that the O/W ratio was between 2.7-3.2, and by X-ray photoelectron spectroscopy, which determined that there was no carbon contamination in the film. Attempts to deposit films at higher temperatures lead to powdery blue deposits on the substrate which were assumed to be non-stoichiometric tungsten oxide.[36]

Since the synthesis of **(4)** was problematic and low yielding, the pre-sublimed off white powder was used in the bubbler during the CVD experiments. This presented no difficulties as the off white powder was relatively easy to handle and sublimation experiments had demonstrated that **(4)** was the only volatile species present. Therefore, the only species reaching the reactor would be **(4)**. CVD experiments were carried out both in the absence of, and in the presence of, an additional oxygen gas flow. As before the films were deposited on a 4mm glass substrate coated with a thin film of SiCO which acts as a blocking layer to prevent sodium diffusion into the film deposited. A schematic of the horizontal cold-wall reactor and bubbler set up can be found in Appendix 7.

Once deposited, the films were analysed by glancing angle X-ray diffraction to determined their composition and by SEM, to give an indication of the surface morphology of the film. The transmission, reflection spectra of the films were also recorded to determine if any selectivity to solar radiation was evident.

3.5.1 Deposition Conditions

APCVD experiments were conducted using **(4)** in the bubbler. The bubbler was loaded with the precursor in a dry-box fitted with a recirculation system and once removed from the dry-box the bubbler was immediately connected to the CVD apparatus and flushed with nitrogen gas. Once connected to the CVD apparatus the deposition run was completed the same day. When the run was completed the bubbler was removed and refilled with fresh precursor in preparation for the next experiment. Several runs under each set of conditions were completed, i.e. with and with out additional oxygen, and the deposition conditions are displayed in Table 3.3.

For r6 the carrier gas flow through the bubbler was not constant during the deposition experiment. For r7 and r8 the carrier gas flow initially dropped when the bubbler was opened but then recovered to the flow rate set. On several other deposition experiments the carrier gas line blocked completely causing the run to be aborted. The blockages were traced to the non-return valve located down-stream of the bubbler which seemed to partially block very easily. For the majority of the deposition runs the carrier gas flow only fluctuated during the first 30 seconds of the run, which could indicate the passage of precursor through the non-return valve and would suggest that films could be deposited in run times much shorter that the 15 to 20 minutes used.

Table 3.3 Summary of deposition conditions used during APCVD experiments.

Film ID	r6	r7	r8
Quantity of precursor used g.	4.44	1.53	2.17
Reactor temp. °C	600	600	600
Bubbler temp. °C	190	190	190
Run time min.	20	20	15
Carrier gas (N_2) flow rate l/min.	1-0.1	1.0	0.5
Diluent gas (N_2) flow rate l/min.	3.0	3.0	3.0
Oxygen gas flow rate l/min.	0	0.6	0.6

3.5.2 Film Analysis

Films r6, r7 and r8 covered the full length of the glass substrate and were well adhered with no powdery surface layer evident. However, r6 was very different in visual appearance from the films deposited when pre-mixing oxygen in the reactive gas flow (r7 and r8).

Film r6 was very thick and there was a grey surface layer to the film which could be carbon or just due to the thickness of the film. Approximately 18 months after deposition the film appears yellow in transmission although the grey surface layer remains. Despite the haziness and dark colour of the film, coloured interference fringes could be seen if the film was held up to the light.

Films r7 and r8 were virtually identical which was no surprise as the deposition conditions were very similar. There were no coloured interference fringes visible on either of the films and both appeared quite hazy. However, the films appeared quite reflective at certain angles and were both yellow in colour when removed from the reactor indicating stoichiometric WO_3.

3.5.2.1 Glancing Angle X-Ray Diffraction

Glancing angle X-ray diffraction patterns from r6 and r7 are illustrated here. The glancing angle X-ray diffraction studies enabled characterisation of the films with regard to the phase or phases of tungsten oxide present and showed if the films were crystalline or amorphous.

The glancing angle X-ray diffraction patterns were obtained using low angle X-ray diffraction (θ fixed at 1.5°). The X-ray diffraction patterns were acquired over the 2 theta range 0° to 75° with a total analysis time of 40 minutes.

The glancing angle X-ray diffraction analysis from the deposition experiment in which no oxygen was pre-mixed to the reactive gas stream, r6, (Figure 3.8) gave a diffraction pattern which indicated that a crystalline film had been deposited.

Peak match software suggested two possible phases of tungsten oxide present in the film deposited. ICDD pattern number 20-1324 and ICDD pattern number 18-1417 (Appendix 5) which correspond to stoichiometric WO_3 and non-stoichiometric $WO_{2.9}$ respectively. The main peak in the diffraction pattern recorded is clearly the peak at approximately 23° from the standard WO_3 pattern, and the enhanced intensity of this peak could indicate some preferred orientation in the 001 (hkl) plane. However, the presence of some non-stoichiometric $WO_{2.9}$ cannot be ruled out as the peak seen in the pattern at ca. 24°, to the right of the main peak, could correspond to the peak seen in the $WO_{2.9}$ standard sample. The presence of some non-stoichiometric $WO_{2.9}$ in this film would not be unexpected as the film was deposited with no additional oxygen added to the reactive gas flow so could easily be oxygen deficient.

The glancing angle X-ray diffraction pattern recorded for the film deposited with oxygen pre-mixed in the reactive gas stream, r7, is illustrated in Figure 3.9. As with the previous example the fact that a diffraction pattern could be collected indicated that the film was crystalline.

Peak match software suggested only one possible phase of tungsten oxide present in this film, stoichiometric WO_3 corresponding to ICDD pattern number 20-1324 (Appendix 5). As is evident, this diffraction pattern is vastly different from that recorded for the previous film, peaks are clearly visible for the majority of those seen in the standard sample of stoichiometric WO_3. The three peaks seen at ca. 24° in the randomly orientated WO_3 standard are clearly seen in the diffraction pattern collected for r7 which is in contrast to the pattern collected for r6 which showed one central peak and a broad undefined peak. Additionally, the peak at ca. 27° is relatively intense when compared with other peaks, this could indicate a degree of preferred orientation in the 120 (hkl) plane within this film. The film was initially yellow in colour, characteristic of stoichiometric WO_3, when removed from the reactor. Therefore, an XRD pattern

indicating only stoichiometric WO_3 present in the film would seem to be reasonable. One other point of interest is the hump seen in the diffraction pattern between about 15 and 32°. This hump indicates either an amorphous component is present in the film or represents sampling of the glass substrate on which the film is deposited. Since visual analysis of the film indicated it was quite thin the hump is almost certainly sampling of the glass substrate. The thickness of the film was subsequently confirmed by SEM analysis, section 3.5.2.2.

Figure 3.8 Glancing angle X-ray diffraction spectra recorded for r6.

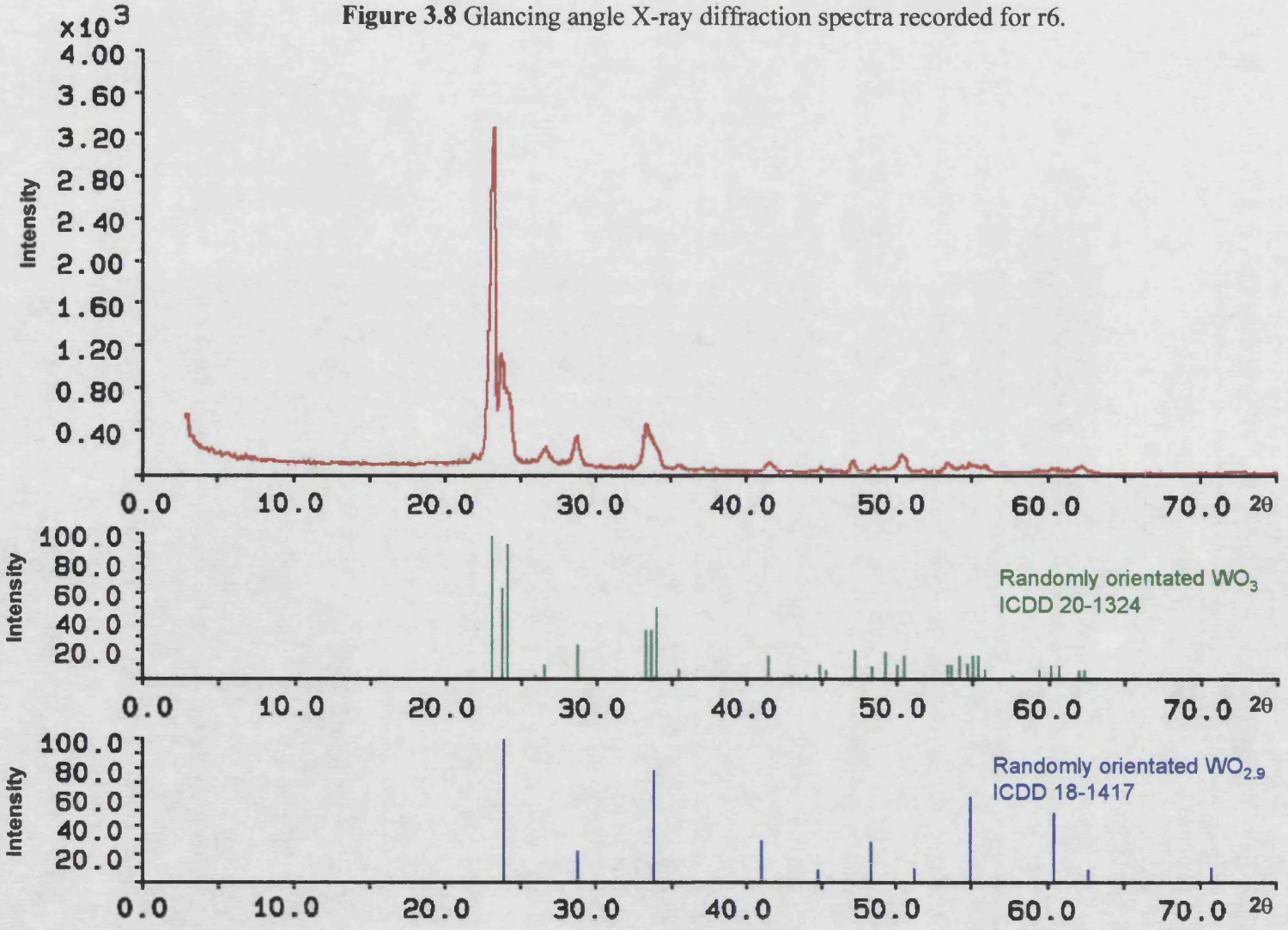

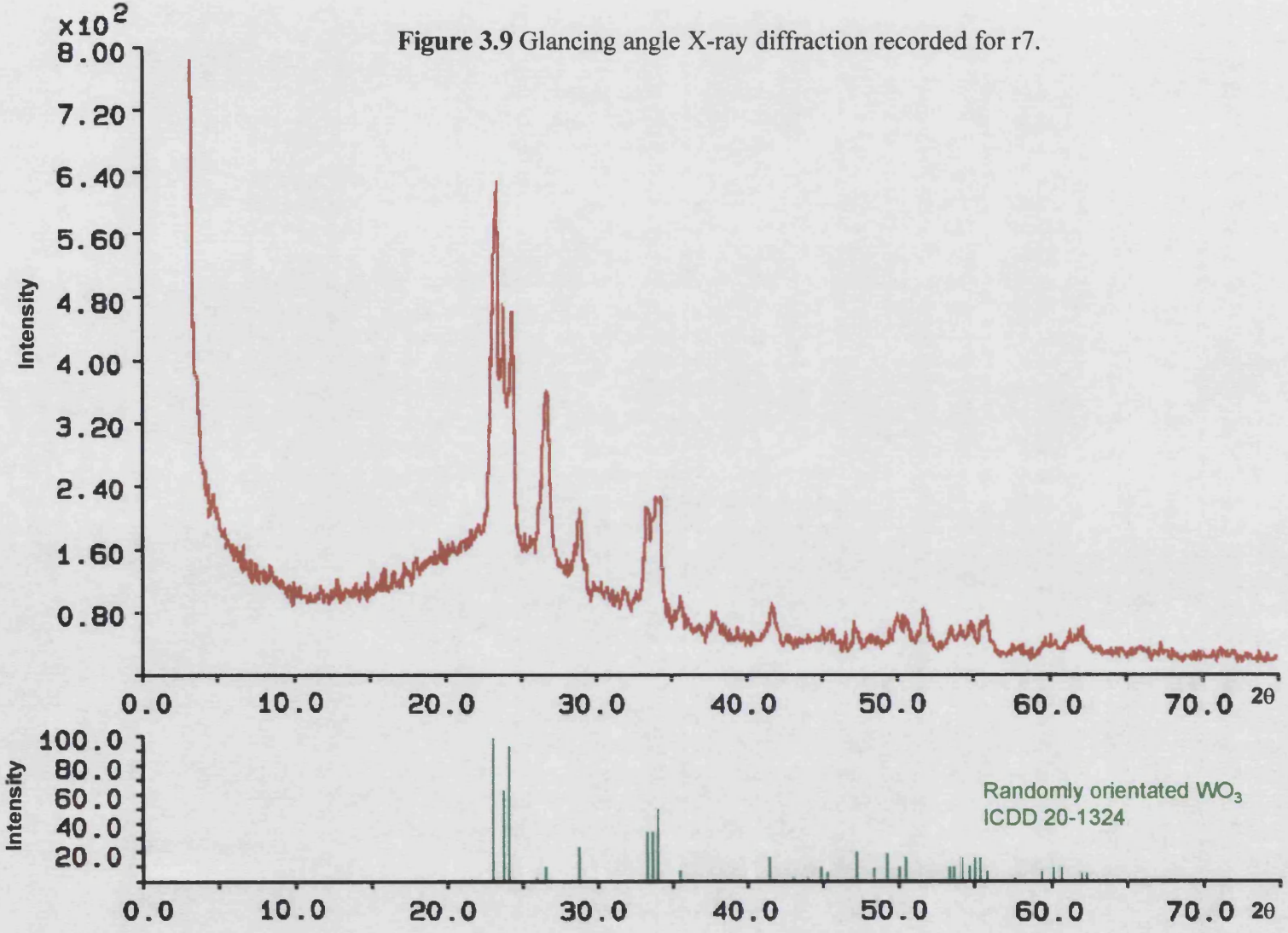

Figure 3.9 Glancing angle X-ray diffraction recorded for r7.

3.5.2.2 SEM

Scanning Electron Microscopy (SEM) was performed in collaboration with Pilkington Glass Ltd. on the two films which have previously been subject to glancing angle X-ray diffraction. The results of these experiments are displayed in Figures 3.10-3.13.

Figures 3.10 and 3.11 display the film deposited in the absence of additional oxygen (r6). Figure 3.10 shows the film at 80° tilt and Figure 3.11 shows the film at 90° tilt. In both pictures the glass substrate, the undercoat and the deposited film are easily seen. As can be seen, the surface roughness of the film appears high and the film seems to have been deposited in an almost random fashion with crystallites appearing to have grown in all directions. One could postulate from the appearance of the film that it has been grown via an island growth method. The surface roughness, and random nature of the crystallites, could well account for the generally poor transmission of the film (following section) as thickness of the film, obtained from the SEM analysis, was only 3030 Å which is not all that thick.

Figures 3.12 and 3.13 display the film deposited with additional oxygen added to the reactive gas flow (r7). Figure 3.12 shows the film from 80° tilt and Figure 3.13 shows the film from 90° tilt. The surface roughness of the film again looks quite high, however, the film appears to have grown in a more uniform fashion than r6. Again from the appearance of the film it could have been deposited via island growth. Figure 3.13 clearly shows how thin this film is which confirms the observations in the glancing angle x-ray diffraction that the amorphous hump was sampling of the glass substrate. Figure 3.13 also shows individual crystallites on the substrate surface which appears to support the hypothesis that the film has been deposited via island growth.

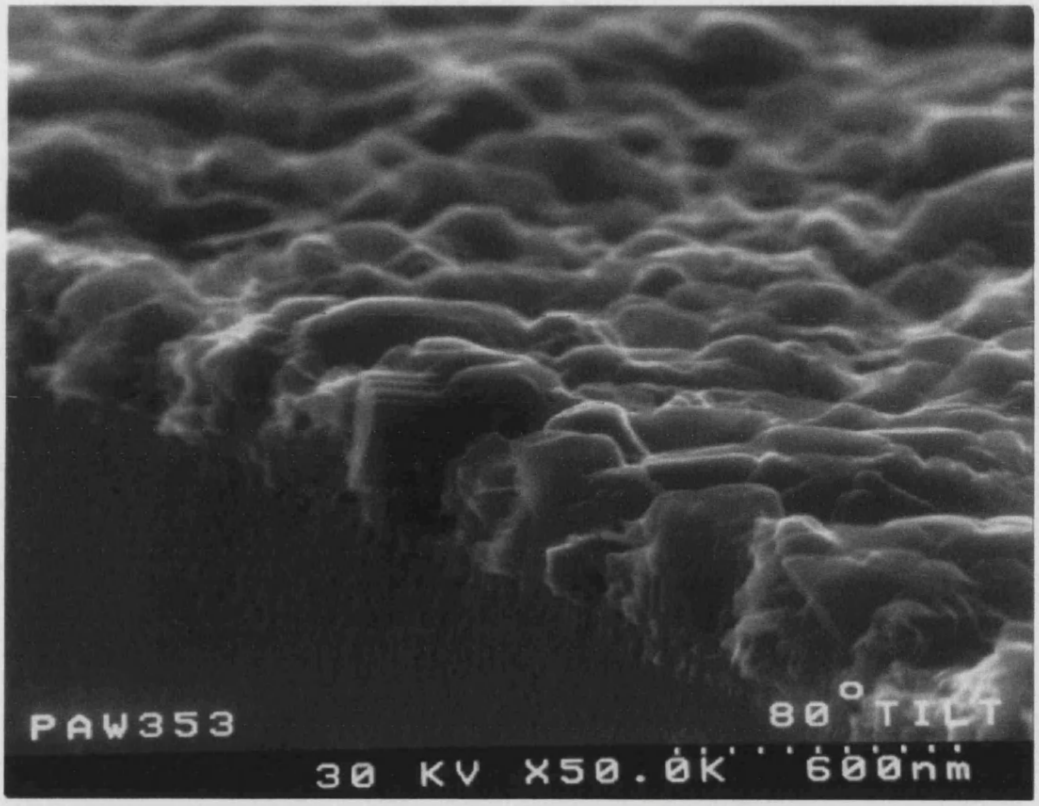

Figure 3.10 80° tilt SEM image for r6.

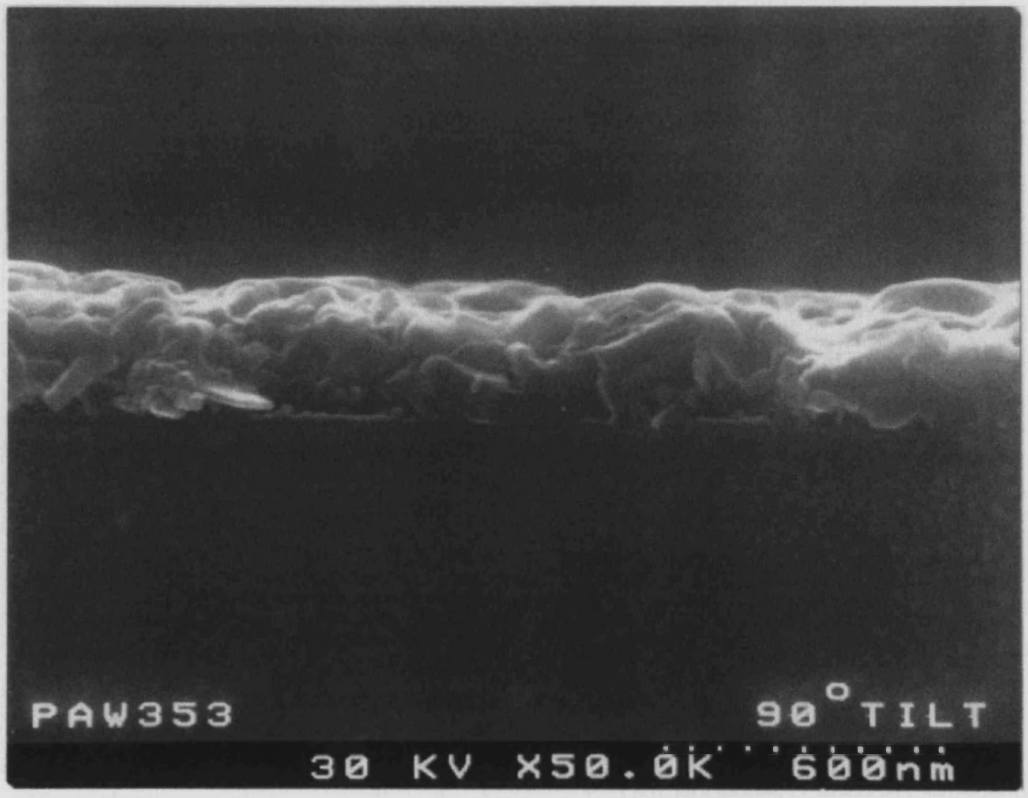

Figure 3.11 90°tilt SEM image for r6.

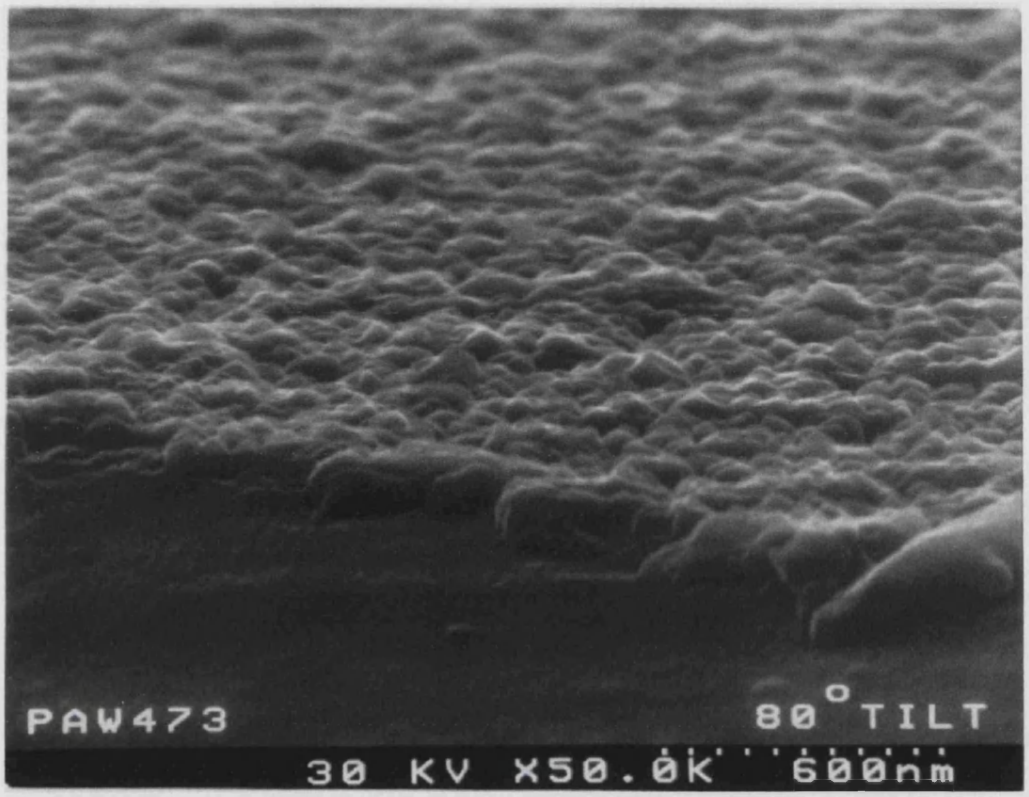

Figure 3.12 80° tilt SEM image for r7.

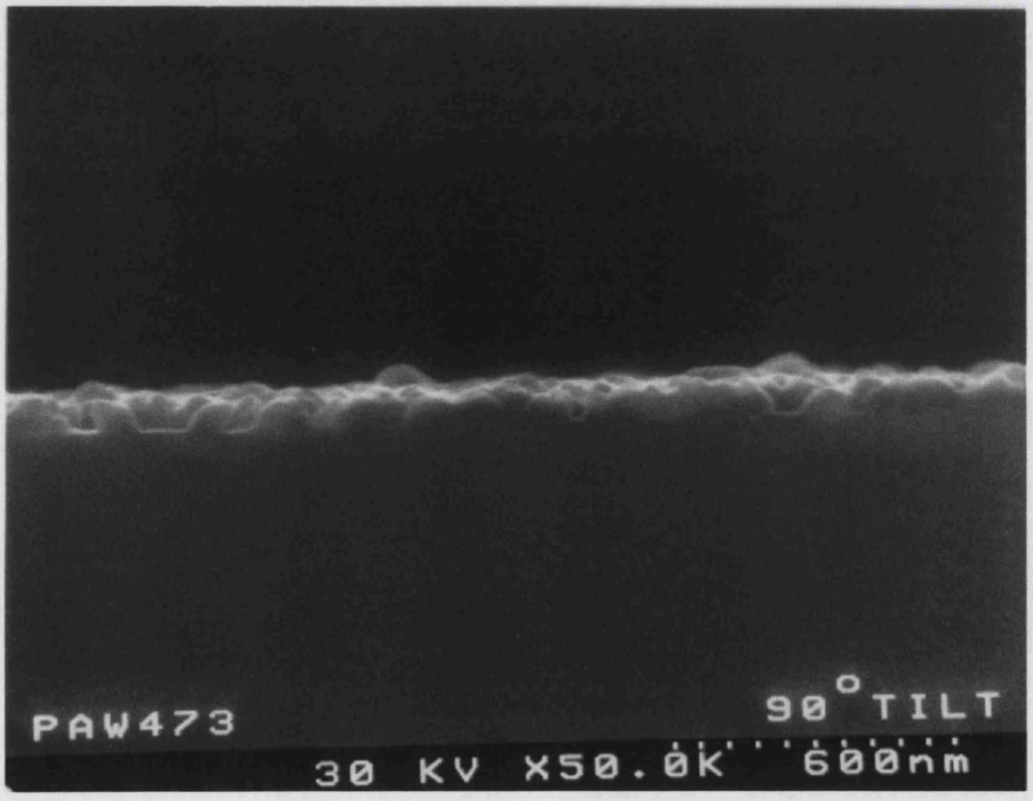

Figure 3.13 90°tilt SEM image for r7.

The 90° SEM images also give an indication as to the films thickness. However, it should be remembered that the thickness measurement is from a small area on the film and both the films described here were non-uniform (Table3.4).

Table 3.4 Approximate film thickness from SEM images.

Film ID	Thickness (Å)
r6	3030 ±120
r7	860 ±90

3.5.2.3 Transmission-reflectance spectra

The transmission-reflectance spectra for all three films highlighted within this Chapter were recorded, however, since the spectra for r7 and r8 were similar in appearance only r6 and r7 are displayed here (Figures 3.14, 3.15). The films were deposited on a static reactor so the thickness of the films was non-uniform, this can have a significant effect on the spectra recorded so should be considered when drawing any conclusions from the data. As in the previous chapter the absorption curve seen in the spectra was calculated from the following equation.

$$\text{Absorption} = 100\% - (\text{Transmission} + \text{Reflectance}) \quad [3.4]$$

The visible region of the solar spectrum is from approximately 350 to 780nm, therefore, to be useful in the building industry good transmission is required in this region. The infrared portion of the solar spectrum is from approximately 780 to 2000nm. Therefore, for the film to have the potential application of a solar control coating it should either reflect or absorb the infrared region of the solar spectrum while allowing transmission in the visible region.

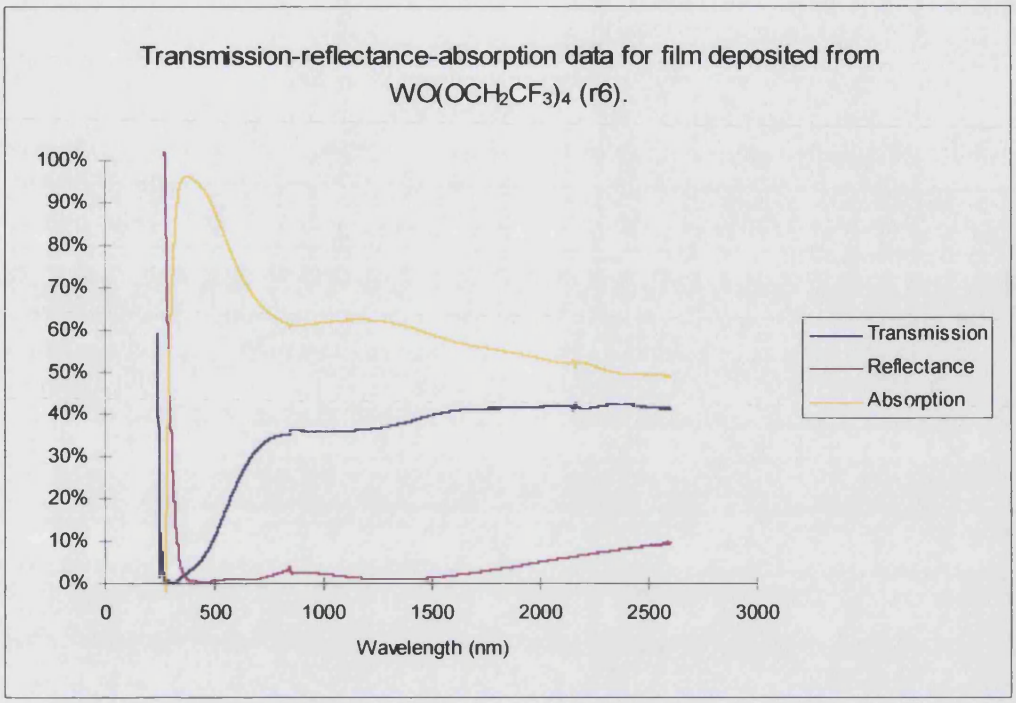

Figure 3.14 Transmission-reflectance-absorption spectra recorded for r6.

Figure 3.14 displays the spectra recorded from r6. As can be seen in the spectra the transmission of visible radiation is very poor with a transmission of approximately 35% at 700nm. This result was not surprising from the visual analysis of the film as it had looked very thick and clearly quite absorbing. However, the SEM analysis seemed to indicate that the poor transmission from this film could be a result of surface roughness rather than the thickness of the film. The calculated absorption curve shows that the film is absorbing around 60% of the visible radiation at 700nm. However, in the infrared portion of the solar spectrum a small hump in the absorption curve can be seen (800-1400nm). This indicates that the film may have some selectivity to the solar spectrum and if a more suitable film had been deposited (i.e. thinner) this selectivity may have been improved.

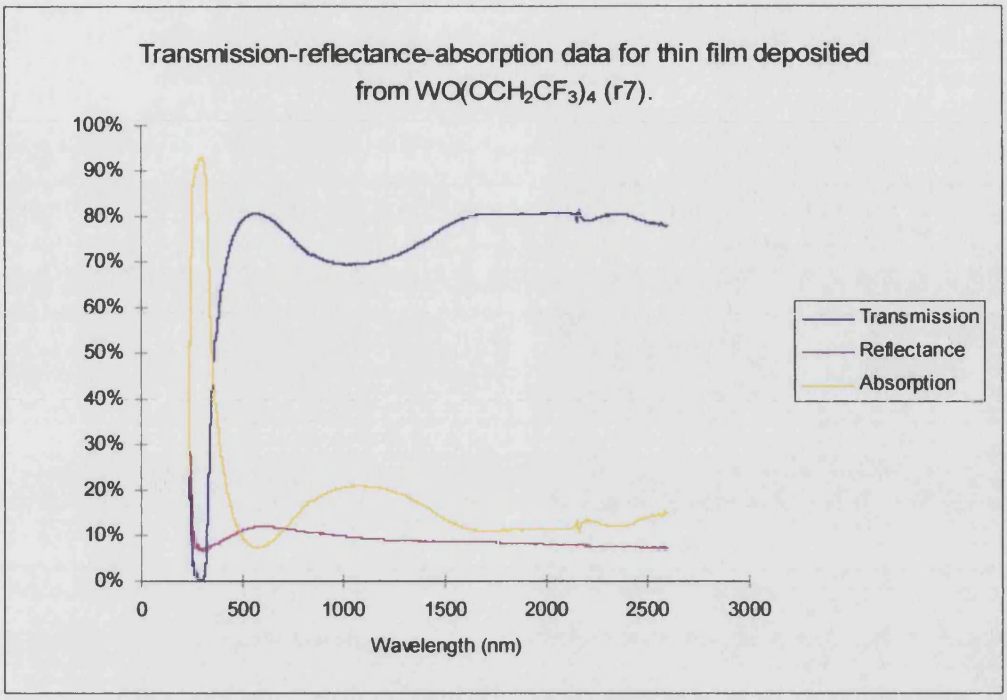

Figure 3.15 Transmission-reflectance-absorption spectra recorded for r7.

Figure 3.15 displays the transmission-reflectance-absorption spectra recorded for r7. This film was deposited while pre-mixing oxygen with the reactive gas flow and has been characterised by glancing angle X-ray diffraction as stoichiometric WO_3. The visible transmission of this film is quite high, over 80% at 550nm. This is slightly surprising as the film had looked quite hazy, however, both visual analysis, glancing angle X-ray diffraction and SEM analysis have indicated that the film was relatively thin. In the infrared region of the solar spectrum (780-2000nm) the film transmission drops to a minimum of about 70% at 1000nm. The reduction in the transmission curve is mirrored by an increase in the absorption curve over the same region. This indicates that the film is absorbing the infrared energy rather than reflecting it. However, the film is displaying selectivity to the solar spectrum in the right region for solar control applications despite the thinness of the film.

In summary, this Chapter has detailed the synthesis of a fluorinated monomeric five co-ordinate tungsten(VI) oxotetraalkoxide. Additionally, the monomeric compound has been sufficiently volatile to allow APCVD experiments to be conducted from which crystalline tungsten oxide thin films have been deposited in a single step with no post

deposition annealing. This is the second example of the APCVD of tungsten oxide in a single step and r7 is the first example of a crystalline stoichiometric WO_3 film being deposited at atmospheric pressure in a single step with pre-mixing of oxygen in the reactive gas stream. The films deposited have been characterised by glancing angle X-ray diffraction and have shown some selectivity to the solar spectrum in the infrared region.

3.6 EXPERIMENTAL

All manipulations during this synthesis were carried out under a nitrogen or argon atmosphere using standard Schlenk techniques or in a dry-box fitted with a recirculation system. Tetrahydrofuran, toluene and hexane were dried over and distilled from sodium-benzophenone immediately prior to use and 2,2,2-trifluoroethanol was purchased from Aldrich and dried over molecular sieves once opened.

3.6.1 Synthesis of $WO(OCH_2CF_3)_4$ (4)

Tungsten oxychloride (5.00g, 14.6mmol) was dissolved in tetrahydrofuran (ca. 120ml) to give an orange solution. To this solution was added 2,2,2-trifluoroethanol (8.79g, 87.8mmol) with stirring. Ammonia was then bubbled through the solution for 25 minutes giving a white precipitate. The white precipitate (NH_4Cl) was filtered off and the solvent removed *in vacuo* to give a brown solid. After extraction into toluene and evaporation of the solvent, the solid residue was washed with hexane and pumped dry to give an off white powder, yield 5.38g (62%). Sublimation of the off white powder at approximately 180-190°C gave a pure white compound which had the appearance of cotton wool **(4)**. Yield [based on $W(O)Cl_4$] 1.35g (16%).

Analysis Found (calculated for $C_8H_8F_{12}O_5W$): C, 14.8 (16.1); H, 1.23 (1.35)%.

^{183}W nmr [δ(ppm), CD_3CN soln.] : -249.7, s.

^{1}H nmr [δ(ppm), CD_3CN soln.] : 4.89 [q, CH_2], $^{3}J_{HF}$ = 8.9Hz.

^{13}C nmr [δ(ppm), CD_3CN soln.] : 71.8 [q, CH_2], $^{2}J_{CF}$ = 35Hz; 125.7 [q, CF_3], $^{1}J_{CF}$ = 277Hz.

^{19}F nmr [δ(ppm), CD_3CN soln.] : -76.9 [t, CF_3], $^{3}J_{FH}$ = 8.7Hz.

IR data (NaCl plates, nujol mull, cm^{-1}) : 1402, 1277, 1194, 1163, 1109, 956, 839, 783, 711, 667, 623cm^{-1}.

Chapter Four

Donor-functionalized Alkoxides

4.1 INTRODUCTION

As discussed in Chapter Three, metal alkoxides have been used extensively as precursors for the CVD of metal oxide thin films.[122,123] However, for the deposition of tungsten oxide thin films relatively little work has been reported. This is probably due to the lack of suitably volatile precursors. A series of tungsten(VI) oxotetraalkoxides $W(O)(OR)_4$ (R = Me, Et, Pr^i, Bu^t and *cyclo*-C_6H_{11}) have been synthesised by several methods.[92] However, these compounds are not suitably volatile to allow APCVD experiments to be conducted as dimers are formed in the solid state by alkoxide bridges (Figure 4.1).

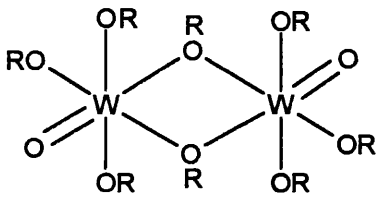

Figure 4.1 Alkoxo bridged dimer.[92]

The previous Chapter detailed how the volatility of these tungsten(VI) oxotetraalkoxides compounds could be enhanced by utilising a fluorinated alkoxide ligand. A second approach, mentioned in Chapter Three, which could enhance the volatility of these dimeric compounds is to use a bidentate ligand to replace one of the monodentate ligands. This would theoretically break up the alkoxide bridges between the tungsten atoms and give monomeric molecules. This approach has already been used for several metal alkoxides including tungsten.[42,132]

Tungsten(VI) oxotetraalkoxides of the type $[W(O)(OR)_4]_2$ and $W(O)(OR)_3L$ (R = Pr^i; L = acac, hfac) have been synthesised and used as precursors in LPCVD studies. The tungsten(VI) oxoalkoxide/β-diketonate complexes have been shown to be ridged on the NMR time scale and have a monomeric pseudo octahedral structure as illustrated in Figure 4.2.[42]

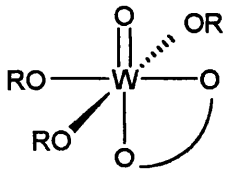

Figure 4.2 Proposed structure of $W(O)(OR)_3L$ complexes.

The use of a bidentate β-diketonate ligand has broken up the dimeric structure of the tungsten(VI) oxotetraalkoxide and yielded a six co-ordinate monomeric molecule. In this example, despite the product being an oil rather than a solid, the volatility was not seen to increase significantly and LPCVD was required to deposit tungsten oxide films via a two step process from the synthesised compounds.

This kind of approach has also been used for $[Ta(OEt)_5]_2$, where instead of using a β-diketonate ligand to break up the dimer, a donor-functionalized alkoxide ligand, 2-dimethyl aminoethanol (Hdmae), has been used (Figure 4.3). This allows the electropositive metal centre to achieve its favoured six co-ordination geometry within a monomeric unit and hence increase its volatility by an order of magnitude (e.g., vapour pressure for $[Ta(OEt)_5]_2$, 0.0075 torr at 108°C; for $Ta(OEt)_4(OCH_2CH_2NMe_2)$, 0.075 torr at 108°C).[133] Since the use of donor-functionalized alkoxide ligands has proved successful in increasing the volatility for this system it was decided to investigate the use of donor-functionalized alkoxides to break up the dimeric structure and hence increase the volatility of the previously synthesised tungsten(VI) oxotetraalkoxides.

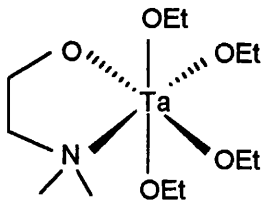

Figure 4.3 Schematic representation of proposed structure for $Ta(OEt)_4(dmae)$.[133]

This Chapter describes the synthesis of $[W(O)(OPr^i)_4]_2$, via previously established literature methods, followed by the synthesis of two monomeric species using donor-functionalized alkoxides ligands, Hdmae and dimethyl aminopropanol (Hdmap) to break up the dimeric structure. $[W(O)(OPr^i)_4]_2$ was chosen as the basis for this study as it was hoped the bulky isopropoxide groups would aid volatility. Thin films were then grown from all three compounds synthesised as part of this study via AACVD and these have been characterised by glancing angle X-ray diffraction, SEM and transmission-reflectance measurements.

4.2 SYNTHETIC ROUTES

$[W(O)(OPr^i)_4]_2$ was prepared by an alcoholysis reaction using $W(O)Cl_4$, $HOPr^i$ and a base (NH_3) to remove the liberated HCl. Once the precipitated NH_4Cl has been removed the final product can be isolated as a white powder.[92]

$$2W(O)Cl_4 + 8HOPr^i + 8NH_3 \xrightarrow{THF} [W(O)(OPr^i)_4]_2 + 8NH_4Cl \quad [4.1]$$

Preparation of the tungsten(VI) oxotetraalkoxide/β-diketonate complexes previously mentioned and a selection of donor-functionalised alkoxide compounds [$Ti(OPr^i)_3$(dmae), $Ta(OEt)_4$(dmae), $Nb(OEt)_4$(dmae)] are all accomplished by the addition of one equivalent of the bidentate ligand being used to a solution containing the metal alkoxide.[133,134] This is then followed by the removal of the solvent and the distillation or sublimation of the desired pure product. Since this methodology has been successful for several different systems it was utilised in the preparation of the donor-functionalised tungsten compounds synthesised during this study.

4.3 STRUCTURAL AND SOLUTION CHEMISTRY

The tungsten(VI) oxotetraalkoxide/β-diketonate complexes which have been synthesised, $W(O)(OR)_3L$ (R = Pr^i; L = acac, hfac), are yellow oils so no structural characterisation has been possible. However, NMR analysis of these complexes have shown them to be monomeric octahedral molecules (Figure 4.2). This was determined by the ratio of 2:1 for the Pr^i groups present on the molecule. One other interesting point is that the compounds were rigid on the NMR time scale which is in contrast to several of the molecules containing the donor-functionalised alkoxide ligands reported in the literature.

The $Ta(OEt)_4$(dmae) monomer previously mentioned is also a liquid which could therefore not be characterised by X-ray crystallography. However, the structure has been confirmed by ^1H NMR. The bridged $[Ta(OEt)_5]_2$ spectrum shows two triplets and two quartets arising from both bridging and terminal OEt ligands present. The ^1H NMR spectrum of $Ta(OEt)_4$(dmae) displays a triplet [OCH_2CH_3] and a quartet [OCH_2CH_3] from the OEt ligands which confirms the monomeric nature of the molecule.

Hdmae has also been used in an attempt to enhance the volatility of $Ti(OPr^i)_4$ for CVD applications. The two compounds which have been synthesised were $Ti(OPr^i)_3$(dmae) and $Ti(OPr^i)_2$(dmae)$_2$. The ^1H NMR spectrum recorded for $Ti(OPr^i)_2$(dmae)$_2$ indicated a single monomeric species had been formed, however, the NMR spectrum for $Ti(OPr^i)_3$(dmae) was more complex. A variable temperature ^1H NMR study showed that at 50°C only a single monomeric species was present. However, as the temperature was lowered there was significant broadening of the proton signals. The most likely explanation for this presented by the authors was a monomer-dimer exchange process (Figure 4.4).[134]

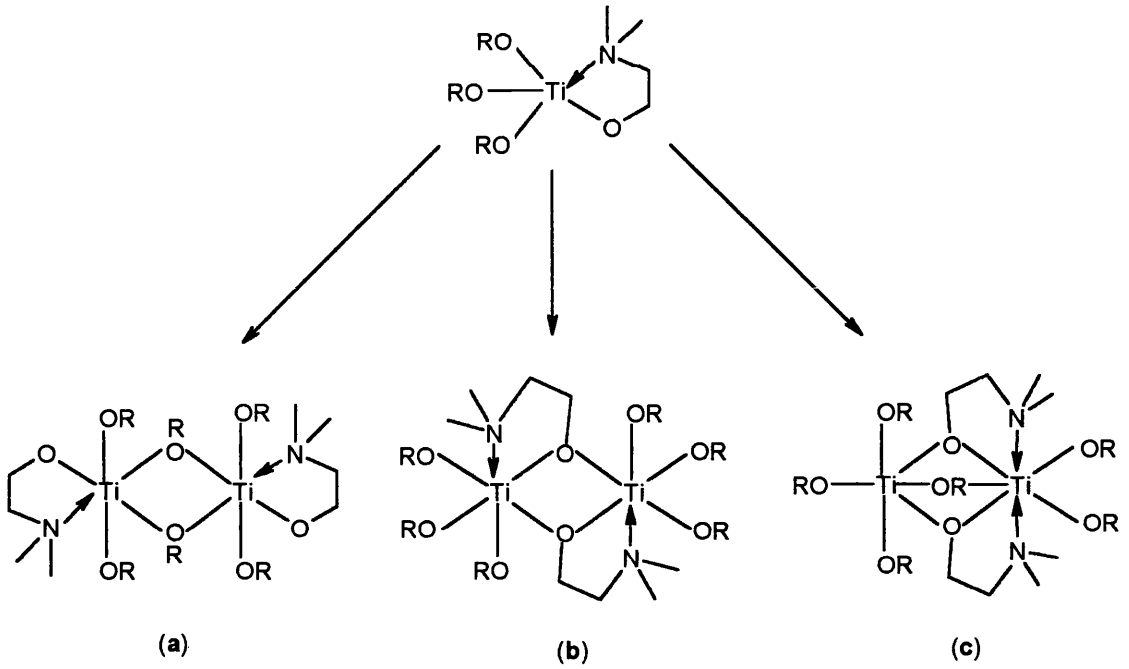

Figure 4.4 Possible structures of $Ti(OPr^i)_3$(dmae) at low temperature.[134]

Of the three low-temperature structures illustrated (**b**) was considered the most likely. The structure illustrated in (**a**) is also possible and has been suggested for related titanium tris(isopropoxide) β-diketonate compounds.[135] The third (**c**) involves bridging through the chelating alkoxy ligands with the amine co-ordinated to the same metal atom in addition to one bridging isopropoxide ligand. However, the co-ordination number of the titanium metal centre is increased to seven which was considered unlikely, therefore, it has been suggested that this structure is the least likely of the three proposed.

4.4 RESULTS AND DISCUSSION

4.4.1 Synthesis

Before synthesis of the donor-functionalised compounds could commence the starting tungsten(VI) oxotetraalkoxide had to be synthesised. As previously noted,

$[W(O)(OPr^i)_4]_2$ **(5)** was chosen as the basis for this work and was synthesised by the methodology in the literature **[4.1]**.[92]

The donor-functionalised tungsten(VI) oxoalkoxides were synthesised by the reaction of one equivalent of the appropriate chelating ligand (Hdmae or Hdmap) with $[W(O)(OPr^i)_4]_2$ in tetrahydrofuran. The mixture was refluxed for several hours to ensure the reaction was complete before the solvent and volatiles were removed **[4.2]**.

$$[W(O)(OCH(Me)_2)_4]_2 + 2Me_2N(CH_2)_nOH \xrightarrow{THF} 2W(O)(CH(Me)_2)_3(O(CH_2)_nNMe_2) + 2HOCH(Me)_2 \quad [4.2]$$

n = 2 **(6)**, 3 **(7)**.

The waxy yellow oils which were recovered from the reaction were then vacuum distilled to yield the pure products as air and moisture sensitive pale yellow oils $[W(O)(OPr^i)_3(dmae)$ **(6)**, $W(O)(OPr^i)_3(dmap)$ **(7)]**. One attempt was made to substitute two of the isopropoxide ligands for two dmae ligands via the same methodology. However, the ^1H NMR spectrum of the recovered compound indicated the presence of only one dmae ligand. While co-ordination numbers higher than six are relatively common for tungsten, a co-ordination number of seven could be considered less favourable in this case.

4.4.2 NMR Spectroscopy

^1H, ^{13}C, and ^{183}W NMR experiments were performed on **(6)** in addition to a variable temperature ^1H NMR analysis. ^1H NMR analysis was also performed on **(7)** at 20 and 60°C in addition to a ^{13}C NMR. **(5)** has previously been fully characterised by means of variable temperature ^1H NMR, ^{13}C NMR, infrared and microanalysis, therefore, only confirmation that the compound had been synthesised was required for this work.

4.4.2.1 ^{1}H NMR Spectroscopy

The ^{1}H NMR spectra collected for **(5)** showed two broad peaks at 4.6 and 0.9ppm in addition to several multiples between 5.3 and 1.0ppm. The ^{1}H NMR spectra and the infrared spectra collected matches the previously published data for **(5)** confirming the compound had been synthesised. This was subsequently used as the starting material for the synthesis of **(6)** and **(7)** and for several AACVD experiments.

The ^{1}H NMR spectra recorded for **(6)** (Figure 4.5) showed the expected peaks for the dmae ligand at around 4.53ppm [(OC*H*$_2$CH$_2$N(CH$_3$)$_2$], 2.49ppm [(OCH$_2$-C*H*$_2$N(CH$_3$)$_2$] and 2.39ppm [(OCH$_2$CH$_2$N(C*H*$_3$)$_2$], and peaks at 4.95ppm [OC*H*(CH$_3$)$_2$] and 1.36ppm [OCH(C*H*$_3$)$_2$] from the OPr^i groups. The integrals from these peaks indicated that one dmae ligand had replaced one OPr^i ligand as was expected. However, there seemed to be two or three OPr^i signals giving two or three overlapping doublets at 1.36ppm and two or three overlapping septets at about 4.95ppm. This could indicate bridging and non-bridging OPr^i ligands or just inequivalent groups on a monomeric species. The two CH$_2$ signals from the dmae ligand also appeared more complex that expected. While there were three peaks associated with each signal these were not triplets as the peak ratios were not 1:2:1 as would be expected for a conventional triplet. Additionally, there were three broad featureless regions at 2.51, 2.55 and 4.71ppm. In an attempt to determine whether **(6)** was a dimer or monomer, a variable temperature ^{1}H NMR analysis was conducted. Before analysing the ^{1}H NMR spectra recorded during this study it would be useful to review some related compounds which have been previously synthesised.

[W(O)(OPr^i)$_4$]$_2$ had been synthesised prior to this work and its solution chemistry analysed by variable temperature ^{1}H NMR.[92] The spectra recorded have been interpreted in terms of a monomer-dimer exchange process in the presence of both W(OPr^i)$_6$ and Pr^{i}OH. The dimer is seen to be prevalent at lower temperatures with the monomer more favourable as the temperature is increased. The free alcohol present is then able to exchange rapidly with the monomer at higher temperatures, ca. 30°C, as indicated by coalescence between the monomer and free alcohol signals.

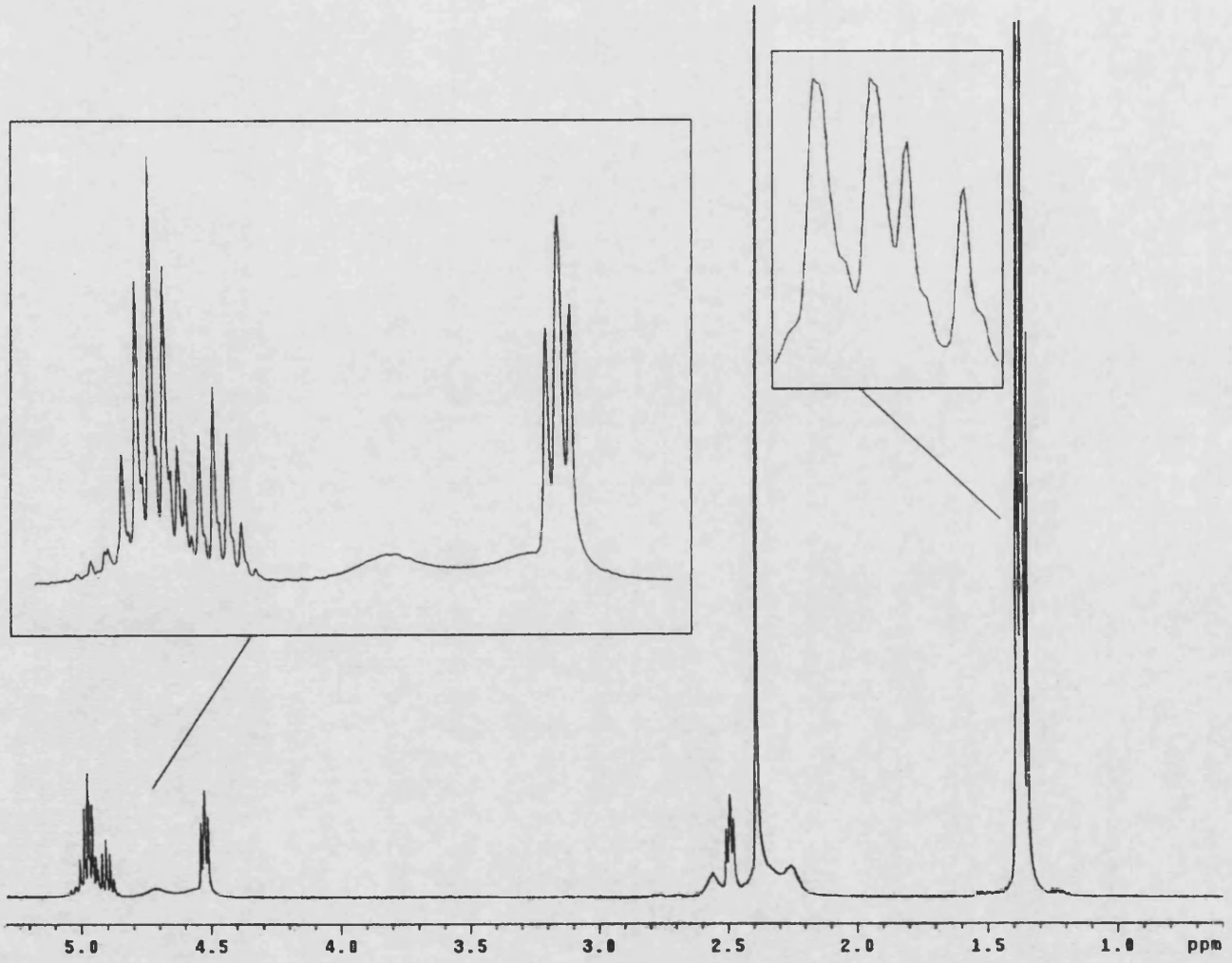

Figure 4.5 ^{1}H NMR spectra recorded for **(6)** at 20°C.

Titanium tetraisopropoxide is a monomeric molecule, however, it was reacted with Hdmae to give $Ti(OPr^i)_3(dmae)$ for use as a precursor in the growth of TiO_2 via liquid injection CVD.[134] Variable temperature ^1H NMR spectra showed that the compound exists almost entirely as a monomer at high temperature, 50°C, with a monomer-dimer exchange evident at lower temperatures. The interesting features seen in this spectra are that at high temperature only one signal is seen from the OPr^i groups indicating all the OPr^i present are equivalent on the monomer, and the dmae CH_2 protons give triplets which are not seen in **(6)** (coupling constant 5.9 Hz).

The dimeric structure of $[Ta(OEt)_5]_2$ has been broken up by the addition of Hdmae to give the monomer $Ta(OEt)_4(dmae)$, Figure 4.3. The monomeric structure has been confirmed by ^1H NMR. The ^1H NMR shows the expected dmae signals in addition to one set of triplets and quartets arising from the ethoxide groups. The bridged structure of $[Ta(OEt)_5]_2$ displayed two sets of triplets and quartets which were assigned to bridging and terminal ethoxide groups. The ^1H NMR of $Ta(OEt)_4(dmae)$ showed only one signal for the ethoxide groups, however, as can be seen in Figure 4.3 the four ethoxide groups are not equivalent. Therefore, the molecule must be rearranging in some fashion to make all the OEt groups equivalent. The most likely proposed rearrangement was via rapid N:→Ta cleavage.[133]

The ^1H NMR experiments were performed on **(6)** at three different solution concentrations and temperatures between -60 and +70°C. A concentration change was seen to move the positions of the dmae signals as shown in Figure 4.6. The isopropoxide signals remain relatively static in relation to the dmae as the concentration changes from approximately 50 to 15 to 5% (top to bottom) by volume. However, the concentration appeared not to effect the overall appearance of the spectra, only the positions of the dmae peaks relative to each other. This could indicate a structure bridged by dmae ligands with dangling nitrogen atoms. High temperature ^1H NMR experiments, detailed later, and the sharpness of the peaks during this experiment would seem to suggest a monomer configuration is more likely. However, bridging dmae ligands can not be completely ruled out.

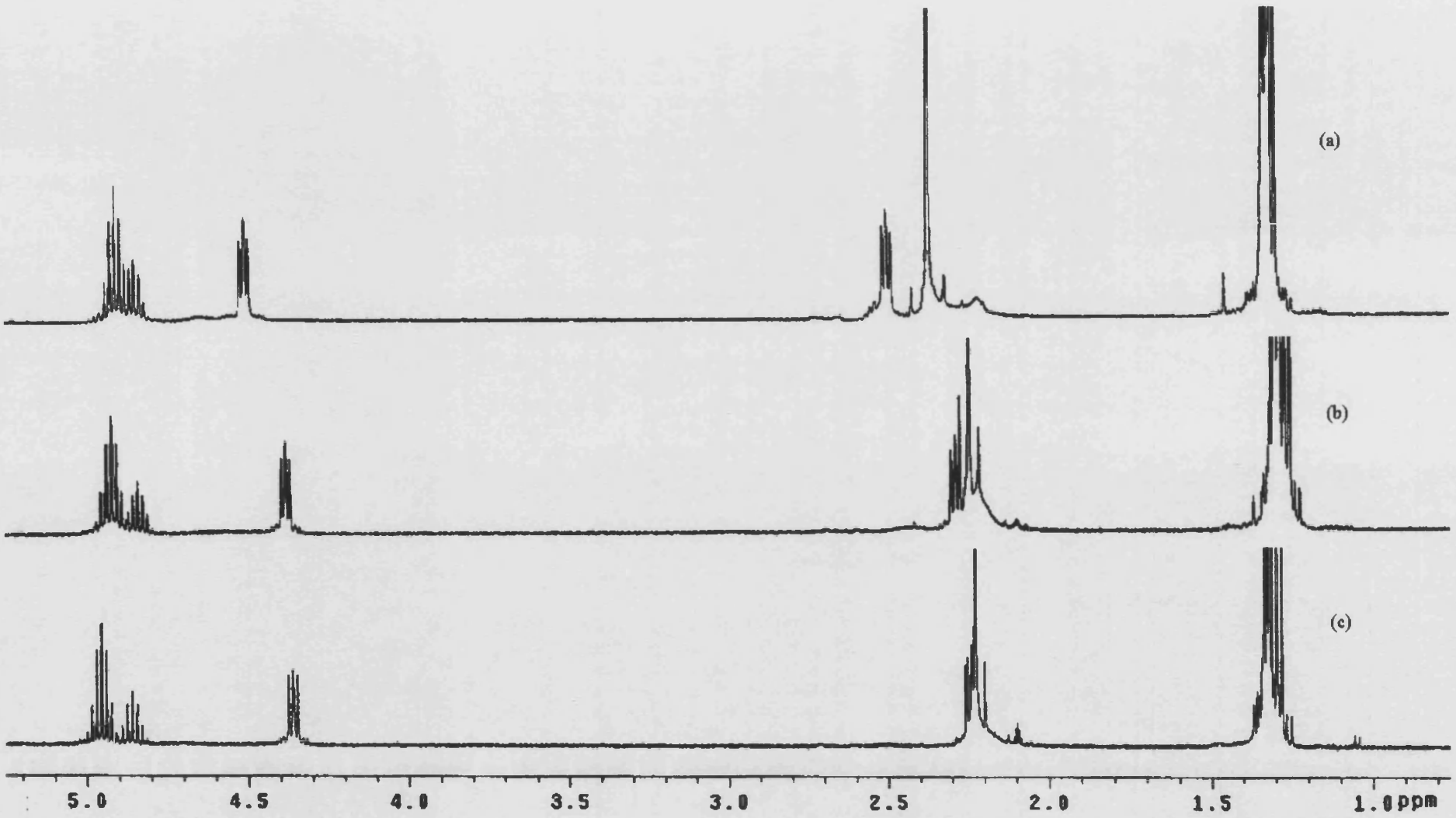

Figure 4.6 ^{1}H NMR spectra for **(6)** at room temperature at (a) 50, (b) 15 and (c) 5% by volume.

The ^{1}H NMR spectrum displayed earlier in Figure 4.5 was recorded at 20°C with a solution concentration of approximately 25% by volume. The expected peaks for the dmae ligand are seen at around 4.5ppm [$(OCH_2CH_2N(CH_3)_2]$, 2.5ppm [$(OCH_2CH_2N(CH_3)_2]$ and 2.4ppm [$(OCH_2CH_2N(CH_3)_2]$. There are two [$OCH(CH_3)_2]$ signals at around 4.9ppm in the ratio of 2:1 and a group of signals for the [$OCH(CH_3)_2]$ protons at 1.36ppm. The 2:1 ratio seen for the [$OCH(CH_3)_2]$ protons could be a result of terminal and bridging OPr^i groups giving a dimer as opposed to the desired monomer. However, this would make the tungsten centre seven co-ordinate which would be less favourable and is not supported by subsequent ^{183}W NMR analysis. An alternative to the dimer structure would be the monomeric structure illustrated in Figure 4.7. As illustrated this structure can adopt two different conformations, *fac* and *mer*.

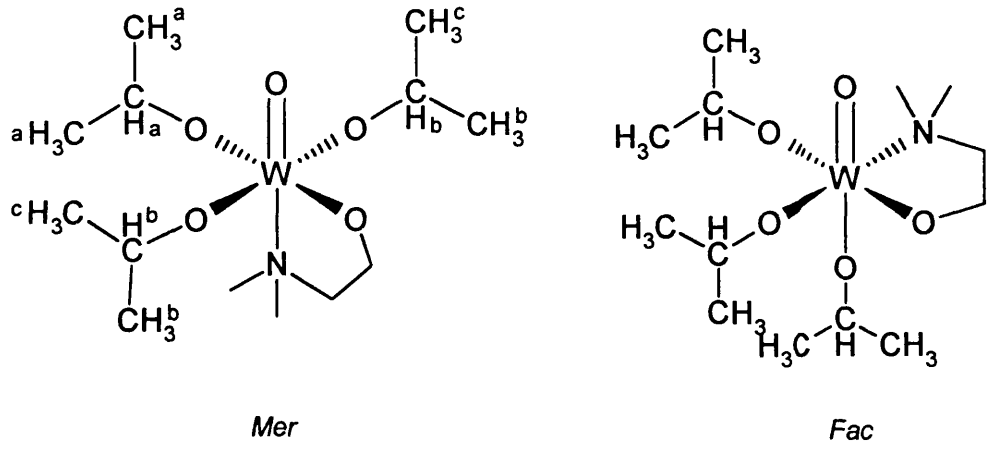

Figure 4.7 *Mer* and *Fac* configurations of **(6)**.

In the *mer* conformation two of the [$OCH(CH_3)_2]$ protons (H_b) are equivalent and the third is not (H_a) giving rise to the 2:1 ratio seen in the ^{1}H NMR spectra recorded. If the *mer* configuration has been adopted by the molecule then the methyl groups which couple with H_b are not equivalent, this would give rise to a quartet of quartets for the H_b signal. However, the coupling constant between H_b and the two sets methyl protons would be virtually identical leading to the apparent septet being observed in the spectrum recorded. As illustrated in Figure 4.7 there are three types of methyl group present in the *mer* isomer of **(6)** in the ratio of 1:1:1. Therefore, in the ^{1}H NMR spectrum recorded

there should be three doublets in the ratio 1:1:1 for the [OCH(CH_3)$_2$] groups. The spectrum illustrated in Figure 4.5 has only four peaks visible in the methyl region presumably due to overlapping of the signals. However, the spectra recorded for the 15% by volume sample of **(6)** at +30°C clearly illustrates the three doublets arising from the methyl protons [OCH(CH_3)$_2$] (Figure 4.8). For these spectra to be observed the N:→W bond would have to be fixed and not undergoing the rapid breaking and reformation seen in the literature examples.

For the *fac* isomer the mirror plane within the molecule has been lost rendering the three methyl protons [OC*H*(CH_3)$_2$] inequivalent. Therefore, the ^{1}H NMR spectrum recorded if the *fac* isomer was predominant would probably show three signals in the 4.9ppm region in a ratio of 1:1:1 rather than the observed 2:1 ratio. For this reason the *fac* isomer can be ruled out as the predominant species in solution.

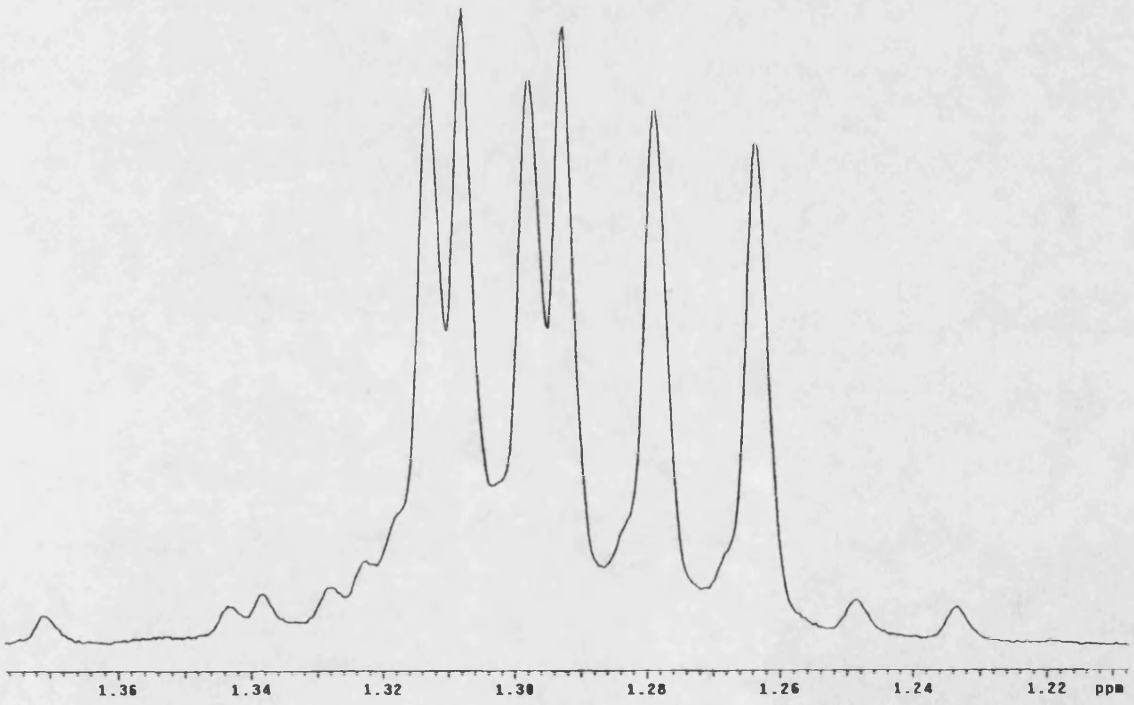

Figure 4.8 Enlargement of methyl region of ^{1}H NMR spectra of **(6)** recorded at 30°C with a solution concentration of 15% by volume.

The signals for the dmae ligand in **(6)** are at 4.5ppm [(OCH_2CH$_2$N(CH_3)$_2$], 2.5ppm [(OCH$_2$CH_2N(CH_3)$_2$] and 2.4ppm [(OCH$_2$CH$_2$N(CH_3)$_2$] (Figure 4.5). The

peaks observed at 4.5 and 2.5ppm are clearly not triplets, as would be expected, but appear to be overlapping doublets. A simplified diagram of **(6)** in *mer* conformation showing the dmae ligand is shown in Figure 4.9.

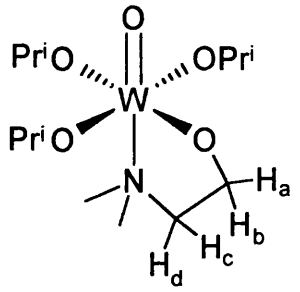

Figure 4.9 Illustration of **(6)** showing dmae protons.

If, as already hypothesised, the dmae ligand is fixed in position, the protons on the two CH_2 groups would no longer be equivalent, this is illustrated in Figure 4.9. However, the dmae ligand is also free to move with a 'windscreen wiper' like motion which would make the protons in each pair equivalent as shown in Figure 4.10. In the two extremes, $H_a \neq H_b$ and $H_c \neq H_d$, however, $H_a = H_b$ and $H_c = H_d$ when the five membered ring is planar (centre picture). The motion of the dmae ligand would be greatly effected by temperature, hence the complex signals seen in the this region of the NMR spectra recorded (Figure 4.11).

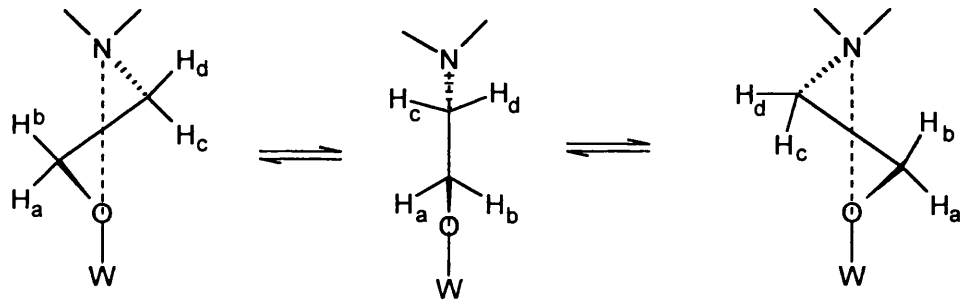

Figure 4.10 Illustration of windscreen wiper motion of dmae ligand.

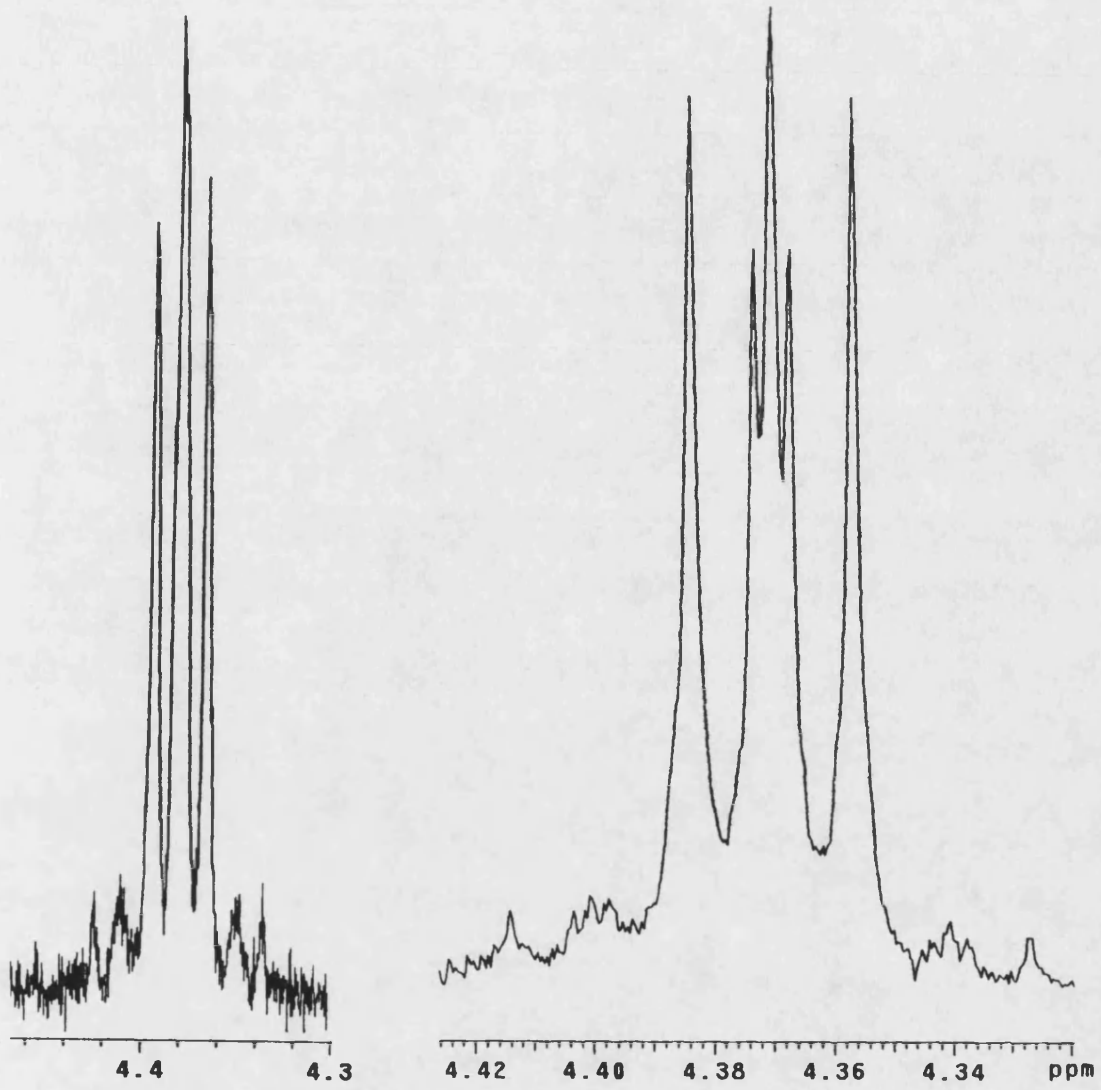

Figure 4.11 Enlargement of ^{1}H NMR spectra due to [(OC*H*$_2$CH$_2$N(CH$_3$)$_2$] recorded at 60°C (left) and 15°C (right) for **(6)** with a solution concentration of 5% by volume.

The coupling constant between H_a/H_b and H_c/H_d is likely to be very small and dependent on the 'windscreen wiper' motion of the dmae ligand, however, so long as the movement of the dmae backbone is restricted, the expected triplets will not be observed. Figure 4.11 illustrates two groups of peaks recorded at different temperatures for the dmae backbone [(OC*H*$_2$CH$_2$N(CH$_3$)$_2$].

A reduction in temperature would appear to give rise to another species in the ^{1}H NMR spectrum of **(6)**. This is best demonstrated in the spectra recorded at -45°C for

the 5% by volume sample (Figure 4.12). There is an additional group of peaks at approximately 4.75ppm which seem to correspond to at additional [OC*H*$(CH_3)_2$] group, there is also an additional singlet at about 2.1ppm which could be a [$OCH_2CH_2N(CH_3)_2$] signal. However, without further experiments no definitive statement about the molecules behaviour at lower temperatures can be made.

At elevated temperatures a clearer picture of the molecule's behaviour is evident. Figure 4.13 illustrates the spectra recorded for the 50% by volume sample at +70°C. This spectra seems to indicate the expected rapid breaking and reformation of the N:→W bond. This is supported by the [OC*H*$(CH_3)_2$] signals, which were previously in a ratio of 2:1, almost becoming a single septet and the [$OCH(CH_3)_2$] now almost a simple doublet. Additionally, extra signals are seen for the dmae ligand at 4.6, 2.57 and 2.45ppm which are two triplets and a singlet for the [$(OCH_2CH_2N(CH_3)_2$], [$(OCH_2CH_2N(CH_3)_2$] and [$(OCH_2CH_2N(CH_3)_2$] protons respectively. This spectrum would seem to indicate that at high temperatures **(6)** is behaving in a similar fashion to the previous examples in the literature (i.e. rapid scrambling of the position of the N:→W bond, which has the effect of rendering the OPr^i groups on the molecule equivalent).

While the precise fluxional process of **(6)** is not fully understood across the whole temperature range, the ^1H VTNMR analysis conducted has demonstrated that the molecule is monomeric and is most stable in the *mer* configuration whilst in solution. The species seems thermally rigid, and equivalence of OPr^i groups only occurs at elevated temperatures. This is in contrast to other compounds in the literature using dmae as a ligand as these have shown the N:→M bond to be breaking and reforming to scramble the alkoxide signals at lower temperatures, most notably for $Ta(OEt)_5$(dmae). For **(6)**, the VTNMR spectra recorded would seem to suggest that the N:→W bond is more stable than previous literature examples, therefore, the OPr^i signals do not merge until at least 70°C. No clear reason presents itself as to why the N:→W dative bond should be more stable in this molecule when compared to others in the literature.

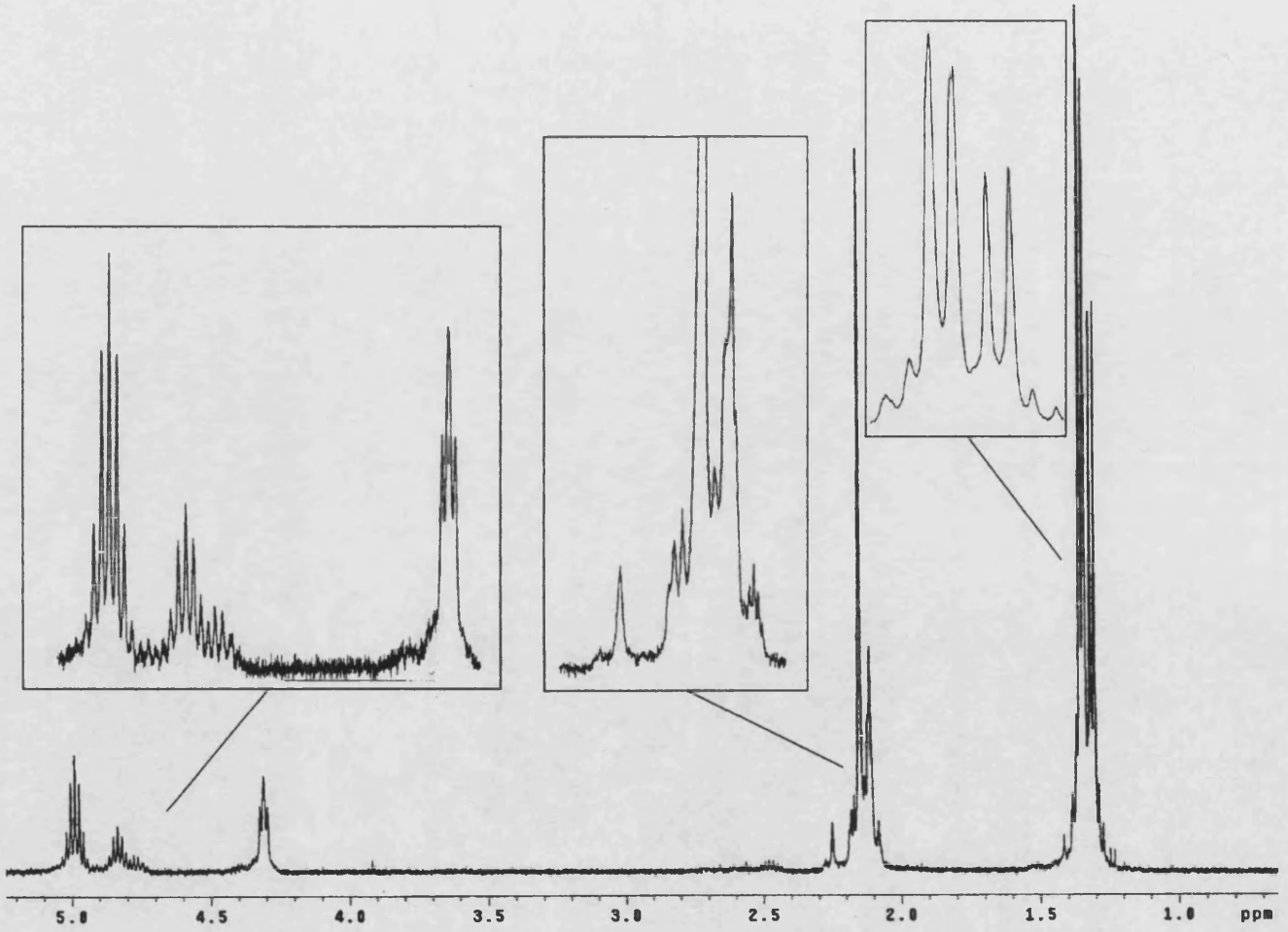

Figure 4.12 ^{1}H NMR spectra recorded at -45°C for **(6)**.

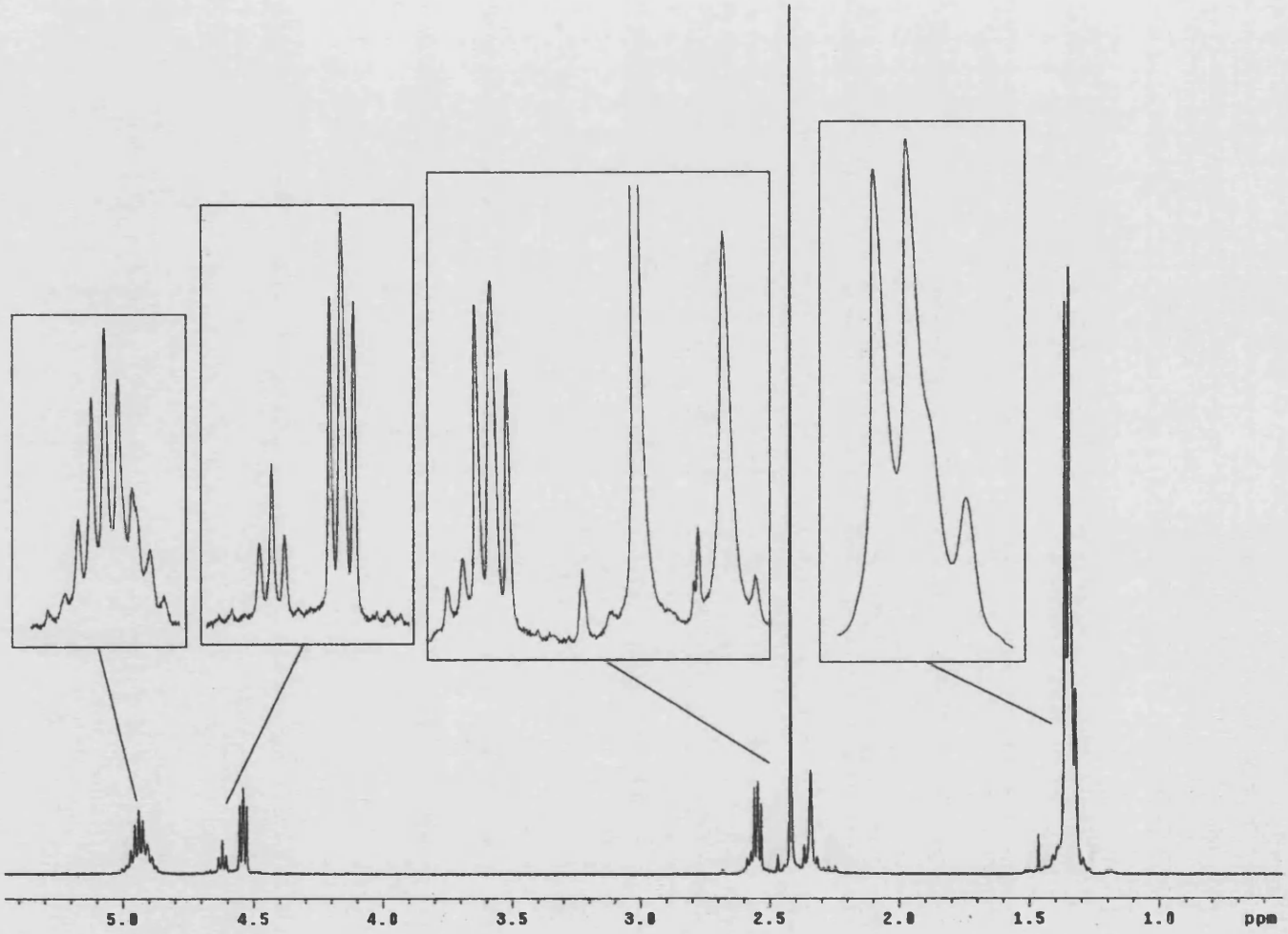

Figure 4.13 ^{1}H NMR spectra recorded at 70°C for **(6)**.

The ^{1}H NMR spectra of **(7)** showed the expected peaks for the dmap ligand at around 1.41ppm [$OCH_2CH_2CH_2N(CH_3)_2$], 2.17ppm [$OCH_2CH_2CH_2N(CH_3)_2$], 2.31ppm [$OCH_2CH_2CH_2N(CH_3)_2$] and 4.53ppm [$OCH_2CH_2CH_2N(CH_3)_2$], and peaks at 1.32ppm [$OCH(CH_3)_2$] and 5.00ppm [$OCH(CH_3)_2$] for the OPr^i ligand. The integrals of these peaks showed that one dmap ligand had replaced one OPr^i ligand as expected. However, as with **(6)**, the peaks for the dmap ligand were not as expected, and while the OPr^i peaks are almost a doublet and a septet, indicating a single environment, they are a little broad and could be overlapping doublets and septets as seen in **(6)**. Additionally, there are again broad humps at 1.64, 2.34 and 4.63ppm, in addition to a sharp peak at 2.14. The positions and integrals of these signals are consistent with a second dmap ligand. This would seem to indicate that the structure is not static in solution, with the N:→W dative bond breaking and reforming quickly in solution giving rise to a second set of broad dmap signals. The ^{1}H NMR spectrum was repeated at 60°C giving broadly the same spectrum, however, the OPr^i signals now looked more like a doublet and a septet and the broad hump which was at 4.53ppm changed to a broad triplet at 4.62ppm with a coupling constant of 5.5 Hz [$OCH_2CH_2CH_2N(CH_3)_2$]. This would seem to indicate that **(7)** is behaving in a similar fashion to **(6)**.

4.4.2.2 ^{183}W NMR Spectroscopy

The ^{183}W NMR spectrum recorded for **(6)** gave one peak at -88.6ppm. This value is consistent with other ^{183}W NMR chemical shift values recorded for six co-ordinate oxotetraalkoxide complexes. Table 2.2 displays the chemical shift values obtained for a selection of five and six co-ordinate complexes of the type $W(O)(OR)_4$.

Both the Me and cyclo-C_6H_{11} derivatives are known to be six co-ordinate by crystallography and the Bu^t derivative is known to be five co-ordinate. Therefore, the difference in chemical shift values (-62.9 to -386.9ppm) is considered to reflect this difference. The chemical shift value recorded for **(6)** was -88.5ppm which is consistent with the tungsten atom being six co-ordinate.

4.5 CRYSTAL STRUCTURE

Crystal structure determination was not possible on **(6)** and **(7)** as these compounds were both oils. However, several weeks after the initial NMR analysis of **(6)** small crystals were observed in the toluene solution in the NMR tube. These crystals proved suitable for single crystal X-ray diffraction using an area detector. However, only a very small amount of crystalline material, $W_4(O)_4(dmae)_4O_6$ **(8)**, was isolated and this proved to be very sensitive once out of solution and no other analysis was possible. Unsuccessful attempts were also made to grow crystals of **(7)** by the same procedure.

The structure determined from the crystals recovered from the toluene solution of **(6)** is displayed in Figure 4.14 with relevant bond lengths and angles in Tables 4.1 and 4.2. In addition to the structure displayed in Figure 4.14, tungsten oxide which was refined to 12.3% was also detected, however, as this was a secondary component the phase of tungsten oxide could not be determined. The tungsten oxide was included to account for the observed residual electron density.

Table 4.1 Selected Bond Lengths for Tungsten Cage **(8)**.

	Bond Lengths Å
W(1)-O(1)	1.922(8)
W(1)-O(2)	1.713(8)
W(1)-O(3)	2.269(9)
W(1)-O(4)	1.903(4)
W(1)-O(3)#1	1.795(9)
W(1)-N	2.387(11)

Table 4.2 Selected Bond Angles for **(8)**.

	Angle (°)		Angle (°)
O(2)-W(1)-O(3)#1	105.1(4)	O(4)-W(1)-O(3)	82.1(4)
O(2)-W(1)-O(4)	96.2(4)	O(1)-W(1)-O(3)	80.3(3)
O(3)#1-W(1)-(4)	98.4(4)	O(2)-W(1)-N(1)	93.1(4)
O(2)-W(1)-O(1)	97.7(4)	O(3)#1-W(1)-N(1)	161.5(4)
O(3)#1-W(1)-O(1)	98.7(4)	O(4)-W(1)-N(1)	82.2(3)
O(4)-W(1)-O(1)	154.3(3)	O(1)-W(1)-N(1)	75.5(4)
O(2)-W(1)-O(3)	170.6(4)	O(3)-W(1)-N(1)	77.5(4)
O(3)#1-W(1)-O(3)	84.3(3)		

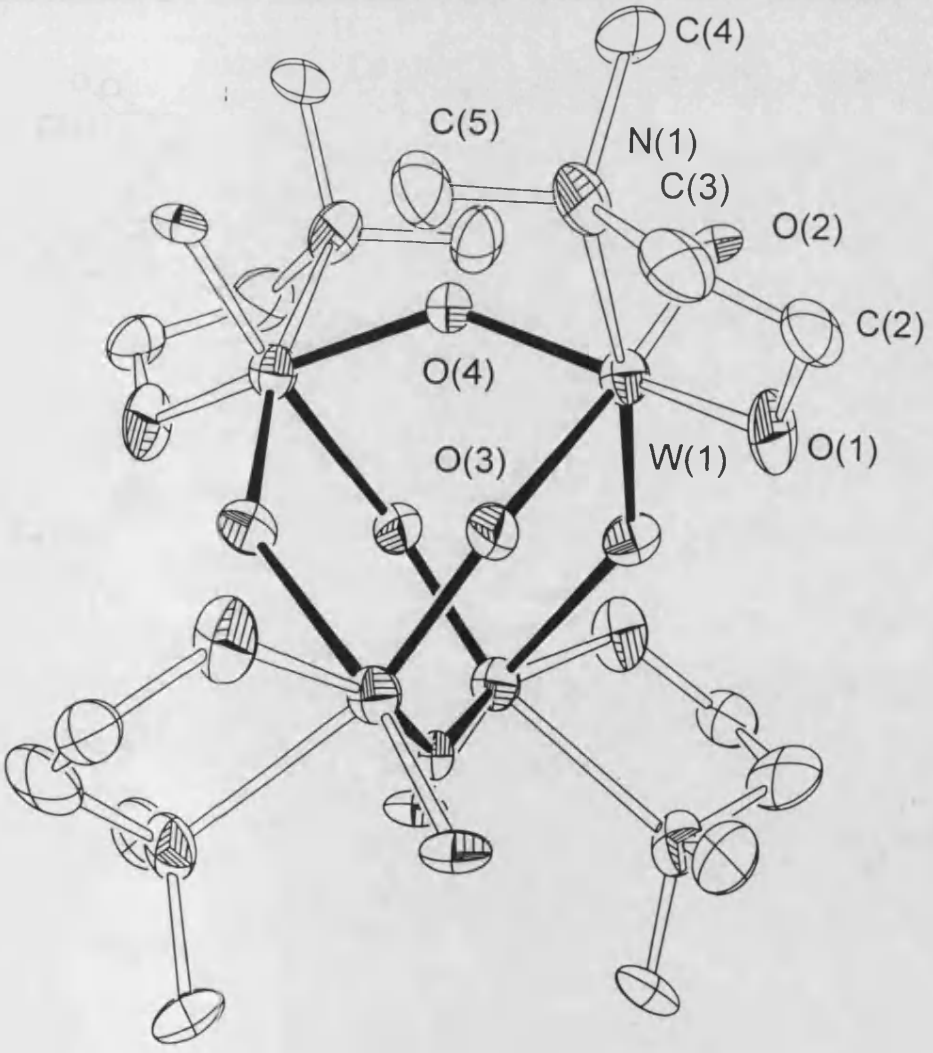

Figure 4.14 Crystal structure of $W_4(O)_4(dmae)_4O_6$ **(8)** showing the W_4O_6 cage.

As can be seen, the structure obtained was a tetranuclear tungsten cage with the tungsten atoms forming a tetrahedron with the oxygen atoms bridging each of the six edges. The tungsten atoms are six co-ordinate with each tungsten atom having a terminal oxygen in addition to the bidentate dmae ligand. The product **(8)** has been formed by partial hydrolysis in which the monodentate iso-propoxide groups have been lost from **(6)** leaving only the chelating dmae ligand. This is the first example of a tetranuclear tungsten cage which is entirely oxo bridged. Two related adamantane-like tungsten structures have previously been reported in the literature. The first was the anion $[(\mu\text{-F})_6(WF_3)_4]^{2-}$ which had bridging fluorine atoms with the W-F-W angles all within the range 141.1(7)-151.5(7)°.[136] The second was the anion $[(\mu\text{-O})_4(\mu\text{-Cl})_4(WCl_2NBu^t)_4]^{2-}$ which has both bridging chlorine and oxygen atoms (Figure 4.15).[137]

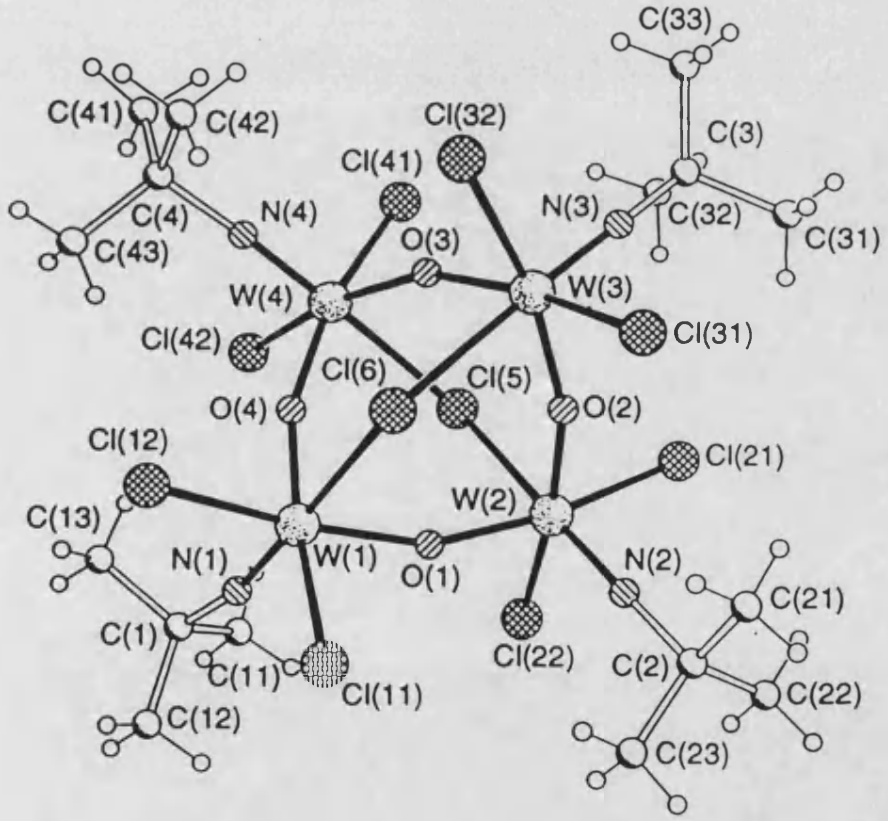

Figure 4.15 Structure of $[(\mu\text{-O})_4(\mu\text{-Cl})_4(WCl_2NBu^t)_4]^{2-}$

The W-Cl-W and W-O-W bond angles for the structure illustrated in Figure 4.15 are between 115.3(1)-115.8(1)° and 157.9(4)-161.3(3)° respectively, the average bridging W-O bond length being 1.88 Å. The *tert*-butylimido groups are *trans* to the bridging chlorides with average W-N bond lengths of 1.70 Å. For the tetranuclear tungsten cage **(8)** the W-O-W bond angle range is between 139.7(4)-144.2(8)° and the average bridging W-O bond length is 1.99 Å. The variation in W-O bond length in **(8)** is between 2.269(9)-1.795(9) Å with the longest W-O bridging bond being *trans* to the terminal W=O bond. The longest bridging W-O bond is also *trans* to the terminal W=O bond in the structures determined for $[W(O)(OMe)_4]_2$ and $[W(O)(OC_6H_{11})_4]_2$.[92] The lengthening of the bridging W-O bond seen in these structures is probably due to the strong π donation from the W=O bond which fills the vacant orbitals on the tungsten atom hence weakening the bond *trans* to the terminal oxygen.

It is interesting to note that the ^1H NMR analysis on **(6)** has suggested the N:→W bond is *trans* to the terminal oxygen, however, in the crystal structure the N:→W is *trans* to a bridging oxygen with a W-N bond length of 2.387(11) Å. This is considerably longer than the tungsten-nitrogen bond length seen in Figure 4.15 and the bond length recorded for $W(NMe_2)_6$ (2.032 Å).[68] However, the W-N bond length recorded for **(8)** is comparable with that found for $WCl_3(=NPh)[OC_6H_2(CH_2NMe)_2$-2,6-Me-4] (Figure 4.16) [2.451(4) Å],[138] as well as other N:→W bond lengths found for tertiary amine dative bonds in tungsten(VI) chemistry.[139] This increase in W-N bond length is consistent with a reduced nitrogen to tungsten π donation which would be expected with the dative bond which has been formed. The W=O terminal bond length is 1.713(8) Å which is similar to the terminal W=O bond lengths seen in $[W(O)(OC_6H_{11})_4]_2$ [1.691(4) Å] and $[W(O)(OMe)_4]_2$ [1.702(7) Å].

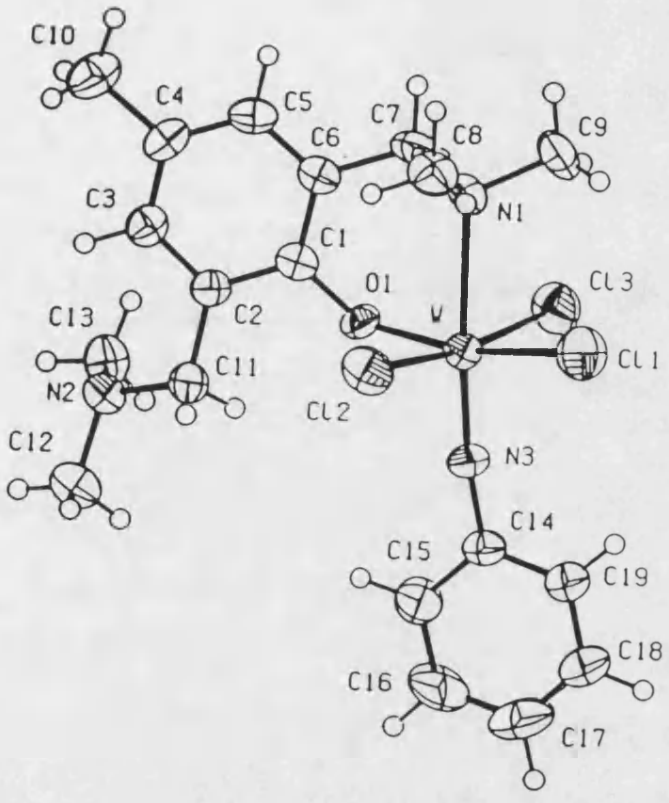

Figure 4.16 ORTEP drawing of $WCl_3(=NPh)[OC_6H_2(CH_2NMe)_2\text{-}2,6\text{-}Me\text{-}4]$.[138]

The tungsten oxo central core in **(8)** has an adamantane like structure which is a thermodynamically stable organic compound (Figure 4.17). There is a wide range of inorganic and organometallic compounds with an adamantane like skeletal structure which have been reviewed by several authors.[140,141,142,143]

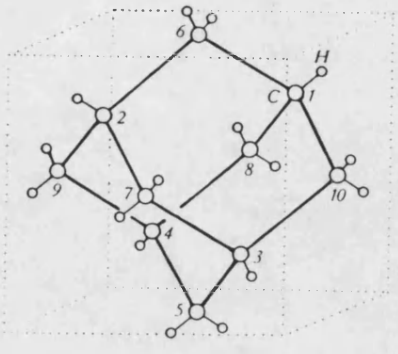

Figure 4.17 Adamantane structure.[144]

As previously mentioned a tetranuclear tungsten compound with exclusively oxo bridges has not been characterised before, however, an example is known for chromium. The chromium complex cation $[(\mu\text{-OH})_6\{Cr(tach)\}_4]^{6+}$ is composed of five adamantane like cages, four from (tach)Cr and the other from a Cr_4O_6 core. Figure 4.18 illustrates the whole molecule whereas the Cr_4O_6 adamantane like core is shown in Figure 4.19.[145]

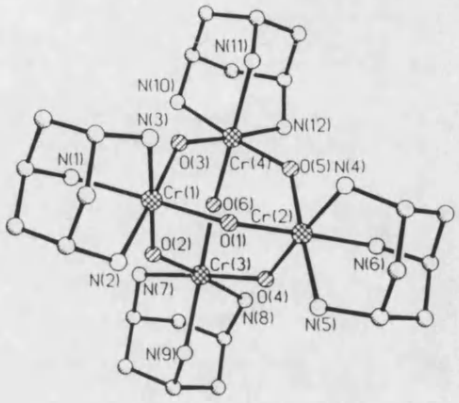

Figure 4.18 Structure of $[(\mu\text{-OH})_6\{Cr(tach)\}_4]$.

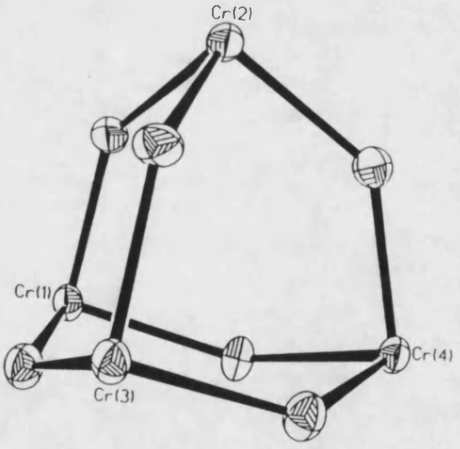

Figure 4.19 Structure of the Cr_4O_6 adamantane like core.[145]

The structure determined during this work appears consistent with the other literature examples examined. The structure also demonstrates that the dmae ligand has replaced one of the OPr^i groups and formed a dative bond from the tertiary amine to the same tungsten centre rather than bridging to an adjacent tungsten atom. The crystal

structure determined supports, in part, the conclusion from the ^{1}H NMR analysis that the most likely configuration of **(6)** is a monomer. The crystal structure obtained could also indicate the first step in the decomposition pathway of **(6)** to give tungsten oxide thin films during the CVD process.

4.6 CVD TESTING OF PRECURSORS

The primary reason for this work was to enhance the volatility of $[W(O)(OPr^i)_4]_2$ by breaking up the alkoxide bridged structure by utilising donor-functionalised alkoxide ligands. This would enable the tungsten atom to achieve its favoured six co-ordinate geometry while being a monomeric molecule. The analysis conducted on **(6)** and **(7)** have indicated that monomeric molecules have been synthesised. The used of donor-functionalized alkoxide ligands has also significantly increased the volatility of the synthesised compounds when compared with $[W(O)(OPr^i)_4]_2$. LPCVD experiments showed temperatures of between 85-90°C at ca. 0.01mmHg were required for sublimation of **(5)**,[42] in contrast, **(6)** and **(7)** were both vacuum distilled at temperatures between 95-115°C at ca. 0.1-0.3mmHg. Thin films from deposition of both these compounds were grown via AACVD, in addition, thin films were also deposited via AACVD from **(5)**.

As described previously, the films were deposited on a 4mm glass substrate undercoated with a thin film of SiCO which acts as a blocking layer to prevent sodium diffusion into the film deposited. The precursors were dissolved in toluene freshly distilled over sodium-benzophenone and transported to the reactor in an aerosol by nitrogen carrier gas. Toluene was chosen as the solvent due to its high boiling point, this would enable the precursors to be transported to the glass substrate with out evaporation of the solvent. In all the deposition experiments carried out in this chapter no additional oxygen was added to the reactive gas stream. Details of the horizontal cold-wall reactor used during these experiments can be found in Appendix 7.

Once deposited, the films were analysed by glancing angle X-ray diffraction to determine their composition, and by SEM to give an indication as to the surface morphology of the films. The transmission-reflectance spectra of the films were also recorded to determine if any selectivity to solar radiation was evident.

4.6.1 Deposition Conditions

AACVD experiments were conducted on three of the compounds (5-7) described in this chapter. All three compounds were aerobically sensitive so the solutions to be nebulised were all handled under nitrogen or argon using standard techniques. Several deposition runs were carried out for each precursor to give a suitable film for analysis. The deposition conditions for the films analysed during this study are given in Table 4.3.

Table 4.3 Summary of Conditions used for AACVD Experiments using **(5)** **(6)** and **(7)**.

Compound	**(5)**	**(6)**	**(6)**	**(7)**	**(7)**
Film ID	r9	r10	r11	r12	r13
Solution concentration gcm^{-3}	0.02	0.01	0.01	0.02	0.01
Reactor temp °C	450	365	400	365	450
Carrier gas (N_2) flow rate $lmin^{-1}$	1.0	0.6	1.0	0.8	1.2
Run time min	30	20	22	17	12

High temperature (≥ 400°C) deposition experiments were conducted on all three compounds synthesised during this study. Low temperature deposition experiments were also conducted on all three compounds synthesised, however, only films from **(6)** and **(7)** are discussed here. Films could be grown from **(5)** at temperatures as low as 260°C, however, since the film deposited at 450°C (r9) was barely crystalline, no analysis has been conducted on the low temperature deposition runs from **(5)**.

4.6.2 Film Analysis

Films r10-13 covered the full length of the glass substrate and had a soft surface layer which could be easily removed with a soft tissue. This left a well adhered blue film with coloured interference fringes clearly visible. The surface layer removed was black in colour and was most likely carbon from the ligands or the solvent used to create the aerosol. While initially blue in colour these films were seen to slowly change colour on standing in the atmosphere. After three to four weeks areas on the edges of the films were yellow in colour although the bulk film was still blue. After 6-8 months the majority of the films were yellow rather than blue in colour, however, the coloured interference fringes were still evident. The glancing angle X-ray diffraction data displayed here was collected several months after the films were deposited, and while the bulk of the films were still blue, areas of yellow on both the films were clearly evident.

Film r9 also had a surface layer which could be easily removed leaving a deep blue film complete with coloured interference fringes. However, this film only covered the first third of the glass substrate as opposed to the whole substrate. The colour of this film appeared stable in the atmosphere and after several months the film was still blue in colour.

4.6.2.1 Glancing Angle X-Ray Diffraction

Glancing angle X-ray diffraction studies were performed to determine if the films deposited were crystalline or amorphous in character and whether tungsten oxide films had been grown. Glancing angle X-ray diffraction also gives an indication as to which phases of tungsten oxide could be present in the films. The X-ray diffraction patterns were obtained by scanning for 40 minutes using standard glancing angle geometry (theta fixed at 1.5 degrees). Peak match software (Appendix 5) was then used to identify the crystalline phases present in the samples.

The glancing angle X-ray diffraction pattern obtained for r9 is displayed in Figure 4.20. As can been seen, the main feature of the pattern is a large hump between 15 and 30° which is indicative of an amorphous component. The amorphous hump could be sampling of the glass substrate. However, the film appeared thick, as indicated by coloured optical interference fringes which were clearly evident from a visual analysis of the film and from subsequent measurement. This indicates that the amorphous hump is most likely a non-crystalline component present in the film and not the glass substrate. There is also some evidence for a low level of crystalline tungsten oxide as indicated by the small peaks on the hump at around 23°, these peaks could correspond to either crystalline stoichiometric WO_3 or non-stoichiometric $WO_{2.9}$. Given the film was deposited in the absence of oxygen, and its intense blue colour, there is certainly some non-stoichiometric $WO_{2.9}$ present in the films composition. Stoichiometric WO_3 could also be present as there is oxygen contained within the molecule which could be incorporated into the film, however, the glancing angle X-ray diffraction clearly indicates that the main component of the film is amorphous. The amorphous nature of this film is perhaps slightly surprising as the film was deposited at a relatively high temperature (450°C). Other films deposited during this work at temperatures in excess of approximately 400°C have been crystalline in nature. It would seem that the precursor as well as the temperature of the glass substrate is important when determining whether a crystalline or amorphous film is deposited for this system.

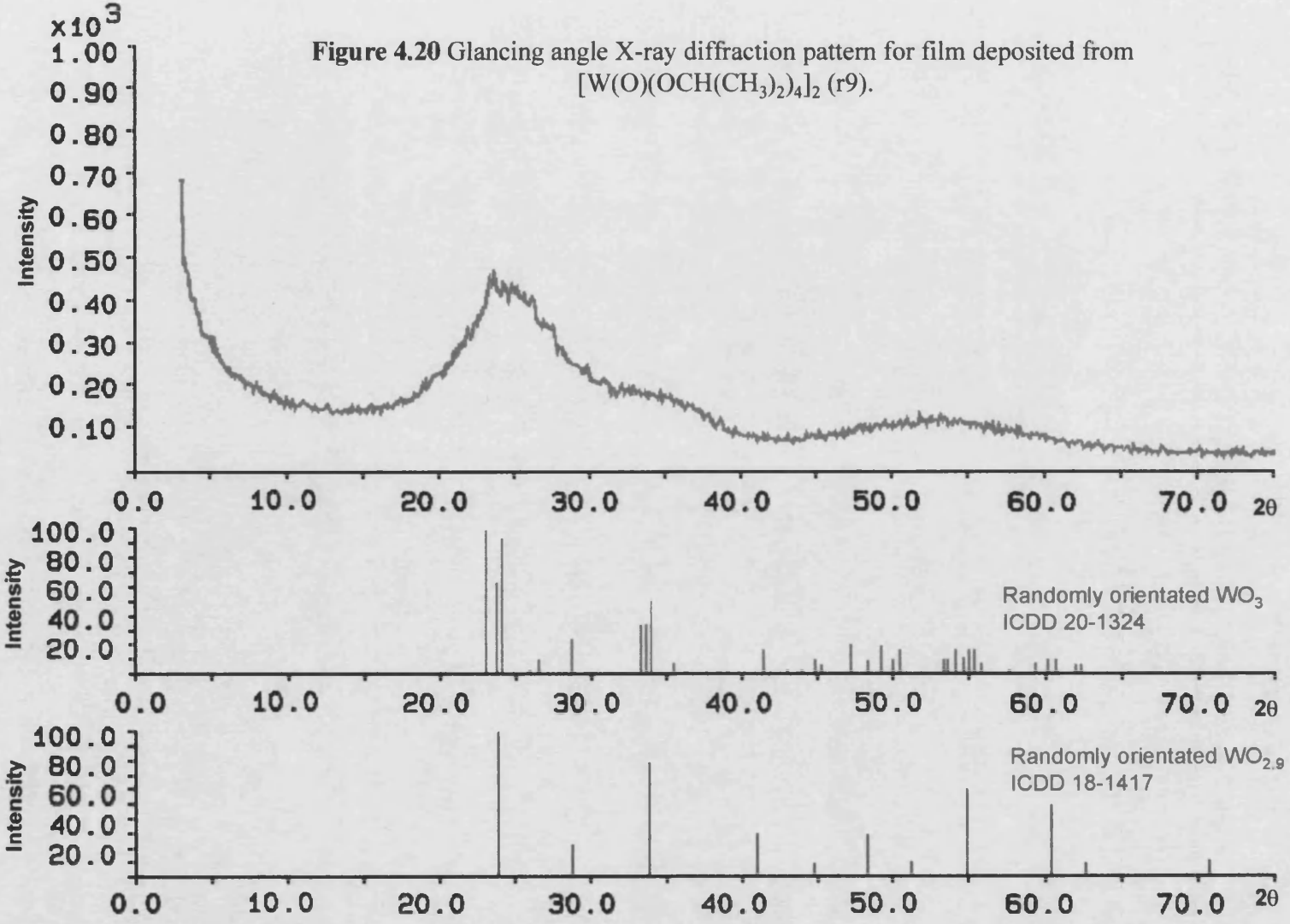

Figure 4.20 Glancing angle X-ray diffraction pattern for film deposited from $[W(O)(OCH(CH_3)_2)_4]_2$ (r9).

The glancing angle X-ray diffraction patterns of the films from the low temperature deposition experiments (r10 and r12) showed the characteristic amorphous hump between 15 and 30° indicating the main component of the film was non-crystalline. However, there was some evidence for a crystalline component present in the film corresponding to non-stoichiometric $WO_{2.9}$. This analysis would seem reasonable as the films were deposited at a relatively low temperature (365°C) and were initially blue in colour which is characteristic of non-stoichiometric WO_{3-x}.

Glancing angle X-ray diffraction of the two high temperature deposition experiments (r11 and r13) gave diffraction patterns which indicated the films were crystalline and composed of tungsten oxide. The diffraction patterns obtained from r11 and r13 are illustrated in Figures 4.21 and 4.22 respectively. Both these diffraction patterns are dominated by a single peak which indicates a highly oriented crystalline structure. The peak match software suggests two possible phases of tungsten oxide could be present, non-stoichiometric $WO_{2.9}$ (ICDD 18-1417) and/or stoichiometric WO_3 (ICDD 20-1324). When deposited the films were intensely blue in colour, characteristic of non-stoichiometric $WO_{2.9}$, however, on standing in the atmosphere over several weeks the blue colour faded on the thinner areas of the films to give a yellow colour, characteristic of stoichiometric WO_3. The glancing angle X-ray diffraction data displayed here was collected several months after the films were deposited, and while the bulk of the films were still blue, areas of yellow on both the films were clearly evident. It is therefore not unreasonable to suggest that the glancing angle X-ray diffraction patterns could contain both $WO_{2.9}$ and WO_3 phases. However, when considering the diffraction patterns the evidence for stoichiometric WO_3 is less convincing. The peak from the reference sample (ICDD 20-1324) which aligns with the main diffraction peak (centre peak from group of three at ca. 23°) is the least intense of the group of three, additionally, no other peaks seen in the reference sample are in the diffraction pattern. The only other peak seen in the diffraction pattern (ca. 48°) is best matched to the corresponding peak in the non-stoichiometric $WO_{2.9}$ reference sample (ICDD 18-1417). Since the films were initially blue in colour, and were deposited in the absence of an oxygen source, both r11 and r13 appear to be entirely non-stoichiometric $WO_{2.9}$ with preferred orientation in the 110 (hkl) plane when first removed from the reactor.

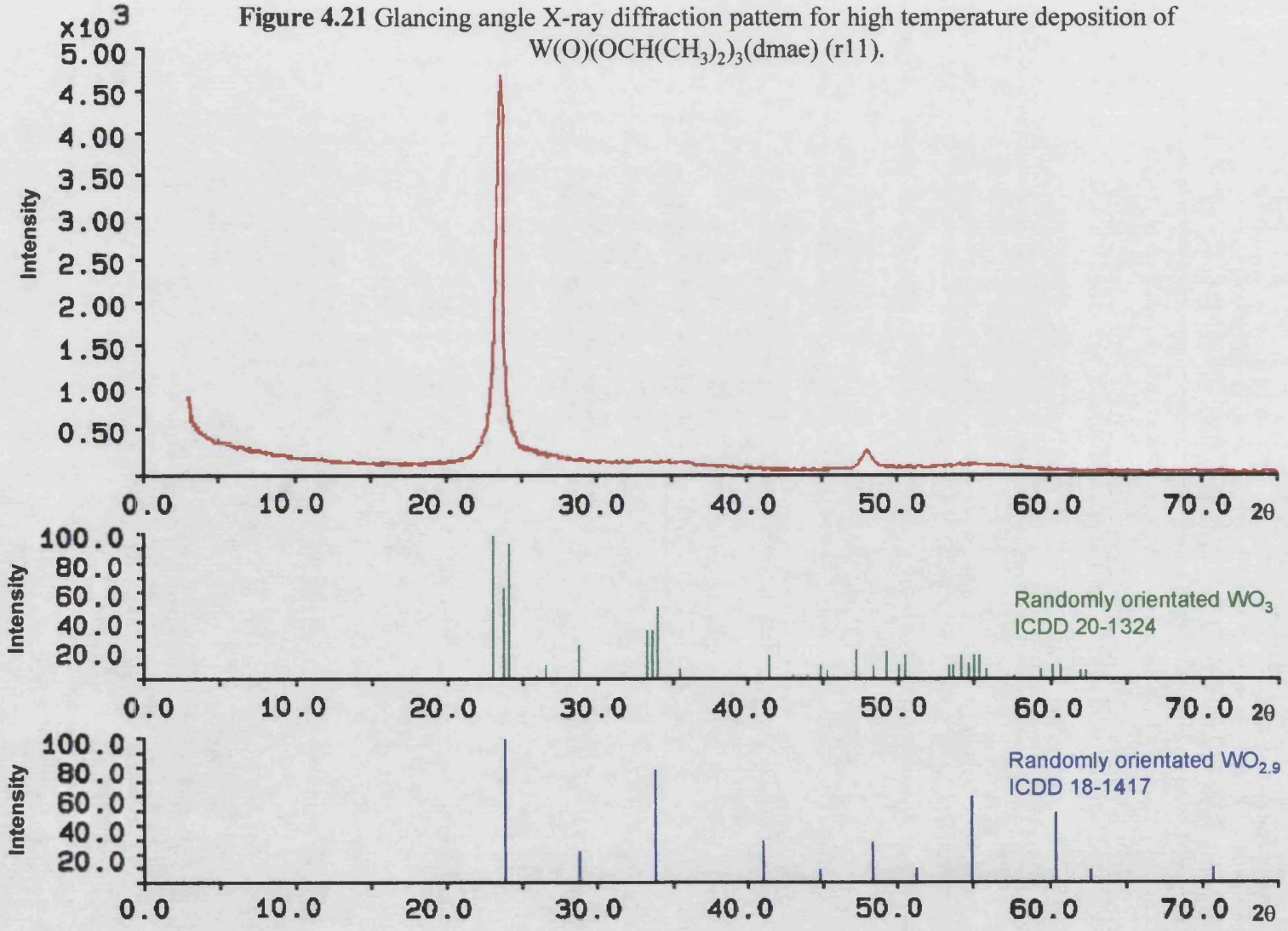

Figure 4.21 Glancing angle X-ray diffraction pattern for high temperature deposition of $W(O)(OCH(CH_3)_2)_3(dmae)$ (r11).

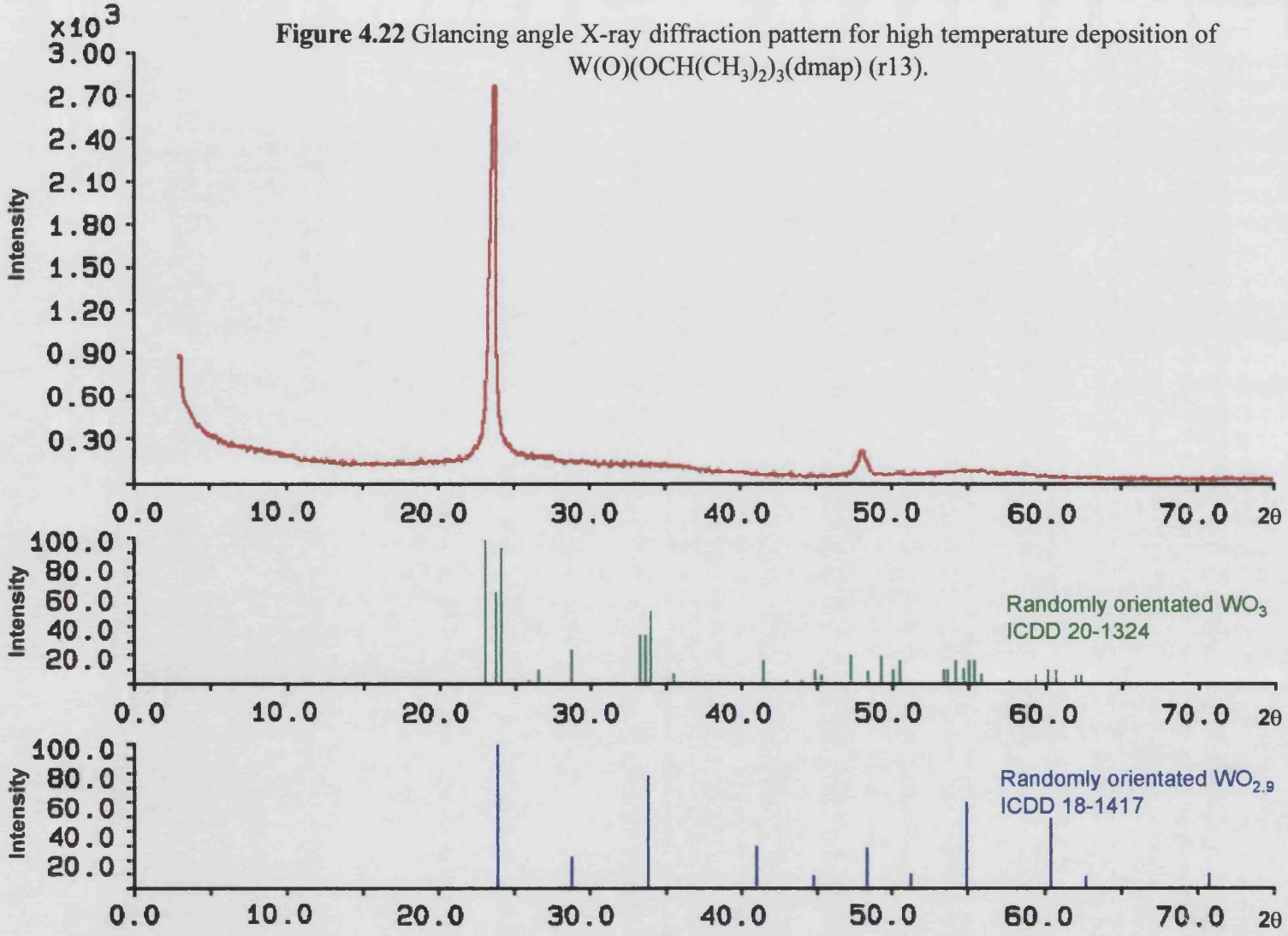

Figure 4.22 Glancing angle X-ray diffraction pattern for high temperature deposition of $W(O)(OCH(CH_3)_2)_3(dmap)$ (r13).

4.6.2.2 SEM

Scanning Electron Microscopy (SEM) was performed in collaboration with Pilkington Glass Ltd on three of the films deposited at high temperature (r9, r11 and r13). The results of these experiments are illustrated in Figures 4.23-4.28.

Figures 4.23 and 4.24 show the film deposited from $[W(O)(OPr^i)_4]_2$ (r9) at a 80° and 90° tilt angle respectively. Figure 4.23 clearly shows the glass substrate surface, the SiCO undercoat and then the tungsten oxide film which has been deposited. The surface of the deposited film appears rough and one could speculate from the surface morphology that the film has grown via an island growth method. The appearance is not entirely as one would expect for an amorphous film, however, the glancing angle X-ray diffraction did indicate a crystalline component within the film. The surface roughness can also be clearly seen in Figure 4.24 which also give an indication as to the thickness of the film.

Figures 4.25 and 4.26 show the film deposited from $W(O)(OCH(CH_3)_2)_3(dmae)$ (r11) from the same angles and magnifications as (r9). As can be clearly seen, the structure and surface morphology of r11 is totally different to that seen in r9, smooth, uniform and no micro-domains. The addition of the dmae ligand has not only enhanced the volatility of **(6)** when compared to **(5)**, but has also deposited a structurally different film. The difference in appearance between r9 and r11 in not that surprising considering the glancing angle X-ray diffraction data and the visual appearance of the two films. The glancing angle X-ray diffraction data showed that r11 was crystalline with a preferred orientation in the 110 plane whereas r9 appeared to be composed of a mainly amorphous component. The visual appearance of the films was also vastly different with r9 covering only the first third of the glass substrate and r11 covering the full substrate. These differences in the films deposited could indicate the different thermal stability characteristics, decomposition temperatures and even decomposition pathways of **(5)** and **(6)**.

Figures 4.27 and 4.28 show the film deposited from $W(O)(OCH(CH_3)_2)_3(dmap)$ r13 from the same angles and magnifications as r9 and r11. The visual appearance of r13 and r11 were similar and the glancing angle X-ray diffraction patterns collected for these films were practically identical, therefore, a similar SEM image would not be a surprise. Figure 4.27 would appear to display greater surface roughness than seen in Figure 4.25. This increase in surface roughness could have been caused from cleaning, transportation or storage of the film rather than a natural feature. However, there appears to be greater structural detail in Figure 4.28 than seen in the corresponding image for r11 (Figure 4.26). This would seem to indicate that the increase of the carbon chain on the functionalised alkoxide could be having a slight effect on the growth of the film.

The 90° SEM images also give an indication as to the thickness of the film deposited. However, it should be remembered that this thickness measurement is at a single point on the film and the films deposited during these experiments were all non-uniform (Table 4.4)

Table 4.4 Approximate film thickness from SEM images.

Film ID	Thickness (Å)
r9	8170 ±300
r11	8500 ±40
r13	3460 ±90

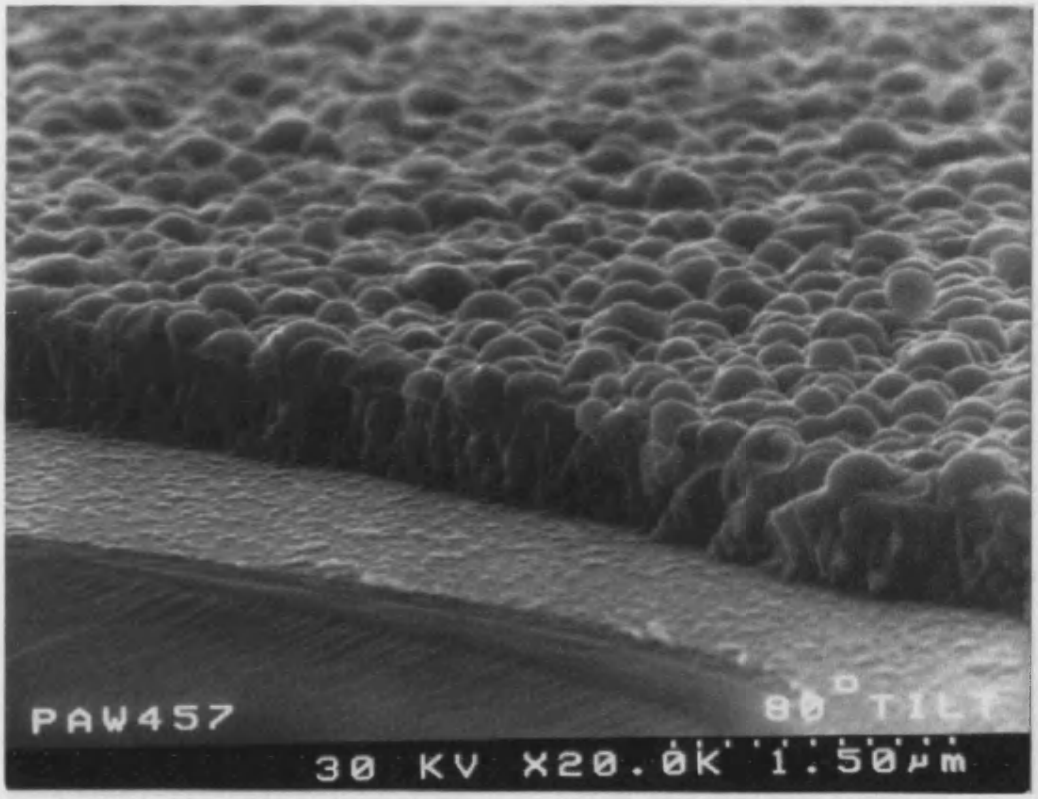

Figure 4.23 80° tilt SEM image from film r9.

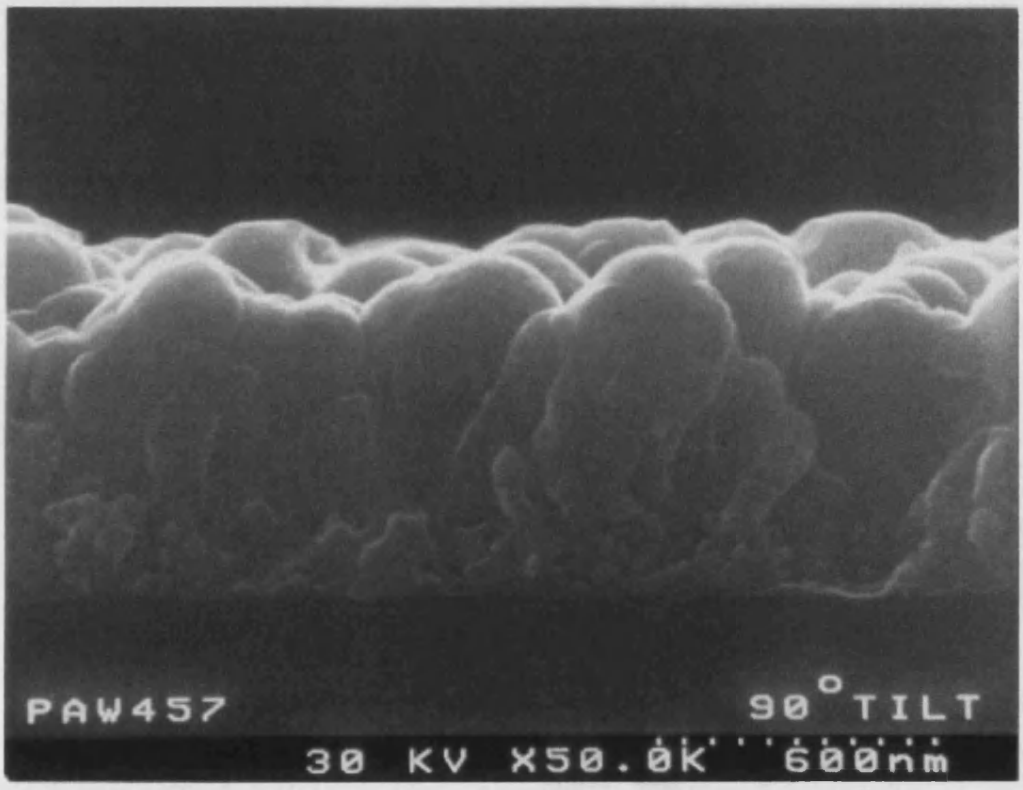

Figure 4.24 90° tilt SEM image from film r9.

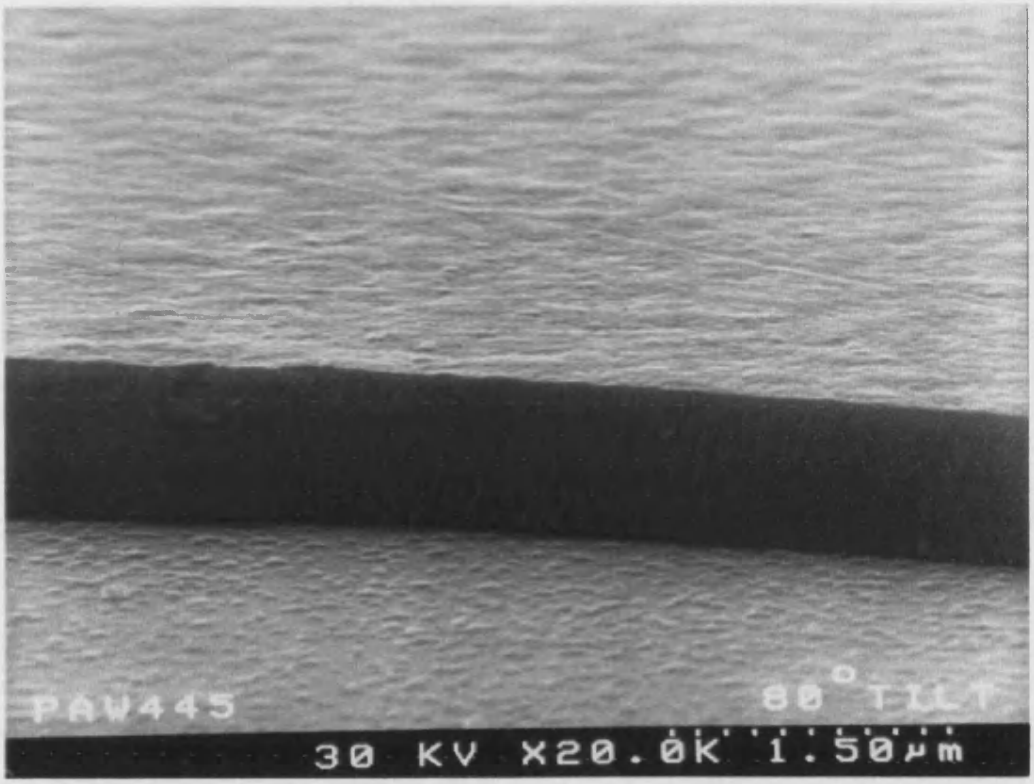

Figure 4.25 80° tilt SEM image from film r11.

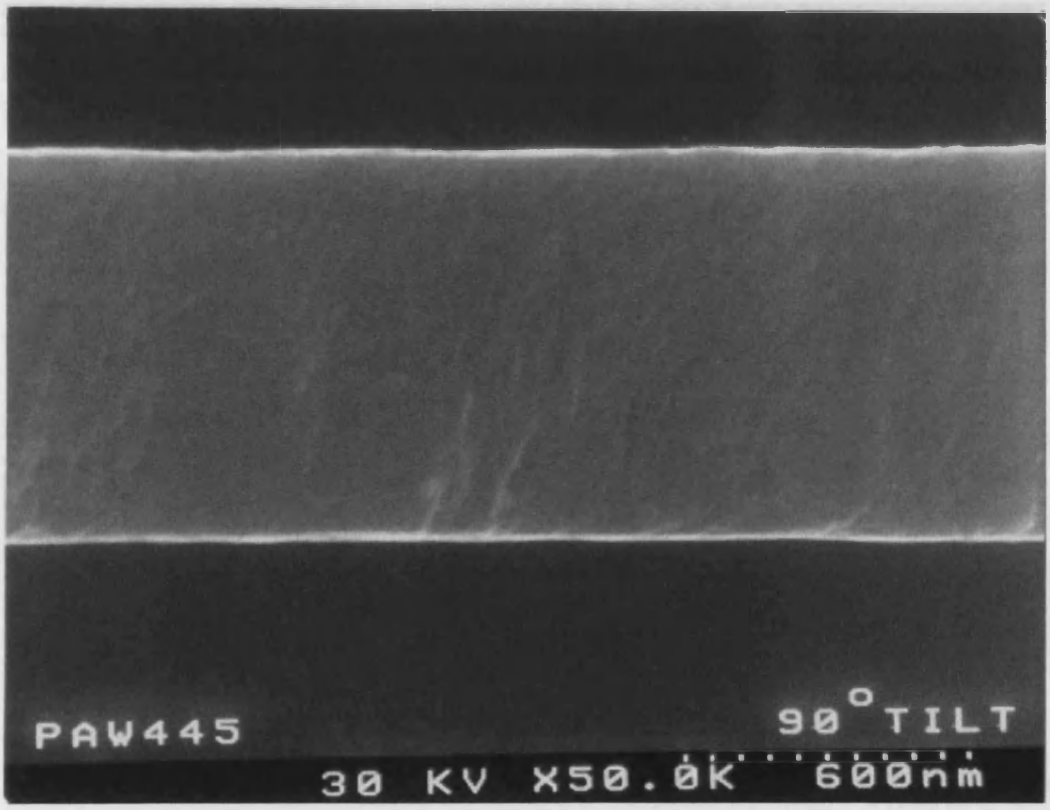

Figure 4.26 90° tilt SEM image from film r11.

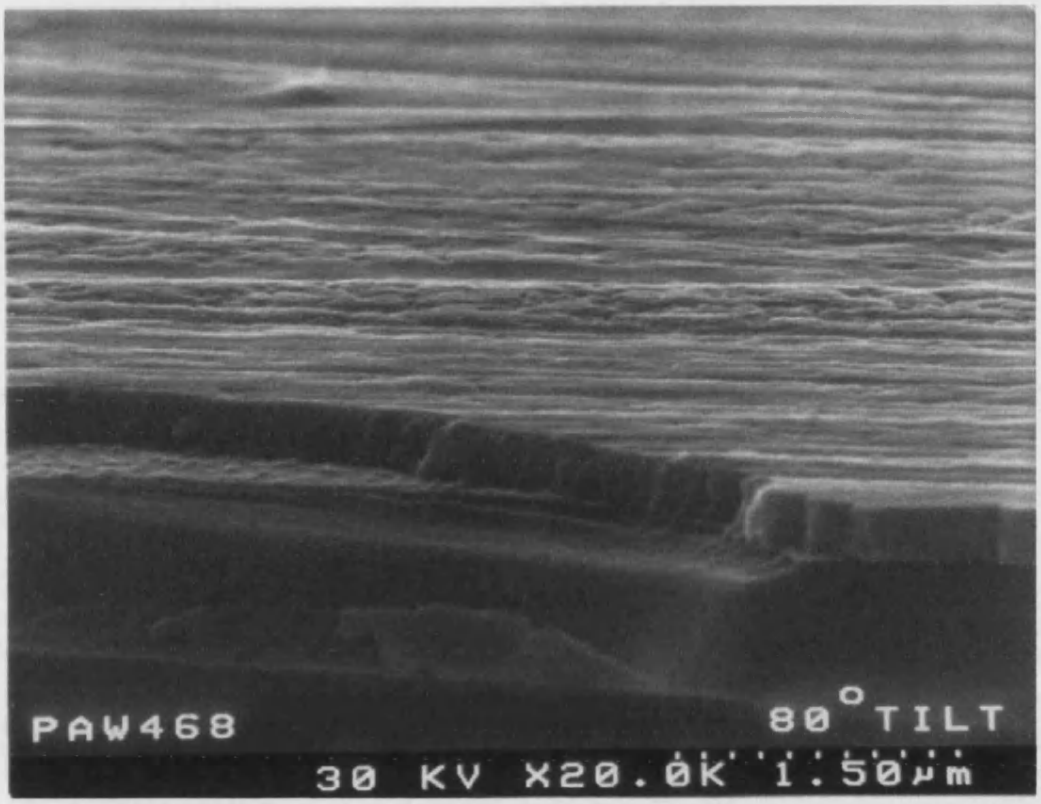

Figure 4.27 80° tilt SEM image from film r13.

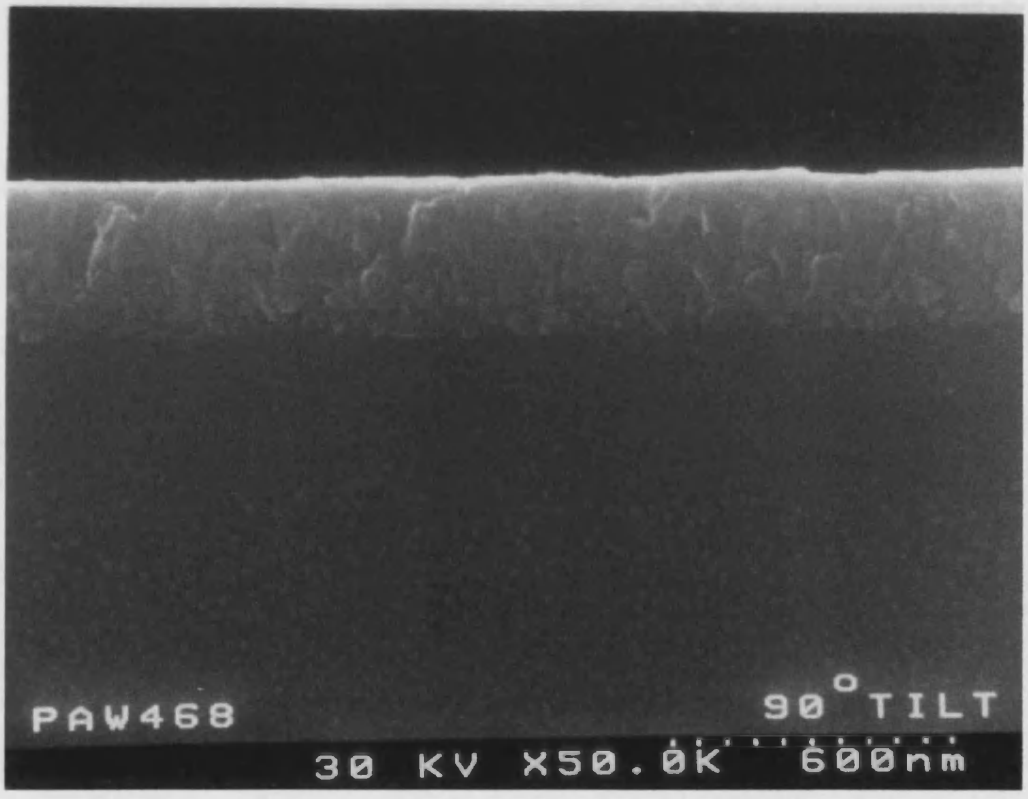

Figure 4.28 90° tilt SEM image from film r13.

4.6.2.3 Transmission-reflectance spectra

The transmission-reflectance spectra were recorded for all five films highlighted in this chapter and are discussed in the following section. As with the spectra illustrated in previous chapters the absorption curve was calculated from the following equation :

$$\text{Absorption} = 100\% - (\text{Transmission} + \text{Reflectance}) \quad [4.3]$$

As with all the films deposited during this work these were deposited on a static cold-walled reactor, therefore, the films are non-uniform over the area measured during the optical analysis performed. This should be remembered when drawing any firm conclusions from the data obtained. The visible region of the solar spectrum is from approximately 350 to 780nm, therefore, to be useful as glazing in the building industry good transmission is required in this region. The infrared portion of the solar spectrum is from approximately 780 to 2000nm. Therefore, for the film to have the potential application of a solar control coating it should either reflect or absorb in this region of the solar spectrum.

Figure 4.29 displays the spectra recorded from r9. SEM analysis has shown the surface of this film to be relatively rough when compared to r11 and r13, however, its thickness is comparable with r11. The transmission of the visible portion of the solar spectrum is poor when compared to films described in other chapters, however, when viewed within the context of this chapter it can be considered typical for the films deposited. The maximum visible transmission is approximately 56% at 460nm, the transmission then falls sharply to a minima of 23% at 1000nm before rising again to 63% at approximately 2350nm. The fall in the transmission of radiation is mirrored by a rise in absorption over the same region demonstrating that the film is absorbing the radiation rather than reflecting it. There is a small rise in the reflectance between 1000-2000nm but only a 10% increase. The region of high absorption and low transmission (590-1600nm) demonstrates that the film is showing some selectivity to the solar spectrum in the infrared region, however, this does extend into the visible portion of the spectrum and the maximum visible transmission is poor.

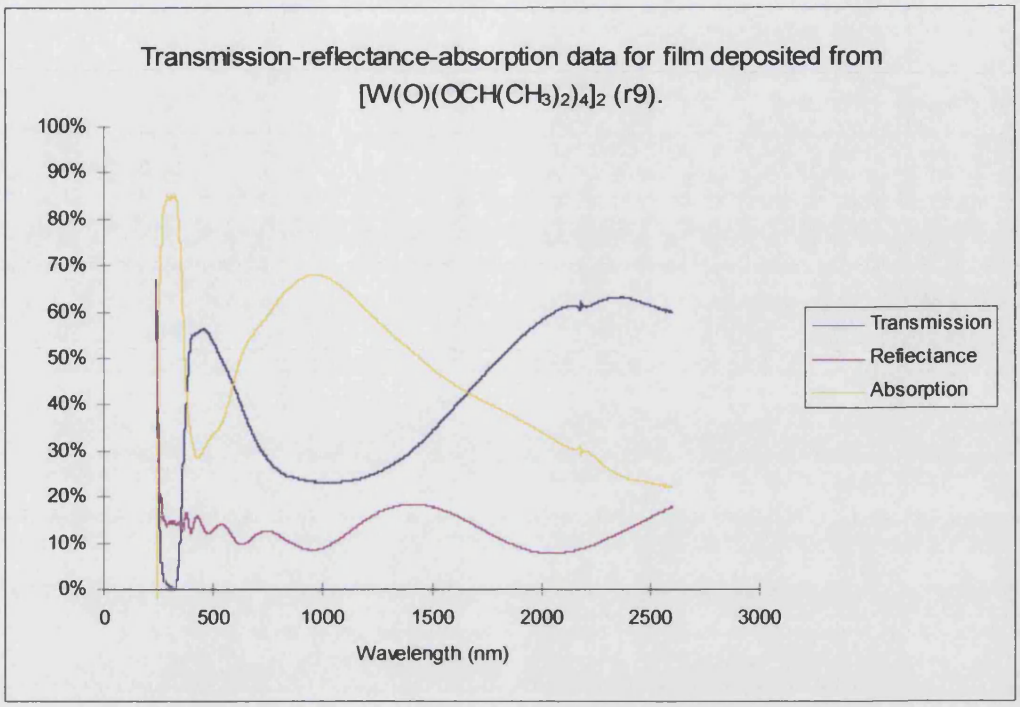

Figure 4.29 Transmission-reflectance-absorption spectra recorded for r9.

The transmission-reflectance-absorption spectra recorded in Figure 4.30 is from the low temperature deposition of **(6)** (r10), therefore, as the film was amorphous no SEM analysis was obtained and the films thickness is not known. The transmission curve is again showing some selectivity to the solar spectrum which is broadly mirrored in the calculated absorption curve. The maximum transmission in the visible region of the solar spectrum was 55% at 550nm, the transmission then falls to a minima of 26% at 1250nm representing a 30% drop in transmitted radiation. The maximum absorption from the film is approximately 64% at 1230nm, this again shows that the majority of the infrared portion of the solar spectrum is being absorbed rather that reflected or transmitted. The reflectance curve is fairly uneventful displaying only a small increase in reflectance at around 800nm. The spectra recorded for this film have again demonstrated that it has some selection in the infrared region of the solar spectrum.

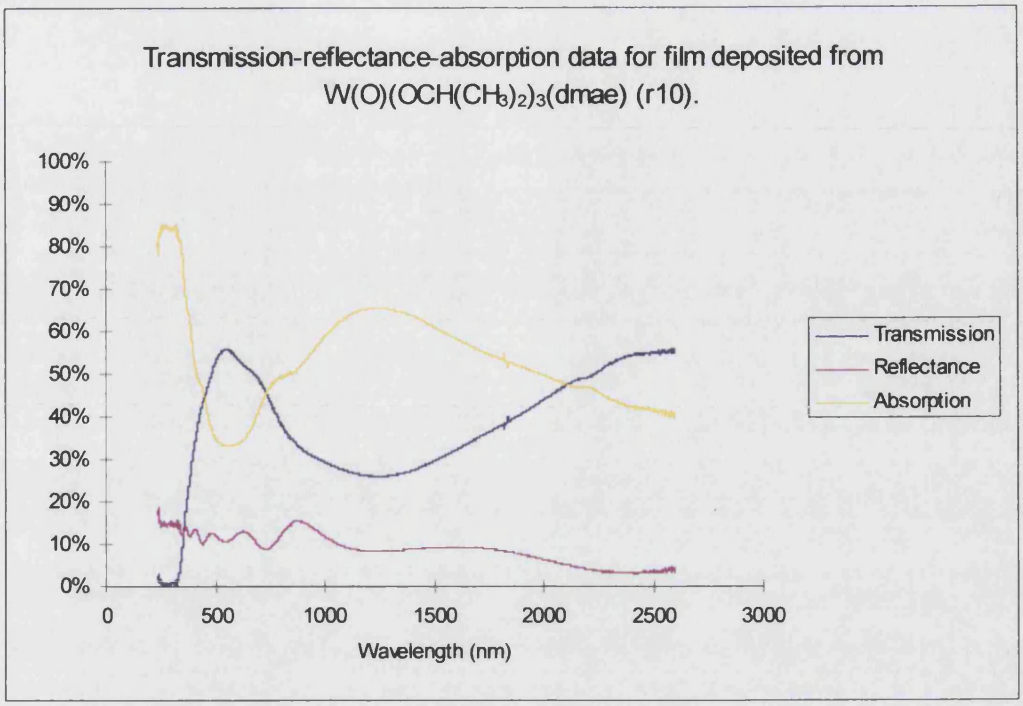

Figure 4.30 Transmission-reflectance-absorption spectra recorded for r10.

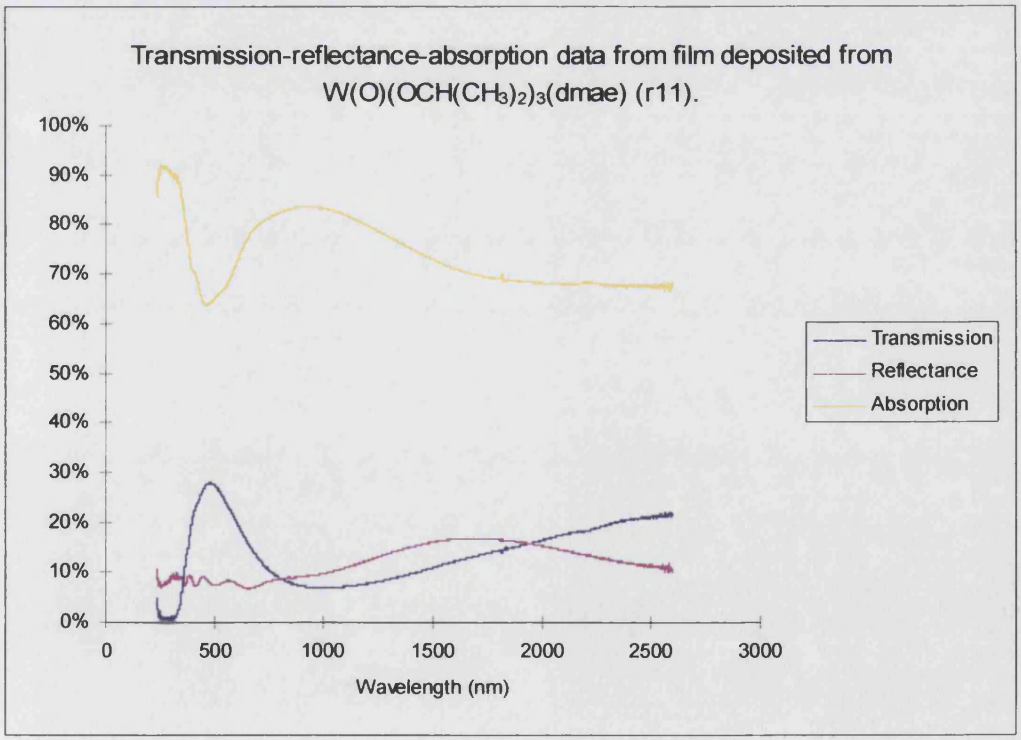

Figure 4.31 Transmission-reflectance-absorption spectra recorded for r11.

The transmission-reflectance-absorption spectra recorded in Figure 4.31 is from the high temperature deposition of **(6)**. As can be seen the film is highly absorbing with the maximum transmission of visible radiation being only 27% at 475nm. This very poor transmission is perhaps to be expected as the SEM analysis had shown the film to be over 8000 Å thick. It should not be forgotten that r9 was also over 8000 Å thick and clearly possesses a much rougher surface, however, it has a maximum transmission in the visible region of 56% at 460nm. This would seem to indicate that factors other than thickness and surface roughness are influencing the transmission-reflectance-absorption properties of the films deposited. The selectivity in the transmission curve over the infrared region of the solar spectrum is mirrored in the calculated absorption curve demonstrating that the coating is absorbing the infrared energy as opposed to reflecting it. When compared to the film deposited at lower temperatures (r10) the transmission and absorption curves behave in a similar fashion as the wavelength increases. The transmission increases in both r10 and r11 from around 1000nm and the absorption decreases as the wavelength increases, this similarity is not seen in the reflectance curve. In r10 the reflectance decreases as the wavelength increases, however, for r11 there is a gradual increase in reflectance from 1000nm at the wavelength increases (r10, 6%; r11, 15% at 2000nm). Despite the relatively poor transmission values from this film the transmission and absorption curves still displays characteristics consistent with solar control applications.

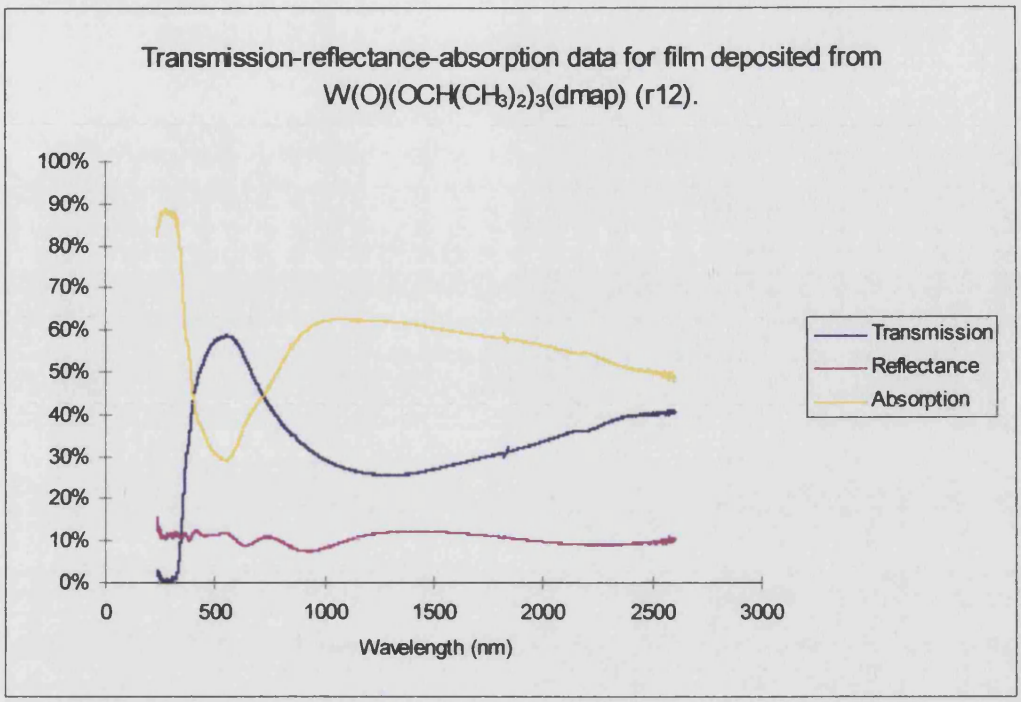

Figure 4.32 Transmission-reflectance-absorption spectra recorded for r12.

The transmission-reflectance-absorption spectra recorded in Figure 4.32 is from the low temperature deposition of **(7)**, as with the previous low temperature film (r11) r12 was also largely amorphous, therefore, no SEM analysis was performed and no thickness data is available. The transmission in the visible region of the solar spectrum was relatively good (58% at 570nm) for the films highlighted in this chapter. The transmission then falls away in the infrared region with minimum transmission of 25% at 1200nm. This reduction in transmitted radiation is mirrored in the calculated absorption curve which demonstrates that the films is absorbing over 60% of the radiation at 1000nm. As with the other films examined during this chapter the transmission and absorption curves indicate that the film has some selectivity in the infrared region of the solar spectrum and could therefore act as a potential solar control coating.

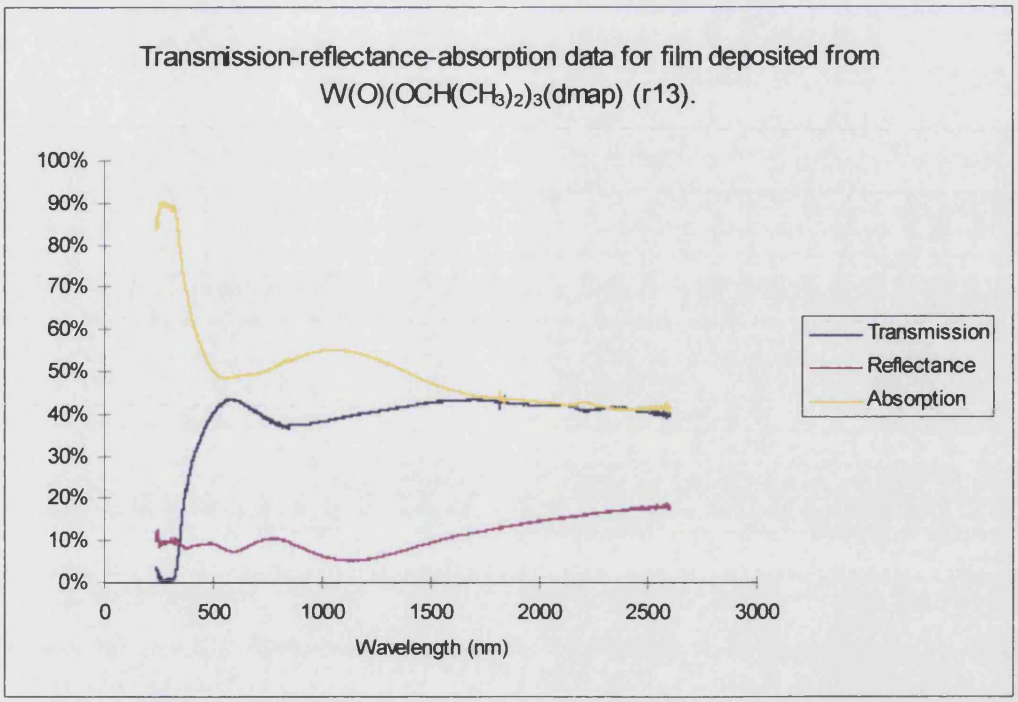

Figure 4.33 Transmission-reflectance-absorption spectra recorded for r13.

The transmission-reflectance-absorption spectra recorded in Figure 4.33 is from the high temperature deposition of **(7)** which deposited a crystalline film which has been characterised by glancing angle X-ray diffraction and SEM. As can be seen from the spectra recorded the transmission the visible region is relatively poor only 43% at 550nm and while there is subsequently a fall in the transmitted radiation it only amounts to a 7% reduction. The absorption curve displays a small increase in the infrared region of the solar spectrum showing the film does have some selectivity to the solar spectrum, however, the properties shown are the most disappointing for the five films deposited.

In summary, this Chapter has detailed the synthesis of two monomeric six co-ordinate tungsten compounds using donor-functionalised alkoxide ligands which have been used to break up the dimeric structure of tungsten(VI) oxotetraalkoxides and hence increase their volatility. The monomeric nature of the synthesised compounds have been confirmed by ^{183}W NMR and ^{1}H VT NMR techniques. Non-stoichiometric tungsten oxide films have been deposited from the synthesised compounds in a single step deposition process via AACVD. These films have subsequently been characterised by

glancing angle X-ray diffraction and have shown some selectivity to solar radiation, however, their transmission of visible light has generally been poor.

4.7 EXPERIMENTAL

All manipulations during this synthesis were carried out under a nitrogen or argon atmosphere using standard Schlenk techniques or in a dry-box fitted with a recirculation system. Tetrahydrofuran, toluene and hexane were dried over and distilled from sodium-benzophenone immediately prior to use and Hdmae, Hdmap and Propan-2-ol were purchased from Aldrich and dried over molecular sieves once opened.

4.6.1 Synthesis of $[W(O)(OPr^i)_4]_2$ (5)

Propan-2-ol (5.35g, 89mmol) was added to a solution of $W(O)Cl_4$ (5.07g, 14.8mmol) in tetrahydrofuran (ca. 120ml) with stirring. Ammonia was bubbled through the solution for approximately 20 minutes. The white precipitate of NH_4Cl was filtered off and the solvent removed from the filtrate under reduced pressure. This was then dissolved in hot toluene (ca. 120ml), filtered, and the solvent removed *in vacuo* to give a white solid. The solid was then washed with hexane and pumped dry. Yield 4.93g (76%).

^1H nmr [δ(ppm), C_6D_6 soln.] : 5.36 [m]; 5.19 [m]; 4.95 [m]; 4.60 [b]; 1.21 [m]; 1.08 [m]; 0.96 [b].

IR data (NaCl plates, nujol mull, cm^{-1}) : 1339, 1164, 1128, 1110, 1022, 981, 852, 767, 762, 665.

4.6.2 Synthesis of W(O)(OCH(CH$_3$)$_2$)$_3$(dmae) (6)

$[W(O)(OPr^i)_4]_2$ (3.30g, 3.78mmol) was dissolved in tetrahydrofuran (ca. 60ml) and two equivalents of Hdmae (0.67g, 7.57mmol) was added with stirring. The solution was then refluxed for 2 hours and allowed to cool. Removal of all volatiles *in vacuo* gave a cloudy yellow oil which was then purified by vacuum distillation (100°C at 0.1-0.2mmHg) to give **(6)** as a clear pale yellow oil. Yield 1.69g (48%).

Analysis : Found (calculated for $C_{13}H_{31}NO_5W$) : C, 33.6 (34.2); H, 6.77 (4.85); N, 4.80 (3.07)%.

^{183}W nmr [δ(ppm), d^8 toluene soln., 20°C] : -88.5, s.

^{1}H nmr [δ(ppm), d^8 toluene soln., 20°C] : 1.36 [18H, m, OCH(C*H*$_3$)$_2$]; 2.39 [6H, s, OCH$_2$CH$_2$N(C*H*$_3$)$_2$]; 2.49 [2H, m, OCH$_2$C*H*$_2$N(CH$_3$)$_2$]; 4.53 [2H, m, OC*H*$_2$CH$_2$N(CH$_3$)$_2$]; 4.95 [3H, m, OC*H*(CH$_3$)$_2$].

^{13}C nmr [δ(ppm), d^8 toluene soln., 20°C] : 23.7 [OCH(*C*H$_3$)$_2$]; 24.1 [OCH(*C*H$_3$)$_2$]; 46.8 [OCH$_2$CH$_2$N(*C*H$_3$)$_2$]; 61.4 [OCH$_2$*C*H$_2$N(CH$_3$)$_2$]; 61.7 [OCH$_2$*C*H$_2$N(CH$_3$)$_2$]; 67.6 [O*C*H$_2$CH$_2$N(CH$_3$)$_2$]; 75.8 [O*C*H(CH$_3$)$_2$]; 76.0 [O*C*H(CH$_3$)$_2$]; 76.1 [O*C*H(CH$_3$)$_2$].

IR data (NaCl plates, cm^{-1}) : 3013, 2966, 2926, 2865, 2817, 2792, 2769, 1455, 1404, 1375, 1376, 1330, 1272, 1256, 1244, 1165, 1113, 1050, 1022, 969, 897, 842, 782, 754, 597.

4.6.3 Synthesis of W(O)(OCH(CH$_3$)$_2$)$_3$(dmap) (7)

(7) was prepared via a similar method to that used for **(6)**. $[W(O)(OPr^i)_4]_2$ (4.00g, 4.59mmol) and two equivalents of Hdmap (0.95g, 9.17mmol) were used in freshly distilled tetrahydrofuran (ca. 60ml). Once the reaction was complete and the

volatiles removed the pure product was obtained by vacuum distillation (98°C at 0.2-0.3 mmHg) in the form of a clear pale yellow oil. Yield 2.15g (49%).

Analysis : Found (calculated for $C_{14}H_{33}NO_5W$) : C, 34.6 (35.0); H, 6.87 (6.94); N, 3.53 (2.92).

^{1}H nmr [δ(ppm), d^8 toluene soln., 21°C] : 1.32 [18H, m, $OCH(CH_3)_2$]; 1.41 [2H, m, $OCH_2CH_2CH_2N(CH_3)_2$]; 2.17 [6H, s, $OCH_2CH_2CH_2N(CH_3)_2$]; 2.31 [2H, m, $OCH_2CH_2CH_2N(CH_3)_2$]; 4.53 [2H, m, $OCH_2CH_2CH_2N(CH_3)_2$]; 5.00 [3H, m, $OCH(CH_3)_2$].

^{13}C nmr [δ(ppm), d^8 toluene soln., 21°C] : 24.6 [$OCH(CH_3)_2$]; 24.9 [$OCH(CH_3)_2$]; 28.1 [$OCH_2CH_2CH_2N(CH_3)_2$]; 48.9 [$OCH_2CH_2CH_2N(CH_3)_2$]; 60.7 [$OCH_2CH_2CH_2N(CH_3)_2$]; 72.1 [$OCH_2CH_2CH_2N(CH_3)_2$]; 76.6 [$OCH(CH_3)_2$].

IR data (NaCl plates, cm^{-1}) : 3015, 2966, 2930, 2864, 2837, 2788, 2722, 1463, 1375, 1369, 1331, 1260, 1244, 1230, 1165, 1109, 1061, 1002, 969, 843, 776, 567.

Conclusions

5 CONCLUSIONS

Three types of tungsten(VI) compounds have been synthesised during this work with the aim of synthesising a precursor that will allow the production of a tungsten oxide thin film on a glass substrate via APCVD in a single step. The compounds synthesised have been fully characterised, and the films deposited analysed by means of glancing angle X-ray diffraction, to determine the composition of the film, SEM, to give an idea as to the surface morphology and transmission-reflectance spectroscopy, to determine if the film has any selectivity to the solar spectrum which could make it useful for solar control applications in the future.

From the compounds synthesised during this work only the five co-ordinate tungsten(VI) fluorinated alkoxide was sufficiently volatile to allow APCVD experiments to be conducted. However, this compound was very air and moisture sensitive and was only synthesised in small quantities which made CVD studies difficult. Films were deposited in the absence of oxygen and with oxygen pre-mixed in the reactive gas flow. Both systems gave crystalline tungsten oxide films, however, the films were of poor quality and while they did show some selectivity to the solar spectrum in the infrared region, the difficulties in synthesis, and the narrow operating window for the CVD process could limit the future use of this class of compound. There are several other fluorinated alkoxide ligands available which could give enhanced volatility, however, a higher yielding synthetic pathway would need to be found if any more than gram scales of the precursor were required.

The best films, from a solar control point of view, were deposited from the tungsten(VI) hexaphenoxides (Chapter two). Tungsten hexaphenoxide and two fluorinated derivatives were synthesised and all were air and moisture stable making handling easy. However, they were not volatile at atmospheric pressure so the films were deposited via AACVD. These films were all blue in colour and transmission-reflectance spectra recorded indicated their potential as solar control coatings. The addition of fluorine to the phenol ring appeared to have little effect on the films

deposited or the volatility of the compounds synthesised. The scope for any further compounds of this class to be synthesised with significantly enhanced volatility would seem limited.

The most encouraging compounds synthesised were those using donor-functionalised alkoxide ligands. The compounds synthesised were not sufficiently volatile to allow APCVD and the films deposited were generally poor with respect to transmission, especially when compared to those deposited from tungsten hexaphenoxides synthesised. However, the films deposited were crystalline with a remarkably smooth morphology and preferred orientation as indicated by glancing angle X-ray diffraction studies. This class of compound, however, remains largely unexplored for tungsten. The compounds were synthesised and purified relatively easily and despite being air and moisture sensitive they were quite stable. Many variations of donor-functionalised alkoxide compounds are known in zirconium, strontium and titanium chemistry, for example. Therefore, the scope for other tungsten(VI) compounds of this type to be synthesised is vast. This should be the area in which any future work in synthesising precursors for the APCVD of tungsten oxide thin films is concentrated.

Appendices

APPENDIX ONE

Crystallographic Analysis and Structural Refinement of $W(OPh)_6$ (1)

A crystal of approximate dimensions 0.25 x 0.25 x 0.3 mm was used for data collection.

Crystal data: C_{36} H_{30} O_6 W, M = 742.45, Monoclinic , a = 13.702(1), b = 16.163(2), c = 13.893(1) Å , β = 90.39(1)°, U = 3076.7(5) Å^3, space group $P2_1/n$, Z = 4, D_c = 1.603 gcm^{-3}, μ(Mo-K_a) = 3.800 mm^{-1}, F(000) = 1472. Crystallographic measurements were made at 293(2) K on a CAD4 automatic four-circle diffractometer in the range $2.08<\theta<23.92°$. Data (4799 reflections) were corrected for Lorentz and polarization and also for absorption.[146] (Max. and Min absorption corrections; 1.000, 0.248 respectively).

In the final least squares cycles all atoms were allowed to vibrate anisotropically. Hydrogen atoms were included at calculated positions where relevant.

The solution of the structure (SHELX86)[147] and refinement (SHELX93)[148] converged to a conventional [i.e. based on 3122 F^2 data with $Fo>4\sigma(Fo)$] $R1$ = 0.0392 and $wR2$ = 0.0952. Goodness of fit = 1.014. The max. and min. residual densities were 0.843 and -1.274 eÅ^{-3} respectively. The asymmetric unit (shown in Figure 2.4), along with the labelling scheme used was produced using ORTEX.[149] Final fractional atomic co-ordinates and isotropic thermal parameters, bond distances and angles are given in Tables A1.2 and A1.3 respectively. Tables of anisotropic temperature factors are available as supplementary data.

Table A1.1 Crystal Data and Structure Refinement for (**1**).

Identification code	97kcm11
Empirical formula	$C_{36}H_{30}O_6W$
Formula weight	742.45
Temperature	293(2) K
Wavelength	0.71069 Å
Crystal system	Monoclinic
Space group	$P2_1/n$
Unit cell dimensions	a = 13.7020(10)Å $\alpha = 90°$
	b = 16.163(2)Å $\beta = 90.390(10)°$
	c = 13.8930(10)Å $\gamma = 90°$
Volume	3076.7(5) $Å^3$
Z	4
Density (calculated)	1.603 Mg/m^3
Absorption coefficient	3.800 mm^1
F(000)	1472
Crystal size	0.25 x 0.25 x 0.3 mm
Theta range for data collection	2.08 to 23.92°.
Index ranges	-15<=h<=15; 0<=k<=18; 0<=l<=15
Reflections collected	4799
Independent reflections	4799 [R(int) = 0.0000]
Reflections observed (>2σ)	3122
Refinement method	Full-matrix least-squares on F^2
Data / restraints / parameters	4786 / 0 / 389
Goodness-of-fit on F^2	1.014
Absorption correction	DIFABS
Max and min absorption corrections	1.000 and 0.248
Final R indices [I>2σ(I)]	R1 = 0.0392 wR2 = 0.0952
R indices (all data)	R1 = 0.0889 wR2 = 0.1254
Largest diff. peak and hole	0.843 and -1.274 $eÅ^{-3}$

Table A1.2 Atomic Co-ordinates (x 10^4) and Equivalent Isotropic Displacement Parameters ($Å^2$ x 10^3) for (**1**).

U(eq) is defined as one third of the trace of the orthogonalized Uij tensor.

Atom	x	y	z	U(eq)
W(1)	93(1)	2426(1)	4179(1)	54(1)
O(1)	-1145(5)	2861(4)	4505(5)	62(2)
O(2)	1350(5)	2023(4)	3921(6)	73(2)
O(3)	-392(5)	1907(4)	3064(5)	67(2)
O(4)	602(5)	2944(4)	5279(5)	72(2)
O(5)	-224(5)	1461(4)	4870(5)	67(2)
O(6)	337(6)	3370(4)	3412(5)	68(2)
C(1)	-1586(8)	3501(6)	4979(7)	59(2)
C(2)	-1129(8)	4231(5)	5191(7)	61(3)
C(3)	-1617(10)	4850(6)	5675(9)	79(3)
C(4)	-2545(10)	4730(7)	5969(8)	73(3)
C(5)	-3022(8)	3991(7)	5774(8)	75(3)
C(6)	-2543(7)	3381(6)	5280(7)	62(2)
C(7)	2304(7)	2178(5)	3750(7)	55(2)
C(8)	2789(10)	1685(7)	3106(8)	77(3)
C(9)	3752(10)	1830(8)	2932(10)	92(4)
C(10)	4249(8)	2473(8)	3363(9)	86(3)
C(11)	3761(9)	2948(8)	4024(9)	87(3)
C(12)	2769(8)	2819(6)	4210(8)	72(3)
C(13)	-440(7)	1210(5)	2518(7)	55(2)
C(14)	75(8)	515(6)	2774(7)	62(2)
C(15)	-27(9)	-187(6)	2205(8)	71(3)
C(16)	-608(10)	-188(7)	1400(9)	84(3)
C(17)	-1090(10)	515(7)	1154(9)	87(4)
C(18)	-1010(8)	1219(6)	1700(8)	71(3)

Atom	x	y	z	U(eq)
C(19)	-1021(8)	1109(5)	5283(7)	60(2)
C(20)	-1398(10)	390(7)	4927(9)	81(3)
C(21)	-2208(11)	47(7)	5388(11)	94(4)
C(22)	-2612(11)	422(10)	6176(11)	100(4)
C(23)	-2200(10)	1130(9)	6528(10)	90(4)
C(24)	-1423(9)	1477(6)	6082(8)	76(3)
C(25)	1082(7)	2847(7)	6138(7)	69(3)
C(26)	1431(10)	2086(9)	6410(12)	106(5)
C(27)	1928(12)	2050(15)	7286(15)	142(9)
C(28)	2089(13)	2665(24)	7864(12)	169(14)
C(29)	1768(14)	3400(18)	7556(12)	149(8)
C(30)	1235(9)	3529(10)	6707(10)	99(4)
C(31)	101(10)	3600(6)	2499(9)	80(3)
C(32)	441(11)	3130(9)	1717(9)	99(4)
C(33)	176(15)	3389(12)	793(10)	124(6)
C(34)	-399(17)	4039(14)	635(15)	150(8)
C(35)	-689(22)	4507(15)	1374(16)	202(13)
C(36)	-438(15)	4278(11)	2343(14)	141(7)

Table A1.3 Bond lengths [Å] and angles [°] for (**1**).

W(1)-O(4)	1.874(7)	O(4)-W(1)-O(1)	88.1(3)
W(1)-O(3)	1.878(6)	O(3)-W(1)-O(1)	92.9(3)
W(1)-O(2)	1.878(7)	O(2)-W(1)-O(1)	176.6(3)
W(1)-O(5)	1.884(6)	O(5)-W(1)-O(1)	88.6(3)
W(1)-O(6)	1.892(6)	O(6)-W(1)-O(1)	89.8(3)
W(1)-O(1)	1.896(6)	C(1)-O(1)-W(1)	142.6(6)
O(1)-C(1)	1.368(11)	C(7)-O(2)-W(1)	149.0(6)
O(2)-C(7)	1.353(11)	C(13)-O(3)-W(1)	147.7(6)
O(3)-C(13)	1.360(10)	C(25)-O(4)-W(1)	146.6(7)
O(4)-C(25)	1.368(12)	C(19)-O(5)-W(1)	138.5(6)
O(5)-C(19)	1.361(12)	C(31)-O(6)-W(1)	134.8(6)
O(6)-C(31)	1.358(13)	C(2)-C(1)-O(1)	123.6(9)
C(1)-C(2)	1.367(13)	C(2)-C(1)-C(6)	119.1(9)
C(1)-C(6)	1.393(14)	O(1)-C(1)-C(6)	117.3(9)
C(2)-C(3)	1.380(14)	C(1)-C(2)-C(3)	120.5(10)
C(3)-C(4)	1.35(2)	C(4)-C(3)-C(2)	120.2(11)
C(4)-C(5)	1.39(2)	C(3)-C(4)-C(5)	120.4(10)
C(5)-C(6)	1.371(14)	C(6)-C(5)-C(4)	119.4(11)
C(7)-C(12)	1.372(13)	C(5)-C(6)-C(1)	120.3(10)
C(7)-C(8)	1.374(14)	O(2)-C(7)-C(12)	120.4(8)
C(8)-C(9)	1.36(2)	O(2)-C(7)-C(8)	118.6(9)
C(9)-C(10)	1.38(2)	C(12)-C(7)-C(8)	121.1(10)
C(10)-C(11)	1.37(2)	C(9)-C(8)-C(7)	119.2(11)
C(11)-C(12)	1.40(2)	C(8)-C(9)-C(10)	122.0(11)
C(13)-C(14)	1.372(13)	C(11)-C(10)-C(9)	118.1(10)
C(13)-C(18)	1.374(14)	C(10)-C(11)-C(12)	121.1(11)
C(14)-C(15)	1.388(14)	C(7)-C(12)-C(11)	118.4(10)
C(15)-C(16)	1.37(2)	O(3)-C(13)-C(14)	120.7(9)
C(16)-C(17)	1.36(2)	O(3)-C(13)-C(18)	118.6(9)
C(17)-C(18)	1.370(14)	C(14)-C(13)-C(18)	120.7(9)

C(19)-C(20)	1.362(14)	C(13)-C(14)-C(15)	118.2(10)
C(19)-C(24)	1.377(14)	C(16)-C(15)-C(14)	121.5(10)
C(20)-C(21)	1.40(2)	C(17)-C(16)-C(15)	118.9(10)
C(21)-C(22)	1.37(2)	C(16)-C(17)-C(18)	121.2(11)
C(22)-C(23)	1.37(2)	C(17)-C(18)-C(13)	119.5(10)
C(23)-C(24)	1.36(2)	O(5)-C(19)-C(20)	120.4(10)
C(25)-C(26)	1.37(2)	O(5)-C(19)-C(24)	119.0(9)
C(25)-C(30)	1.37(2)	C(20)-C(19)-C(24)	120.5(10)
C(26)-C(27)	1.39(2)	C(19)-C(20)-C(21)	118.2(11)
C(27)-C(28)	1.30(3)	C(22)-C(21)-C(20)	121.0(12)
C(28)-C(29)	1.34(3)	C(23)-C(22)-C(21)	119.3(12)
C(29)-C(30)	1.40(2)	C(24)-C(23)-C(22)	120.4(13)
C(31)-C(36)	1.34(2)	C(23)-C(24)-C(19)	120.6(11)
C(31)-C(32)	1.41(2)	O(4)-C(25)-C(26)	120.6(12)
C(32)-C(33)	1.40(2)	O(4)-C(25)-C(30)	118.7(11)
C(33)-C(34)	1.33(2)	C(26)-C(25)-C(30)	120.7(12)
C(34)-C(35)	1.34(3)	C(25)-C(26)-C(27)	117(2)
C(35)-C(36)	1.44(2)	C(28)-C(27)-C(26)	126(2)
		C(27)-C(28)-C(29)	115(2)
O(4)-W(1)-O(3)	178.9(3)	C(28)-C(29)-C(30)	125(2)
O(4)-W(1)-O(2)	88.5(3)	C(25)-C(30)-C(29)	116(2)
O(3)-W(1)-O(2)	90.5(3)	C(36)-C(31)-O(6)	120.3(13)
O(4)-W(1)-O(5)	92.3(3)	C(36)-C(31)-C(32)	120.1(14)
O(3)-W(1)-O(5)	88.2(3)	O(6)-C(31)-C(32)	119.6(11)
O(2)-W(1)-O(5)	91.5(3)	C(33)-C(32)-C(31)	118(2)
O(4)-W(1)-O(6)	91.9(3)	C(34)-C(33)-C(32)	123(2)
O(3)-W(1)-O(6)	87.6(3)	C(33)-C(34)-C(35)	120(2)
O(2)-W(1)-O(6)	90.4(3)	C(34)-C(35)-C(36)	120(2)
O(5)-W(1)-O(6)	175.5(3)	C(31)-C(36)-C(35)	120(2)

Table A1.4 Anisotropic Displacement Parameters ($Å^2 \times 10^3$) for (**1**).

The anisotropic displacement factor exponent takes the form:

$$-2\,pi^2\,[\,h^2\,a^{*2}\,U11 + ... + 2\,h\,k\,a^*\,b^*\,U12\,]$$

Atom	U11	U22	U33	U23	U13	U12
W(1)	53(1)	54(1)	55(1)	-7(1)	0(1)	-1(1)
O(1)	61(4)	59(3)	66(4)	-7(3)	9(3)	2(3)
O(2)	63(5)	65(4)	91(5)	-11(4)	16(4)	-3(3)
O(3)	79(5)	61(4)	62(4)	-13(3)	-7(4)	3(3)
O(4)	82(5)	63(4)	70(5)	-8(3)	-16(4)	6(3)
O(5)	69(5)	55(3)	77(5)	0(3)	1(4)	-6(3)
O(6)	84(5)	61(4)	60(4)	-2(3)	-3(4)	-13(3)
C(1)	65(7)	69(6)	44(5)	0(4)	2(5)	8(5)
C(2)	51(6)	63(5)	69(7)	-7(5)	8(5)	5(4)
C(3)	91(9)	62(6)	84(8)	-8(5)	-11(7)	8(6)
C(4)	88(9)	75(6)	57(7)	-5(5)	7(6)	24(6)
C(5)	66(7)	101(8)	58(7)	10(6)	17(5)	18(6)
C(6)	58(6)	74(6)	55(6)	-7(5)	11(5)	5(5)
C(7)	52(6)	54(4)	60(6)	3(4)	6(4)	10(4)
C(8)	89(9)	83(7)	59(7)	-10(5)	14(6)	-3(6)
C(9)	85(9)	104(9)	88(9)	1(7)	34(7)	14(7)
C(10)	61(6)	103(9)	95(8)	25(7)	25(6)	-9(7)
C(11)	67(7)	118(9)	76(8)	-7(7)	10(6)	-28(7)
C(12)	69(7)	70(6)	76(7)	-17(5)	10(6)	2(5)
C(13)	60(6)	57(5)	48(5)	-8(4)	8(5)	-9(4)
C(14)	61(6)	73(6)	53(6)	-3(4)	5(5)	4(5)
C(15)	83(8)	63(5)	67(7)	-7(5)	9(6)	15(5)
C(16)	100(10)	73(7)	80(8)	-23(6)	-7(7)	2(6)
C(17)	97(9)	97(8)	68(8)	-30(6)	-24(7)	11(7)
C(18)	83(8)	69(6)	63(7)	-12(5)	-16(6)	6(5)

Atom	U11	U22	U33	U23	U13	U12
C(19)	67(7)	51(5)	62(6)	7(4)	-1(5)	3(4)
C(20)	95(9)	72(6)	77(8)	-5(5)	16(7)	-6(6)
C(21)	95(10)	81(7)	106(11)	3(7)	13(9)	-25(7)
C(22)	86(10)	118(10)	98(11)	22(8)	42(8)	-1(8)
C(23)	83(9)	102(9)	86(9)	22(7)	29(7)	10(7)
C(24)	95(9)	65(6)	67(7)	-1(5)	10(6)	1(6)
C(25)	48(6)	104(7)	56(6)	11(6)	4(5)	-8(5)
C(26)	72(9)	109(9)	136(13)	51(9)	-14(8)	-1(7)
C(27)	79(11)	232(23)	115(15)	110(16)	-11(11)	-9(12)
C(28)	74(10)	369(43)	65(10)	64(19)	-20(8)	-20(18)
C(29)	103(14)	278(27)	64(10)	-41(13)	-19(9)	-32(16)
C(30)	69(8)	146(12)	82(9)	-26(8)	-17(7)	-2(8)
C(31)	93(9)	67(6)	80(8)	0(6)	-5(7)	-9(6)
C(32)	108(11)	121(10)	67(8)	4(7)	21(7)	-6(8)
C(33)	156(17)	158(14)	57(8)	-8(9)	11(10)	-42(12)
C(34)	187(22)	159(17)	104(15)	18(13)	-43(14)	28(15)
C(35)	309(36)	190(21)	105(16)	0(15)	-56(19)	127(22)
C(36)	171(19)	134(13)	117(14)	-4(11)	-16(13)	53(13)

Table A1.5 Hydrogen Co-ordinates (x 10^4) and Isotropic Displacement Parameters ($Å^2$ x 10^3) for (**1**).

Atom	x	y	z	U(eq)
H(2)	-485(8)	4312(5)	5007(7)	73
H(3)	-1307(10)	5350(6)	5799(9)	95
H(4)	-2865(10)	5146(7)	6305(8)	88
H(5)	-3660(8)	3910(7)	5977(8)	90
H(6)	-2859(7)	2884(6)	5145(7)	75
H(8)	2464(10)	1256(7)	2792(8)	92
H(9)	4083(10)	1485(8)	2510(10)	110
H(10)	4896(8)	2583(8)	3210(9)	104
H(11)	4095(9)	3362(8)	4354(9)	104
H(12)	2435(8)	3159(6)	4634(8)	86
H(14)	481(8)	513(6)	3313(7)	75
H(15)	306(9)	-667(6)	2376(8)	85
H(16)	-670(10)	-663(7)	1027(9)	101
H(17)	-1483(10)	520(7)	606(9)	105
H(18)	-1338(8)	1698(6)	1519(8)	86
H(20)	-1124(10)	135(7)	4393(9)	98
H(21)	-2476(11)	-444(7)	5156(11)	113
H(22)	-3160(11)	196(10)	6467(11)	120
H(23)	-2454(10)	1376(9)	7078(10)	109
H(24)	-1159(9)	1968(6)	6317(8)	91
H(26)	1341(10)	1619(9)	6029(12)	127
H(27)	2166(12)	1535(15)	7475(15)	171
H(28)	2406(13)	2599(24)	8453(12)	203
H(29)	1909(14)	3860(18)	7934(12)	179
H(30)	997(9)	4049(10)	6538(10)	119
H(32)	827(11)	2663(9)	1813(9)	118
H(33)	410(15)	3095(12)	267(10)	149

Atom	x	y	z	U(eq)
H(34)	-599(17)	4167(14)	12(15)	181
H(35)	-1055(22)	4982(15)	1259(16)	242
H(36)	-649(15)	4598(11)	2857(14)	169

APPENDIX TWO

Crystallographic Analysis and Structural Refinement of $W(OC_6H_4F)_6$ (2)

A crystal of approximate dimensions 0.5 x 0.4 x 0.4 mm was used for data collection.

Crystal data: $C_{36}\ H_{24}\ F_6\ O_6\ W$, M = 850.40, Monoclinic , a = 14.086(3), b = 16.863(4), c = 14.205(4) Å , β = 103.37(2)°, U = 3282.7(14) Å^3, space group $P2_1/n$, Z = 4, D_c = 1.721 gcm^{-3}, μ(Mo-K_a) = 3.599 mm^{-1}, F(000) = 1664. Crystallographic measurements were made at 293(2) K on a CAD4 automatic four-circle diffractometer in the range $2.19<\theta<23.93°$. Data (5121 reflections) were corrected for Lorentz and polarization and also for absorption.[146] (Max. and Min absorption corrections; 1.000, 0.178 respectively).

The larger than average crystal used was the second one selected from the sample as measurements on the first smaller crystal indicated that this material did not diffract strongly at higher Bragg angles.

In the final least squares cycles all atoms were allowed to vibrate anisotropically. Hydrogen atoms were included at calculated positions where relevant.

The solution of the structure (SHELX86)[147] and refinement (SHELX93)[148] converged to a conventional [i.e. based on 2723 F^2 data with $Fo>4\sigma(Fo)$] $R1$ = 0.0580 and $wR2$ = 0.1448. Goodness of fit = 0.931. The max. and min. residual densities were 0.730 and -1.044 eÅ^{-3} respectively. The asymmetric unit (shown in Figure 2.5), along with the labelling scheme used was produced using ORTEX.[149] Final fractional atomic co-ordinates and isotropic thermal parameters, bond distances and angles are given in Tables A2.2 and A2.3 respectively. Tables of anisotropic temperature factors are available as supplementary data.

Table A2.1 Crystal data and structure refinement for (**2**).

Identification code	98kcm4/p.williams
Empirical formula	$C_{36}H_{24}F_6O_6W$
Formula weight	850.40
Temperature	293(2) K
Wavelength	0.70930 Å
Crystal system	Monoclinic
Space group	$P2_1/n$
Unit cell dimensions	a = 14.086(3)Å $\alpha = 90°$
	b = 16.863(4)Å $\beta = 103.37(2)°$
	c = 14.205(4)Å $\gamma = 90°$
Volume	3282.7(14) $Å^3$
Z	4
Density (calculated)	1.721 Mg/m^3
Absorption coefficient	3.599 mm^{-1}
F(000)	1664
Crystal size	0.5 x 0.4 x 0.4 mm
Theta range for data collection	2.19 to 23.93 °.
Index ranges	-16<=h<=15; 0<=k<=19; 0<=l<=16
Reflections collected	5121
Independent reflections	5121 [R(int) = 0.0000]
Absorption correction	DIFABS
Max. and min. transmission	1.000 and 0.178
Refinement method	Full-matrix least-squares on F^2
Data / restraints / parameters	5117 / 0 / 443
Goodness-of-fit on F^2	0.931
Final R indices [$I>2\sigma(I)$]	R1 = 0.0580 wR2 = 0.1448
R indices (all data)	R1 = 0.1321 wR2 = 0.1737
Largest diff. peak and hole	0.730 and -1.044 $eÅ^{-3}$
Weighting scheme	calc $w=1/[\sigma^2(Fo^2)+(0.0963P)^2+0.0000P]$ where
	$P=(Fo^2+2Fc^2)/3$
Extinction coefficient	0.0003(3)
Extinction expression	$Fc^*=kFc[1+0.001xFc^2\lambda^3/\sin(2\theta)]^{-1/4}$

Table A2.2 Atomic Co-ordinates (x 10^4) and Equivalent Isotropic Displacement Parameters ($Å^2$ x 10^3) for (**2**).

U(eq) is defined as one third of the trace of the orthogonalized Uij tensor.

Atom	x	y	z	U(eq)
W(1)	2061(1)	837(1)	4027(1)	67(1)
F(1)	4977(7)	1950(6)	842(7)	126(3)
F(2)	4670(7)	-2742(5)	4014(7)	120(3)
F(3)	-2952(6)	1808(6)	3509(8)	143(4)
F(4)	-1315(8)	-1428(7)	666(7)	156(4)
F(5)	2256(8)	4943(5)	4731(8)	140(4)
F(6)	4339(8)	499(8)	8943(7)	166(5)
O(1)	2317(5)	861(5)	2764(6)	78(2)
O(2)	3155(6)	171(5)	4436(6)	75(2)
O(3)	925(5)	1448(5)	3686(7)	76(2)
O(4)	1253(6)	-64(5)	3651(6)	82(3)
O(5)	2852(5)	1769(5)	4271(7)	83(3)
O(6)	1950(6)	811(5)	5346(6)	77(2)
C(1)	2995(9)	1140(7)	2295(9)	67(3)
C(2)	3959(8)	1024(8)	2646(10)	84(4)
C(3)	4631(10)	1288(9)	2163(12)	91(5)
C(4)	4286(12)	1678(9)	1319(13)	91(5)
C(5)	3337(12)	1824(9)	941(11)	98(5)
C(6)	2666(9)	1535(7)	1420(11)	77(4)
C(7)	3506(8)	-561(8)	4290(10)	67(3)
C(8)	4165(8)	-915(8)	5086(9)	71(3)
C(9)	4548(10)	-1654(8)	4961(12)	83(4)
C(10)	4283(10)	-2023(9)	4106(13)	83(4)
C(11)	3638(11)	-1721(8)	3323(11)	86(4)
C(12)	3266(10)	-974(8)	3445(10)	84(4)

Atom	x	y	z	U(eq)
C(13)	-43(8)	1533(7)	3677(10)	71(3)
C(14)	-450(9)	1158(7)	4307(10)	71(4)
C(15)	-1439(11)	1253(9)	4257(11)	87(4)
C(16)	-1973(10)	1723(9)	3564(12)	87(4)
C(17)	-1571(10)	2115(11)	2921(14)	133(8)
C(18)	-591(11)	2003(10)	3008(14)	120(6)
C(19)	609(8)	-372(8)	2890(10)	67(3)
C(20)	210(9)	57(9)	2065(10)	77(4)
C(21)	-405(10)	-294(10)	1305(10)	84(4)
C(22)	-660(11)	-1048(13)	1392(14)	110(7)
C(23)	-265(12)	-1522(10)	2180(13)	100(5)
C(24)	376(10)	-1167(9)	2956(11)	81(4)
C(25)	2617(9)	2572(8)	4404(9)	70(3)
C(26)	3216(10)	3100(9)	3985(10)	85(4)
C(27)	3053(12)	3920(10)	4125(12)	101(5)
C(28)	2375(12)	4144(10)	4626(13)	99(5)
C(29)	1839(12)	3608(10)	5030(13)	107(6)
C(30)	2011(11)	2850(9)	4910(11)	100(5)
C(31)	2582(9)	747(7)	6218(10)	69(3)
C(32)	3580(10)	914(8)	6395(10)	89(4)
C(33)	4154(10)	837(9)	7335(11)	90(4)
C(34)	3743(11)	587(12)	8022(11)	108(6)
C(35)	2792(11)	397(12)	7941(11)	114(6)
C(36)	2191(10)	485(10)	7019(11)	97(5)

Table A2.3 Bond lengths [Å] and angles [°] for (**2**).

W(1)-O(3)	1.871(8)	C(9)-C(10)	1.34(2)
W(1)-O(2)	1.887(8)	C(10)-C(11)	1.36(2)
W(1)-O(4)	1.899(8)	C(11)-C(12)	1.39(2)
W(1)-O(1)	1.910(8)	C(13)-C(14)	1.33(2)
W(1)-O(5)	1.912(8)	C(13)-C(18)	1.34(2)
W(1)-O(6)	1.916(8)	C(14)-C(15)	1.39(2)
F(1)-C(4)	1.39(2)	C(15)-C(16)	1.35(2)
F(2)-C(10)	1.35(2)	C(16)-C(17)	1.35(2)
F(3)-C(16)	1.370(14)	C(17)-C(18)	1.37(2)
F(4)-C(22)	1.37(2)	C(19)-C(20)	1.38(2)
F(5)-C(28)	1.37(2)	C(19)-C(24)	1.39(2)
F(6)-C(34)	1.39(2)	C(20)-C(21)	1.35(2)
O(1)-C(1)	1.368(14)	C(21)-C(22)	1.34(2)
O(2)-C(7)	1.363(14)	C(22)-C(23)	1.38(2)
O(3)-C(13)	1.367(13)	C(23)-C(24)	1.39(2)
O(4)-C(19)	1.345(14)	C(25)-C(30)	1.32(2)
O(5)-C(25)	1.416(14)	C(25)-C(26)	1.45(2)
O(6)-C(31)	1.353(14)	C(26)-C(27)	1.42(2)
C(1)-C(2)	1.35(2)	C(27)-C(28)	1.37(2)
C(1)-C(6)	1.39(2)	C(28)-C(29)	1.38(2)
C(2)-C(3)	1.37(2)	C(29)-C(30)	1.32(2)
C(3)-C(4)	1.36(2)	C(31)-C(32)	1.40(2)
C(4)-C(5)	1.34(2)	C(31)-C(36)	1.44(2)
C(5)-C(6)	1.37(2)	C(32)-C(33)	1.40(2)
C(7)-C(12)	1.36(2)	C(33)-C(34)	1.31(2)
C(7)-C(8)	1.42(2)	C(34)-C(35)	1.36(2)
C(8)-C(9)	1.38(2)	C(35)-C(36)	1.39(2)

O(3)-W(1)-O(2)	175.3(3)	C(7)-C(12)-C(11)	123.3(14)
O(3)-W(1)-O(4)	87.0(4)	C(14)-C(13)-C(18)	119.5(12)
O(2)-W(1)-O(4)	90.2(4)	C(14)-C(13)-O(3)	121.9(12)
O(3)-W(1)-O(1)	94.6(4)	C(18)-C(13)-O(3)	118.6(12)
O(2)-W(1)-O(1)	89.0(3)	C(13)-C(14)-C(15)	119.7(13)
O(4)-W(1)-O(1)	89.1(4)	C(16)-C(15)-C(14)	119.3(13)
O(3)-W(1)-O(5)	91.2(4)	C(15)-C(16)-C(17)	122.0(13)
O(2)-W(1)-O(5)	91.9(4)	C(15)-C(16)-F(3)	119.1(14)
O(4)-W(1)-O(5)	174.3(4)	C(17)-C(16)-F(3)	119(2)
O(1)-W(1)-O(5)	85.7(4)	C(16)-C(17)-C(18)	116.3(14)
O(3)-W(1)-O(6)	90.5(4)	C(13)-C(18)-C(17)	123.3(14)
O(2)-W(1)-O(6)	86.0(4)	O(4)-C(19)-C(20)	123.1(13)
O(4)-W(1)-O(6)	94.5(4)	O(4)-C(19)-C(24)	116.4(13)
O(1)-W(1)-O(6)	173.9(3)	C(20)-C(19)-C(24)	120.5(14)
O(5)-W(1)-O(6)	90.9(4)	C(21)-C(20)-C(19)	120.5(14)
C(1)-O(1)-W(1)	140.3(8)	C(22)-C(21)-C(20)	119(2)
C(7)-O(2)-W(1)	142.4(8)	C(21)-C(22)-F(4)	122(2)
C(13)-O(3)-W(1)	148.3(8)	C(21)-C(22)-C(23)	124(2)
C(19)-O(4)-W(1)	141.7(8)	F(4)-C(22)-C(23)	114(2)
C(25)-O(5)-W(1)	131.8(7)	C(22)-C(23)-C(24)	117(2)
C(31)-O(6)-W(1)	135.5(8)	C(19)-C(24)-C(23)	119(2)
C(2)-C(1)-O(1)	121.8(11)	C(30)-C(25)-O(5)	127.6(13)
C(2)-C(1)-C(6)	119.9(12)	C(30)-C(25)-C(26)	121.1(14)
O(1)-C(1)-C(6)	118.3(11)	O(5)-C(25)-C(26)	111.0(11)
C(1)-C(2)-C(3)	121.5(12)	C(27)-C(26)-C(25)	114.3(14)
C(4)-C(3)-C(2)	117.0(13)	C(28)-C(27)-C(26)	119.8(14)
C(5)-C(4)-C(3)	124.2(14)	C(27)-C(28)-F(5)	117(2)
C(5)-C(4)-F(1)	119.4(14)	C(27)-C(28)-C(29)	123(2)
C(3)-C(4)-F(1)	116.4(14)	F(5)-C(28)-C(29)	120(2)
C(4)-C(5)-C(6)	118.2(14)	C(30)-C(29)-C(28)	116(2)
C(5)-C(6)-C(1)	119.0(13)	C(29)-C(30)-C(25)	125(2)

C(12)-C(7)-O(2)	124.9(13)	O(6)-C(31)-C(32)	124.7(12)
C(12)-C(7)-C(8)	118.1(13)	O(6)-C(31)-C(36)	117.2(11)
O(2)-C(7)-C(8)	117.0(12)	C(32)-C(31)-C(36)	118.1(12)
C(9)-C(8)-C(7)	118.6(13)	C(31)-C(32)-C(33)	119.3(14)
C(10)-C(9)-C(8)	120.0(14)	C(34)-C(33)-C(32)	118.8(14)
C(9)-C(10)-F(2)	118(2)	C(33)-C(34)-C(35)	128(2)
C(9)-C(10)-C(11)	124.1(14)	C(33)-C(34)-F(6)	117.4(14)
F(2)-C(10)-C(11)	118(2)	C(35)-C(34)-F(6)	115(2)
C(10)-C(11)-C(12)	115.9(14)	C(34)-C(35)-C(36)	115.4(14)
		C(35)-C(36)-C(31)	121.0(13)

Table A2.4 Anisotropic Displacement Parameters ($Å^2$ x 10^3) for (**2**).

The anisotropic displacement factor exponent takes the form:

$-2\ pi^2\ [\ h^2\ a^*\ 2\ U11 + ... + 2\ h\ k\ a^*\ b^*\ U12\ ]$

Atom	**U11**	**U22**	**U33**	**U23**	**U13**	**U12**
W(1)	67(1)	67(1)	67(1)	3(1)	15(1)	3(1)
F(1)	130(7)	128(8)	133(8)	15(6)	60(6)	-28(6)
F(2)	131(7)	69(6)	162(9)	-17(6)	36(6)	25(5)
F(3)	79(5)	163(9)	195(10)	46(8)	51(6)	19(6)
F(4)	147(8)	176(10)	113(8)	-64(8)	-35(7)	1(8)
F(5)	203(11)	56(6)	155(10)	-4(6)	33(8)	-3(6)
F(6)	132(8)	279(15)	79(7)	3(8)	5(6)	-8(9)
O(1)	66(4)	110(7)	64(6)	5(6)	24(4)	5(5)
O(2)	68(5)	70(6)	81(6)	-9(5)	5(4)	3(4)
O(3)	63(5)	64(6)	101(7)	5(5)	16(5)	6(4)
O(4)	91(6)	71(6)	62(6)	10(5)	-27(5)	-26(5)
O(5)	61(5)	67(6)	118(8)	2(6)	12(5)	-4(4)
O(6)	95(6)	78(6)	61(6)	-6(5)	23(5)	-2(5)
C(1)	70(7)	67(8)	58(8)	6(7)	6(6)	17(6)
C(2)	69(7)	114(12)	66(9)	45(8)	5(6)	15(7)
C(3)	63(8)	113(12)	100(13)	-3(10)	25(8)	6(8)
C(4)	98(11)	88(12)	93(13)	7(10)	35(10)	-1(9)
C(5)	108(11)	106(13)	81(11)	34(9)	24(9)	-50(10)
C(6)	68(7)	61(9)	95(11)	2(8)	7(7)	7(7)
C(7)	67(7)	72(9)	63(9)	-2(7)	17(6)	-3(6)
C(8)	71(7)	82(9)	56(8)	4(8)	5(6)	-4(7)
C(9)	87(9)	65(10)	96(12)	20(9)	19(8)	16(8)
C(10)	80(9)	80(11)	94(12)	-6(10)	31(9)	6(8)
C(11)	109(11)	71(10)	83(11)	-19(8)	31(9)	6(8)
C(12)	85(8)	89(11)	68(10)	-2(8)	-3(7)	-5(8)

Atom	U11	U22	U33	U23	U13	U12
C(13)	64(7)	60(8)	89(10)	5(8)	17(7)	3(6)
C(14)	77(8)	66(8)	74(9)	27(7)	25(7)	-2(6)
C(15)	97(10)	88(10)	80(11)	5(9)	29(9)	-18(9)
C(16)	70(8)	103(12)	96(12)	3(10)	32(8)	3(8)
C(17)	77(9)	165(17)	168(18)	107(14)	52(11)	48(10)
C(18)	96(11)	115(13)	168(18)	75(13)	72(11)	12(10)
C(19)	68(7)	74(10)	62(9)	6(8)	18(7)	10(7)
C(20)	81(8)	81(10)	71(9)	8(9)	22(7)	5(8)
C(21)	85(9)	104(13)	58(10)	-17(9)	9(7)	9(9)
C(22)	81(10)	159(19)	86(13)	-73(13)	11(9)	12(11)
C(23)	105(11)	88(12)	99(14)	-25(11)	9(10)	-9(10)
C(24)	76(8)	83(10)	81(11)	6(9)	14(8)	8(8)
C(25)	80(8)	78(10)	52(8)	-4(7)	15(6)	7(7)
C(26)	105(10)	79(11)	66(10)	16(8)	8(8)	-37(9)
C(27)	113(12)	99(14)	92(12)	17(10)	28(10)	-45(10)
C(28)	112(11)	73(11)	102(13)	16(11)	7(10)	4(10)
C(29)	134(13)	77(11)	132(15)	-18(11)	77(12)	-20(10)
C(30)	121(12)	84(12)	112(13)	-36(10)	62(10)	-29(9)
C(31)	72(7)	69(9)	64(8)	-5(8)	12(6)	6(7)
C(32)	88(9)	111(12)	68(9)	-27(9)	18(8)	-5(9)
C(33)	77(8)	95(11)	92(11)	-29(10)	6(8)	-13(8)
C(34)	77(9)	191(19)	58(10)	-7(11)	19(8)	16(11)
C(35)	96(11)	199(19)	50(9)	24(11)	23(8)	19(12)
C(36)	84(9)	129(13)	87(12)	-26(10)	39(9)	18(9)

Table A2.5 Hydrogen Co-ordinates (x 10^4) and Isotropic Displacement Parameters ($Å^2$ x 10^3) for (**2**).

Atom	x	y	z	U(eq)
H(2)	4171(8)	758(8)	3230(10)	101
H(3)	5295(10)	1203(9)	2402(12)	109
H(5)	3139(12)	2112(9)	372(11)	118
H(6)	2001(9)	1602(7)	1162(11)	92
H(8)	4336(8)	-657(8)	5679(9)	85
H(9)	4989(10)	-1893(8)	5470(12)	99
H(11)	3458(11)	-1998(8)	2742(11)	104
H(12)	2830(10)	-745(8)	2922(10)	101
H(14)	-74(9)	834(7)	4779(10)	85
H(15)	-1730(11)	996(9)	4697(11)	105
H(17)	-1939(10)	2442(11)	2447(14)	159
H(18)	-292(11)	2268(10)	2580(14)	144
H(20)	365(9)	591(9)	2031(10)	92
H(21)	-645(10)	-15(10)	734(10)	100
H(23)	-423(12)	-2057(10)	2190(13)	120
H(24)	645(10)	-1457(9)	3511(11)	97
H(26)	3670(10)	2919(9)	3652(10)	102
H(27)	3405(12)	4302(10)	3878(12)	121
H(29)	1381(12)	3774(10)	5367(13)	129
H(30)	1681(11)	2483(9)	5205(11)	120
H(32)	3858(10)	1076(8)	5894(10)	107
H(33)	4815(10)	960(9)	7471(11)	108
H(35)	2556(11)	221(12)	8464(11)	137
H(36)	1529(10)	374(10)	6918(11)	116

APPENDIX THREE

Crystallographic Analysis and Structural Refinement of $W(OC_6H_3F_2)_6$ (3).

A crystal of approximate dimensions 0.25 x 0.25 x 0.25 mm was used for data collection.

Crystal data: $C_{36}H_{18}F_{12}O_6W$, M = 1916.71, Monoclinic , a = 20.546(3), b = 12.056(2), c = 26.991(7) Å , β = 95.76(2)°, U = 6652.0(23) Å^3, space group $C2/c$, Z = 8, D_c = 1.914 gcm^{-3}, μ(Mo-K_a) = 3.588 mm^{-1}, F(000) = 3712. Crystallographic measurements were made at 293(2) K on a CAD4 automatic four-circle diffractometer in the range $2.14<\theta<22.00°$. Data (3979 reflections) were corrected for Lorentz and polarization and also for absorption.[146] (Max. and Min absorption corrections; 1.000, 0.198 respectively).

In the final least squares cycles all atoms were allowed to vibrate anisotropically, although isotropic restraints were placed on atoms C3, C4, C9, C10, C11 and C17. Phenyl rings were refined as rigid hexagons. Hydrogen atoms were included at calculated positions where relevant.

The solution of the structure (SHELX86)[147] and refinement (SHELX93)[148] converged to a conventional [i.e. based on 2165 F^2 data with $Fo>4\sigma(Fo)$] $R1$ = 0.0801 and $wR2$ = 0.1756. Goodness of fit = 0.987. The max. and min. residual densities were 1.051 and -0.765 eÅ^{-3} respectively. The asymmetric unit (shown in Figure 2.6), along with the labelling scheme used was produced using ORTEX.[149] Final fractional atomic co-ordinates and isotropic thermal parameters, bond distances and angles are given in Tables A.3.2 and A3.3 respectively. Tables of anisotropic temperature factors are available as supplementary data.

Table A3.1. Crystal Data and Structure Refinement for (3).

Identification code	98kcm13/p.williams
Empirical formula	$C_{36}H_{18}F_{12}O_6W$
Formula weight	1916.71
Temperature	293(2) K
Wavelength	0.71069 Å
Crystal system	Monoclinic
Space group	C2/c
Unit cell dimensions	a = 20.546(3)Å $\alpha = 90^\circ$
	b = 12.056(2)Å $\beta = 95.76(2)^\circ$
	c = 26.991(7)Å $\gamma = 90^\circ$
Volume	6652(2) $Å^3$
Z	8
Density (calculated)	1.914 Mg/m^3
Absorption coefficient	3.588 mm^{-1}
F(000)	3712
Crystal size	0.25 x 0.25 x 0.25 mm
Theta range for data collection	2.14 to 22.00 °.
Index ranges	-23<=h<=23; 0<=k<=13; 0<=l<=30
Reflections collected	3979
Independent reflections	3979 [R(int) = 0.0000]
Absorption correction	DIFABS
Max. and min. transmission	1.000 and 0.198
Refinement method	Full-matrix least-squares on F^2
Data / restraints / parameters	3979 / 36 / 478
Goodness-of-fit on F^2	0.987
Final R indices [$I>2\sigma(I)$]	R1 = 0.0801 wR2 = 0.1756
R indices (all data)	R1 = 0.1543 wR2 = 0.1983
Largest diff. peak and hole	1.051 and -0.765 $eÅ^{-3}$
Weighting scheme	calc $w=1/[\sigma^2(Fo^2)+(0.0910P)^2+0.0000P]$
	where $P=(Fo^2+2Fc^2)/3$

Table A3.2 Atomic Co-ordinates (x 10^4) and Equivalent Isotropic Displacement Parameters ($Å^2$ x 10^3) for (**3**).

U(eq) is defined as one third of the trace of the orthogonalized Uij tensor.

Atom	**x**	**y**	**z**	**U(eq)**
W(1)	3578(1)	2791(1)	1232(1)	50(1)
F(1)	5195(8)	-899(12)	627(7)	131(6)
F(2)	6287(7)	-42(12)	385(6)	101(5)
F(3)	4382(14)	-2111(19)	2047(12)	233(12)
F(4)	3197(8)	-2667(12)	2121(6)	126(6)
F(5)	592(10)	3543(19)	1689(8)	175(8)
F(6)	787(6)	5600(12)	1913(6)	98(5)
F(7)	2562(9)	7703(14)	586(9)	169(9)
F(8)	3751(8)	8523(11)	719(6)	114(6)
F(9)	4345(11)	6331(18)	2989(8)	175(9)
F(10)	4303(9)	4935(16)	3656(6)	139(7)
F(11)	1464(7)	-820(12)	401(6)	105(5)
F(12)	550(6)	715(13)	187(6)	108(5)
O(1)	4315(6)	2640(10)	878(5)	52(4)
O(2)	3843(6)	1516(10)	1611(5)	55(4)
O(3)	2805(6)	2919(11)	1579(5)	56(4)
O(4)	3318(6)	4085(10)	863(5)	50(4)
O(5)	4041(7)	3679(12)	1721(5)	65(4)
O(6)	3101(6)	1874(9)	761(5)	51(4)
C(1)	4772(8)	1976(13)	740(7)	42(5)
C(2)	4725(9)	806(13)	726(8)	59(6)
C(3)	5230(10)	206(16)	616(8)	49(5)
C(4)	5776(11)	605(18)	515(8)	57(6)
C(5)	5892(11)	1749(20)	502(8)	74(7)
C(6)	5362(8)	2463(17)	630(8)	62(7)

Atom	x	y	z	U(eq)
C(7)	3673(4)	535(8)	1738(4)	57(6)
C(8)	4140(5)	-282(9)	1857(5)	66(7)
C(9)	3947(6)	-1340(8)	1985(4)	84(8)
C(10)	3287(6)	-1582(7)	1995(6)	75(7)
C(11)	2820(5)	-765(7)	1876(6)	104(9)
C(12)	3013(4)	294(7)	1748(3)	68(7)
C(13)	2313(7)	3575(8)	1663(6)	70(7)
C(14)	1689(6)	3123(10)	1641(6)	54(6)
C(15)	1207(12)	3911(24)	1730(10)	84(8)
C(16)	1316(11)	5001(18)	1843(10)	72(8)
C(17)	1891(11)	5478(19)	1863(9)	71(7)
C(18)	2430(13)	4693(19)	1780(8)	80(8)
C(19)	3444(10)	5169(15)	831(8)	56(6)
C(20)	2924(9)	5895(18)	719(9)	65(7)
C(21)	3045(12)	7015(19)	673(11)	79(8)
C(22)	3642(16)	7424(16)	734(10)	80(8)
C(23)	4207(15)	6753(22)	849(9)	88(8)
C(24)	4098(13)	5611(17)	877(8)	73(7)
C(25)	4062(10)	3962(17)	2208(9)	67(7)
C(26)	4158(13)	5076(16)	2327(10)	83(8)
C(27)	4230(13)	5319(25)	2854(11)	82(8)
C(28)	4188(15)	4522(27)	3191(11)	85(9)
C(29)	4114(14)	3477(30)	3104(12)	114(11)
C(30)	4066(13)	3216(23)	2593(10)	93(9)
C(31)	2471(12)	1632(15)	623(7)	60(6)
C(32)	2233(11)	558(14)	555(9)	71(7)
C(33)	1643(13)	237(22)	441(10)	74(8)
C(34)	1193(12)	1074(28)	327(8)	81(8)
C(35)	1346(13)	2166(21)	358(9)	79(7)
C(36)	1976(10)	2415(17)	489(9)	62(7)

Table A3.3 Bond lengths [Å] and angles [°] for (**3**).

W(1)-O(1)	1.879(12)	C(7)-O(2)-W(1)	144.8(10)
W(1)-O(5)	1.882(13)	C(13)-O(3)-W(1)	144.3(11)
W(1)-O(6)	1.883(13)	C(19)-O(4)-W(1)	142.2(13)
W(1)-O(2)	1.896(12)	C(25)-O(5)-W(1)	142.1(13)
W(1)-O(4)	1.899(12)	C(31)-O(6)-W(1)	137.5(12)
W(1)-O(3)	1.932(11)	O(1)-C(1)-C(6)	117(2)
F(1)-C(3)	1.33(2)	O(1)-C(1)-C(2)	125(2)
F(2)-C(4)	1.38(2)	C(6)-C(1)-C(2)	118(2)
F(3)-C(9)	1.29(2)	C(3)-C(2)-C(1)	120(2)
F(4)-C(10)	1.37(2)	C(4)-C(3)-C(2)	125(2)
F(5)-C(15)	1.33(3)	C(4)-C(3)-F(1)	116(2)
F(6)-C(16)	1.33(2)	C(2)-C(3)-F(1)	120(2)
F(7)-C(21)	1.30(2)	C(3)-C(4)-F(2)	123(2)
F(8)-C(22)	1.35(2)	C(3)-C(4)-C(5)	122(2)
F(9)-C(27)	1.29(3)	F(2)-C(4)-C(5)	115(2)
F(10)-C(28)	1.35(3)	C(4)-C(5)-C(6)	116(2)
F(11)-C(33)	1.33(3)	C(1)-C(6)-C(5)	119(2)
F(12)-C(34)	1.40(2)	O(2)-C(7)-C(8)	120.7(7)
O(1)-C(1)	1.32(2)	O(2)-C(7)-C(12)	119.3(7)
O(2)-C(7)	1.289(14)	C(8)-C(7)-C(12)	120.0
O(3)-C(13)	1.32(2)	C(9)-C(8)-C(7)	120.0
O(4)-C(19)	1.34(2)	F(3)-C(9)-C(8)	118.9(14)
O(5)-C(25)	1.35(2)	F(3)-C(9)-C(10)	120.8(14)
O(6)-C(31)	1.34(2)	C(8)-C(9)-C(10)	120.0
C(1)-C(6)	1.40(2)	F(4)-C(10)-C(11)	128.8(10)
C(1)-C(2)	1.41	F(4)-C(10)-C(9)	111.2(10)
C(2)-C(3)	1.32(2)	C(11)-C(10)-C(9)	120.0
C(3)-C(4)	1.28(3)	C(10)-C(11)-C(12)	120.0
C(4)-C(5)	1.40(3)	C(11)-C(12)-C(7)	120.0
C(5)-C(6)	1.46(3)	O(3)-C(13)-C(18)	120(2)

C(7)-C(8)	1.39	O(3)-C(13)-C(14)	118.4(8)
C(7)-C(12)	1.39	C(18)-C(13)-C(14)	121.6(13)
C(8)-C(9)	1.39	C(13)-C(14)-C(15)	112.9(14)
C(9)-C(10)	1.39	F(5)-C(15)-C(16)	118(3)
C(10)-C(11)	1.39	F(5)-C(15)-C(14)	116(3)
C(11)-C(12)	1.39	C(16)-C(15)-C(14)	126(2)
C(13)-C(18)	1.40(2)	C(17)-C(16)-F(6)	120(2)
C(13)-C(14)	1.39	C(17)-C(16)-C(15)	124(2)
C(14)-C(15)	1.41(3)	F(6)-C(16)-C(15)	116(2)
C(15)-C(16)	1.36(3)	C(16)-C(17)-C(18)	113(2)
C(16)-C(17)	1.31(3)	C(13)-C(18)-C(17)	122(2)
C(17)-C(18)	1.49(3)	O(4)-C(19)-C(20)	119(2)
C(19)-C(20)	1.39	O(4)-C(19)-C(24)	123(2)
C(19)-C(24)	1.44(3)	C(20)-C(19)-C(24)	119(2)
C(20)-C(21)	1.38(3)	C(19)-C(20)-C(21)	120(2)
C(21)-C(22)	1.32(3)	F(7)-C(21)-C(22)	118(2)
C(22)-C(23)	1.42(3)	F(7)-C(21)-C(20)	120(2)
C(23)-C(24)	1.40(3)	C(22)-C(21)-C(20)	122(2)
C(25)-C(30)	1.37(3)	C(21)-C(22)-F(8)	121(3)
C(25)-C(26)	1.39	C(21)-C(22)-C(23)	123(2)
C(26)-C(27)	1.45(3)	F(8)-C(22)-C(23)	116(3)
C(27)-C(28)	1.33(4)	C(24)-C(23)-C(22)	116(3)
C(28)-C(29)	1.29(4)	C(23)-C(24)-C(19)	121(2)
C(29)-C(30)	1.41(3)	O(5)-C(25)-C(30)	124(2)
C(31)-C(32)	1.39	O(5)-C(25)-C(26)	117(2)
C(31)-C(36)	1.41(3)	C(30)-C(25)-C(26)	118(2)
C(32)-C(33)	1.28(3)	C(25)-C(26)-C(27)	115(2)
C(33)-C(34)	1.38(3)	F(9)-C(27)-C(28)	121(3)
C(34)-C(35)	1.35(3)	F(9)-C(27)-C(26)	118(3)
C(35)-C(36)	1.34(3)	C(28)-C(27)-C(26)	121(3)
		C(29)-C(28)-C(27)	127(3)
O(1)-W(1)-O(5)	92.1(6)	C(29)-C(28)-F(10)	123(3)

O(1)-W(1)-O(6)	89.5(5)	C(27)-C(28)-F(10)	111(3)
O(5)-W(1)-O(6)	177.8(6)	C(28)-C(29)-C(30)	113(3)
O(1)-W(1)-O(2)	89.6(6)	C(25)-C(30)-C(29)	126(3)
O(5)-W(1)-O(2)	89.1(6)	O(6)-C(31)-C(32)	124(2)
O(6)-W(1)-O(2)	89.4(6)	O(6)-C(31)-C(36)	125(2)
O(1)-W(1)-O(4)	90.7(5)	C(32)-C(31)-C(36)	111(2)
O(5)-W(1)-O(4)	89.8(6)	C(33)-C(32)-C(31)	129(2)
O(6)-W(1)-O(4)	91.6(6)	C(32)-C(33)-F(11)	124(2)
O(2)-W(1)-O(4)	179.0(6)	C(32)-C(33)-C(34)	116(3)
O(1)-W(1)-O(3)	178.2(5)	F(11)-C(33)-C(34)	121(3)
O(5)-W(1)-O(3)	89.8(6)	C(35)-C(34)-C(33)	123(3)
O(6)-W(1)-O(3)	88.6(6)	C(35)-C(34)-F(12)	122(3)
O(2)-W(1)-O(3)	90.5(5)	C(33)-C(34)-F(12)	115(3)
O(4)-W(1)-O(3)	89.2(5)	C(36)-C(35)-C(34)	117(3)
C(1)-O(1)-W(1)	146.9(11)	C(35)-C(36)-C(31)	125(2)

Table A3.4 Anisotropic Displacement Parameters ($Å^2 \times 10^3$) for (**3**).

The anisotropic displacement factor exponent takes the form:

$-2\ pi^2\ [\ h^2\ a^*\ 2\ U11 + ... + 2\ h\ k\ a^*\ b^*\ U12\ ]$

Atom	U11	U22	U33	U23	U13	U12
W(1)	51(1)	49(1)	51(1)	0(1)	6(1)	0(1)
F(1)	138(14)	88(11)	171(19)	5(11)	36(13)	3(11)
F(2)	67(9)	96(11)	141(15)	-16(10)	15(10)	12(8)
F(3)	240(26)	170(21)	297(35)	27(22)	62(25)	33(19)
F(4)	167(15)	84(10)	123(14)	37(10)	-2(11)	-54(11)
F(5)	147(18)	187(20)	191(22)	-2(18)	27(17)	6(17)
F(6)	74(10)	101(12)	124(14)	2(10)	30(10)	29(9)
F(7)	130(15)	99(12)	271(27)	50(16)	-21(17)	13(12)
F(8)	163(15)	59(9)	128(14)	20(9)	54(12)	0(10)
F(9)	239(24)	139(18)	140(18)	-54(15)	-15(17)	25(17)
F(10)	161(16)	185(18)	76(13)	-39(12)	32(12)	-26(13)
F(11)	112(12)	74(10)	128(14)	-4(9)	10(10)	-39(9)
F(12)	59(9)	166(15)	98(12)	-28(11)	5(8)	-18(9)
O(1)	44(8)	58(9)	53(9)	0(7)	4(7)	5(7)
O(2)	59(9)	30(8)	69(11)	10(7)	-16(8)	-2(7)
O(3)	37(7)	72(10)	61(10)	21(8)	12(7)	5(7)
O(4)	60(9)	38(8)	53(10)	7(7)	7(7)	2(7)
O(5)	81(11)	68(10)	38(10)	-4(8)	-24(8)	-16(8)
O(6)	43(8)	43(9)	62(10)	-3(7)	-12(7)	-7(6)
C(1)	40(11)	51(14)	36(12)	14(10)	8(10)	10(10)
C(2)	36(12)	88(17)	51(15)	-9(13)	3(11)	-14(12)
C(3)	52(7)	46(7)	48(7)	-1(5)	4(5)	-1(5)
C(4)	55(7)	58(7)	57(7)	-1(5)	0(5)	3(5)
C(5)	72(16)	92(18)	56(16)	-18(14)	2(13)	-2(14)
C(6)	33(11)	71(18)	84(18)	-6(12)	7(11)	-5(10)

Atom	U11	U22	U33	U23	U13	U12
C(7)	52(14)	56(14)	61(16)	3(12)	-6(13)	7(12)
C(8)	74(16)	85(17)	36(14)	16(13)	-8(12)	-23(14)
C(9)	87(9)	81(9)	83(9)	3(5)	7(5)	4(5)
C(10)	78(8)	73(8)	73(8)	-1(5)	7(5)	-7(5)
C(11)	106(10)	103(10)	101(10)	0(5)	5(5)	4(5)
C(12)	77(16)	44(13)	81(19)	1(12)	2(15)	-12(12)
C(13)	66(15)	47(13)	102(21)	24(13)	40(15)	23(12)
C(14)	49(12)	47(13)	71(16)	15(11)	24(12)	1(10)
C(15)	53(16)	119(25)	80(21)	8(17)	14(15)	-21(16)
C(16)	53(15)	47(14)	116(23)	-29(14)	14(15)	1(12)
C(17)	70(8)	72(8)	69(8)	-1(5)	6(5)	1(5)
C(18)	115(21)	77(17)	48(16)	-18(14)	2(15)	-15(16)
C(19)	72(16)	45(13)	50(15)	-5(11)	8(13)	-17(12)
C(20)	27(11)	101(19)	66(17)	2(15)	-3(12)	-4(12)
C(21)	52(14)	51(17)	128(24)	22(15)	-18(16)	13(13)
C(22)	123(24)	29(14)	89(21)	2(12)	5(18)	0(13)
C(23)	137(25)	80(18)	48(17)	-1(15)	9(17)	-1(18)
C(24)	109(21)	46(14)	62(17)	-17(12)	8(15)	-4(14)
C(25)	59(15)	79(17)	55(18)	-33(15)	-33(13)	-25(13)
C(26)	92(19)	83(19)	74(21)	-13(16)	6(17)	-3(17)
C(27)	89(20)	80(20)	74(22)	-51(19)	-6(17)	1(17)
C(28)	112(24)	86(22)	53(20)	-13(19)	-7(18)	27(19)
C(29)	113(25)	132(29)	91(28)	-43(23)	-26(20)	-16(22)
C(30)	132(25)	83(19)	66(20)	15(17)	20(18)	-22(17)
C(31)	97(19)	49(13)	37(14)	-23(11)	26(13)	-20(14)
C(32)	83(19)	61(16)	68(18)	32(14)	8(16)	21(14)
C(33)	59(17)	81(19)	83(21)	-15(16)	21(16)	-10(16)
C(34)	66(18)	146(28)	36(15)	-9(17)	30(14)	-33(19)
C(35)	96(19)	63(15)	75(18)	-25(16)	-4(15)	-9(17)
C(36)	50(13)	52(16)	85(18)	0(12)	12(13)	-2(11)

Table A3.5 Hydrogen Co-ordinates (x 10^4) and Isotropic Displacement Parameters ($Å^2$ x 10^3) for (**3**).

Atom	x	y	z	U(eq)
H(2)	4340(24)	459(20)	794(74)	70
H(5)	6286(11)	2036(20)	417(8)	88
H(6)	5413(8)	3230(17)	639(8)	75
H(8)	4582(5)	-120(11)	1850(7)	79
H(11)	2378(5)	-926(8)	1883(8)	124
H(12)	2700(4)	840(7)	1669(3)	82
H(14)	1598(5)	2378(11)	1575(6)	65
H(17)	1956(11)	6232(19)	1922(9)	85
H(18)	2857(13)	4955(19)	1806(8)	96
H(20)	2497(26)	5627(36)	676(67)	78
H(23)	4625(15)	7056(22)	902(9)	106
H(24)	4453(13)	5131(17)	926(8)	87
H(26)	4175(111)	5623(41)	2086(32)	100
H(29)	4093(14)	2949(30)	3353(12)	137
H(30)	4035(13)	2469(23)	2508(10)	112
H(32)	2544(78)	-3(38)	599(43)	85
H(35)	1031(13)	2715(21)	291(9)	95
H(36)	2095(10)	3159(17)	491(9)	74

APPENDIX FOUR

Crystallographic Analysis and Structural Refinement of $W_4C_{16}H_{40}N_4O_{14}$ (8).

Crystals were mounted on a thin glass fibre using silicon grease and cooled on the diffractometer to 100 K using an Oxford Cryostream low temperature attachment. Approximate unit cell dimensions were determined by the Nonius Collect program[150] from 5 index frames of width 2° in ϕ using a Nonius ^{Kappa}CCD diffractometer, with a detector to crystal distance of 30 mm. The Collect program was then used to calculate a data collection stratgey to 99.5 % completeness for $\theta = 27.5°$ using a combination of 2° ϕ and ω scans of 10 - 60 s deg^{-1} exposure time (depending on crystal quality). Crystals were indexed using the DENZO-SMN package[151] and positional data were refined along with diffractometer constants to give the final unit cell parameters. Integration and scaling (DENZO-SMN, Scalepack[151]) resulted in unique data sets corrected for Lorentz and polarisation effects and for the effects of crystal decay and absorption by a combination of averaging of equivalent reflections and an overall volume and scaling correction. Structures were solved using SHELXS-97[152] and developed *via* alternating least squares cycles and difference Fourier synthesis (SHELXL-97[152]) with the aid of the program XSeed.[153] In general all non-hydrogen atoms were modelled anisotropically, while hydrogen atoms are assigned an isotropic thermal parameter 1.2 times that of the parent atom (1.5 for terminal atoms) and allowed to ride, except for acidic protons which were located on the final difference Fourier map and refined freely. All calculations were carried out with either a Silicon Graphics Indy workstation or an IBM compatible PC.

We thank the EPSRC and King's College London for the provision of the X-ray diffractometer and the Nuffield Foundation for the provision of computing equipment.

Table A4.1 Crystal data and structure refinement for (**8**).

Identification code	pw1	
Empirical formula	C16 H40 N4 O14 W4	
Formula weight	1247.92	
Temperature	100(2) K	
Wavelength	0.71073 Å	
Crystal system	Tetragonal	
Space group	P42/nbc	
Unit cell dimensions	a = 13.4048(19) Å	α= 90°.
	b = 13.4048(19) Å	β= 90°.
	c = 19.731(4) Å	γ = 90°.
Volume	3545.4(10) $Å^3$	
Z	4	
Density (calculated)	2.338 Mg/m^3	
Absorption coefficient	12.991 mm^{-1}	
F(000)	2288	
Crystal size	0.10 x 0.10 x 0.02 mm^3	
Theta range for data collection	3.68 to 24.97°.	
Index ranges	-15<=h<=15, -11<=k<=11, -23<=l<=23	
Reflections collected	18139	
Independent reflections	1556 [R(int) = 0.1599]	
Completeness to theta = 24.97°	99.4 %	
Absorption correction	Scalepack	
Max. and min. transmission	0.7812 and 0.3566	
Refinement method	Full-matrix least-squares on F^2	
Data / restraints / parameters	1556 / 0 / 126	
Goodness-of-fit on F^2	1.054	
Final R indices [I>2sigma(I)]	R1 = 0.0490, wR2 = 0.1047	
R indices (all data)	R1 = 0.0791, wR2 = 0.1171	
Extinction coefficient	0.00011(6)	
Largest diff. peak and hole	1.652 and -1.952 $e.Å^{-3}$	

Table A4.2 Atomic Co-ordinates (x 10^4) and Equivalent Isotropic Displacement Parameters ($Å^2$x 10^3) for (**8**).

U(eq) is defined as one third of the trace of the orthogonalized U^{ij} tensor.

Atom	x	y	z	U(eq)
W(1)	2293(1)	8835(1)	3207(1)	25(1)
O(1)	1491(6)	9972(6)	2971(5)	37(2)
C(5)	385(11)	7668(10)	3910(8)	39(4)
O(2)	2983(6)	9389(6)	3834(4)	29(2)
O(3)	1182(6)	8079(6)	2507(5)	27(2)
O(4)	2500	7500	3503(7)	18(3)
C(2)	662(10)	10289(10)	3367(7)	36(3)
C(3)	125(12)	9436(10)	3608(8)	49(4)
N(1)	849(8)	8693(7)	3907(6)	32(3)
C(4)	1072(10)	8957(10)	4610(7)	36(3)
C(1S)	-2510(30)	8360(20)	4813(17)	49(9)
C(2S)	-2500	7500	4180(20)	34(10)
C(3S)	-2440(30)	8430(40)	4410(20)	74(12)
C(4S)	-2500	7500	3450(40)	90(20)
W(1A)	1174(4)	7736(4)	3195(3)	36(1)
O(1A)	2020(60)	7250(70)	3550(50)	50(30)
O(2A)	660(50)	7180(50)	3870(40)	14(16)
O(3A)	20(50)	8780(50)	3100(40)	34(19)
O(4A)	1510(80)	8470(70)	3810(50)	60(30)
O(5A)	1890(60)	8670(50)	2560(40)	40(20)

Table A4.3 Bond lengths [Å] and angles [°] for (**8**).

W(1)-O(2)	1.713(8)	C(2)-C(3)-N(1)	109.5(12)
W(1)-O(3)#1	1.759(9)	C(4)-N(1)-C(5)	107.6(11)
W(1)-O(4)	1.903(4)	C(4)-N(1)-C(3)	110.0(10)
W(1)-O(1)	1.922(8)	C(5)-N(1)-C(3)	109.7(11)
W(1)-O(3)	2.269(9)	C(4)-N(1)-W(1)	111.3(8)
W(1)-N(1)	2.387(11)	C(5)-N(1)-W(1)	114.1(8)
O(1)-C(2)	1.425(15)	C(3)-N(1)-W(1)	104.0(8)
C(5)-N(1)	1.508(15)	C(1S)#4-C(1S)-C(3S)	169(9)
O(3)-W(1)#2	1.759(9)	C(1S)#4-C(1S)-C(3S)#4	6(5)
O(4)-W(1)#3	1.903(4)	C(3S)-C(1S)-C(3S)#4	168(7)
C(2)-C(3)	1.433(19)	C(1S)#4-C(1S)-C(2S)	137.3(14)
C(3)-N(1)	1.511(17)	C(3S)-C(1S)-C(2S)	51(5)
N(1)-C(4)	1.461(17)	C(3S)#4-C(1S)-C(2S)	141(3)
C(1S)-C(1S)#4	0.74(7)	C(3S)-C(2S)-C(3S)#5	140(6)
C(1S)-C(3S)	0.80(5)	C(3S)-C(2S)-C(4S)	110(3)
C(1S)-C(3S)#4	1.53(7)	C(3S)#5-C(2S)-C(4S)	110(3)
C(1S)-C(2S)	1.69(4)	C(3S)-C(2S)-C(1S)	28(2)
C(2S)-C(3S)	1.34(5)	C(3S)#5-C(2S)-C(1S)	113(4)
C(2S)-C(3S)#5	1.34(5)	C(4S)-C(2S)-C(1S)	137.3(14)
C(2S)-C(4S)	1.45(8)	C(3S)-C(2S)-C(1S)#5	113(4)
C(2S)-C(1S)#5	1.69(4)	C(3S)#5-C(2S)-C(1S)#5	28(2)
C(3S)-C(1S)#4	1.53(7)	C(4S)-C(2S)-C(1S)#5	137.3(14)
W(1A)-O(1A)	1.48(10)	C(1S)-C(2S)-C(1S)#5	85(3)
W(1A)-O(4A)	1.63(10)	C(1S)-C(3S)-C(2S)	102(6)
W(1A)-O(2A)	1.68(7)	C(1S)-C(3S)-C(1S)#4	5(4)
W(1A)-O(5A)#2	1.88(8)	C(2S)-C(3S)-C(1S)#4	106(4)
W(1A)-O(5A)	2.01(8)	O(1A)-W(1A)-O(4A)	73(5)
W(1A)-O(3A)	2.09(7)	O(1A)-W(1A)-O(2A)	75(4)
W(1A)-O(1A)#3	2.52(9)	O(4A)-W(1A)-O(2A)	78(4)
O(1A)-O(1A)#3	1.45(16)	O(1A)-W(1A)-O(5A)#2	91(5)

O(1A)-W(1A)#3	2.52(9)	O(4A)-W(1A)-O(5A)#2	157(4)
O(5A)-W(1A)#1	1.88(8)	O(2A)-W(1A)-O(5A)#2	114(3)
		O(1A)-W(1A)-O(5A)	101(4)
O(2)-W(1)-O(3)#1	105.1(4)	O(4A)-W(1A)-O(5A)	87(4)
O(2)-W(1)-O(4)	96.2(4)	O(2A)-W(1A)-O(5A)	165(3)
O(3)#1-W(1)-O(4)	98.4(4)	O(5A)#2-W(1A)-O(5A)	80(3)
O(2)-W(1)-O(1)	97.7(4)	O(1A)-W(1A)-O(3A)	154(4)
O(3)#1-W(1)-O(1)	98.7(4)	O(4A)-W(1A)-O(3A)	82(4)
O(4)-W(1)-O(1)	154.3(3)	O(2A)-W(1A)-O(3A)	94(3)
O(2)-W(1)-O(3)	170.6(4)	O(5A)#2-W(1A)-O(3A)	114(3)
O(3)#1-W(1)-O(3)	84.3(3)	O(5A)-W(1A)-O(3A)	83(3)
O(4)-W(1)-O(3)	82.1(4)	O(1A)-W(1A)-O(1A)#3	30(5)
O(1)-W(1)-O(3)	80.8(3)	O(4A)-W(1A)-O(1A)#3	62(4)
O(2)-W(1)-N(1)	93.1(4)	O(2A)-W(1A)-O(1A)#3	100(3)
O(3)#1-W(1)-N(1)	161.5(4)	O(5A)#2-W(1A)-O(1A)#3	97(3)
O(4)-W(1)-N(1)	82.2(3)	O(5A)-W(1A)-O(1A)#3	73(3)
O(1)-W(1)-N(1)	75.5(4)	O(3A)-W(1A)-O(1A)#3	137(3)
O(3)-W(1)-N(1)	77.5(4)	O(1A)#3-O(1A)-W(1A)	119(9)
C(2)-O(1)-W(1)	122.7(8)	O(1A)#3-O(1A)-W(1A)#3	31(5)
W(1)#2-O(3)-W(1)	139.7(4)	W(1A)-O(1A)-W(1A)#3	127(5)
W(1)#3-O(4)-W(1)	144.2(8)	W(1A)#1-O(5A)-W(1A)	148(4)
O(1)-C(2)-C(3)	109.6(10)		

Symmetry transformations used to generate equivalent atoms:
#1 y-1/2,-x+1,-z+1/2 #2 -y+1,x+1/2,-z+1/2 #3 -x+1/2,-y+3/2,z
#4 -x-1/2,y,-z+1 #5 -x-1/2,-y+3/2,z

Table A4.4 Anisotropic Displacement Parameters ($Å^2 x\ 10^3$) for (**8**).

The anisotropic displacement factor exponent takes the form:

$$-2p^2[\ h^2\ a^{*2}U^{11} + ...\ + 2\ h\ k\ a^*\ b^*\ U^{12}\ ]$$

Atom	U^{11}	U^{22}	U^{33}	U^{23}	U^{13}	U^{12}
W(1)	27(1)	24(1)	26(1)	-1(1)	0(1)	2(1)
O(1)	40(5)	19(4)	53(6)	-4(5)	-2(5)	13(4)
C(5)	43(9)	30(8)	43(9)	-7(8)	8(8)	3(7)
O(2)	45(5)	28(5)	12(5)	4(4)	-1(4)	0(4)
O(3)	33(5)	25(4)	24(5)	-2(4)	4(4)	-2(4)
O(4)	12(7)	21(7)	20(7)	0	0	0(6)
C(2)	48(8)	31(7)	30(9)	-8(7)	-6(7)	16(7)
C(3)	66(10)	43(8)	37(9)	-13(8)	14(9)	19(8)
N(1)	29(6)	28(6)	37(7)	-11(6)	3(6)	9(5)
C(4)	45(8)	41(8)	21(7)	9(7)	-15(7)	1(7)

Table A4.5 Hydrogen Co-ordinates (x 10^4) and Isotropic Displacement Parameters ($Å^2$x 10^3) for (**8**).

Atom	x	y	z	U(eq)
H(5A)	882	7176	4056	58
H(5B)	155	7502	3452	58
H(5C)	-182	7658	4223	58
H(2B)	216	10712	3089	43
H(2A)	899	10691	3756	43
H(3A)	-245	9124	3229	58
H(3B)	-364	9643	3957	58
H(4A)	1244	9667	4636	54
H(4B)	1635	8556	4771	54
H(4C)	486	8826	4893	54

Table A4.6 Torsion Angles [°] for (**8**).

O(2)-W(1)-O(1)-C(2)	-77.8(10)
O(3)#1-W(1)-O(1)-C(2)	175.6(9)
O(4)-W(1)-O(1)-C(2)	44.2(16)
O(3)-W(1)-O(1)-C(2)	92.9(9)
N(1)-W(1)-O(1)-C(2)	13.5(9)
O(2)-W(1)-O(3)-W(1)#2	-150.6(18)
O(3)#1-W(1)-O(3)-W(1)#2	28.5(6)
O(4)-W(1)-O(3)-W(1)#2	-70.8(7)
O(1)-W(1)-O(3)-W(1)#2	128.3(8)
N(1)-W(1)-O(3)-W(1)#2	-154.6(8)
O(2)-W(1)-O(4)-W(1)#3	-142.9(3)
O(3)#1-W(1)-O(4)-W(1)#3	-36.6(3)
O(1)-W(1)-O(4)-W(1)#3	94.8(11)
O(3)-W(1)-O(4)-W(1)#3	46.4(2)
N(1)-W(1)-O(4)-W(1)#3	124.8(3)
W(1)-O(1)-C(2)-C(3)	-39.3(14)
O(1)-C(2)-C(3)-N(1)	47.9(14)
C(2)-C(3)-N(1)-C(4)	83.8(13)
C(2)-C(3)-N(1)-C(5)	-158.0(11)
C(2)-C(3)-N(1)-W(1)	-35.6(12)
O(2)-W(1)-N(1)-C(4)	-8.5(8)
O(3)#1-W(1)-N(1)-C(4)	-179.4(10)
O(4)-W(1)-N(1)-C(4)	87.3(9)
O(1)-W(1)-N(1)-C(4)	-105.6(9)
O(3)-W(1)-N(1)-C(4)	170.8(9)
O(2)-W(1)-N(1)-C(5)	-130.6(9)
O(3)#1-W(1)-N(1)-C(5)	58.6(16)
O(4)-W(1)-N(1)-C(5)	-34.8(10)
O(1)-W(1)-N(1)-C(5)	132.3(10)
O(3)-W(1)-N(1)-C(5)	48.8(9)

O(2)-W(1)-N(1)-C(3)	109.9(8)
O(3)#1-W(1)-N(1)-C(3)	-61.0(14)
O(4)-W(1)-N(1)-C(3)	-154.3(8)
O(1)-W(1)-N(1)-C(3)	12.8(8)
O(3)-W(1)-N(1)-C(3)	-70.7(8)
C(1S)#4-C(1S)-C(2S)-C(3S)	-170(16)
C(3S)#4-C(1S)-C(2S)-C(3S)	-176(8)
C(1S)#4-C(1S)-C(2S)-C(3S)#5	6(13)
C(3S)-C(1S)-C(2S)-C(3S)#5	176(4)
C(3S)#4-C(1S)-C(2S)-C(3S)#5	0(5)
C(1S)#4-C(1S)-C(2S)-C(4S)	-178(10)
C(3S)-C(1S)-C(2S)-C(4S)	-8(7)
C(3S)#4-C(1S)-C(2S)-C(4S)	176(3)
C(1S)#4-C(1S)-C(2S)-C(1S)#5	2(10)
C(3S)-C(1S)-C(2S)-C(1S)#5	172(7)
C(3S)#4-C(1S)-C(2S)-C(1S)#5	-4(3)
C(1S)#4-C(1S)-C(3S)-C(2S)	141(47)
C(3S)#4-C(1S)-C(3S)-C(2S)	168(25)
C(3S)#4-C(1S)-C(3S)-C(1S)#4	27(22)
C(2S)-C(1S)-C(3S)-C(1S)#4	-141(47)
C(3S)#5-C(2S)-C(3S)-C(1S)	-6(5)
C(4S)-C(2S)-C(3S)-C(1S)	174(5)
C(1S)#5-C(2S)-C(3S)-C(1S)	-9(7)
C(3S)#5-C(2S)-C(3S)-C(1S)#4	-2.6(16)
C(4S)-C(2S)-C(3S)-C(1S)#4	177.4(16)
C(1S)-C(2S)-C(3S)-C(1S)#4	3(6)
C(1S)#5-C(2S)-C(3S)-C(1S)#4	-6(3)
O(4A)-W(1A)-O(1A)-O(1A)#3	-63(7)
O(2A)-W(1A)-O(1A)-O(1A)#3	-145(7)
O(5A)#2-W(1A)-O(1A)-O(1A)#3	101(7)
O(5A)-W(1A)-O(1A)-O(1A)#3	21(7)
O(3A)-W(1A)-O(1A)-O(1A)#3	-78(9)

O(4A)-W(1A)-O(1A)-W(1A)#3	-99(7)
O(2A)-W(1A)-O(1A)-W(1A)#3	180(7)
O(5A)#2-W(1A)-O(1A)-W(1A)#3	65(6)
O(5A)-W(1A)-O(1A)-W(1A)#3	-15(7)
O(3A)-W(1A)-O(1A)-W(1A)#3	-113(8)
O(1A)#3-W(1A)-O(1A)-W(1A)#3	-36(3)
O(1A)-W(1A)-O(5A)-W(1A)#1	66(10)
O(4A)-W(1A)-O(5A)-W(1A)#1	138(9)
O(2A)-W(1A)-O(5A)-W(1A)#1	142(10)
O(5A)#2-W(1A)-O(5A)-W(1A)#1	-23(7)
O(3A)-W(1A)-O(5A)-W(1A)#1	-139(9)
O(1A)#3-W(1A)-O(5A)-W(1A)#1	77(9)

Symmetry transformations used to generate equivalent atoms:

#1 y-1/2,-x+1,-z+1/2 #2 -y+1,x+1/2,-z+1/2 #3 -x+1/2,-y+3/2,z

#4 -x-1/2,y,-z+1 #5 -x-1/2,-y+3/2,z

APPENDIX FIVE

ICDD Pattern Number Data.

The crystalline phases present in the films deposited in this thesis were characterised by utilising the International Centre for Diffraction Data (ICDD) database held on CD-ROM. The two tungsten oxide patterns which have been identified as being present in the films deposited were ICDD pattern numbers 20-1324 and 18-1417. Tables A5.1 and A5.2 displays the data for ICDD pattern numbers 20-1324 and 18-1417.

Table A5.1 ICDD 20-1324 WO_3

2θ	Int	h	k	l	2θ	Int	h	k	l
23.101	100	0	0	1	49.367	20	4	0	0
23.726	65	0	2	0	50.121	10	1	4	0
24.118	95	2	0	0	50.536	16	1	1	2
25.977	2	0	1	1	53.525	10	0	2	2
26.608	10	1	2	0	53.728	10	2	0	2
28.799	25	1	1	1	54.348	16	0	4	1
33.358	35	0	2	1	54.841	10	2	4	0
33.667	35	2	0	1	55.162	16	4	0	1
34.049	50	2	2	0	55.451	16	4	2	0
35.553	6	1	2	1	55.891	6	1	4	1
41.558	16	2	2	1	57.726	2	3	3	1
43.095	2	0	3	1	59.523	6	2	2	2
44.043	2	3	2	0	60.293	10	2	4	1
44.917	10	1	3	1	60.863	10	4	2	1
45.391	6	3	1	1	62.175	6	3	4	0
47.267	20	0	0	2	62.50	6	4	3	0
48.471	10	0	4	0					

Table A5.2 ICDD 18-1417 $WO_{2.9}$

2θ	Int	h	k	l
23.791	100	1	1	0
28.799	20	1	0	1
33.824	80	2	0	0
41.025	30	2	0	1
44.870	10	2	1	1
48.416	30	2	2	0
51.328	10			
54.983	60	3	1	0
60.511	50	3	1	1
62.782	10	2	1	2
70.848	10	4	0	0
76.154	10	3	3	0
82.430	10	3	2	2

APPENDIX SIX

Instrumentation

Microanalysis

Carbon, hydrogen and nitrogen were analysed for using a Carlo-Erba Strumentazione E. A. mod 1106 microanalyser operating at 500°C. Results were calibrated against an acetanilide [$PhNHC(O)CH_3$] standard.

Infra-red Spectrometry

Infra-red spectra were recorded as nujol (liquid paraffin) mulls or liquid films between NaCl plates. Measurements were taken using a Nicolet 510P Fourier Transform spectrometer within the range 4000 - 600 cm^{-1} with a medium slit width and a peak resolution of 4.0 cm^{-1}.

Mass Spectroscopy

Mass spectra were collected on a V.G. 70-70E instrument under electron impact conditions.

Scanning Electron Microscopy (SEM)

SEM images were collected on a JOEL 6310 scanning electron microscope operating at an accelerating voltage of 30 kV.

^1H and $^{13}C\{^1H\}$ Nuclear Magnetic Resonance Spectroscopy

Proton and carbon-13 NMR spectra were recorded using either Jeol JNM-GX-270FT (270 MHz) or Jeol EX-400 (400 MHz) Fourier Transform spectrometers using $SiMe_4$ as an internal reference.

^{19}F and ^{183}W Nuclear Magnetic Resonance Spectroscopy

Fluorine-19 and tungsten-183 NMR spectra were recorded on a Jeol EX400 (400 MHz) Fourier Transform spectrometer. Chemical shifts [$\delta(^{19}F)$] are relative to $CFCl_3$, and chemical shifts [$\delta(^{183}W)$] are relative to a 1 mol dm^{-3} solution of Na_2WO_4/D_2O.

X-Ray Diffraction (XRD)

Samples of coating for XRD were of approximate dimensions 1.5 x 2.0 cm. The X-ray diffraction equipment consisted of a Philips PW1130 generator operating at 45 kV and 40 mA to power a copper long fine focus X-ray tube. A PW 1820 goniometer fitted with "thin film optics" and proportional X-ray detector was used. The non focusing thin film optics employed a ¼ degree primary beam slit to irradiate the specimen at a fixed incident angle of 1.5°. Diffraction radiation from the sample was collimated with a flat plate collimator and passed through a Graphite flat crystal monochromator to isolate diffracted Copper Kα peaks onto the detector. The equipment was situated in a total enclosure to provide radiation safety for the highly collimated narrow beams of X-rays. Data was acquired by a PW1710 microprocessor and processed using Philips APD VMS software on a Micro VAX computer. Crystalline phases were identified from the International Centre for Diffraction Data (ICDD) database held on CD-ROM (Appendix 5).

Transmission-Reflectance

Samples of coatings for transmission-reflectance analysis were of approximately 2cm square. The transmission and reflectance of the coated samples was measured using a Hitachi u-4000 spectrometer between wavelengths 240-2600nm calibrated against a rhodium mirror.

APPENDIX SEVEN

CVD Reactor

The CVD apparatus used in this study has been assembled as a general screening rig for the use in this and other related projects. The system consists of a horizontal cold wall reactor with associated gas lines and electrical heater controls. The reactor contains two separate systems, a heated bubbler assembly and an ultrasonic nebuliser equipment. Screening tests for this study have used both the heated bubbler and the ultrasonic nebuliser. A schematic of the apparatus is shown in Figure A7.1. Detailed diagrams of the ultrasonic nebuliser, the heated bubbler assembly and the CVD reactor are shown in Figures A7.2, A7.3 and A7.4 respectively.

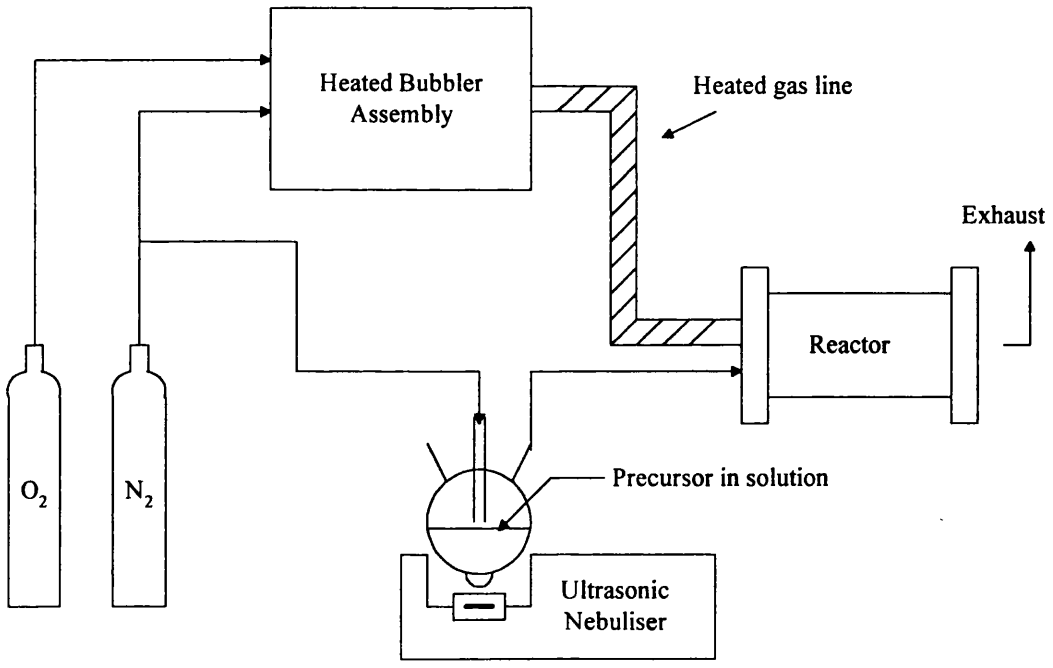

Figure A7.1 Schematic representation of the CVD apparatus.

The ultrasonic nebuliser used is an ultrasonic humidifier from Pifco Health (model No 1077) bought in Argos. The piezoelectric transducer, situated in the reservoir containing water, transmits ultrasound through the water and the glass of the

flask into the solution to be nebulised. The distance between the piezoelectric transducer and the flask is approximately 3-4 cm. The water in the reservoir is replaced every 30 minutes in order to cool the transducer.

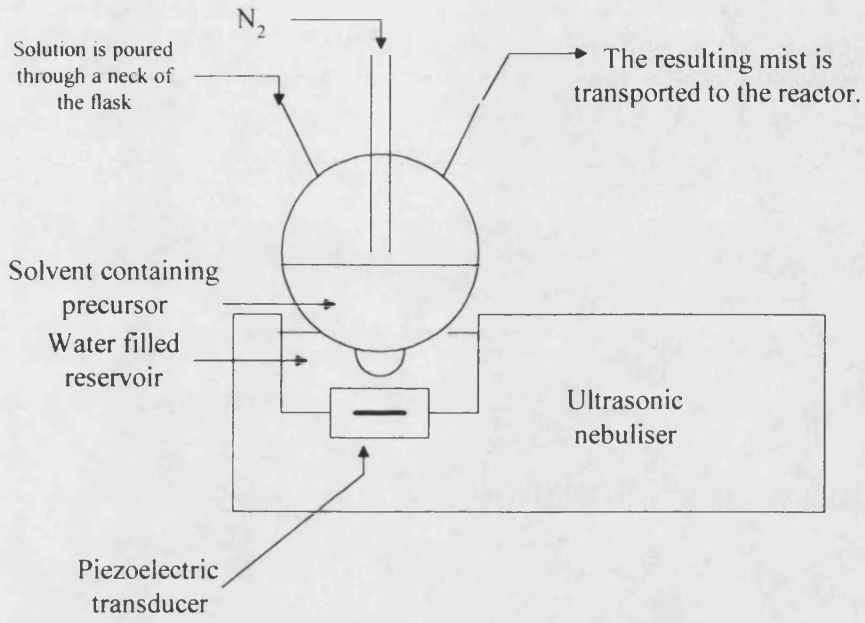

Figure A7.2 Schematic representation of the nebuliser.

A solution of the precursor is poured into the three neck round-bottomed flask and placed on the nebuliser. When the power is switched on, the solution in the flask fountains to generate an aerosol of fine droplets of the solution (droplet size: 0.2-5 microns). The mist can be controlled via two controls, the mist output (MO) and the humidity level (HL). For a solution in THF, the efficiency of the nebuliser is 1.2 $cm^3.min^{-1}$ when the MO button is in position 1/2 or 3/4 of its full power and the HL button is in position 3/4 of its full power.

The aerosol is simply swept out of the flask by a flow of nitrogen gas and transported to a horizontal cold wall CVD reactor. Before the mist reaches the reactor, it is passed through a baffle to promote laminar flow. A schematic representation of the CVD reactor is represented in Figure A7.4.

For precursors which were suitably volatile a stainless steel bubbler which was encased in an oven was used. The bubbler could be removed from the oven and sealed at the gas taps which enabled air sensitive precursors to be loaded in a dry box before the bubbler was attached to the pipework. The pipework inside the oven contained a by-pass system which enabled the gas flows and temperatures to be set before the nitrogen carrier gas flow was turned to the bubbler to transport the vaporised precursor. A schematic of the bubbler assembly is shown in Figure A7.3.

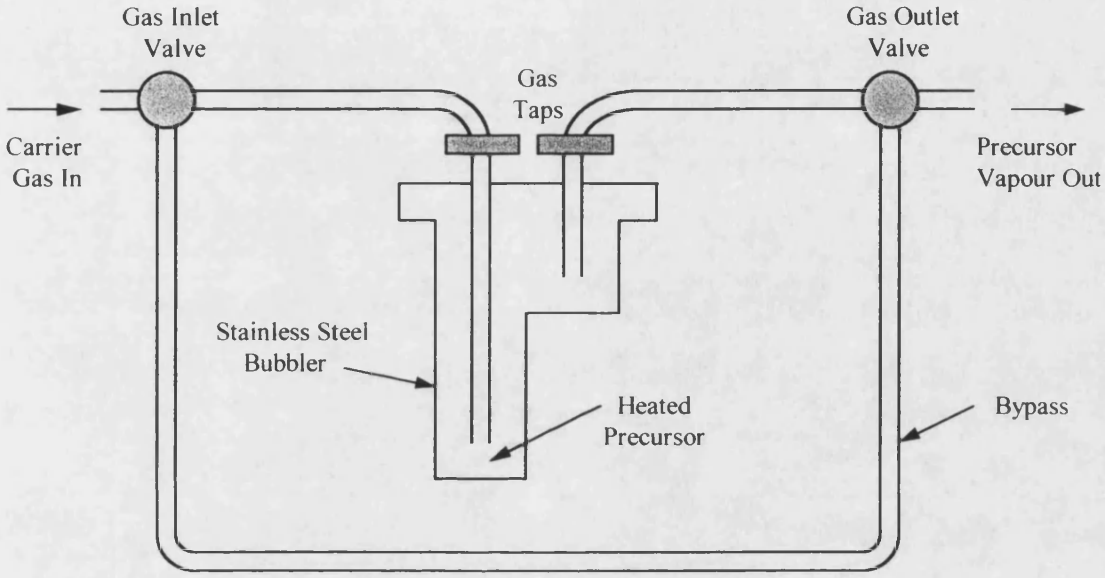

Figure A7.3 Schematic of the Bubbler Assembly

The bubbler was designed in such a way as to maximise the level of liquid contained. This prevented the need for vast quantities of precursor and made deposition experiments possible with relatively small quantities of material.

Following the turning of the valves to direct the gas flow to the bubbler, the precursor was swept from the bubbler and then mixed with nitrogen diluent and oxygen (if required) before being transported from the oven. The mixture was then transported along the heated external pipework to the CVD reactor. Before the vapour reached the CVD reactor, it passed through a baffle to promote laminar flow. A schematic of the reactor is shown in Figure A7.4.

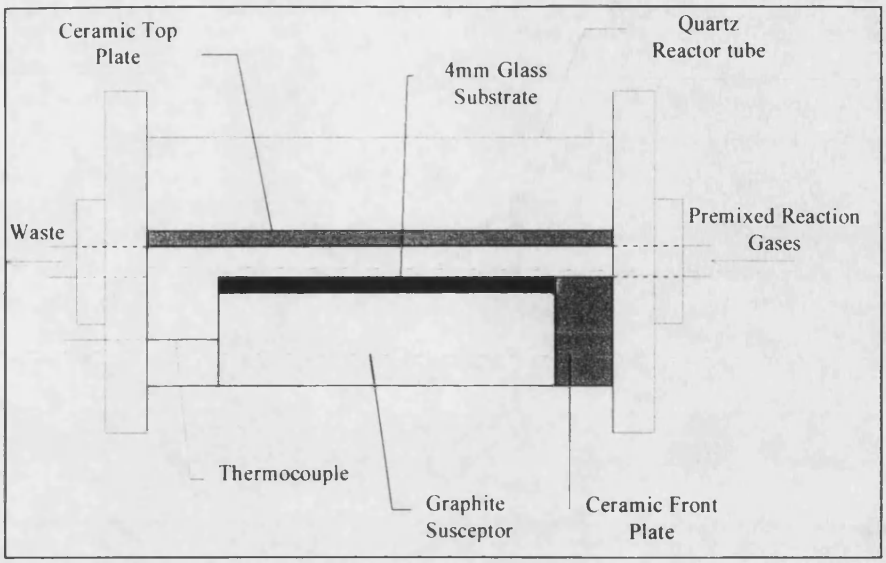

Figure A7.4 Schematic representation of the CVD reactor chamber.

After passing through the baffle, the precursor, in either vapour or aerosol form, depending on which transport system was being used, was passed directly into the reactor chamber which is 8 mm high, 40 mm wide and 300 mm long. The ceiling tile and walls consist of silica plates. The glass substrate is positioned upon a large graphite susceptor which is heated by three Watlow firerod cartridge heaters. The temperature of the graphite block is maintained by a Watlow series 965 controller which monitors the temperature by means of thermocouples positioned inside the block. The graphite susceptor is held inside a large silica tube (330 mm long, 100 mm diameter) suspended between stainless steel flanges upon which many of the electrical and gas line fittings are fixed. Air-tight seals are provided by "Viton" O-rings.

Substrate Preparation Procedure

All of the glass substrates were cleaned in an identical manner prior to use. The cleaning routine was as follows:

(i) The glass was washed thoroughly with tap water.

(ii) The glass was then washed thoroughly with copious amounts of distilled water.

(iii) The substrate was finally washed with a generous amount of isopropyl alcohol (IPA) and allowed to drain.

The glass was always prepared immediately prior to a deposition experiment to ensure as clean a substrate surface as possible. Following preparation and subsequent film deposition, the glass was handled very carefully and always outside of the deposition area.

Following the completion of the screening of each precursor, the bubbler, or the nebuliser, and associated pipework were thoroughly cleaned with a NaOH solution followed by acetone to prevent unwanted contamination in films deposited from subsequent precursors.

APPENDIX EIGHT

Numerical Index of Compounds Prepared in this Thesis

(1) $W(OPh)_6$

(2) $W(OC_6H_4F\text{-}4)_6$

(3) $W(OC_6H_3F_2\text{-}3,4)_6$

(4) $W(O)(OCH_2CF_3)_4$

(5) $[W(O)(OCH(CH_3)_2)_4]_2$

(6) $W(O)(OCH(CH_3)_3(dmae)$

(7) $W(O)(OCH(CH_3)_3(dmap)$

(8) $W_4(O)_4(dmae)O_6$

References

REFERENCES

1. C. G. Grenqvist, *Appl. Phys. A.*, **57**, 3 (1993).
2. S. K. Deb, *Appl. Opt.*, **3**, 192 (1969).
3. A. Kuzmin, J. Purans, E. Cazzanelli, C. Vinegoni and G. Mariotto, *J. Appl. Phys.*, **84**, 5515 (1998).
4. N. N. Greenwood and A. Earnshaw, *Chemistry of the Elements*, 1st Ed. Pergamon Press (1995).
5. F. A. Cotton and G. Wilkinson, *Advanced Inorganic Chemistry*, 5th Ed. John Wiley & Sons, Inc. (1988).
6. D. J. M. Bevan, *Comprehensive Inorganic Chemistry*, **4**, 491, Pergamon Press (1973).
7. J. V. Gabrusenoks, P. D. Cikmach, A. R. Lusis, J. J. Klepers and G. M. Ramans, *Solid State Ionics*, **14**, 25 (1984).
8. K. Bange and T. Gambke, *Adv. Mater.*, **2**, 10 (1990).
9. K. A. Gesheva and D. S. Gogova, *J. de Phys. IV*, **3**, 475 (1993).
10. O. A. Harizanovo, K. A. Gesheva and P. L. Stefchev, *Ceram. Int.*, **22**, 91 (1996).
11. C. G. Granqvist, *Thin Solid Films*, **193**, 730 (1990).
12. B. Buffat, *J. de Phys. IV*, **2**, C2 (1992).
13. Se-Hee Lee, H. M. Cheong Ji. Zhang and A. Mascarenhas, *Appl. Phys. Lett.*, 74, **242**, (1999).
14. T. J. Vink, E. P. Boonekamp and R. G. F. A. Verbeek, *J. Appl. Phys.*, **85**, 1540 (1999).
15. E. Brescacin, M. Basato and E. Tondell, *Chem. Mater.*, **11**, 314 (1999).
16. T. Matuyama and T. Kanagawa, *J. Electrochem. Soc.*, **141**, 2435 (1994).
17. T. Matuyama and T. Kanagawa, *J. Electrochem. Soc.*, **141**, 1021 (1994).
18. P. V. Ashrit, G. Bader and Vo-Van Truong, *Thin Solid Films*, **320**, 324 (1998).
19. C. Sella, M Maaza, O. Nemraoui, J. Lafait, N. Renard and Y. Sampeur, *Surfaces and Coatings*, **98**, 1477 (1998).
20. A. L. Dawar and J. C. Joshi, *J. Mat. Sci.*, **19**, 1 (1984).
21. T. Maekawa, J. Tamaki, N. Miura and N. Yamazoe, *Chem. Lett.*, 639 (1992).

22. J. H. Choy, Y. I. Kim, G. Campet, J. Portier and V. P. Huong, *J. Solid State Chem.*, **142**, 368 (1999).
23. M. D. Antonik, J. E. Schneider, E. L. Wittman, K. Snow and J. F. Vetelino, *Thin Solid Films*, **256**, 247 (1995).
24. B. Fruhberger, B, Grunze and D. J. Dwyer, *Sensors and Actuators B-Chem.*, **31**, 167 (1996).
25. Y. Yan, N. Miura and N. Yamazo, *Chem. Lett.*, 1753 (1994).
26. C. Cantalini, H. T. Sun, M, Faccio, M. Pelino, S. Santucci, L. Lozzi and M. Passacantando, *Sensors and Actuators B-Chem.*, **31**, 81 (1996).
27. A. A. Tomchenko, V. V. Khatko and I. L. Emelianov, *Sensors and Actuators B-Chem.*, **46**, 8 (1998).
28. D. Manno, A. Serra, M. Digiulio, G. Micocci and A. Tepore, *Thin Solid Films*, **324**, 44 (1998).
29. M. Penza, M. A. Tagliente, L. Mirenghi, C. Gerardi, C. Martucci and G. Cassano, *Sensors and Actuators B-Chem.*, **50**, 9 (1998).
30. M. Di. Gulio, D. Manno, G. Micocci, A. Serra and A. Tepore, *J. Mat. Sci. Mater. in Electronics.*, **9**, 317 (1998).
31. A. Donnadieu, D. Davazoglou and A. Abdellaoui, *SPIE*, **1016**, 124 (1988).
32. B. P. Jelle and G. Hagen, *J. Electrochem. Soc.*, **140**, 3560 (1993).
33. M. Rubin, *J. Vac. Sci. Technol. A.*, **10**, 1905 (1992).
34. J. Stanley, *PhD Thesis*, Universtiy of Bath (1997).
35. R. B. Nikodem, *J. Vac. Sci. Technol. A.*, **10**, 1884 (1992).
36. U. Riaz, *Thin Solid Films*, **235**, 15 (1993).
37. Ford Motor Company, *European Patent*, **22.10.92**, 92309656.4.
38. D. Davazoglou and A. Donnadieu, *Thin Solid Films*, **147**, 131 (1987).
39. D. Davazoglou and A. Donnadieu, *Thin Solid Films*, **164**, 369 (1988).
40. Z. Guanghui, S. A. Wessel and K. Colbow, *J. Phys. D: Appl. Phys.*, **21**, 1802 (1988).
41. D. Craigen, A. Mackintosh, J. Hickman and K. Colbow, *J. Electrochem. Soc.*, 1530 (1986).

42. D. V. Baxter, M. H. Chisholm, S. Doherty and N. E. Gruhn, *J. Chem. Soc., Chem.Commun.*, 1129 (1996).
43. O. Yamaguchi, D. Tomihisa, H. Kawabata and Kiyoshi, *J. Am. Ceram. Soc.*, **70**, C 94 (1987).
44. M. A. Habib and D. Glueck, *Sol. Energy Mater.*, **18**, 127 (1989).
45. J. P. Zhang and K, Colbow, *Appl. Phys. Lett.*, **58**, 1013 (1991).
46. J. M. Blocher, *Thin Solid Films*, 77, 51 (1981).
47. H. O. Pierson, *Handbook of Chemical Vapour Deposition*, Noyes Publications (1992).
48. K. L. Chopra, S. Major and D. K. Pandya, *Thin Solid Films*, **102**, 1 (1983).
49. K. F. Jenson and W. Kern, *Thin Film Processes II*, Academic Press (1991).
50. M. J. Hampden-Smith and T. T. Kodas, *Chem. Vap. Deposition*, **1**, 8 (1995).
51. M. J. Hampden-Smith and T. T. Kodas, *The Chemistry of Metal CVD*, VCH, Weinheim (1994).
52. J. T. Spencer, *Prog. Inorg. Chem.*, **41**, 145 (1994).
53. F. Maury, *Chem. Vap. Deposition*, **2**, 113 (1996).
54. B. E. Bent, R. G. Nuzzo and L. H. Dubios, *J. Am. Chem. Soc.*, **111**, 1634 (1989).
55. A. Gurav, T. Kodas, T. Pluym and Y. Xiong, *Aerosol Sci. and Technol.*, **19**, 411 (1993).
56. A. H. Lefebvre, *Atomisation and Sprays*, Hemisphere Publishing (1989).
57. K. R. May, *J. Aerosol Sci.*, **4**, 235 (1973).
58. R. A. Gussman, *Am. Ind. Hyg. Assoc. J.*, **45**, B8 (1984).
59. J. L. Vossen, *Physics of Thin Films*, **9**, 31 (1977).
60. R. U. Kirss and L. Meda, *Appl. Organometal. Chem.*, **12**, 155 (1998).
61. G. Watkins and D. Smith, *Autosport*, **156**, 13 (1999).
62. K. M. Mackay and R. A. Mackay, *Modern Inorganic Chemistry*, 5th Ed. Blackie (1999).
63. Z. Dori, *Prog. Inorg. Chem.*, **28**, 239 (1981).
64. Z. Dori, *Comprehensive Coordination Chemistry*, Pergamon Press **3**, 974 (1987).

65. R. A. Walton, *Prog. Inorg. Chem.*, **16**, 1 (1972).

66. G. W. Fraser, C. J. W. Gibbs and R. D. Peacock, *J. Chem. Soc. (A)*, 1708 (1970).

67. D. C. Bradley, M. H. Chisholm and M. W. Extine, *Inorg. Chem.*, **16**, 1792 (1977).

68. D. C. B Bradley, M. H. Chisholm, M. W. Extine and M. B. Hursthouse, *J. Chem. Soc., Chem. Commun.*, 1261 (1969).

69. D. C. Bradley, M. H. Chisholm, M. W. Extine and M. E. Stager, *Inorg. Chem.*, **16**, 1794 (1977).

70. J. S. Basi, D. C. Bradley and M. H. Chisholm, *J. Chem. Soc. (A)*, 1433 (1971).

71. D. C. Bradley and M. H. Gitlitz, *J. Chem. Soc., Chem. Commun.*, 289 (1965).

72. M. H. Chisholm, F. A. Cotton, M. Extine and B. R. Stults, *J. Am. Chem. Soc.*, **98**, 4477 (1976).

73. M. Akiyama, M. H. Chisholm, F. A. Cotton, M. W. Extine, D. A. Haitko, D. Little and P. E. Fanwick, *Inorg. Chem.*, **18**, 2266 (1979).

74. M. H. Chisholm, *J. Chem. Soc., Dalton Trans.*, 1781 (1996).

75. M. H. Chisholm, *Polyhedron*, **2**, 681 (1983).

76. A. L. Galyer and G. Wilkinson, *J. Chem. Soc. (A)*, 2235 (1976).

77. A. J. Shortland and G. Wilkinson, *J. Chem. Soc. (A)*, 872 (1973).

78. M. Green and H. S. Taylor *J. Chem. Soc. (A)*, 2629 (1972).

79. P. I. Mortimer and M. I. Strong, *Aust. J. Chem.*, **18**, 1579 (1965).

80. S. R. Fletcher, A. Shortland, A. S. Skapski and G. Wilkinson, *J. Chem. Soc., Chem. Commun.*, 922 (1972).

81. R. A. Jones, G Wilkinson, A. M. Galas and M. B. Hursthouse, *J. Chem. Soc., Chem. Commun.*, 926 (1979).

82. S. R. Fletcher and A. C. Skapski, *J. Organomet. Chem.*, **59**, 299 (1973).

83. H. Hess and H. Hartung, *Z. Anorg. Allg. Chem.*, **344**, 157 (1966).

84. A. J. Edwards and G. R. Jones, *J. Chem. Soc. (A)*, 2074 (1968).

85. I. R. Beattie and D. J. Reynolds, *J. Chem. Soc., Chem. Commun.*, 1531 (1968).

86. M. J. Bennett, T. E. Hass and J. T. Purdham, *Inorg. Chem.*, **11**, 207 (1972).

87. G. A. W. Fowles and J. L. Frost, *J. Chem. Soc. (A)*, 671 (1967).

88. H. Funk and G. Mohaupt, *Z. Anorg. Allg. Chem.*, **315**, 204 (1962).

89. M. G. B. Drew and R. Mandyczewsky, *J. Chem. Soc., Chem. Commun.*, 292 (1970).

90. C. Persson, A. Oskarsson and C. Andersson, *Polyhedron*, **11**, 2039 (1992).

91. K. Yamanouchi and S. Yamada, *Inorg. Chim. Acta*, **11**, 223 (1974).

92. W. Clegg, R. J. Errington, P. Kraxner and C. Redshaw, *J. Chem. Soc., Dalton Trans.*, 1431 (1992).

93. O. Jarchow, F. Schröder and H. Schulz, *Z. Anorg. Allg. Chem.*, **363**, 58 (1968).

94. C. G. Barraclough and J. Stals, *Aust. J. Chem.*, **19**, 741 (1966).

95. I. R. Beattie, K. M. S. Livingston, D. J. Reynolds and G. A. Ozin, *J. Chem. Soc. (A)*, 1210 (1967).

96. B. J. Brisdon, *Inorg. Chem.*, **6**, 1791 (1967).

97. K. Dreisch, C. Andersson and C. Stålhandske, *Polyhedron*, **10**, 2417 (1991).

98. A. Nikolovski, *Croatica Chemica Acta*, **40**, 143 (1968).

99. B. Šoptrajanov, A. Nikolovski and I. Petrov, *Spectrochimica Acta*, **24A**, 1617 (1968).

100. A. A. Eagle, E. R. T. Tiekink and C. G. Young, *Inorg. Chem.*, **36**, 6315 (1997).

101. W. P. Griffith and T. D. Wickins, *J. Chem. Soc. (A)*, 400 (1968).

102. R. S. Taylor, P. Gans, P. F. Knowles and A. G. Sykes, *J. Chem. Soc., Dalton Trans.*, 24 (1972).

103. M. S. Rau, C. M. Kretz, L. A. Meracando and G. L. Geoffroy, *J. Am. Chem. Soc.*, **113**, 7420 (1991).

104. M. S. Rau, C. M. Kretz and G. L. Geoffroy, *Organometallics*, **12**, 3447 (1993).

105. I. Feinstein-Jaffe, J. C. Dewan and R. R. Schrock, *Organometallics*, **4**, 1189 (1985).

106. M. H. Chisholm and I. P. Rothwell, *Comprehensive Coordination Chemistry*, **2**, 335 (1987).

107. K. C. Malhotra and R. L. Martin, *J. Organomet. Chem.*, **239**, 195 (1982).

108. F. Lefebvre, M. Leconte, S. Pagano, A. Mutch and J-M. Basset, *Polyhedron*, **14**, 3209 (1995).

109. H. Funk and W. Baumann, *Z. Anorg. Allg. Chem.*, **231**, 264 (1937).

110. H. Funk and W. Baumann, *Z. Anorg. Allg. Chem.*, **315**, 204 (1962).

111. M. W. Glenny, A. J. Nielson and C. E. F. Rickard, *Polyhedron*, **17**, 851 (1998).

112. A. Lehtonen and R. Sillanpää, *Polyhedron*, **18**, 175 (1998).

113. J. I. Davies, J. F. Gibson, A. C. Skapski, G. Wilkinson and W. Wong, *Polyhedron*, **1**, 641 (1982).

114. M. Minelli, J. H. Enemark, R. T. C. Brownlee, M. J. O'Connor and A.G.Wedd, *Coord. Chem. Rev.*, **68**, 169 (1985).

115. C. Brevard and P. Granger, *Handbook of High Resolution Multinuclear NMR*, John Wiley & Sons (1981).

116. W. McFarlane, A. M. Noble and J. M. Winfield, *J. Chem. Soc. A*, 948 (1971).

117. A. C. McDonell, S. G. Vasudevan, M. J. O'Connor and A. G. Wedd, *Aust. J. Chem.*, **38**, 1017 (1985).

118. L. P. Kazansky, P. Chaqiun, M. Fournier and G. Hervé, *Polyhedron*, **17**, 4353 (1998).

119. E. Breitmaier and G. Bauer, *^{13}C NMR Spectroscopy*, Harwood Academic Publishers (1984).

120. C. H. Dungan and J. R. Van Wazer, *Compilation of Reported ^{19}F NMR Chemical Shifts*, Wiley (1970).

121. Yu. T. Struchkov and G. M. Lobanova, *Chem. Abs.*, **54**, 8208a (1960).

122. D. C. Bradley, *Chem. Rev.*, **89**, 1317 (1989).

123. M. H. Chisholm, *J. Solid State Chem.*, **57**, 120 (1985).

124. D. C. Bradley, R. C. Mehrotra and P. D. Gaur, *Metal Alkoxides*, Academic Press (1978).

125. C. H. Peng and S. B. Desu, *J. Am. Ceram. Soc.*, **77**, 1799 (1994).

126. J. H. Wengrouvis and R. R. Schrock, Organometallics, **1**, 148 (1982).

127. H. Plenio, E. Egert, M. Nieger, H. W. Roesky, H. G. Schmidt and G. M. Sheldrick, *J. Fluorine Chem.*, **38**, 187 (1988).

128. F. A. Cotton, W. Schwotzer and E. S. Shamshoum, *Inorg. Chem.*, **23**, 4111 (1984).

129. P. Ballinger and F. A. Long, *J. Am. Chem. Soc.*, **81**, 1050 (1959).

130. G. M Loudon, *Organic Chemistry*, Benjamin Cummings (1988).

131. J. A. Samuels, Wen-C. Chiang, Chung-P. Yu, E. Aspen, D. C. Smith, D. V. Baxter and K. G. Caulton, *Chem. Mater.*, **6**, 1684 (1994).

132. W. A. Hermann, N. W. Hauber and O. Runte, *Angew. Chem., Int. Ed. Engl.*, **34**, 2187 (1995).

133. A. C. Jones, *Chem. Vap. Deposition*, **4**, 169 (1998).

134. A. C. Jones, T. J. Leedham, P. J. Wright, M. J. Crosbie, K. A. Fleeting, D. J. Otway, P. O'Brian and M. E. Pemble, *J. Mater. Chem.*, **8**, 1773 (1998).

135. U. B. Saxena, K. A. Rai, V. K. Mathur, R. C. Mehrotra and D. Radford, *J. Chem. Soc. A*, 904 (1970).

136. T. S. Cameron, T M. Klapotke, A. Shultz and J. Valkonen, *J. Chem. Soc., Dalton Trans.*, 659 (1993).

137. W. Clegg, R. J. Errington, D. C. R. Hockless and C. Redshaw, *J. Chem. Soc., Dalton Trans.*, 1965 (1993).

138. P. A. Van der Schaaf, J. Boersma, W. J. J. Smeets, A. L. Spek and G. Van Koten, *Inorg. Chem.*, **32**, 5108 (1993).

139. P. A. Van der Schaaf, W. J. J. Smeets, G. J. Van Koten, *Chem. Soc., Chem. Commun.*, 717 (1992).

140. J. J. Vittal, *Polyhedron*, **15**, 1585 (1996).

141. G. Fritz, *Angew. Chem., Int. Edn Engl.*, **26**, 1111 (1987).

142. I. G. Dance, *Polyhedron*, **5**, 1037 (1986).

143. J. Clade, F. Frick and M. Jansen, *Adv. Inorg. Chem.*, **41**, 327 (1994).

144. W. Nowacki, *Helv. Chim. Acta*, **28**, 1233 (1945).

145. J. Glerup, H. Weihe, P. A. Goodson and D. J. Hodgson, *Inorg. Chim. Acta*, **212**, 281 (1993).

146. N.Walker and D.Stewart, *Acta Cryst., Sect A*, **39**, 158 (1983).

147. Sheldrick G.M., *Acta Cryst.*, **A46**, 467-73 (1990)

148. Sheldrick G.M., SHELXL, a computer program for crystal structure refinement, University of Göttingen (1993).

149. McArdle P., *J.Appl.Cryst.*, **27**, 438 (1994).

150. R. Hooft, 'Collect', Nonius B.V., Delft, 1998.

151. Z. Otwinowski and W. Minor, in *Methods in Enzymology*, **276**, 1996, *pp* 307 - 326. C. W. Carter and R. M. Sweet (Eds.), Academic Press, New York.

152. G. M. Sheldrick, 'SHELXL-97', University of Göttingen, 1997.

153. L. J. Barbour, 'XSeed, A Program of the Manipulation and Display of Crystallographic Models', University of Missouri - Columbia, 1999.